Flywheel Rotor Safe-Life Technology
Literature Search Summary

J.K.H. Ratner, J.B. Chang, and D.A. Christopher
Aerospace Corporation, El Segundo, California

Flywheel Rotor Safe-Life Technology

Literature Search Summary

J.K.H. Ratner, J.B. Chang, and D.A. Christopher
Aerospace Corporation, El Segundo, California

National Aeronautics and
Space Administration

Glenn Research Center

July 2002

Acknowledgments

Available from

iii

Since its founding, NASA has been dedicated to the advancement of aeronautics and space science. The NASA Scientific and Technical Information (STI) Program Office plays a key part in helping NASA maintain this important role.

The NASA STI Program Office is operated by Langley Research Center, the Lead Center for NASA's scientific and technical information. The NASA STI Program Office provides access to the NASA STI Database, the largest collection of aeronautical and space science STI in the world. The Program Office is also NASA's institutional mechanism for disseminating the results of its research and development activities. These results are published by NASA in the NASA STI Report Series, which includes the following report types:

- TECHNICAL PUBLICATION. Reports of completed research or a major significant phase of research that present the results of NASA programs and include extensive data or theoretical analysis. Includes compilations of significant scientific and technical data and information deemed to be of continuing reference value. NASA's counterpart of peer-reviewed formal professional papers but has less stringent limitations on manuscript length and extent of graphic presentations.

- TECHNICAL MEMORANDUM. Scientific and technical findings that are preliminary or of specialized interest, e.g., quick release reports, working papers, and bibliographies that contain minimal annotation. Does not contain extensive analysis.

- CONTRACTOR REPORT. Scientific and technical findings by NASA-sponsored contractors and grantees.

- CONFERENCE PUBLICATION. Collected papers from scientific and technical conferences, symposia, seminars, or other meetings sponsored or cosponsored by NASA.

- SPECIAL PUBLICATION. Scientific, technical, or historical information from NASA programs, projects, and missions, often concerned with subjects having substantial public interest.

- TECHNICAL TRANSLATION. English-language translations of foreign scientific and technical material pertinent to NASA's mission.

Specialized services that complement the STI Program Office's diverse offerings include creating custom thesauri, building customized data bases, organizing and publishing research results . . . even providing videos.

For more information about the NASA STI Program Office, see the following:

- Access the NASA STI Program Home Page at *http://www.sti.nasa.gov*

- E-mail your question via the Internet to help@sti.nasa.gov

- Fax your question to the NASA Access Help Desk at 301–621–0134

- Telephone the NASA Access Help Desk at 301–621–0390

- Write to:
  NASA Access Help Desk
  NASA Center for AeroSpace Information
  7121 Standard Drive
  Hanover, MD 21076

ABSTRACT

Since the 1960s, research has been conducted into the use of flywheels as energy storage systems. The proposed applications include energy storage for hybrid and electric automobiles, attitude control and energy storage for satellites, and uninterruptible power supplies for hospitals and computer centers. For many years, the use of flywheels for space applications was restricted by the total weight of a system employing a metal rotor. With recent technological advances in the manufacturing of composite materials, lightweight composite rotors have begun to be proposed for such applications.

Flywheels with composite rotors provide much higher power and energy storage capabilities than conventional chemical batteries. The failure of a high speed flywheel rotor could be a catastrophic event. For this reason, flywheel rotors are classified by the NASA Fracture Control Requirements Standard as fracture critical parts. Currently, there is no industry standard to certify a composite rotor for safe and reliable operation for the required lifetime of the flywheel. Technical problems hindering the development of this standard include composite manufacturing inconsistencies, insufficient nondestructive evaluation (NDE) techniques for detecting defects and/or impact damage, lack of standard material test methods for characterizing composite rotor design allowables, and no unified proof (over-spin) test for flight rotors.

As part of a flywheel rotor safe-life certification program funded by the government, a review of the state of the art in composite rotors is in progress. The goal of the review is to provide a clear picture of composite flywheel rotor technologies. The literature review has concentrated on the following topics concerning composites and composite rotors: durability (fatigue) and damage tolerance (safe-life) analysis and test methods, in-service NDE and health monitoring techniques, spin test methods and procedures, and containment options. This report presents the papers selected for their relevance to this topic, and summarizes them.

vi

Contents

viii

Introduction

Flywheels are mechanical devices that store kinetic energy in a rotating mass. A simple example is the potter's wheel, which was widely used by people in ancient times. The first use of such devices dates from between 3500 and 3000 BC. According to archeological evidence, these early flywheels were built from wood, stone and clay. One type of potter's wheel was the a rim made from a unidirectional material (bamboo) wound in the hoop direction and embedded in a matrix (clay). This design option is clearly a foreshadowing of the later use of composites for their inherent strength and lightweight nature.

It was, however, only since the 1970s that the use of flywheels as energy storage systems has gained some serious attention from energy researchers due to the constant threat of a shortage of fossil fuel supplies. Today, a typical flywheel energy system consists of a flywheel rotor, a supporting device (magnetic bearing), a charge/discharge device (motor/generator), and a safety containment (housing). For space applications, due to weight constraints, the use of a bulky safety containment system may not be a desirable design. Thus, from a safety point of view, the design of flywheel energy systems must concentrate on reliability and longevity.

Current flywheel energy storage technology is made possible by the use of high-strength, carbon-fiber-based composite materials in the rotor. Flywheel energy storage systems are designed to both control spacecraft attitude and to store energy, functions which have historically been performed by two separate systems. The stored energy is needed for the dark portions of the orbit when Earth's shadow makes solar power unavailable for spacecraft. For many spacecraft, flywheels offer the potential to significantly reduce weight and extend service life. However, use of composite materials, coupled with variations in design approaches and demanding operating conditions, combine to present certification challenges for the rotor assemblies.

The Flywheel Rotor Safe-Life Working Group (FRSL/WG) is one element of NASA Glenn Research Center's (GRC's) FRSL technologies project. The goals of this project are to "...define a standard man-rated flywheel qualification process for aerospace applications using a safe-life approach for rotor certification that is accepted by the user community." NASA has tasked The Aerospace Corporation with providing leadership to the WG. Mr. Jim Chang provides this leadership as the WG chairman. The Air Force Research Laboratory (AFRL) also provides technical support to the WG. Other elements of GRC's FRSL technologies project include tasks to provide innovative material characterization and life-cycle test methods, NDE techniques, and facilities for rotor testing.

The FRSL/WG intends to define requirements that provide for different levels of certification for different types of spacecraft, such as low-cost, small NASA satellites, high-value military spacecraft, or manned space stations like the International Space Station. The focus in all cases will be on defining a common approach to ensure rotor safety, reliability, and longevity. The resulting standard will aid flywheel manufacturers in marketing their systems, and assure customers that this technology will meet their requirements.

As part of a flywheel rotor safe-life certification program, a review of the state of the art in composite rotors is being conducted. The goal of the review is to provide a clear picture of composite flywheel rotor technologies. This will ensure that the technology has been thoroughly reviewed in order to produce a complete set of requirements that provide for different levels of certification for flywheel assemblies in different types of spacecraft. The literature review has concentrated on the following topics concerning composites and composite rotors: durability (fatigue) and damage tolerance (safe-life) analysis/test methods, in-service NDE and health monitoring techniques, spin test methods/procedures, and containment options. This report presents the papers selected for their relevance to this topic, and summarizes them.

1.0 Certification Plans & Standards

This section contains the review summaries of the following articles:

- Flanagan, R. C. and D. A. Flanagan, Flywheel Systems Inc., *Integrated Power and Attitude Control System Rotor Safe Life Program Preliminary Plan—Non-Confidential Version*, Report No. CSA-ST-CR-2000-0011, 2000.
- Anon, *Flywheel Energy Storage System (FESS) Rotor Certification Plan*, NASA 69011-B01-PLAN-M-311, 2000.
- Anon, *Space Systems – Composite Overwrapped Pressure Vessels (COPVs)*, ANSI/AIAA S-081-2000, 2000.
- Anon, *Fracture Control Implementation Handbook for Payloads, Experiments, and Similar Hardware* (Draft), 2000.
- Anon, *Damage Resistance, Damage Tolerance, and Durability*, MIL-HDBK17-98 (DRAFT), 1998.
- Bender, D. A., "Criteria for Safe Flywheel Operation, Revision 0.1," White Paper – Trinity Flywheel Power, 1997.
- Anon, *Fracture Control Requirements for Payloads Using the Space Shuttle*, NASA-STD-5003, 1996.
- Tropis, A., *et al.*, "Certification of the Composite Outer Wing of the ATR72," *Proceedings of the Institution of Mechanical Engineers*, Part G, Vol. 209:327-339, 1994.

CATEGORY

Certification Plans & Standards

REFERENCE

Flanagan, R. C. and D. A. Flanagan, Flywheel Systems Inc., *Integrated Power and Attitude Control System Rotor Safe Life Program Preliminary Plan—Non-Confidential Version*, Report No. CSA-ST-CR-2000-0011, 2000.

ABSTRACT

This report describes a program plan to develop flight ready composite energy storage rotors-The Rotor Safe Life Program – For Integrated Power and Attitude Control Systems (IPACS).

Initially, flywheel rotor design, fabrication, acceptance and certification standards, applicable to all composite rotors, are proposed. Thereafter, a preliminary Rotor Safe Life Plan is presented for the IPACS rotor.

SUMMARY

The objective of this work was to develop a preliminary plan for a Rotor Safe-Life Program specific to the Integrated Power and Attitude Control System. It is intended that this plan form the basis for discussions among the development team and user community to establish a final, community agreed upon standard IPACS Rotor Safe-Life Program. Figure 1-1 presents a conceptual view of the IPACS flywheel.

The plan first proposes a standard applicable to all composite flywheel rotors. The standard addresses rotor design, fabrication, acceptance and certification. Thereafter, a technical plan establishes the effort required to bring the IPACS rotor to flight qualified status.

Rotor safe-life must be an integral part of any flywheel development program. Well justified concerns have been raised about the safety of using a composite rotor for energy storage. Rotor safety is seen as one of the foremost challenges to be resolved for the commercial deployment of flywheels.

From numerous meetings and discussions with members of the flywheel and aerospace communities, and from this investigation, it is concluded:

a) flywheel rotor safety can be assured, and
b) the only acceptable approach to flywheel safety is safe-life with rigorous design, fabrication, acceptance and certification standards.

Rotor Safe-Life
There are two fundamental requirements that must be respected for rotor safety. First, design margins for all safety critical rotor failure modes must be based on a statistical margin at end of

life. These statistical margins must be determined from test articles fabricated by the rotor vendor. Second, monitoring, controlling, and documenting the composite fabrication process must be at a level that will assure no deviation among the flight hardware, the certification hardware and the test articles.

The reasons for these two overriding constraints are well known:

a) There are literally thousands of combinations of fibers, resins and hardeners.
b) The properties of each composite material is fabrication and process dependent.
c) The mechanical properties and fatigue characteristics of composites can vary widely not only due to the raw materials selected but also due to the fabrication process employed.

The proposed rotor design and fabrication standards address both of these requirements. The design standard recommends a very conservative six sigma (6σ - one in one billion) statistical margin at end of life for all safety critical rotor failure modes. Statistical data is to be determined from representative test articles (e.g. rotor size hydroburst rings) that are wholly traceable to the flight rotor in all aspects of fabrication. Additionally, for composite materials, a minimum safety factor of two (2) must be shown at the beginning of life for worst case or extreme environmental and operating conditions. The rotor fabrication standard assures that all procedures are fixed prior to the fabrication of the test articles and further assures that the process does not deviate for flight rotors.

The rotor acceptance standard recommends that measurement, non-destructive inspection and a spin test operational compliance be used for all flight and flight-like rotors. Among other properties, measurement includes composite rim mass in air and mass in water. These properties largely assure composite consistency (volume fraction, void content).

The acceptance spin test recommended twice exposes the rotor to an overspeed condition for a duration of 10 minutes. The overspeed condition specified (105% normal operating upper speed) has been selected, instead of an overstress condition, to provide a proof test state that is readily verified, independent of analysis and, consequently, free from analytical error. The data collected provide a baseline for comparison after cycle testing and assure the operational compliance of the rotor.

Between the two overspeed runs, the rotor is cycled between normal operating upper and lower speed limits for 100 cycles. While this test consumes only 0.2% of the anticipated useful cycle life of the rotor (assuming 50,000 cycles in one lifetime), it exposes the materials to greater than 40% of the fatigue degradation anticipated from usage. If the rotor has undetected fatigue sensitive flaws, these are likely to show up early in the cycle life.

Rotor certification is to be conducted by a wholly independent laboratory. All certification tests are performed on flight-like rotors. The beginning of life design margin is assured from three burst tests. If the tests do not confirm the design margins, up to ten additional burst tests can be used to establish the rotor mean failure speed. Based on these data, the statistical margin at end of life is adjusted and the rotor operating speed or cycle life is adjusted accordingly to assure compliance with the design standard.

All non-safety critical failures of the rotor are considered safety critical until demonstrated by flight-like hardware to be non-safety critical. Certification of the non-safety critical failure modes is assured by operating a failed flight-like rotor through a complete acceptance spin test including the ten minute duration pre- and post-overspeed cycles. If a rotor does not pass this test, the safety critical design standards are imposed on that failure mode.

For end of life design margin verification, two life cycle approaches are presented for consideration. Approach 1 uses three flight-like rotors. One rotor is subjected to full life cycle events, including environmental conditioning and random vibration, for one complete lifetime (1x life). The aged rotor is end of life tested to demonstrate the existence of design margin at end of life. Recommended end of life tests are as follows:

a) the rotor is held at 105% of the normal operating speed at each temperature extreme for a period of ten minutes;
b) the rotor is spun through failure onset and burst at normal operating conditions. The two additional rotors are subjected to full life cycle events, including environmental conditioning and operational effects, for four sequential lifetimes (4 x life).

Approach 2 recommends that one flight-like rotor be subjected to full life cycle events, including environmental conditioning and random vibration, for four sequential lifetimes (4 x life). The aged rotor is end of life tested as above.

IPACS Rotor Safe-Life Program
The IPACS Rotor Safe-Life Program is composed of three distinct, parallel streams: development, certification, and process control. The development stream provides resolution of all technical aspects necessary to deploy a flight rotor. The process control stream provides adequate proof that the flight rotor does not deviate from the certified flight-like rotor in any substantive manner. The certification stream provides an independent, unvarnished verification that a flight-like rotor has performed as required. Figure 1-2 below shows how these streams constitute a technology roadmap from the existing state of the art to a flight rotor.

The rotor development and process control streams have been integrated in this plan. Tasks 1 through 7 focus on the material mechanical and fatigue properties required for rotor design and certification. Tasks 8 through 11 focus on the IPACS rotor design, composite rim refinement and analysis verification. While the rotor development and process control requirements can be defined with good certainty, this was not the case for the rotor certification stream. As such, two approaches are presented for consideration. The two approaches differ only in the number of rotors subjected to life cycle testing. Approach 1 uses three rotors for life cycle testing while Approach 2 uses one rotor.

The thrust of the rotor development and process control program is based on:

a) obtaining material mechanical properties that relate directly to or control the failure modes of the rotor,
b) internally verifying the rotor design,
c) implementing process and documentation controls for all procedures.

The IPACS composite rim is a multi-material multi-ring design employing four composite rings fabricated from four different fibers. To meet the rotor design standards, a directed and comprehensive materials property program has been structured. Mechanical and fatigue properties for the composite materials used in the rotor are determined from test articles that are representative of the rotor composite rings. Table S-4 summarizes the material properties test plan. This table also incorporates data from Task 11 where the evaluation of flight-like rotors enables final rim adjustments and correlations with the material database developed to ensure that the rotor design standards are met.

Process and documentation controls, suitable for incorporation into an ISO 9000 quality manual, are implemented for all fabrication and test procedures. This includes rim and test articles, composite filament winding, curing, machining, and assembly. Also, composite fabrication and rim/component assembly are conducted in a "good housekeeping" area.

Rotor analysis verification occurs at the development level and at the certification level to provide complete independent rotor analysis certification.

Table S-5 summarizes the tasks where rotor analysis verification occurs. At the development level, test programs are structured to enable confirmation and refinement of the analysis and models being used. Task 7.4 specifically targets hub-rim integrated analysis (as opposed to just hub FEA which is easy to verify but not meaningful) by direct comparison of experimental and analytical hub yield under overspeed test conditions. For this test, IPACS rotors are used. These tests will also provide the overspeed dynamic characteristics of the IPACS rotor correlated to rpm. This data will allow control and detection strategies, at the flywheel level, to be developed as part of the overall safety of the flywheel.

The composite rim analysis is evaluated in Tasks 8 and 10. Task 8.3 targets longitudinal stress analysis, again by direct comparison of rim burst test speeds with analytical projections. For these tests, IPACS rotors are again used. Transverse rim stress analysis is evaluated in Task 10.2. Here IPACS sized rings are fabricated and dynamically spun to failure. Each of the four materials is individually tested. Again, rim analysis is based on the direct comparison of analytical and experimental failure speeds. As above, this data will also allow control and detection strategies, at the flywheel level, to be developed as integral to the overall safety of the flywheel.
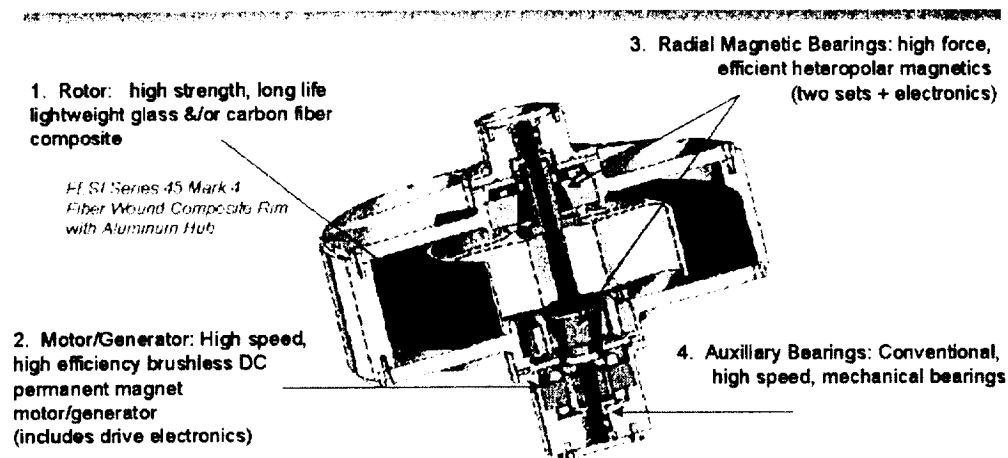
The rotor design standard must be verified during the certification tests. The tests defined in Tasks 14, 15 and 16 are designed to verify, and specifically target, the rotor design standards. Hub and composite rim stress verification in Task 14.2 are identical in procedure to Tasks 7.4 and 8.3 described above except that they are conducted, at the certification level, by an independent laboratory and on final flight-like rotors.

In Task 15.2, tests verify certain rotor failure modes as non-safety critical. Here, four flight-like IPACS rotors are intentionally failed to replicate the worst case failure scenario of each of the non-safety critical features. The failed rotors are then subjected to a complete acceptance standard spin test: each failed rotor will be spun to 105% operating speed and held for ten minutes, followed by 100 cycles over the normal operating range, and then returned to 105% speed for ten minutes.

End of life rotor design margins are proven in Task 16.2. The tests include overspeed at the operating temperature extremes followed by a burst test.

Figures 1-3 to 1-5 show composite rims and a flex-rim hub that are proposed to be tested. One aspect of the safe life program is that of testing the rotors for 4 lifetimes. Flywheels that could be put of the Space Station would need to perform their duties for a single lifetime of up to 10 years. The IPACS plan discusses the issue of cost, and proposes the testing of multiple flight-like rotors in one facility concurrently. This does not totally cover the issue of time. Accelerated testing methods must be discussed to test the rotors appropriately and under the right conditions.

Introduction to Flywheels

1. Rotor: high strength, long life lightweight glass &/or carbon fiber composite

   HESI Series 45 Mark 4 Fiber Wound Composite Rim with Aluminum Hub

2. Motor/Generator: High speed, high efficiency brushless DC permanent magnet motor/generator (includes drive electronics)

3. Radial Magnetic Bearings: high force, efficient heteropolar magnetics (two sets + electronics)

4. Auxiliary Bearings: Conventional, high speed, mechanical bearings

A Flywheel stores kinetic energy in a high speed rotating composite rotor and provides on-demand electrical power with a high efficiency motor/generator

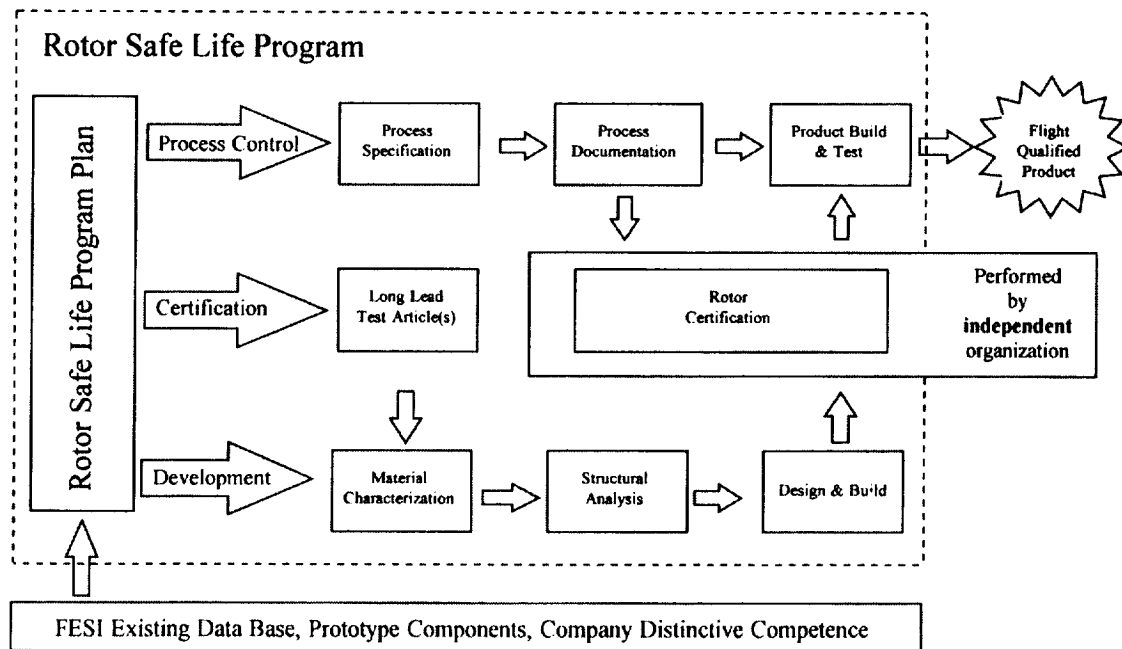Figure 1-1: IPACS Flywheel (courtesy of Honeywell International Inc.).
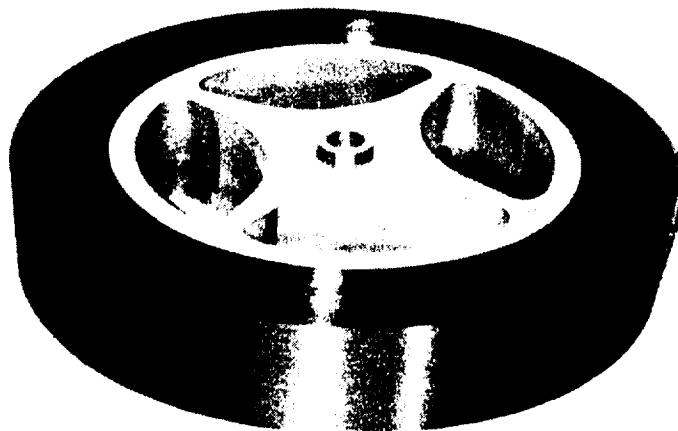
1-6

Figure 1-2: Rotor technology roadmap.

Figure 1-3: IPACS Series 45 Mark 4 Rotor.

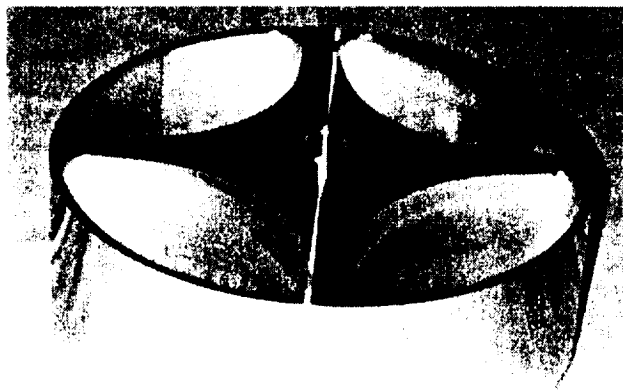**Figure 1-4: Series 45 Composite Rims (Mark 4, Mark 3, Mark 2, Mark 1).**

Figure 1-5: Flex-rim hub.

CATEGORY

Certification Plans & Standards

REFERENCE

Anon, *Flywheel Energy Storage System (FESS) Rotor Certification Plan*, NASA 69011-B01-PLAN-M-311, 2000.

SCOPE

This document defines the approach that will be used to satisfy the requirements of SSP 41172C "Qualification and Acceptance Environmental Test Requirements," SSP 30558B "Fracture Control Requirements of Space Station" and SSP 30559B "Structural Design and Verification Requirements" specifically for the FESS rotor. This document pertains to all the components that comprise the FESS rotor assembly. This is also the document which gives direction, guidelines and safety criteria for the rotor designers, manufacturers and their subcontractors. Deviations from this document during the design, manufacturing or testing phases of the FESS rotor by entities under contract with NASA must not be undertaken without prior approval of the FESS project management.

SUMMARY

The rotor and shaft are considered fracture critical.

The main criteria for certifying the rotors is:

a) Verifying positive margins on strength through analysis and test under extremes of service loads and environments.
b) Designing for fatigue/safe-life showing proper margins on fatigue/fracture and durability.

The way in which this will be accomplished will involve:

a) Materials testing to determine the design allowables for the composite used in the composite rim.
b) Structural analysis, design development testing (sub-component level) and damage tolerance testing to identify failure modes and hot spots in the design, with static fatigue tests to be done on specimens of adequate fidelity to simulate the full-scale failure mode.
c) Full scale certification test to demonstrate the overall reliability of the rotor and identify any unanticipated hot spots, with separate static strength and fatigue tests taking into account worst case environment extremes.
d) Proper manufacturing, inspection and overall Q/A processes relying on comprehensive NDE plan to relate quality of test rotors to flight hardware and to ensure superior workmanship of flight hardware.

Testing to four service life cycles will be accelerated. Prior to testing the rotors will be cold temperature soaked, subject to Qualification level random vibration loads and exposed to 4 x expected total dose of radiation.

The project goal is for the FESS rotor to have a calculated structural reliability 0f 0.9_6 over its service life. The plan included the following list for comparison of reliability requirements:

Reliability requirements on Safe-life designs:

- U.S. ARMY (1992): Helicopter safe-life components fatigue design - 0.9_6 (over design life)
- Airbus Aircraft (system reliability against catastrophic failures) - 0.9_6 (per flight)
- Automatic landing systems (Airworthiness req. against fatal accident) - 0.9_7 (per landing)
- Boeing Defense and Space Group Helicopter division (1991): Rotorcraft component design - 0.9_6 (over service life)
- U.S. ARMY (1988): Light Experimental Helicopter Program - 0.9_6 (over service life)
- Oil rig platform (system reliability against a class III (serious) failure - 0.9_6 (per platform year)
- Automotive transmission components (for comparison) – 0.9_4 (over warranty life)
- US industry at-large worker survival record (1990) - 0.999945 (per 1000 man hours)
- U.S. Space Transportation System (Space Shuttle- post Challenger) - 0.999 (crew survival per flight)

Table 1-1: Factors of Safety for Test Verified Structure

	Yield	Ultimate
A. Minimum Factors of Safety for Metallic Flight Structures		
Space Shuttle	1.0	1.4
On-Orbit	1.1	1.5
B. Minimum Factors of Safety for Non-metallic Flight Structures		
Non-discontinuity areas		
Space Shuttle	N/A	1.4
On-Orbit	N/A	1.5
Discontinuity areas		
Space Shuttle	N/A	2.0
On-Orbit	N/A	2.0

Table 1-2: Rotor Component Classification

Component	Polar Inertia (lb-in-sec^2)	Energy @ 53.1 krpm (Joules)	Classification
Mag. Bearing (TE)	.010	17280	Nonfracture Critical - Contained
Mag. Bearing stack #1 (NTE)	.006	10368	Nonfracture Critical - Contained
Mag. Bearing stack #2 (NTE)	.006	10368	Nonfracture Critical - Contained
Mag. Bearing Spacer (NTE)	.0004	6912	Nonfracture Critical - Contained
Motor magnets, Be-Cu sleeve, overwrap, back iron	.0110	19008	Nonfracture Critical - Contained
T/D sleeves (TE or NTE)	.0002	345	Nonfracture Critical - Contained
Sensor lams (TE)	.003	5184	Nonfracture Critical - Contained
Sensor lams (NTE)	.002	3456	Nonfracture Critical - Contained
Motor magnet retainer	.005	8640	Nonfracture Critical - Contained
Shaft	25.17	43.4937e6	Fracture Critical
Rim	74.18	128.183e6	Fracture Critical

Table 1-3: Rotor Speed Definitions

Term	Speed	Definition
Max.Normal Operating Speed (MNOS)	53,000 rpm	Same as nominal speed. Maximum speed during normal operation.
Maximum Operating Speed (MOS)	53,100 rpm (TBR)	Speed at which two fault tolerant alarms and shutdowns are set in control system. Also the "limit load" speed. Also the "design speed."
"Failure event" Speed	> 122% MOS (equal 1.5 S.F. on stress)	Speed at which tensile failure of rotor occurs or any failure that potentially creates a catastrophic hazard.

1-11

Table 1-4: Key FESS Rotor Certification Requirements

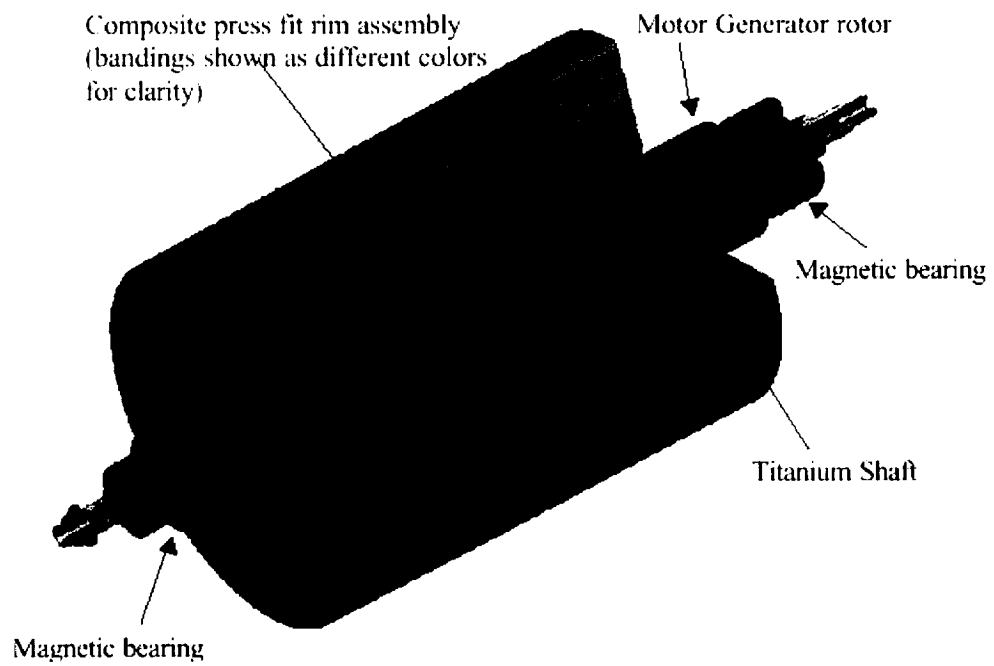| ISS Requirements	FESS Minimum Certification Plan	FESS Goals
Verify positive margin (S.M >0.0) on Static strength with Safety Factor of 1.5 on composite and metallic components using A-Basis allowables	Verify positive safety margin on Static strength with Safety Factor of 1.5 on composite and metallic components. A basis aallowables determined by MIL-HDBK-17 approach.	
No requirement for static strength safety factors at end of service life.	Safelife test articles to be burst tested after safelife verification to determine margins	• Demonstrate positive static strength margin on 1.5 S.F after safelife testing • Verify 0.9₉ probability of survival at end of service life
Verify Safelife requirement that largest undetected flaw will not grow to failure when subjected to cyclic and sustained loads of 4x service lives. • Analysis is acceptable for metallic components • Test verification required on composite parts. *(4x safelife safety factor only applies to the control of fracture, and only applies to fracture critical parts.)*	**Fracture Critical metallic components** Analysis- FLAGRO analysis to 4x service life cycles. Fracture Critical composite components: • Coupon tests (all environments, flaws) • Three (3) preflawed rotor spin test articles cycled to 4x service lives cycles, at max temp.	Composite Life Prediction Modeling to verify 4x service life Test 3 **full** (composite and metallic) FESS rotor assemblies to full Safelife requirements
Creep analysis- demonstrate a minimum calculated life of 4.0x the service life, where limit strain is multiplied by a minimum factor of 1.15 to determine creep life	Creep testing/analysis will be per ISS requirements. Will assume 100% of service life will be at **max** temperature, providing most conservative condition for creep effects.	
No requirement for Safelife designed hardware to incorporate failsafe/redundant design features		Incorporate PLM as redundant feature to safelife design. Rotor design would fatigue gracefully, with noticeable signature- progressive loss of balance
Flight acceptance of composite structures will be by **either** of 1) proof test to 120% limit load or 2) demonstration that manufacturing is done by trained personnel, follows certified spec's and is properly inspected for quality and hardware integrity	Flight Hardware will be accepted by accomplishing **both** 120% proof test **and** demonstrating acceptable Q/A processes inferred by the ISS requirements	
No present requirement for "fleet leader" or certification test articles.	Flight hardware will be made with extra stock from which random burst test articles, cycle test articles and/or general Q/A specimens can be made- same manufacturing heritage as flight hardware.	PT, EM or Qual hardware can become fleet leader unit(s) for cyclic ground testing at realistic duty cycles

Composite press fit rim assembly
(bandings shown as different colors
for clarity)

Motor Generator rotor

Magnetic bearing

Titanium Shaft

Magnetic bearing

Figure 1-6: FESS rotor assembly – cutaway view

CATEGORY

Certification Plans & Standards

REFERENCE

Anon, *Space Systems – Composite Overwrapped Pressure Vessels (COPVs)*, ANSI/AIAA S-081-2000, 2000.

ABSTRACT

This standard establishes baseline requirements for the design, fabrication, test inspection operation and maintenance of composite overwrapped pressure vessels (COPVs) used for pressurized, hazardous or non-hazardous, liquid or gas storage in space systems such as spacecraft and launch vehicles. These requirements, when implemented on a particular system, will assure a high level of confidence in achieving safe and reliable operation.

SUMMARY

Important requirements are:

Strength Requirements:

a) COPVs must be sufficiently strong to withstand limit loads and simultaneously occurring internal pressures in the expected operating environments throughout their service lives without experiencing detrimental deformation.
b) The margin of safety shall be positive and shall be determined by analysis or test at ultimate and limit load levels at the temperature expected for all critical conditions.
c) The margins of safety shall be based on A-basis allowables.
d) The minimum burst factor shall be 1.5.

Stress Analysis Requirements:

a) Loads shall be combined by using the appropriate design safety factors on the individual loads and comparing the results to A-basis allowables.
b) Finite element or other proven equivalent structural analysis techniques shall be used to calculate the stresses, strains, and displacements for complex geometries and loading conditions.
c) A methodology using composite laminate theory shall be employed to analyze the composite. Effects of ply orientation, stacking sequence, and geometrical discontinuities shall be assessed.

Leak-Before-Burst Requirements:

a) Only the regions of the COPV covered by the composite are required to exhibit a leak-before-burst (LBB) failure mode at MEOP.

b) When the liner remains elastic at all pressures and/or loads in the serve life, linear elastic mechanics shall be used to show that the following conditions must be satisfied:

- An initial part through crack (surface flaw) with a shape (a/2c) ranging from 0.1 to 0.5 shall not fail (cause catastrophic burst) at any stress intensity factor applied during the service life, and
- This part-through crack shall grow through the wall of the pressure vessel liner to become a through crack with a length equal to ten times the wall thickness thereby leaking out the contents before burst can occur.

Fatigue-Life Requirements:

For COPVs with LBB metallic liners that contains non-hazardous fluids, fatigue analysis or test shall be conducted as follows:

a) A fatigue analysis is required to demonstrate the fatigue life of an unflawed COPV.

b) Testing of unflawed specimens to demonstrate fatigue-life of specific hardware together with stress analysis is an acceptable alternative to analytical prediction.

c) Fatigue-life requirements are considered demonstrated when the unflawed specimens successfully sustain the limit loads and MEOP in the expected operating environments for the specified test cycles and duration without rupture.

d) The required test duration is four (4) times the specified service life or number of cycles.

Safe-Life Requirements:

For COPVs contain hazardous fluids, or the metallic liners exhibit brittle fracture failure mode, it shall demonstrate that the liner has adequate safe-life.

a) Safe-life shall be demonstrated by analysis or test. Initial flaw size assumptions shall be based on NDE flaw detection ability. Safe-life requirements only apply to the metallic liner and integral bosses.

b) A life factor of four (4) shall be applied.

Stress-Rupture Requirements:

a) The COPV shall be designed to meet the design life considering the time it is under sustained load.

b) There shall be no credible stress rupture failure modes based on stress rupture data for a probability of survival of 0.999.

Damage Control Requirements:

a) COPVs with a burst factor of 4.0 or greater and a total wall thickness of 0.25 mm or greater are exempted from the requirements below.

b) For mechanical damage mitigation, a minimum of one of the following approaches shall be adapted:
- Mechanical Damage Protection/Indication
- Damage Tolerance Demonstration

The requirement for protection gives specific instructions about the protective cover to be chosen. Protective covers are required when personnel will be exposed to pressurized COPVs having stored energy levels in excess of 14,240 ft-lbf or containing hazardous fluids. They shall allow the transmission of less than 5 ft-lbf of energy or reduce the transmitted energy to a level not to exceed one half that demonstrated as acceptable by pressurized damage tolerance or residual strength testing.

Acceptance Test Requirements

Acceptance tests shall be conducted on every COPV as follows:

a) Nondestructive inspection
b) Proof testing to a minimum of 1.25 x MEOP
c) Leak test

Qualification Test Requirements

As a minimum, the following tests shall be conducted:

a) Acceptance testing
b) Vibration/External load testing
c) Leak testing
d) Burst testing

CATEGORY

Certification Plans & Standards

REFERENCE

Anon, *Fracture Control Implementation Handbook for Payloads, Experiments, and Similar Hardware* (Draft), 2000.

SUMMARY

Appendix B of the handbook is pertains to containment of rotating parts. The "Punch" equation is the most favored for use in containment assessment, and is supported by a limited amount of test data. The equation is based on data generated to establish the energy required to "punch out" various sizes of circular areas in metals with given thicknesses and yield strengths. The equation is as follows:

$$T = \left[\frac{MV^2}{2\pi D F_{cy}} \right]^{1/2}$$

    F_{cy} = Compressive yield strength of the container
    D = Diameter of the projectile
    M = Mass of the projectile
    T = Thickness required to contain the projectile
    V = Impact velocity

For use in the equation, an effective diameter for other, non-circular impact shapes may be determined by relating the perimeter length of the predicted impact area and shape to a circle with an equal perimeter having a diameter, D'. Only the radial component of velocity is needed because the tangential velocity is nearly negligible in causing penetration. If the calculated "T" is thicker than the actual enclosure, then the rotating part will not be contained in the event of failure. In the case that a rotating part cannot be contained, it must be assessed for safe-life using a conventional fracture mechanics approach.

CATEGORY

Certification Plans & Standards

REFERENCE

Anon, *Damage Resistance, Damage Tolerance, and Durability*, MIL-HDBK17-98 (DRAFT), 1998.

SCOPE

The brittle nature of most polymer resins causes concern about their ability to resist damage and, if damaged, to sustain required levels of strength. In metal structures the focus is on cracks. In polymer matrix composites, other damages are more dominant as discussed in Sections 5.2 and 5.3. The ability of a structure to resist a particular threat, as measured by the type and amount of damage which occurs, is discussed in Section 5.4. Given that damage can occur, it is important to understand and apply the methods and techniques that can detect its presence. This is discussed in Section 5.5.

Once a structure sustains damage (whether detected or undetected) it is important to be able to tolerate it under the anticipated loads and environments. This aspect is discussed in Section 5.6.

Sections 5.7 through 5.9 discuss specific requirements for damage resistance and damage tolerance of composite aircraft structure and how they are satisfied. Civilian requirements are different from military and there are differences between and Air Force and Navy.

An Aircraft structure is subjected to a wide variety of loads and environments during its service life. Its ability to maintain strength and stiffness throughout its life is affected, but this is covered by damage tolerance requirements. Fatigue damage can also be a concern if widespread enough to cause costly maintenance actions. Thus durability is an economic issue. This is discussed in Section 5.11.

The practical significance of studies that quantify the damage resistance of a specific component as exposed to a service environment. Service history may be needed to gain a more complete understanding of potential threats and to achieve the desired reliability in a composite design. The practical significance of studies that quantify the damage tolerance of a specific composite structure related to the safe design and maintenance of that component while in service. Again, service history can supplement a structural database and help to establish realistic design and maintenance goals for damage tolerance. As is characteristic of trades in other structural properties, several technical and economical issues must be considered in balancing the damage resistance and damage tolerance of a given design. These will be discussed in subsequent sections.

SUMMARY

The document mostly concerns itself with damage induced by impact. Although damage tolerance is very important in this circumstance, impact damage is not expected to be the primary mode of failure for composite flywheel rotors. However, some of the figures provide relevant information to the current research topic.

There are two ways to characterize damage, by stage of occurrence and by physical anomaly. Stage of occurrence is separated into manufacturing and in-service categories. It is expected that most manufacturing damage will be detected by routine quality inspection. However, the possibility of the existence of undetected damage must be assumed in the design procedure. The following are possible types of physical imperfection that could occur in composite structures: fiber breakage, matrix imperfections, delaminations, and any combination of the above. Combinations of damage may be more critical than isolated damage. See Figures 1-7 and 1-8 below for a view of the relative severity of different types of damage.

In the late 1980s, several aerospace companies conducted an extensive evaluation of impact in wing-gage structure for the U.S. Air Force. The focus was on impact damage resistance of material, laminate, and structural variables. Figure 1-9 shows the effect of laminate thickness and impact energy on the resulting damage, as measured by visible dent depth. It is observed that an energy cutoff, rather than visibility limits, has been used to bound ultimate load design requirements for thick structures.

Damage tolerance, according to the report, is defined as a measure of the structure's ability to sustain a level of damage or presence of a defect and yet be able to perform its operating functions. Concern with damage tolerance is ultimately with the damaged structure having adequate residual strength and stiffness to continue in service safely until the damage can be detected by scheduled maintenance inspection and repaired.

Degradation in the residual strength of a tension-loaded structure is most sensitive to fiber failure. Fiber failure normally localizes within a zone which is roughly the size of the impactor. Delamination and matrix cracks do not decrease the integrity of tension-loaded structures in most cases. However, the combined effect of matrix damage surrounding fiber failure should not be ignored because the former may actually increase tensile residual strength by softening the stress concentration.

Fracture toughness is the value of the stress intensity factor calculated for initial cut length and failure load. Values of fracture toughness are plotted against thickness (number of plies) in Figure 1-10 for center-cracked, compact, and three-point-bend specimens made of a quasi-isotropic laminate.

Low velocity impact damage, especially those made from a blunt object, may cause considerable internal damage without producing visible indications on the surface. Damage to the resin may be particularly severe. However, low velocity impact damage is potentially more of a problem for thin laminates such as composite overwrapped pressure vessels (COPVs). Figure 1-11 shows

a bar graph of minimum kinetic energy to reduce burst pressure for two filament-wound cylinders with the same membrane material and lay-up but with different sizes.

In metal structures, a major damage tolerance concern is not only initial damage but also growth of damage prior to the time of detection. In contrast, fibers in composite laminates, act to inhibit tensile crack growth. Through-thickness damage growth occurs only at relatively high stress levels. In this case, in-plane damage growth associated with delaminations or impact damage must be considered. Unlike cracks in metals, delaminations and impact damage in composites will probably not be detected if they occur. Both civil and military aviation authorities have published requirements for monitoring damage growth during cyclic tests conducted during development and validation. Based on these tests, design values can be established with sufficient margins to ensure that damage growth will not occur. Figure 1-12 shows design requirements for Ultimate, Limit, and Continued Safe Flight load conditions versus increasing damage severity. The load and damage requirements are balanced such that there is an extremely low probability of failure.

An analysis and testing methodology to support certification and maintenance of civilian aviation composite structures is explained in the report. The methodology is based on (a) establishment of residual strength versus damage size relationships; (b) establishing methods of damage detection and minimum detectable damage sizes; and (c) determination of allowable ultimate load damage limits and limit load capability damage thresholds. The residual strength curve in Figure 1-13 starts near ultimate strength and spans the range to discrete source damage sizes. Figure 1-14 is a flowchart that outlines the damage tolerance assessment for fail-safe loads.

In the applications section of the report, the damage tolerance approach of Sikorsky Rotorcraft is discussed. The approach for rotorcraft under cyclic loading combines analysis and building block testing to demonstrate the required level of reliability (A or B basis) of composite parts in the presence of damage. The approach demonstrates no growth of damage under spectrum loading for the required number of cycles at the representative environment(s) and with the appropriate load enhancement factors for statistical reliability. In order to avoid increased costs of environmental testing, tests can be conducted at room temperature ambient conditions provided the applied loads are adjusted for the environment with the use of an appropriate load acceleration factor. Discussion of accelerated testing procedures are also included. At the end of a successful fatigue test, residual strength must be demonstrated. The damage tolerance certification procedure for rotorcraft composites under fatigue loading is shown in Figure 1-15.
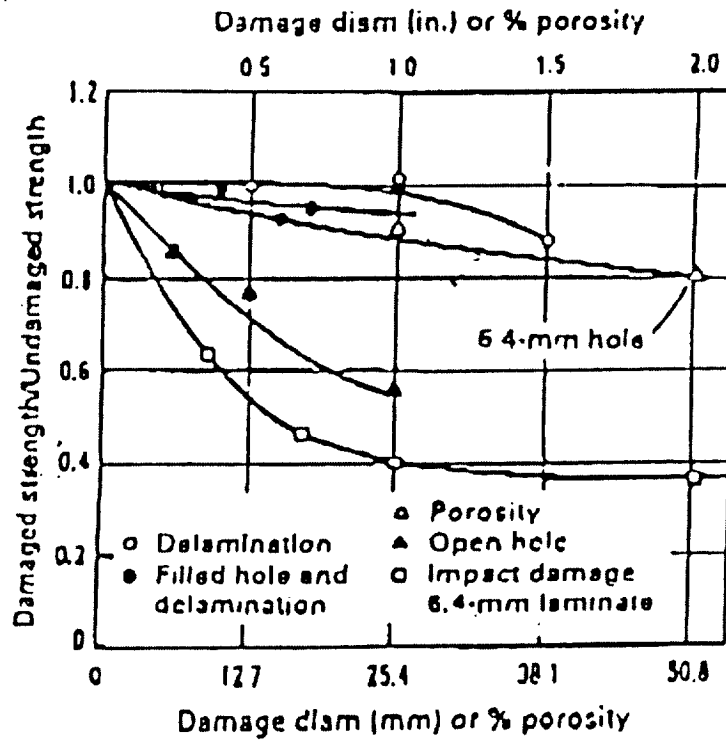
Figure 1-7: Relative severity of defect damage on
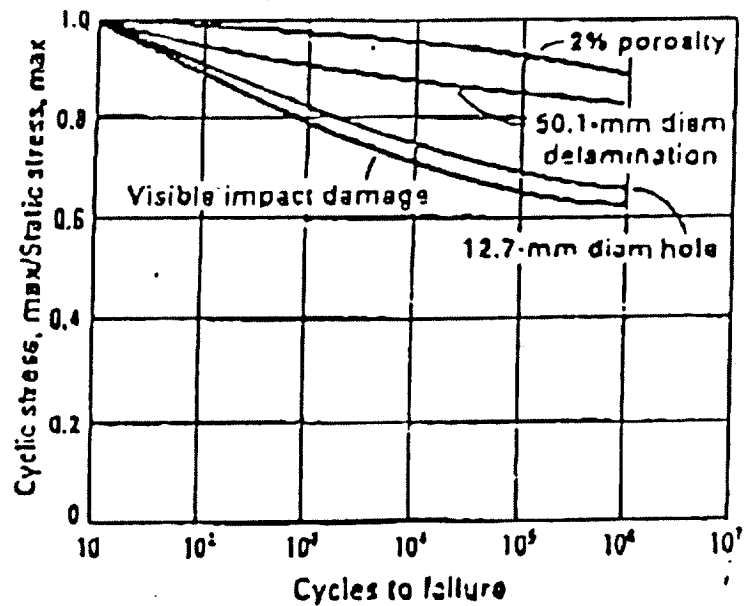static compression strength.

Figure 1-8: Relative severity of defect damage on
compression fatigue strength, R = 10.
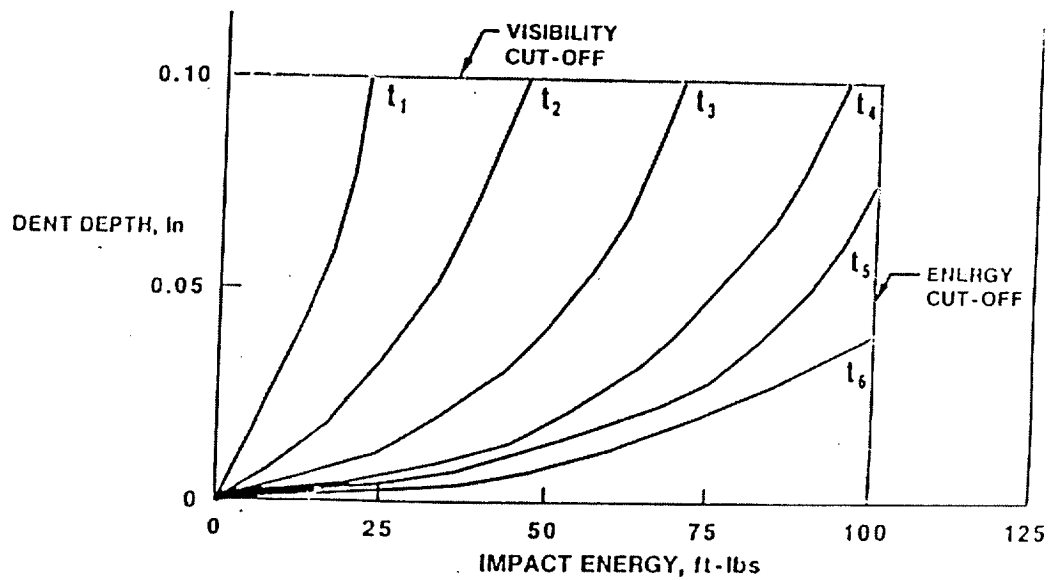
Figure 1-9: Test results for the effects of laminate thickness on dent depth for a rang of impact energies.
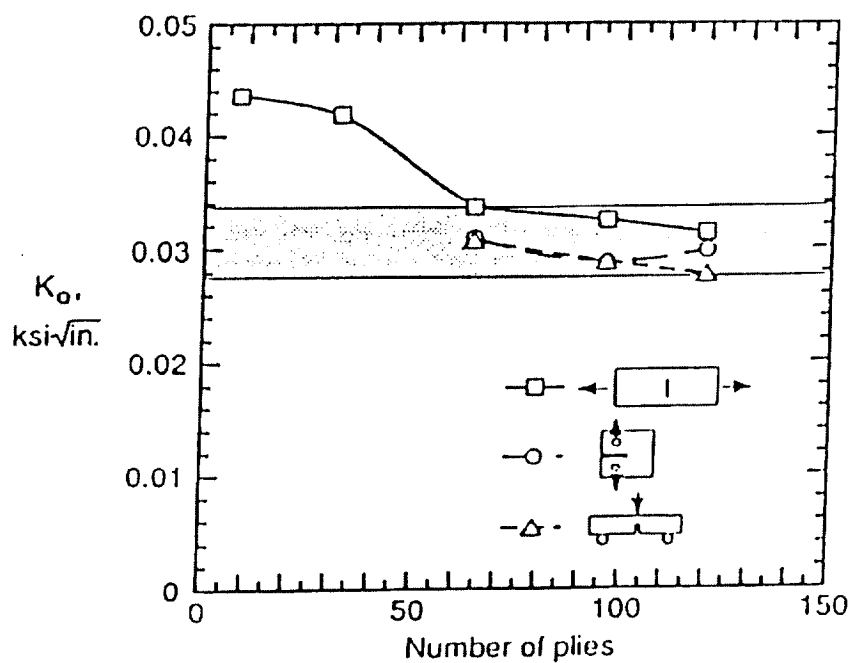

Figure 1-10: Fracture toughness for center-crack, compact, and three-point-bend specimens for [0/±45/90]ns T300/5208 laminates.
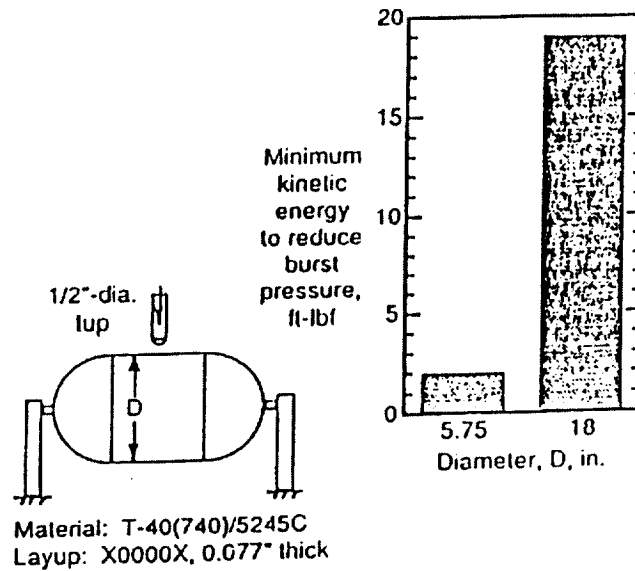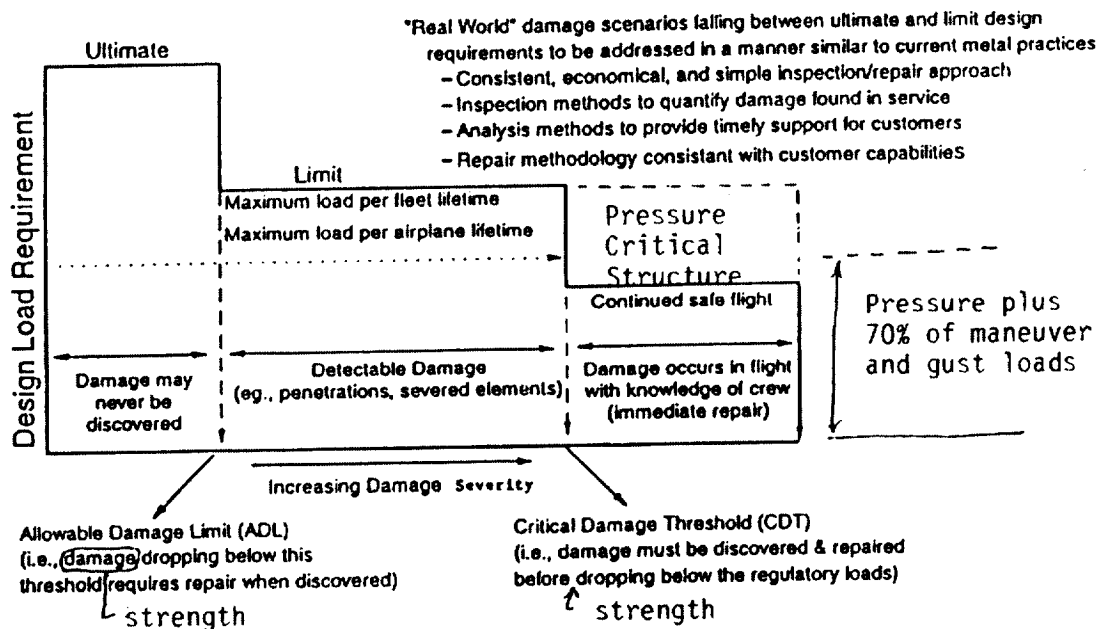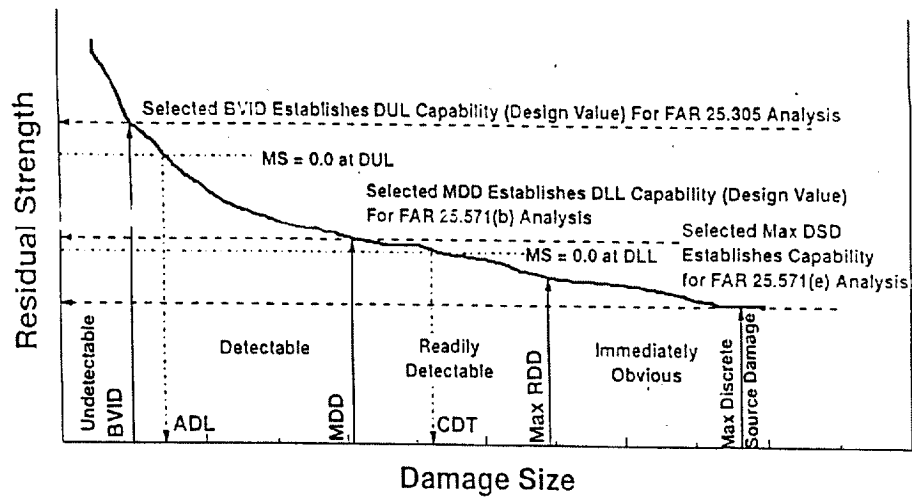
Figure 1-11: Impact response of small and large pressure vessels.

Figure 1-12: Damage tolerant design philosophy.

Figure 1-13: Residual strength versus damage size.

BVID: Barely visible impact damage
DUL: Design ulimate load
MDD: Maximum design damage
ADL: Allowable damage limit
CDT: Critical damage thershold

DLL: Design limit load
DSD: Discrete source damage
RDD: Readily detectable damage
MS: Margin of safety
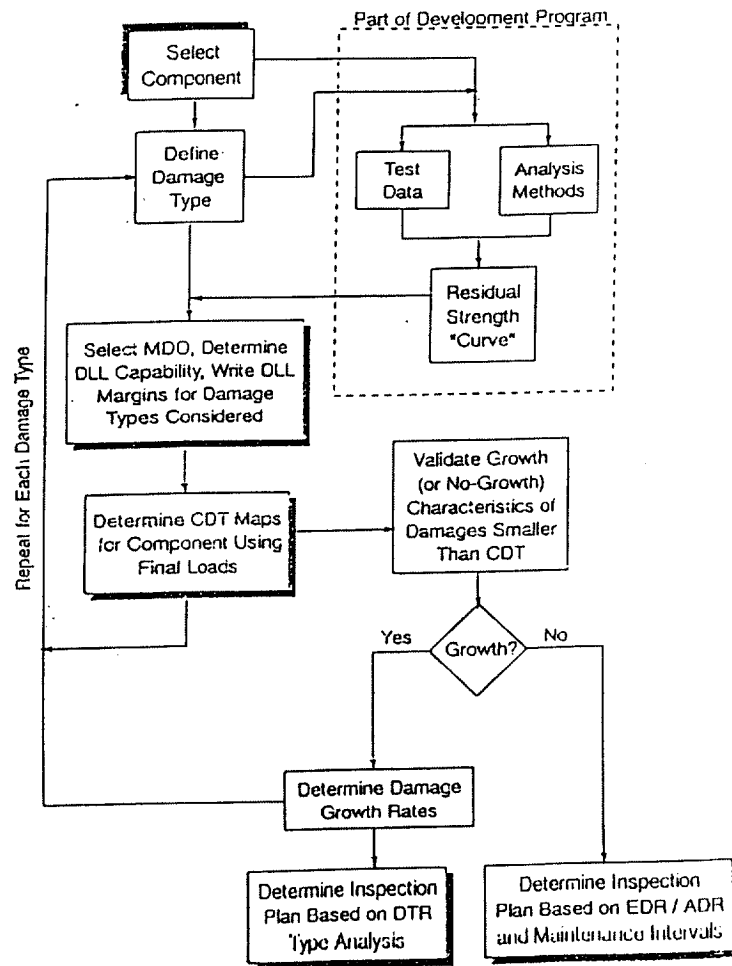
Figure 1-14: Damage tolerance assessment flowchart for fail-safe loads.
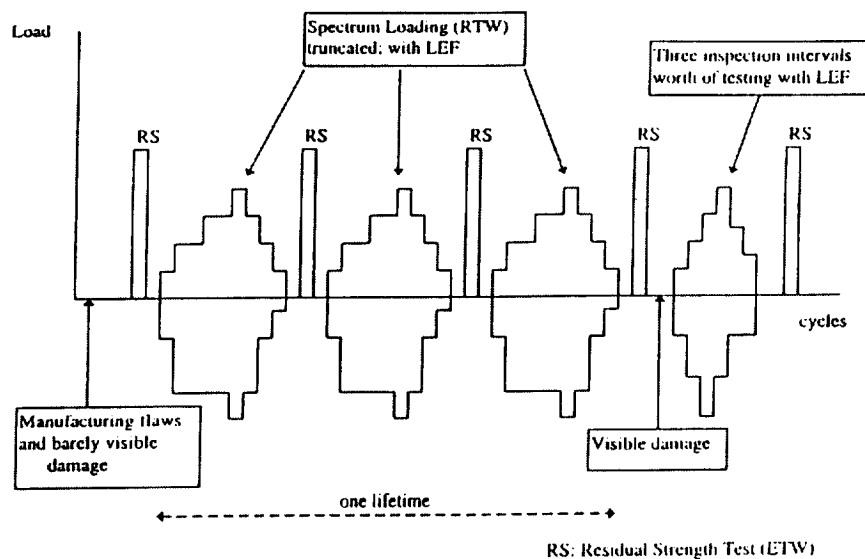
Figure 1-15: Schematic of fatigue testing for rotorcraft.

CATEGORY

Certification Plans & Standards

REFERENCE

Bender, D. A., "Criteria for Safe Flywheel Operation, Revision 0.1," White Paper – Trinity Flywheel Power, 1997.

ABSTRACT

Criteria for safe operation of flywheel systems are proposed. These criteria are presented as a white paper to elicit response from the developers and potential users of the technology. The paper proposes criteria for operation of a flywheel system without containment and criteria for the acceptance of a containment structure. It is intended that conformance to either set of criteria would be sufficient to assure safe operation of a flywheel system.

SUMMARY

Trinity Flywheel Power is a company that develops flywheels for use in terrestrial applications. The paper proposes the technical basis for a standard for safe testing and qualification of a flywheel. The paper is separated into two sections; one dealing with flywheels operating without the use of burst containment. The other section proposes criteria for ensuring the effectiveness of a containment system.

The following is a summary of the criteria laid out for flywheel operating without containment:

Design margin:

a) Rotor design margin based on relevant accepted criteria:
- Margin: 2.00 → max. operating speed 70.7% of burst speed
- Margin: 2.25 → max. operating speed 67.7% of burst speed
- Margin: 2.40 → max. operating speed 64.5% of burst speed
a) Design margin qualification test

Physical and operational safety:

a) Assure snubbing of loose rotor event
b) Bushing/bearing restraint of spindle
c) Demonstrate with rotor drop at full speed
d) Withstand externally applied loads
e) Demonstrate by operating at full speed in upset condition
f) Protection against overspeed
g) Configuration specific safety plan
h) Demonstrate protection against overspeed through two tests:
- Deliberate setting of software parameters to allow overspeed

1-26

- Elevated bus voltage

System fault tolerance:

a) Assure flywheel system safety under fault conditions
b) Demonstrate with physical faults:
- Loss of vacuum
- Loss of coolant (for liquid cooled systems)
- Loss of DSP/microprocessor control voltage for power electronics
- Loss of DSP/microprocessor control voltage for magnetic bearings

Electrical short which could cause overcurrent in the flywheel stator
Loss of control signals (e.g. phase angle, bearing temperature, etc.)

Homology of test system with respect to deployed system. Homology is defined as having same or similar structure and origin.

Proof testing (every system)

Rotor margin:

Operate flywheel at 120% of design speed for 2 minutes.

System fault:

Demonstrate automatic shutdown for electronically simulated set of faults.

Documentation and acceptance

CATEGORY

Certification Plans & Standards

REFERENCE

Anon, *Fracture Control Requirements for Payloads Using the Space Shuttle*, NASA-STD-5003, 1996.

PURPOSE

This document is to establish the fracture control requirements for all payload hardware to be launched or retrieved using the Space Shuttle. Meeting these requirements implements the minimum fracture control requirements of National Space Transportation System (NSTS) 1700.7, *Safety Policy and Requirements for Payloads Using the Space Transportation System.* All payload fracture control shall be in accordance with the requirements stated herein.

SUMMARY

The standard defines safe-life as the design criterion under which a flaw is assumed to be consistent with the inspection process specified, and under which it can be shown that the largest undetected flaw that could exist in the structure will not grow to failure in *four service lifetimes* when subjected to the cyclic and sustained loads in the environments encountered [emphasis added]. One complete service lifetime is characterized as including all significant loadings that occur after flaw screening to establish minimum initial flaw size and shall include testing, transportation, lift-off, ascent, on-orbit operations, descent, landing, and post-landing events.

High-energy Rotating Machinery

For the purpose of fracture control, a rotating mechanical assembly that has a kinetic energy of 14,240 foot-pounds (19,310 Joules) or greater (based on $1/2I\omega^2$) is fracture critical by definition. In addition to other requirements for fracture-critical components, rotating machinery shall be proof-tested (spin-tested) to screen for flaws and shall be subjected to NDE before and after proof testing or shall be shown to be contained if failure occurs at maximum speed and if loss of function is not safety critical. The proof-test level shall be greater than or equal to the level derived by fracture mechanics analysis. Rotating mechanisms with lower kinetic energy levels are to be classified by the same criteria as other structural components.

Composite Structures

All composite structures deemed fracture critical shall be shown to meet fracture control requirements by one of the following methods:

a) A proof test (static or dynamic) to no less than 120 percent of the limit load. The proof test shall be conducted on the flight article. The test may be accomplished at the component or subassembly level if the loads on the test article duplicate those that would be seen in a fully

1-28

assembled test article. Caution should be exercised when testing the flight article to 1.20 to prevent detrimental yielding to the metallic fittings and fasteners in the flight assembly and damage to the composite. Test loads on the composite should not exceed 80 percent of ultimate strength.

b) A damage tolerance test program to establish that these structures possess at least four service lifetimes. These tests shall be conducted on full-scale, flight-like elements of critical components and samples with controlled flaws or damage. The size and shape of the flaws or damage must corresponded to the detection capability of the NDE to be imposed on the flight part. The type of flaws and damage considered must be representative of that which could occur on the flight part.

CATEGORY

Certification Plans & Standards

REFERENCE

ABSTRACT

The ATR72 was the first civil aircraft with a composite wing to be certified JAR/FAR 25 (Joint Aviation Requirements/Federal Aviation Regulations). Using the latest developments composites ACJ 25603, AC20-107A comply with the requirements of JAR/FAR 25; the ATR72 composite outer wing box was certified by the DGAC in September 1989 and the FAA in December 1989.

This paper deals with Aerospatiale's innovative approach, focusing on four major certification topics:

1) determination of allowables from statistical analysis substantiated by tests on cross-ply plain and notched laminates;
2) fatigue and damage tolerance substantiations performed by analysis to show the non-initiation of fatigue damage and by full-scale test for the no-growth of acceptable manufacturing defects and accidental damages;
3) development of a probabilistic approach to determine the inspection intervals for accidental impacts in damage-tolerance justifications;
4) compliance philosophy developed to qualify a second source material (approved by the company in 1992).

SUMMARY

Figure 1-16 shows the ATR72, the first civil aircraft of its size to have a carbon fiber reinforced plastic (CFRP) wing.

The FAA recommends the following to determine allowables (ref. 5 in paper), also see Table 1-5 below:

a) 0° and 90° tension and compression, in plane shear and short beam shear (interlaminar shear) for the three environmental conditions – minimum temperature/dry, room temperature/dry and maximum temperature/wet;
b) tests need to be performed on fiber batches with six coupons per test configuration.

Figure 1-17 gives a schematic of the damage tolerance philosophy of Aerospatiale for the ATR72 outer wing box. The company kept NDE methods to a minimum, and based impact damage detection only on visual detection.

Analysis and fatigue tests were also conducted on the wing during the certification process. ACJ 25603 requires, "Inspection intervals should be established such that the damage will be detected between the time it becomes detectable and the time at which the extent of damage reaches the limit for required residual strength capability."(6.2.4) In metals, it is assumed that if no damage propagates and if its size never reaches critical size, the damage tolerance assumption is always met. This is not always the case for composites, as is seen in Figure 1-18.

Carbon self-stiffened structure

Carbon/Nomex sandwich

Carbon monolithic structure

Kevlar/Nomex sandwich

Kevlar/Nomex sandwich
with stiffening carbon plies

Glass fibre/Nomex sandwich

MTOW	21 500 kg
MOWE	12 200 kg
Str. weight	7300 kg
Composites	
Str. weight	1650 kg
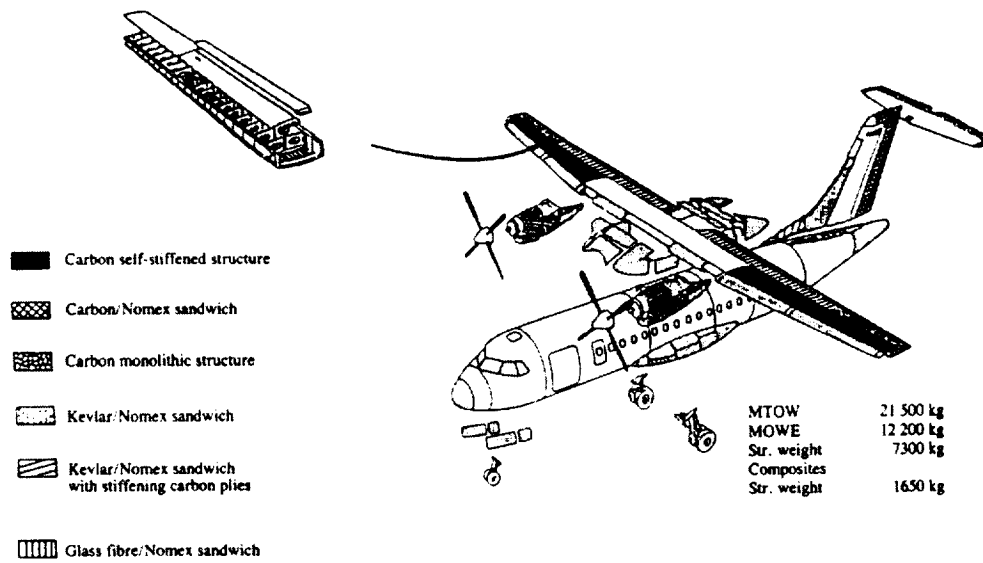
Figure 1-16: Composites on the ATR72.
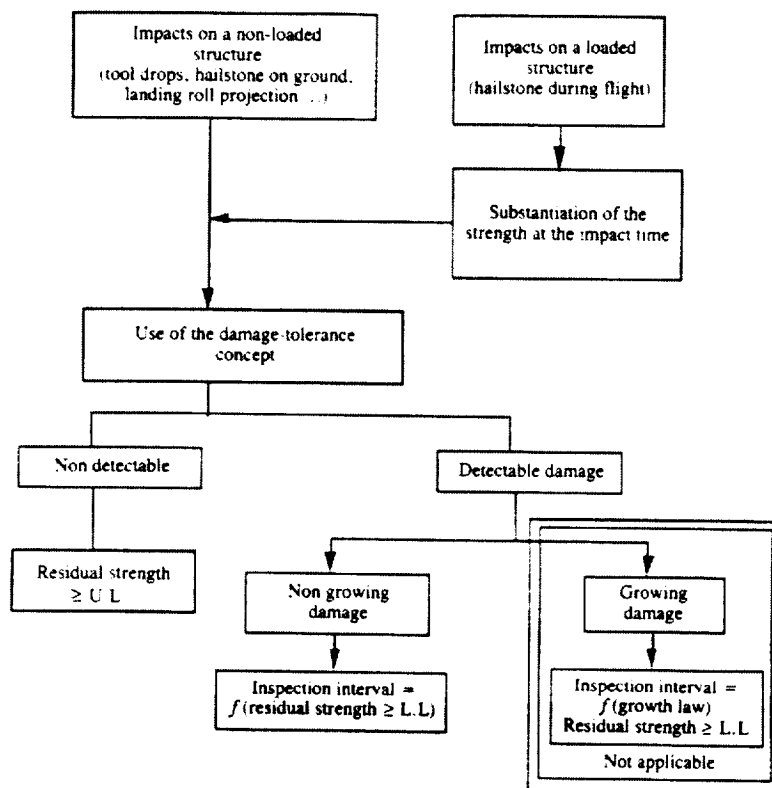
Figure 1-17: Company damage tolerance philosophy.

Table 1-5: Method Proposed by the FAA

Test	Mean value	Analysis	Calculation values	Mathematical model
Test on UD	Modulus Strength Strain	Scatter	'Allowables' on UD	Statistical analysis (SBMP 17)
Test on design feature	Modulus Strength Strain		'Design value' on typical features	Empirical coefficient combined with UD allowables (laminate theory)
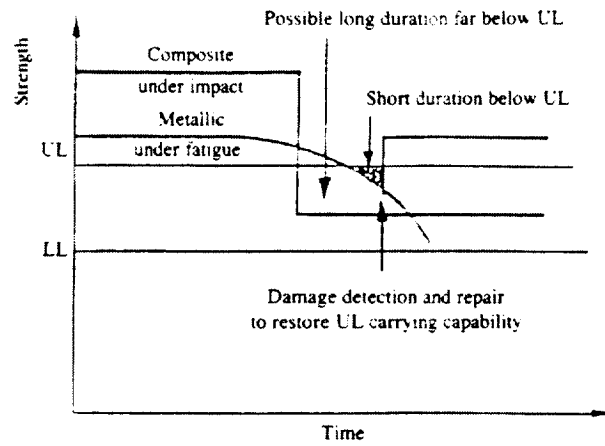
Figure 1-18: Damage tolerance philosophy.

2.0   Analysis

This section contains the review summaries of the following articles.

- Abdul-Aziz, A., G. Baaklini, and J. Trudell, *Structural Analysis of Composite Flywheels: An Integrated NDE and FEM Approach*, NASA TM-2001-210461, 2001.
- Bandorawalla, T., *et al.*, "Strength and Rupture Modeling of Unidirectional Polymer Composites," 42nd AIAA/ASME/ASCE/AHS/ASC Structures, Structural Dynamics, and Materials Conference and Exhibit, AIAA-2001-1283, 2001.
- Gowayed, Y., *et al.*, "Optimal Design of Multi-direction Composites Flywheel Rotors," Proceedings of the 46th International SAMPE Symposium, Vol. 46, Book 2:1657-1667, 2001.
- Hassan, R., *et al.*, "Parametric Analysis of Fiber-reinforced Laminated Momentum Wheel Rotors," 42nd AIAA/ASME/ASCE/AHS/ASC Structures, Structural Dynamics, and Materials Conference and Exhibit, AIAA-2001-1596, 2001.
- Robinson, D. N., Binienda, W. K., "Optimal Fiber Orientation in Locally Transversely Isotropic Creeping Structures," *Journal of Applied Mechanics*, Vol. 68: 213-217, 2001.
- Tzeng, J. T., "Stress Relaxation in Composite Flywheels," *Proceedings of the 46th International SAMPE Symposium*, Vol. 46, Book 2:1621-1630, 2001.
- Ganley, J. M., *et al.*, "Quantifying Process Induced Residual Stresses in Filament Wound Composite Parts," 44th International SAMPE Symposium, Vol. 2:2095-2109, 1999.
- Huang, B. C., "Polar Woven Flywheel Rim Design," 44th International SAMPE Symposium, Vol. 2:2133-2144, 1999.
- Ha, S. K. and D. J. Kim, "Optimal Design of a Hybrid Composite Flywheel Rotor Using Finite Element Methods," *Proceedings of the 44th International SAMPE Symposium*, Vol. 2:2119-2132, 1999.
- Gabrys, C. W. and C. E. Bakis, "Simplified Analysis of Residual Stresses in In-situ Cured Hoop-Wound Rings," *Journal of Composite Materials*, Vol. 32, No. 13:1325-1343, 1998.
- Tzeng, J. T., "Viscoelastic Behavior of Composite Rotors at Elevated Temperatures," *IEEE Transactions on Magnetics*, Vol. 33, No. 1: 413-418, 1997.
- Raghavan, J. and M. Meshii, "Activation Theory for Creep of Matrix Resin and Carbon Fibre-reinforced Polymer Composite," *Journal of Materials Science*, Vol. 29: 5078-5084, 1994.
- McCartney, L. N., "Analytical Micromechanical Models for the Prediction of Multiple Cracking in Composites," *Journal De Physique III*, Vol. 3:1637-1646, November 1993.
- Lekhnitskii, S.G., S. Tsai, and T. Cheron, *Anisotropic Plates*, Gordon & Breach Science Publishers, New York, 1968.

CATEGORY

Analysis

REFERENCE

ABSTRACT

A structural assessment by integrating finite-element methods (FEM) and a nondestructive evaluation (NDE) of two flywheel rotor assemblies is presented. Composite rotor A is pancake like with a solid hub design, and composite rotor B is cylindrical with a hollow hub design. Detailed analyses under combined centrifugal and interference-fit loading are performed. Two- and three-dimensional stress analyses and two-dimensional fracture mechanics analyses are conducted. A comparison of the structural analysis results obtained with those extracted via NDE findings is reported. Contact effects due to press-fit conditions are evaluated. Stress results generated from the finite-element analyses were corroborated with the analytical solution. Cracks due to rotational loading up to 48,000 rpm for rotor A and 34,000 rpm for rotor B were successfully imaged with NDE and predicted with FEM and fracture mechanics analyses. A procedure that extends current structural analyses to a life prediction tool is also defined.

SUMMARY

The FEA showed that the rotor first crack, as detected by the computed tomography (CT) scan, can be modeled with finite elements provided the material properties and residual loads are adequately quantified. The crack location cited via CT corresponded well with that simulated by the fracture mechanics analysis. It was found that the aluminum hub design is a crucial factor affecting the durability of the rotor because an improper hub design can result in high bending stresses that in turn result in complex crack propagation behavior.

Figures 2-1 and 2-2 show two rotor assemblies modeled for the analyses. Each rotor rim is interference fit onto its aluminum hub. Figures 2-3 and 2-4 show two of the models analyzed. Nonlinear, two- and three-dimensional contact analysis was performed. A fracture mechanics analysis was also conducted on Rotor B, modeled with a crack as seen in Figure 2-4.

Selected results are presented for summary. Figures 2-5 through 2-8 give results for the radial and hoop stresses in Rotor A at a rotational speed of 48,000 rpm. The peak hoop stress is 141 kpsi at the rim contact region with the hub (Figure 2-9). The peak radial stress of 3.4 kpsi occurs at a radial location of 4.35 in. as indicated in Figure 2-10.
Figure 2-9 shows the variation in radial stress versus radius for several rotational speeds. The location of peak radial stress moves from the outer radius to the center as speed increases because the centrifugal loading continues to offset the compressive preload during assembly.

Figures 2-10 and 2-11 show the two- and three-dimensional radial stress in Rotor B respectively. In both cases the maximum stress level in the hub is in the hub holes, an indication that the hub is very likely to fail at that particular section if a higher rotational load is applied. Figure 2-12 shows the two-dimensional radial stress results from the fracture mechanics analysis at a rotational speed of 34,000 rpm.
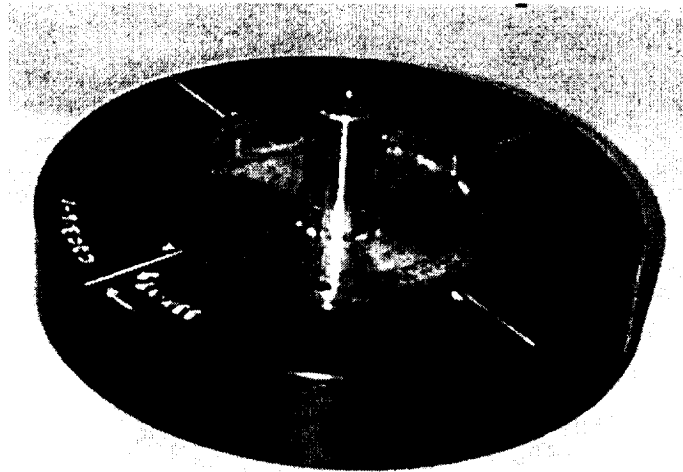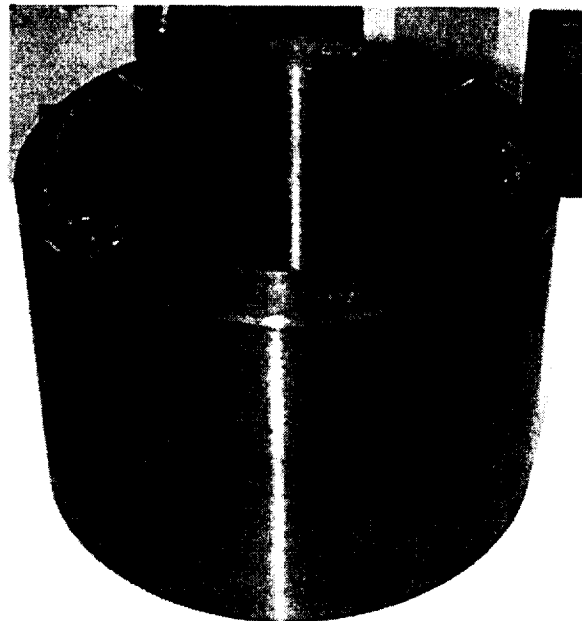

Figure 2-1: Pancake rotor assembly A with aluminum hub.

Figure 2-2: Composite rotor assembly B.
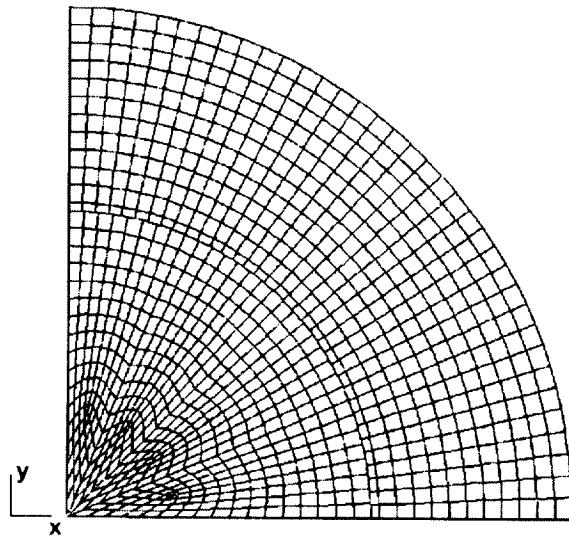
Figure 2-3: Pancake rotor A two-dimension, finite element model consisting of 912 quad4 elements and 995 nodes. Based on MARC analysis.
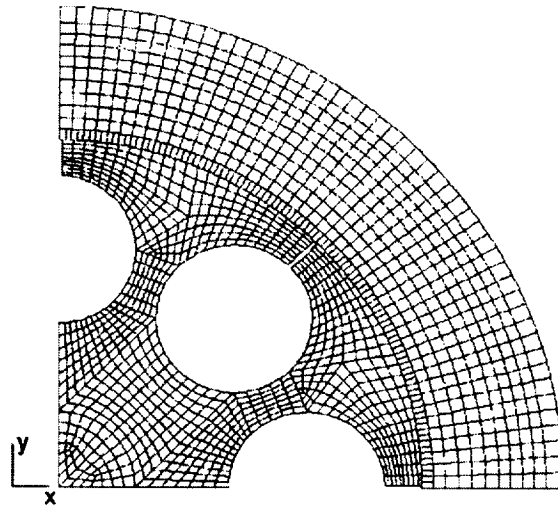
Figure 2-4: Rotor B two-dimensional, finite element model consisting of 408 quad4 and quad8 elements and 2592 nodes.

2-4
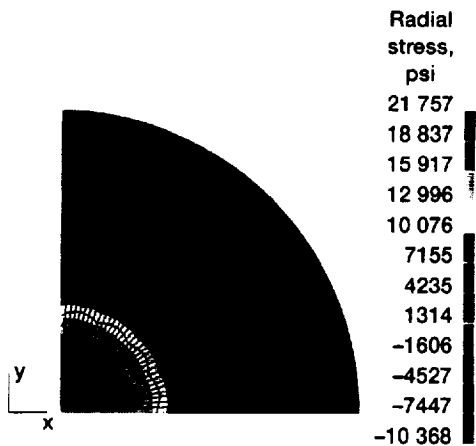
Figure 2-5: Radial stress distribution for rotor A based on MARC analysis. Rotational speed, 48,000 rpm.
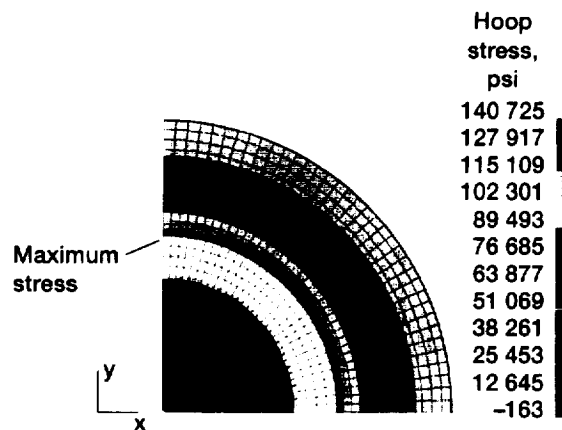

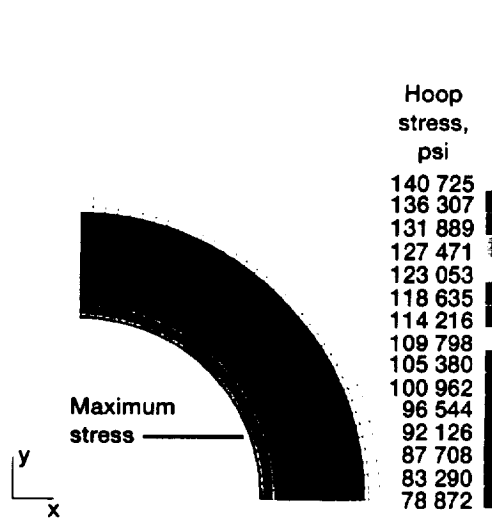**Figure 2-6: Hoop stress distribution for rotor A based on MARC analysis. Rotational speed, 48,000 rpm.**

Figure 2-7: Rim hoop stress distribution for rotor A based on MARC analysis. Rotational speed 48,000 rpm.
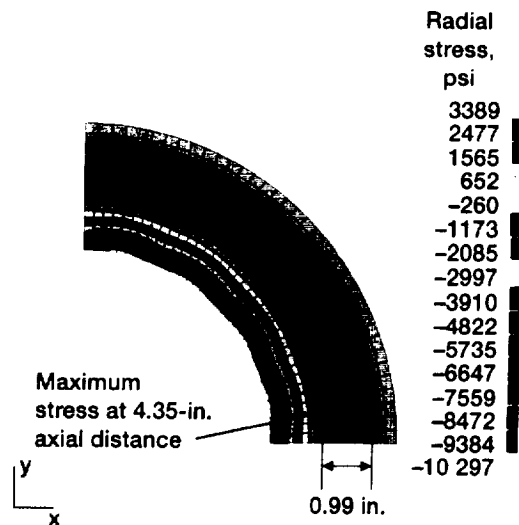

Figure 2-8: Rim radial stress distribution for rotor A based on MARC analysis. Rotational speed 48,000 rpm.
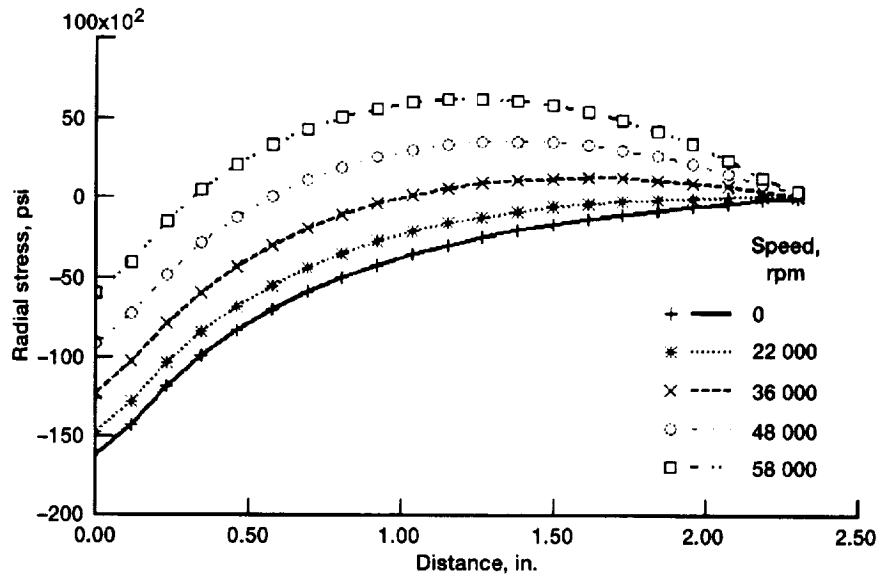
Figure 2-9: Rim radial stress distribution as a function of radius at several speeds for rotor A based on ANSYS analysis.
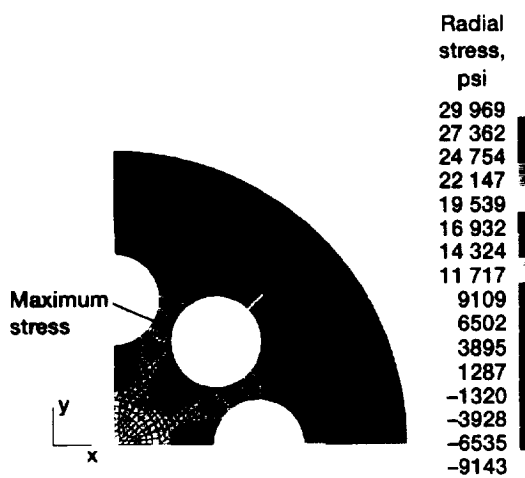

Figure 2-10: Radial stress distribution for rotor B based on MARC 2-D analysis. Rotational speed 34,000 rpm.
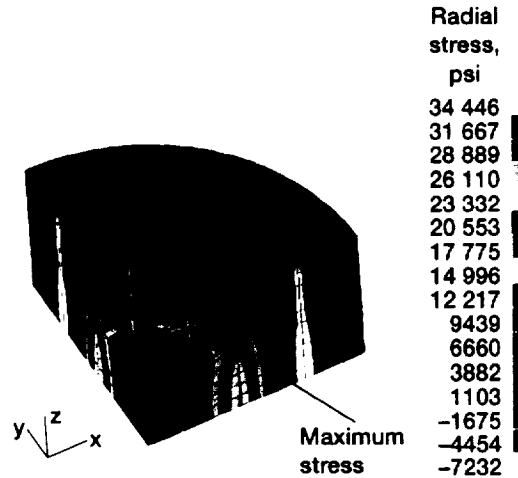

Figure 2-11: Radial stress distribution for rotor B based on ANSYS 3-D analysis. Rotational speed 34,000 rpm.
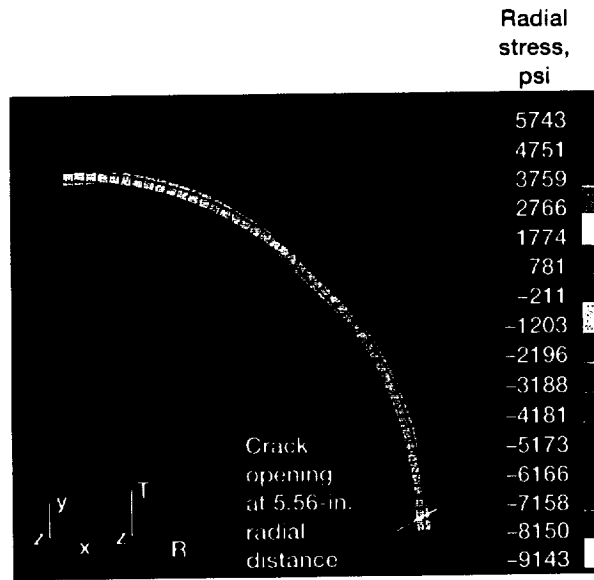
Figure 2-12: Rim fracture mechanics radial stress distribution for rotor B based on MARC analysis. Rotational speed 34,000 rpm.

CATEGORY

Analysis

REFERENCE

Bandorawalla, T., *et al.*, "Strength and Rupture Modeling of Unidirectional Polymer Composites," 42nd AIAA/ASME/ASCE/AHS/ASC Structures, Structural Dynamics, and Materials Conference and Exhibit, AIAA-2001-1283, 2001.

ABSTRACT

With the increasing use of composite materials a detailed understanding of the micromechanical events that lead to material failure is necessary. In this work, numerical techniques for prediction of the static strength and rupture lifetime of carbon fiber/polymer matrix composites are developed. Statistical static strength and rupture lifetimes of Grafil 700 carbon fiber/Polyphenylene Sulfide (PPS) thermoplastic matrix are presented for purposes of comparison. The key ideas in developing micromechanical models for failure are the interaction between the fiber and matrix, its response to time and temperature, and the fiber strength distribution. Fiber/matrix interaction is studied through the use of model composites. Three-dimensional model composites, representative of unidirectional polymer matrix composites, are fabricated with hexagonal fiber packing. Strain gages mounted onto the fibers provide strain concentration measurements due to a break in one of the fibers. Three-dimensional finite element (FE) analysis is performed to model the load-sharing. There is very good agreement between the finite element analysis and experimental results. A comparison is also made between the load-sharing calculated by finite element analysis and that obtained by a modified Hedgepeth and Van Dyke (HVD) "shear-lag" analysis. The HVD analysis yields greater stress concentrations on the unbroken neighboring fibers. The finite element load-sharing is incorporated into a Monte Carlo simulation for the static strength of carbon fiber/polymer matrix composite. The composite material Weibull distribution computed by the simulation has a location and shape parameter of 1.71 GPa and 47.3, respectively, at a length of 76 mm. The experimentally obtained Weibull location and shape parameters are 1.57 GPa and 29.4, respectively, at a length of 76 mm. The Monte Carlo approach for rupture modeling is briefly discussed.

SUMMARY

Materials used in applications requiring long service lives are typically subjected to constant dead loads, cyclic loads, and often aggressive environments including elevated temperatures. The interaction between the polymeric matrix and the fibers is not well understood with respect to load and temperature. As part of a method of better understanding these interactions, models are developed that can accurately predict this behavior. The models in this paper are based on the simplifying assumption that the loads of failed fibers are redistributed only onto the nearest surviving neighbors. The static strength and rupture lifetime models are based on the finite element calculations of load-sharing.

Carbon fibers are assumed to undergo very little strength degradation over time. Hence, stress rupture in carbon fiber polymer matrix composites occurs as a result of viscoelastic relaxation of the polymer matrix. Figure 2-13 shows a unidirectional polymer composite with seven hexagonally packed fibers. In order to fracture the central glass rod at a predetermined location, it is scored to introduce an artificial weakness. Three-dimensional finite element analysis is performed to model the strain concentrations within the rod. Perfect fiber/matrix adhesion is assumed. The finite element strain results were averaged over the surface of the fiber.

A comparison is also made between the axial stress concentrations of the finite element analysis and those predicted in the "shear-lag" analysis. Figures 2-14 and 2-15 show the comparison between the finite element effective stress concentration and the "shear-lag" results for the broken and unbroken fibers respectively.

Based on the load-sharing assumption, a Weibull distribution for fiber strengths is developed. Load-sharing is the key component in the rupture lifetime modeling of carbon fiber/polymer matrix composites. Matrix viscoelasticity causes the stress profile on fibers to evolve with time. The overstressed region of surviving fibers near a break location increases with time resulting in an increased probability of failure. A time-dependent load-sharing framework was developed that was incorporated into a simulation for stress rupture modeling. Quasi-static tensile tests were conducted. Figure 2-16 shows the probability of failure, at room temperature, of the composite with increasing load. Tensile rupture tests were also conducted at higher temperatures. Figure 2-17 shows the rupture curve fits for 90, 80, and 70° F at normalized stresses of 90 and 87.5% with respect to the Weibull location parameter of the composite.
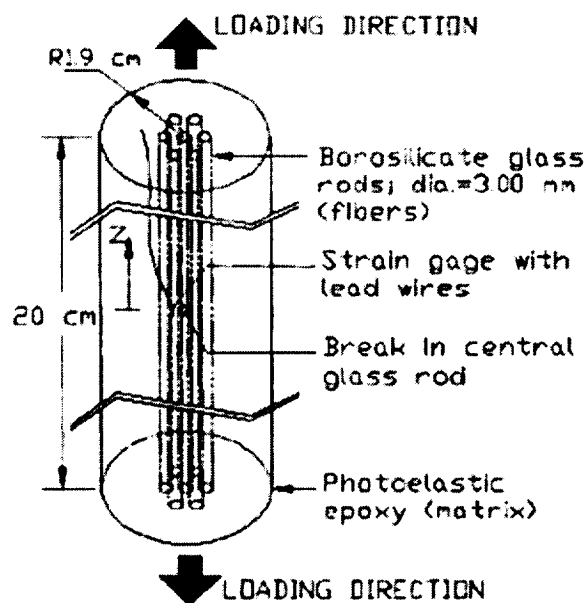

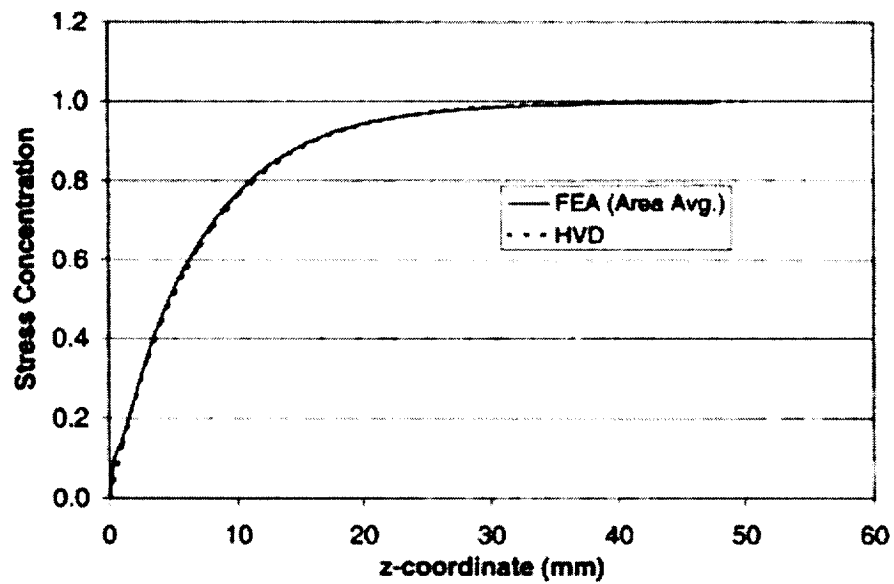Figure 2-13: Schematic of model composite.

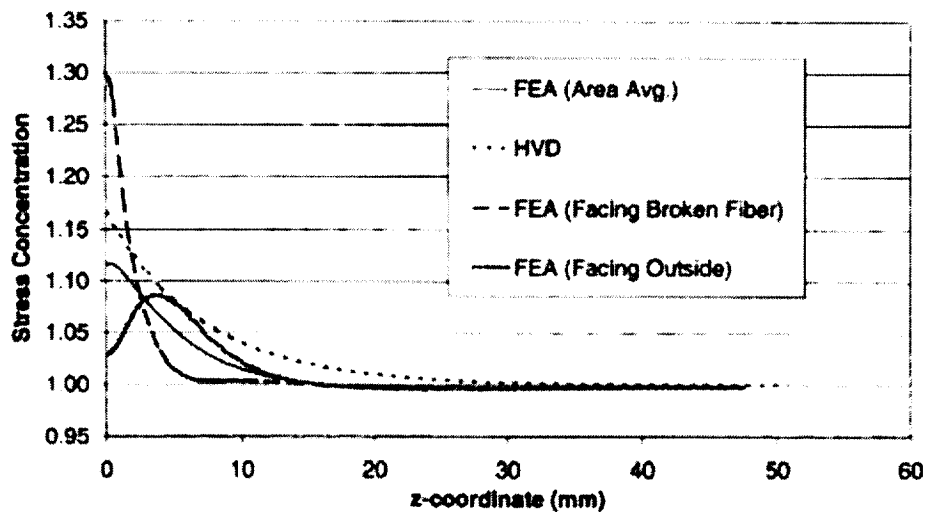**Figure 2-14: Comparison of FE and HVD analysis for broken fiber.**

Figure 2-15: Comparison of FE and HVD analysis for unbroken fiber.
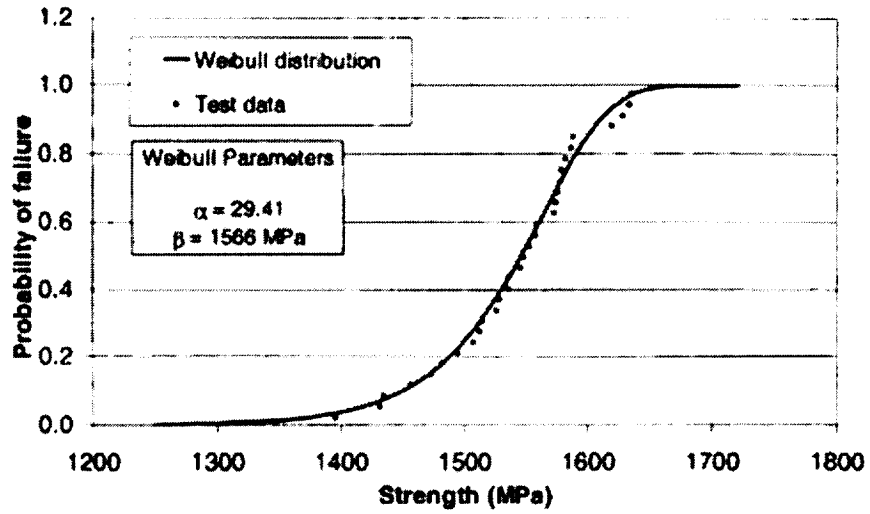
2-10

Figure 2-16: Probability of failure for material from 1 run of the carbon fiber/PPS composite as received.
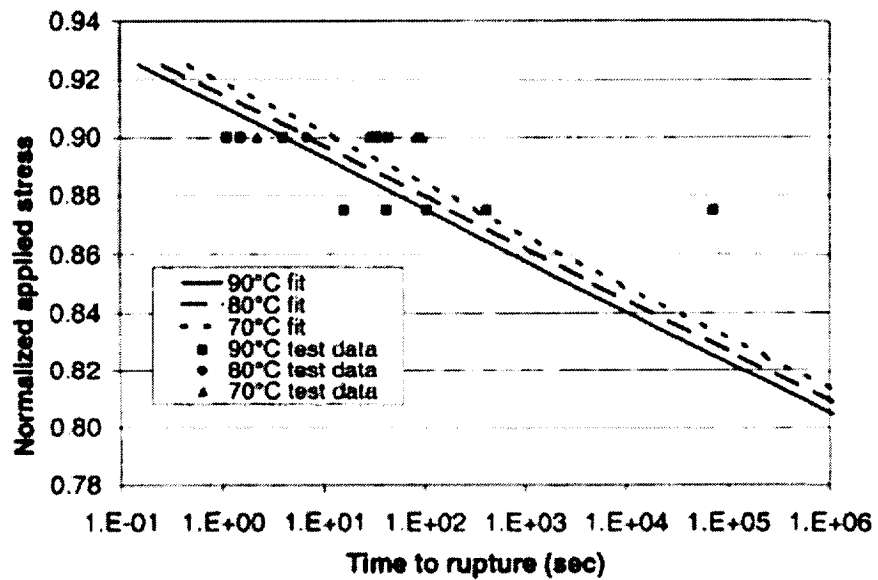

Figure 2-17: Time to rupture at temperature.

CATEGORY

Analysis

REFERENCE

ABSTRACT

Design of composite flywheels made with reinforcement in the hoop and radial directions (Multiple Direction Composites) involves a large multitude of parameters such as those related to the flywheel operation, flywheel geometry, material characteristics, material layup, and stress spatial distribution and values. The problem is further complicated due to the fact that most design parameters are interactive and that one parameter cannot be optimized independent of the other parameters. Optimum structural design of MDC flywheels using nonlinear optimization via a sequential quadratic programming approach and parametric finite element analysis are used to address this problem. Numerical examples are solved to compare the efficacy of the two approaches.

SUMMARY

A new type of flywheel rotor design is proposed that contains reinforcing fibers in both the hoop and radial directions. The rotor is assembled by a layering method with individual layers of pure hoop or radial reinforcements as shown in Figure 2-18. This approach helps remedy the classical problem of radial crack propagation of filament wound wheels. It allows the designer to increase the tip speed enhancing the specific energy of the wheel by safely allowing radial tensile stress distributions. The current paper compares optimization codes' results for the design of the rotor. Experimental tests are needed to further determine whether this is a viable design.

Finding an optimum design for a composite flywheel rotor is a very complex process. A constrained nonlinear optimization procedure is used to estimate the optimum design of multi-direction composite flywheels. In this method, the total energy of the rotor is maximized with respect to several parameters including the inner and outer radii of the hub, the radial fiber volume fraction, the shape of the hub, and the rotational speed.

The Finite Element Analysis (FEA) representation of the flywheel allows verification of the analytical solution and the detailed structural design to be performed by accounting for the 2D and 3D features of the MDC flywheel as well as any non-axisymmetric spacecraft induced loads.

Results are shown in Table 2-1 for the rim and Table 2-2 for the hub for four cases. The rotational speed is in krpm; Beta is the ratio of the outer diameter and inner diameter of the rim; Radial VFR is the fiber volume fraction of the radial fiber layers to the overall fiber volume

2-12

fraction; H-layer refers to the hoop layers of the rim or hub; R-layer refers to the radial reinforcement layers of the rim or hub; Hub Outer Diameter is the inner diameter of the rim needed for expansion matching of the hub and rim; shear stress is the interfacial shear stress between hoop and radial fibers.

In Table 2-1, the hoop and radial stresses for the ANSYS and DOC solutions were within 4%. In Table 2-2, the hoop and radial layer stresses were ~ 25% apart, primarily due to local stress concentration of the hollow hub and the manufacturing process selected.
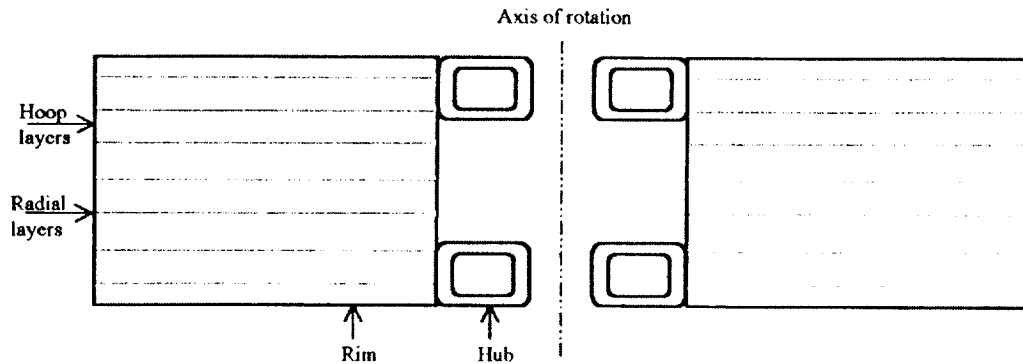

Figure 2-18: A schematic of MDC design showing hoop and radial layers of reinforcement as well as a box hub construction.

Table 2-1: Comparison of Rim Analytical and FEA Solutions

	Rim Outer diameter (m)	Rim Height (m)	Rot. Speed krpm	Beta	Rim Radial VFR	Rim H-Layer Hoop Stress (MPa)	Rim H-Layer Radial Stress (MPa)	Rim R-Layer Hoop Stress (MPa)	Rim R-Layer Radial Stress (MPa)	Rim Shear Stress (MPa)
DOC case 1	0.33	0.1	60	0.4968	0.10	1437	31.8	48.1	654	—
Ansys Case 1	0.33	0.1	60	0.4968	0.10	1435	33.0	47.5	644	10.5
DOC case 2	0.33	0.1	50	0.4750	0.10	974	23.1	32.6	488	—
Ansys Case 2	0.33	0.1	50	0.4750	0.10	987	24.0	32.1	483	7.6
DOC case 3	0.33	0.1	70	0.4326	0.10	1810	49.0	60.6	1086	—
Ansys Case 3	0.33	0.1	70	0.4326	0.10	1785	50.9	60.5	1084	16.5
DOC case 4	0.33	0.1	73	0.4041	0.10	1890	55.8	63.2	1269	—
Ansys Case 4	0.33	0.1	73	0.4041	0.10	1856	57.9	64.3	1271	19.5

Table 2-2: Comparison of Hub Analytical and FEA Solutions

	Hub Outer Diam (m)	Hub Radial VFR	Hub H-Layer Hoop Stress (MPa)	Hub H-Layer Radial Stress (MPa)	Hub R-Layer Hoop Stress (MPa)	Hub R-Layer Radial Stress (MPa)	Hub Shear Stress (MPa)
DOC case 1	0.164	0.20	514	61.3	80.0	300	—
Ansys Case 1	0.164	0.20	491	85.3	71.2	287	25.2
DOC case 2	0.157	0.20	321	40.5	50.0	196	—
Ansys Case 2	0.157	0.20	316	53.2	45.7	181	16.3
DOC case 3	0.143	0.20	505	71.3	78.5	311	—
Ansys Case 3	0.143	0.20	526	95.1	75.7	288	27.0
DOC case 4	0.133	0.20	469	71.5	72.7	289	—
Ansys Case 4	0.133	0.20	505	93.3	72.7	269	26.3

CATEGORY

Analysis

REFERENCE

Hassan, R., *et al.*, "Parametric Analysis of Fiber-reinforced Laminated Momentum Wheel Rotors," 42nd AIAA/ASME/ASCE/AHS/ASC Structures, Structural Dynamics, and Materials Conference and Exhibit, AIAA-2001-1596, 2001.

ABSTRACT

The objective of this study is to analyze the parameters involved in the design of a graphite-reinforced-epoxy rotor, which is made from axisymmetric laminated concentric rings with interferences. This design is proposed for use in a Momentum Wheel that is used for attitude stabilization of geo-synchronous satellites. The formulation of the problem is addressed in the domain of the elasticity theory under plane stress conditions. An analytic model is developed by solving the non-homogenous variable-coefficients total differential equilibrium equation using the displacement formulation (Navier's approach). Four parameters of interest are investigated: the number of concentric rings, the amount of radial interferences, reinforcement volume fraction in each ring, and the lamination angle of the fibers in the hoop-radial plane with respect to the global hoop direction of the rings.

The parametric analysis shows that the amount of interferences between the neighboring rings should be kept at the minimum values required to keep the rings in contact at maximum operating speeds. The analysis also proves that by increasing the amount of reinforcement volume fraction, the minimum interferences needed can be reduced proportionally. Finally, it was found that at the required operating high speeds, the graphite fibers should be aligned in the circumferential direction, and the number of rings the rotor consists of should be kept at a minimum.

SUMMARY

Geo-stationary satellites are put in an equatorial orbit that is synchronous with Earth's rotation about its axis. Momentum Wheels are attitude control actuators that provide gyroscopic stiffness for the spacecraft as a means of stabilization about a single axis. Since the development of magnetic bearings, the design of wheels has shifted to lighter materials to be run at higher speeds. The design of the magnetically suspended rotor is to be made from a number of concentric rings with interferences as shown in Figure 2-19. The innermost ring must be made from steel to provide the required interaction with the magnetic bearings.

The first part of the study compared the performance of a multi-ring composite rotor versus an equivalent multiple ring rotor made from aluminum with the inner ring made of steel as well. One rotor is made from one steel ring and 5 aluminum. The second is made with an inner steel ring and 5 graphite-reinforced-epoxy (GRE) rings. The mass is fixed to be 2 kg, giving an angular velocity of 25,641 rpm. Two reinforcement volume fractions in the GRE case are used:

2-15

30% and 60% for all 5 rings. In both cases the fibers are aligned in the hoop direction. The interferences between the rings are designed such that the contact normal pressure at the interface between the 5 rings under study (either aluminum or GRE) is minimal. The radial stress distributions of the three materials are shown in Figure 2-20. The interferences required to attain such radial stress distributions are shown in Table 2-3. The interferences required for the aluminum rings are on the average five times those required for the 30% GRE rings and ten times those required for the 60% GRE rings.

The hoop stress distribution is shown in Figure 2-21. The hoop stress in the aluminum case reaches 425 MPa in the outermost ring whereas it is only 275 MPa at the same point for the 30% and 60% GRE cases. At this speed, the aluminum rotor would start yielding at the outermost contact surface. Table 2-4 shows the comparative maximum hoop stresses in each rotor at speeds of 5000, 10000, 15000, and 20000 rpm, with implementation of minimal interferences strategy. At all the speeds in Table 2-4, the maximum hoop stresses developed in the aluminum rotor are approximately 1.5 times those developed in the 50% GRE rotor. The final comparison between rotors is between an aluminum rotor and the 50% GRE rotor. Both rotors are tested to find the maximum speed each one can reach at a safety factor close to unity. For a safety factor of 1.04, the maximum speed the aluminum rotor can reach is 25,000 rpm, whereas the 50% GRE rotor can reach up to 45,000 rpm. The aluminum rotor needs around 2.6 times the amount of interferences used for the GRE rotor at 45,000 rpm.

Several parametric studies were conducted on four variables of the design of the rotor:

- Amount of interference
- Reinforcement volume fraction
- Lamination angle
- Number of laminated rings.

For the interference study, two possible interferences were studied: using equal amounts of interferences at all interfaces, and using larger amounts of interferences at larger contact radii. Figure 2-22 shows the radial stress distribution of a 6-ring rotor (inner steel ring and 5 GRE rings) with 60% volume fraction for equal interferences. Figure 2-23 shows the hoop stress distribution for the same configuration. In the second case where the interferences increase as the contact radii increases, the minimum amount of interferences are found by trial and error. Figure 2-20 shows the radial distribution in this case. Figure 2-24 compares the hoop stresses.

The parametric study of reinforcement volume fraction is based on the premise that an increase in the volume fraction results in an increase in the overall material elastic moduli and strength. The radial stress distribution of the 60% GRE with interference of 0.03 and 0.06 mm at all interfaces, and 30% GRE with interferences of 0.06 mm at all interfaces is shown in Figure 2-25. It can be observed that the 60% GRE with interferences of 0.06 mm is overstressed.

The lamination angle can also be varied within the composite layers. In this case, 0° refers to the case where the fibers are perfectly aligned in the hoop direction. At 90° the fibers are perfectly aligned in the radial direction. Figure 2-26 shows the radial stress distribution of a 60% GRE at 0° ply angle and at ±20° ply angle. The interferences needed for the ±20° laminated rotor are 6

times those needed for the 0° laminated rotor. Figure 2-28 shows that the maximum hoop stress for the ±20° ply angle laminates exceeds that of the 0° ply angle laminates by 75 MPa. It can be concluded that the fibers should be aligned in the hoop direction to increase the stiffness in that direction, thus minimizing the high stresses resulting from the centrifugal effect.

The rotor can be split into several layers of laminated composite in order to reduce the high hoop stresses induced from the high angular velocity of the rotor. Although the idea of the use of shrink-fitting decreases the hoop stresses in the inner rings significantly, the outer ring suffers from exaggerated stresses; therefore, it can be concluded that the fewer the number of rings used, the less the maximum hoop stress.

A rotor design is proposed that consists of 2 concentric rings of GRE. The inner ring is made from steel and the outer one from 70% unidirectional GRE laminate. The reinforcement is oriented in the hoop direction. The interference between the rings is 0.01 mm. The maximum angular velocity is 42,735 rpm. According to Tsai-Wu failure criterion, the factor of safety is 1.33. At this maximum operational speed, the hoop stress distribution is shown in Figure 2-27.
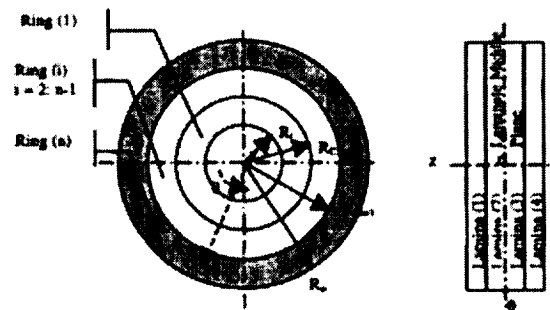

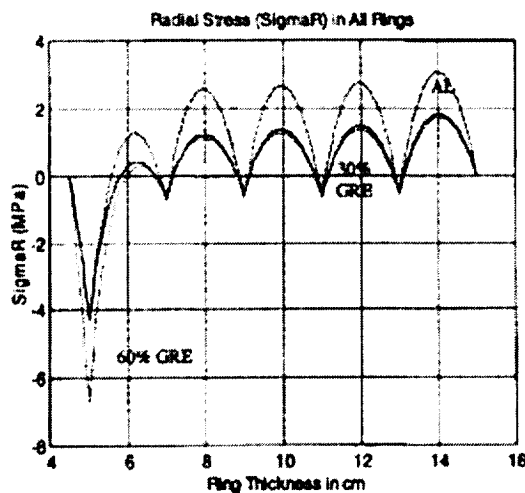**Figure 2-19: Top and side views of the laminated multi-ring rotor.**

Figure 2-20: Radial stress in a 6-ring rotor with minimal interferences @ 25,641 rpm.
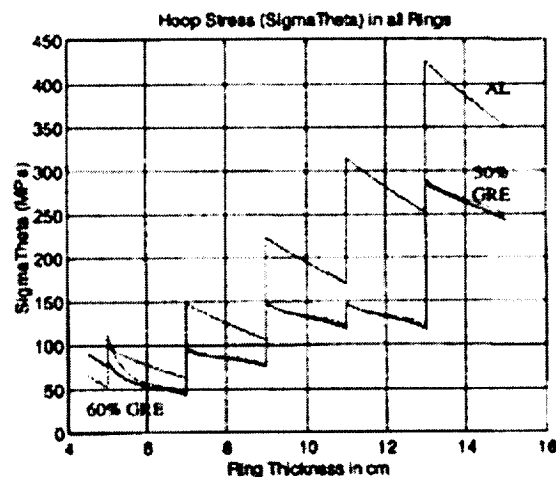
Figure 2-21: Hoop stress in a 6-ring rotor with minimal interferences @ 25,641 rpm.

Table 2-3: Comparative Amounts of Interferences for a 6-Ring Rotor at 25,641 rpm

mm			
Interference 2	0.0850	0.0080	0.0175
Interference 3	0.1517	0.0150	0.0310
Interference 4	0.2270	0.0240	0.0490
Interference 5	0.3227	0.0350	0.0700

Table 2-4: Comparative Amounts of Max Hoop Stresses for a 6-Ring Rotor at Different Speeds

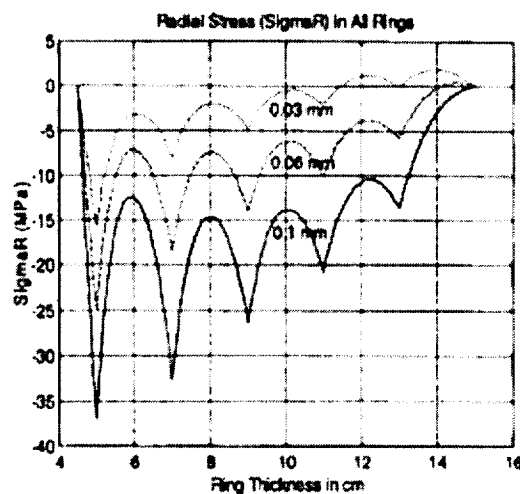| Speed		
5,000	12	18
10,000	43	65
15,000	100	150
20,000	170	260

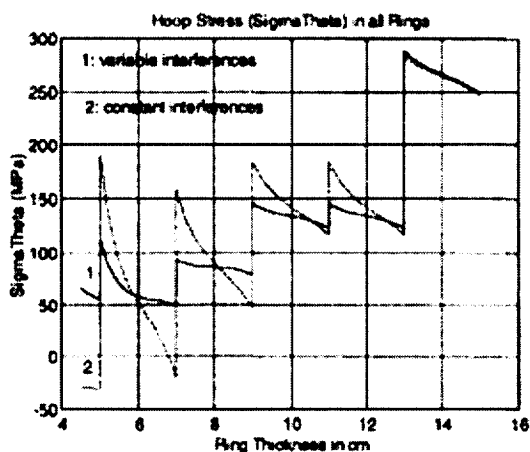Figure 2-22: Radial stress for a 6-ring rotor using different values of equal interferences.

Figure 2-23: Hoop stress distribution of a 6-ring rotor @ 25,461 rpm.
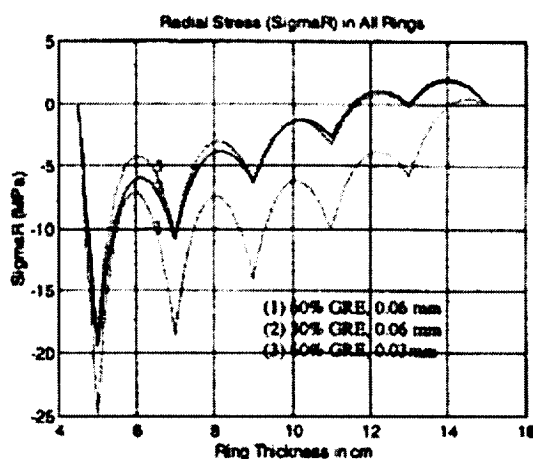

Figure 2-24: Radial stress of a 6-ring rotor with 60% and 30% GRE (Equal Interferences).
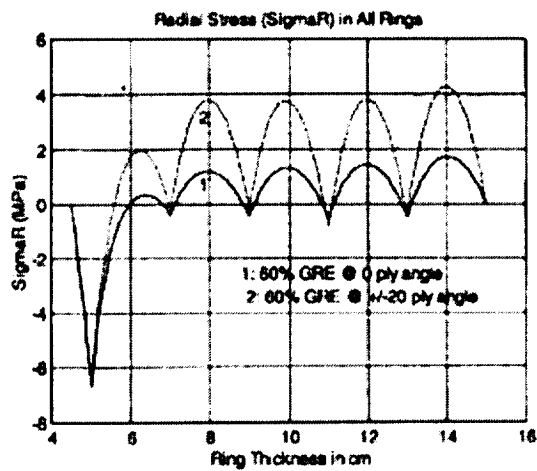
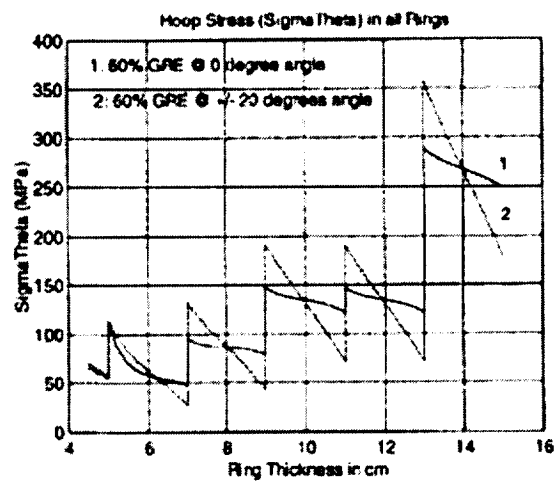**Figure 2-25:** Radial stress distribution for a 6-ring rotor @ 25,461 rpm.

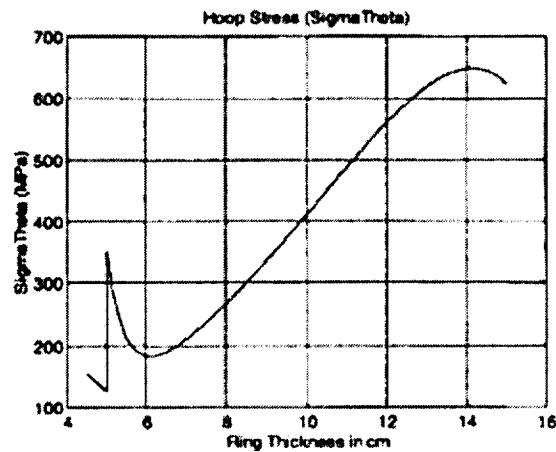**Figure 2-26:** Hoop stress distribution for a 6-ring rotor @ 25,461 rpm.

Figure 2-27: Hoop stress distribution for optimum solution @ 42,735 rpm.

2-19

CATEGORY

Analysis

REFERENCE

ABSTRACT

An approximate method is developed for comparing various fiber configurations in a composite structure with the objective of achieving optimal resistance to creep failure. The class of composite structures addressed has a single family of long or continuous strong fibers embedded in a creeping matrix material, e.g., a polymer, metal, etc. Thus, the structure is locally transversely isotropic with the fiber orientation generally varying throughout the structure. The proposed method, intended as an early design tool, is based on an upper bound on creep rupture time and an associated representative failure stress. The latter is evaluated and compared for different fiber configurations, thereby identifying that with optimal creep rupture resistance. This approach allows a substantial saving in computational time by avoiding a detailed analysis of the actual failure process. Application is made to a fiber-reinforced thick-walled cylindrical pressure vessel.

SUMMARY

When strongly reinforced composite structures operate at temperatures in the creep range of their matrix material, they suffer time-dependent deformation and eventually fail. A structure susceptible to creep damage initially incurs damage in regions of relatively high stress, leading to local softening and subsequent redistribution of stress as the damage zone spreads throughout the structure. Detailed numerical calculations of the stress redistribution and corresponding failure require substantial computing time. For this reason, an approximate method is proposed that makes use of a constitutive model for a creeping, damaging, anisotropic material. It incorporates an isochronous damage function that depends on an invariant specifying the maximum tensile stress normal to the local fiber-matrix interface. This damage function is used in bounding the rupture time. Following a previously published process, a global representative failure stress is calculated based on the upper bound on failure time. This is computed for each fiber configuration of interest in a composite structure; the configuration with the smallest representative failure stress has, relatively, the best creep failure resistance.

This method is applied to a fiber-reinforced thick-walled cylinder under interior pressure p. In order to apply the proposed approximate method, several fiber configurations are chosen. For each, a representative failure stress, σ_R, is determined. For the purposes of the paper, two fiber-reinforcement configurations are chosen for the cylinder, circumferential and axial. The cylinder has closed ends with inner and outer radii denoted as shown in Figure 2-28.

For the circumferentially oriented fibers, the representative failure stress is

$$\sigma_{RC} = \frac{p}{\left(\dfrac{b}{a}\right)^2 - 1} \; .$$

For the axially reinforced cylinder, the representative failure stress is

$$\sigma_{RA} = p\left[\frac{2}{\left(\dfrac{b}{a}\right)^2 - 1}\right]^{1/v}\left[\frac{\left(\dfrac{v-2}{v-1}\right)}{\left(\dfrac{b}{a}\right)^{(v-2)/(v-1)} - 1}\right]^{(v-1)/v} \; .$$

The better fiber configuration in terms of creep failure resistance is the smaller of the two. The ratio of σ_{RA}/σ_{RC} is

$$\frac{\sigma_{RA}}{\sigma_{RC}} = 2^{1/v}\left[\left(\frac{v-2}{v-1}\right)\frac{\left(\dfrac{b}{a}\right)^2 - 1}{\left(\dfrac{b}{a}\right)^{(v-2)/(v-1)} - 1}\right]^{(v-1)/v}$$

This ratio is plotted in Figure 2-29 versus the material parameter v for specified ratios of outer to inner radius of the cylinder, b/a. As $\sigma_{RA}/\sigma_{RC} > 1$, circumferential reinforcement is the better fiber arrangement.
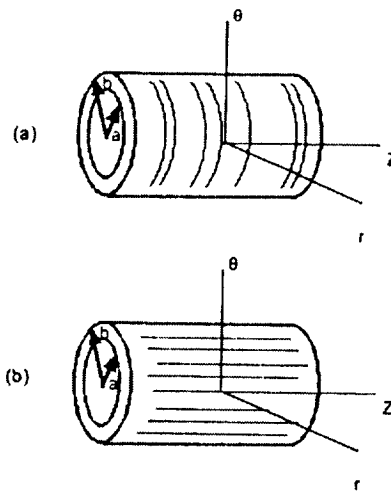

Figure 2-28: Thick-walled cylinder under interior
pressure (a) circumferential reinforcement,
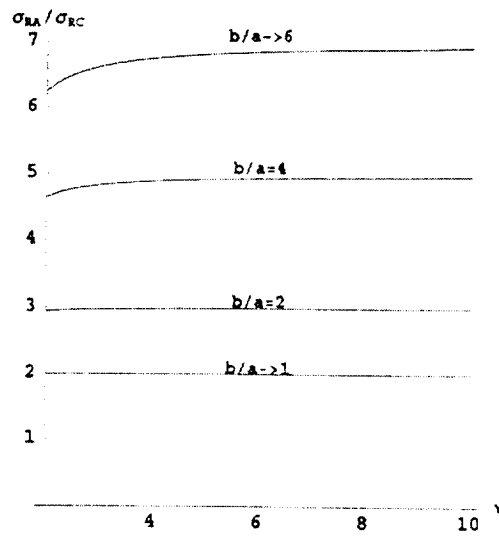(b) axial reinforcement.

2-21

Figure 2-29: Ratio of representative failure stresses
σ_{RA}/σ_{RC} **versus v for various b/a.**

CATEGORY

Analysis

REFERENCE

ABSTRACT

A viscoelastic analysis has been developed to investigate stress relaxation and creep in a multi-layered composite cylinder subjected to rotation. The analysis accounts for ply-by-ply variation of material properties, fiber orientations, and density gradients through the thickness of cylinders. A closed form solution based on the corresponding elastic problem is derived for a generalized plane strain state in a thick-walled multi-layered cylinder. Laplace transform is then applied to obtain the numerical solution procedure. A numerical simulation shows substantial creep and stress relaxation in thick-walled cylinders at an elevated temperature. Viscoelastic effects of composites can result in a drastic change of stress and strain profiles in a cylinder over a period of time, which is critical in terms of structural durability for application such as energy storage flywheels.

SUMMARY

It is very critical to ensure that the stress profiles and rotor dimensions do not change during the service life of the rotor. However, polymer matrix composites generally creep over a long period of time, especially at an elevated temperature. The objective of the study is to develop an analytical method to study the viscoelastic behavior of thick-walled composite cylinders subjected to rotation. The analysis accounts for ply-by-ply variation of properties, temperature changes, and fiber orientations.

The method is developed for a filament wound axisymmetric thick composite cylinder consisting of N layers with the axial coordinate z, the radial coordinate r, and the circumferential coordinate θ, shown in Figure 2-30. There is a corresponding thermoelastic problem with the transformed displacement components u, v and w in the axial direction, the circumferential direction, and the radial direction, respectively, for each layer.

The numerical simulation uses a thick composite cylinder with a 3 inch inner diameter and a 6 inch outer diameter. The cylinder is subjected to rotation of 50,000 rpm. Two lay-ups are considered: an all-hoop wound $[90]_{30}$ and a cross-ply architecture $[(90)_4,(0)_2,(90)_4]_3$. The ply thickness in all cases is 0.1 inch. The cylinders are constructed from IM7-graphite/8552-epoxy. Creep compliance of the 8552 epoxy near resin at 75° C is characterized from DMA measurements. The time-dependent characteristics of neat resin is then used for the creep compliance of the composite.

Figures 2-31 – 2-33 show the radial displacement, radial stress, and hoop stress distribution in the all-hoop wound thick-walled cylinders at three time instants. The radial displacement shown in Figure 2-31 illustrates significant creep over a period of time, which causes an increase of the total radial growth. The radial stress decreases significantly over a period of time due to stress relaxation. For this reason, a significant redistribution is observed in the hoop stress shown in Figure 2-33. Figures 2-34 – 2-36 show the results for a lay-up construction of $[(90)_4,(0)_2,(90)_4]_3$ at three time instants. The deformation profile is not as smooth because of the change of fiber orientation through the thickness. The radial stress also shows significant relaxation over a period of time. In Figure 2-36, the hoop stress profile shows significant variation over a period of time. The hoop stress is low in the $0°$ plies because of low stiffness in the circumferential direction. The stress gradient also increases in the $90°$ plies and the stress in the outer radius significantly increases.
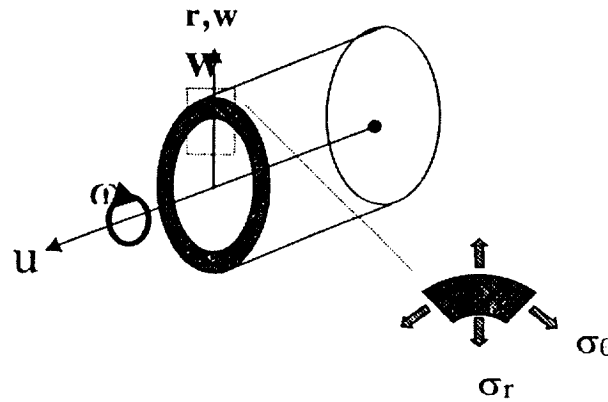
Figure 2-30: Coordinate system and stress components in a rotating cylinder.
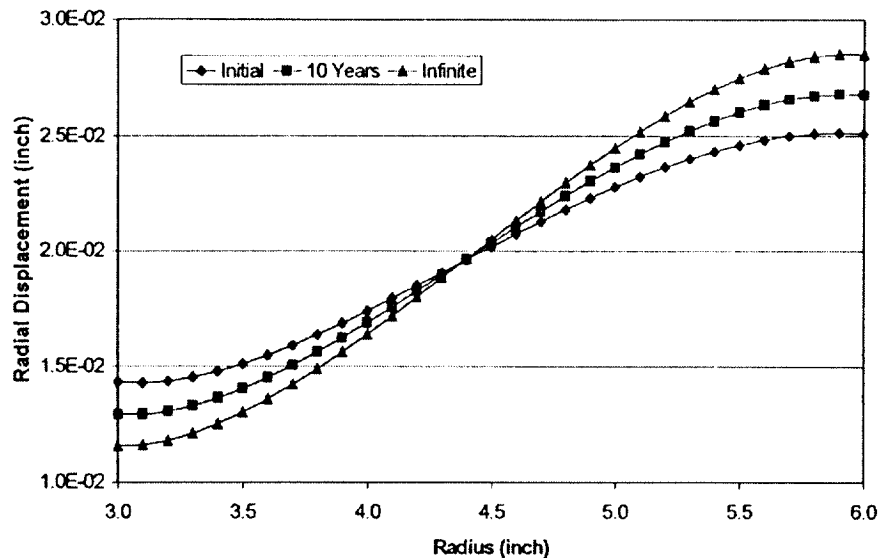
Figure 2-31: Creep of radial displacement in an all-hoop wound cylinder.

2-24
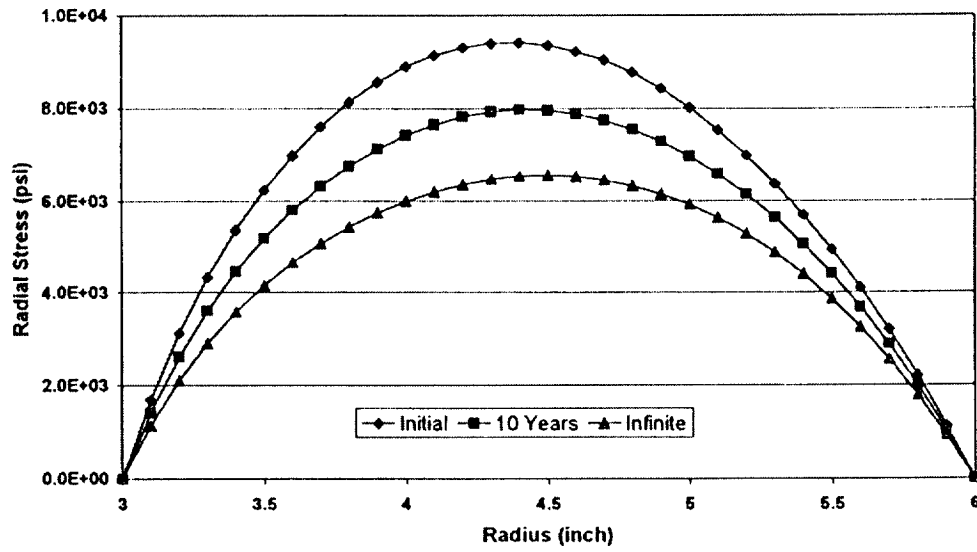
Figure 2-32: Relaxation of radial stress in an all-hoop wound cylinder.
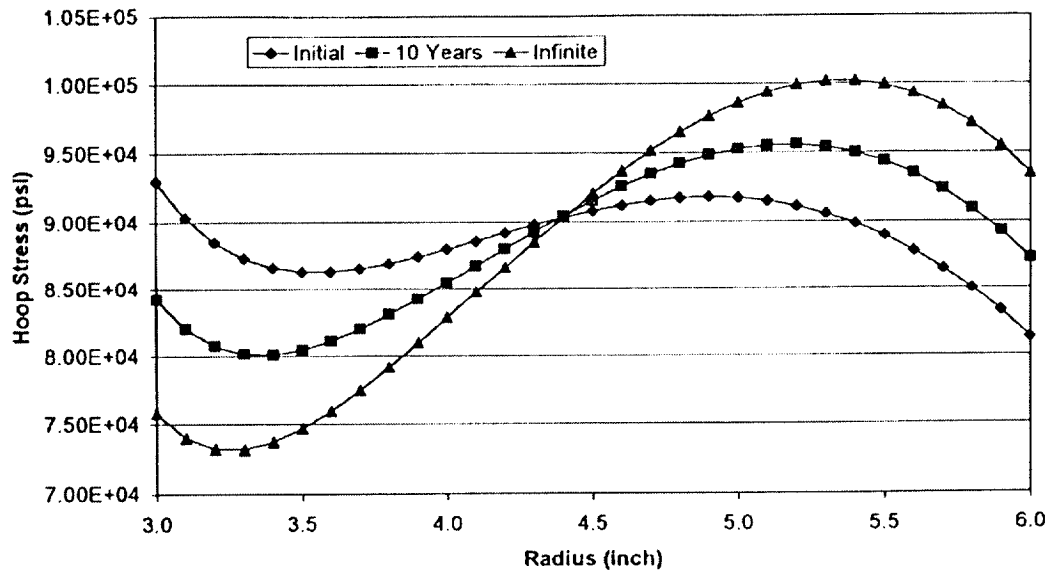
Figure 2-33: Relaxation of hoop stress in an all-hoop wound cylinder.

2-25
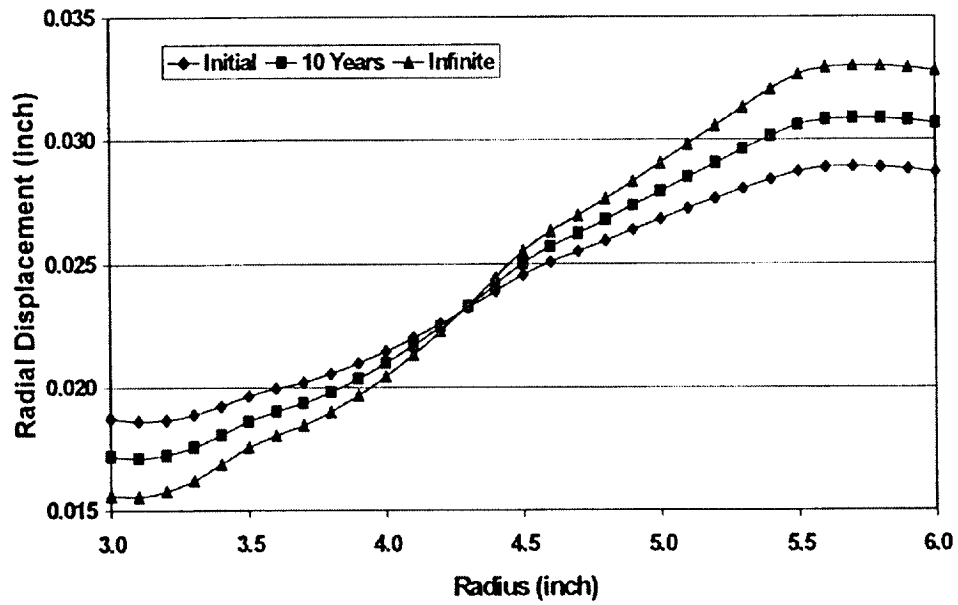
Figure 2-34: Creep of radial stress in a cross-ply wound cylinder.
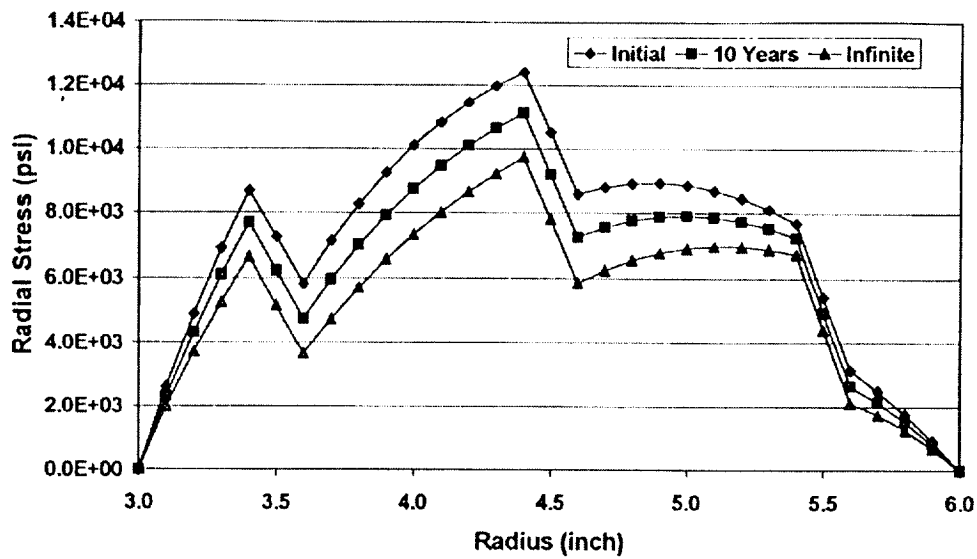
Figure 2-35: Relaxation of radial stress in a cross-ply wound cylinder.

Figure 2-36: Relaxation of hoop stress in a cross-ply wound cylinder.

CATEGORY

Analysis

REFERENCE

Ganley, J. M., *et al.*, "Quantifying Process Induced Residual Stresses in Filament Wound Composite Parts," 44th International SAMPE Symposium, Vol. 2:2095-2109, 1999.

ABSTRACT

Residual stresses are generated during the various steps of the composite part filament winding process (winding, curing, part removal, and cutting). Apart from decreasing the tendency of a circular part to reduce its radius of curvature upon radial cutting. The vario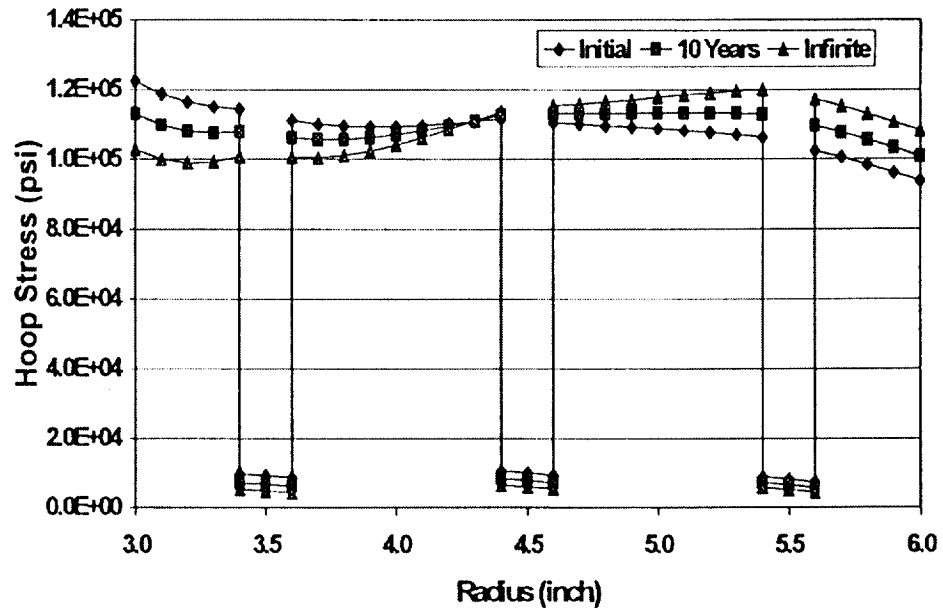us possible causes of "spring-in" were quantified, including those mechanisms proposed in the existing theories used to explain "spring-in", and the mechanics-based model that includes the contribution of the relevant process parameters was developed. The residual stresses through the composite part thickness were experimentally verified by a process of progressive precision cutting and associated strain relief. These strain changes were monitored with precision strain gages. A finite element model (FEM) of the anisotropic, curved composite part was then developed to obtain the exact through-thickness residual stress profile from the experimental data.

SUMMARY

There are three prevailing theories to explain spring-in in composite parts: anisotropy with initial curvature, through thickness inhomogeneity, and part compaction. The basis of the theory of anisotropy combined with initial curvature is that the part can experience a different strain in the radial and circumferential directions. This difference in strain can lead to a curvature change (i.e., spring), as seen in Figure 2-37. The second theory, of through thickness inhomogeneity, has as its basis the concept that the fiber and resin in a composite system have different mechanical properties. If an inhomogeneity exists through the thickness of the part, the difference will lead to differential straining through the thickness, and thus a curvature change. In order to obtain a highly compacted finished part both the excess resin and air voids are bled out during the cure process. This is accomplished using vacuum suction and autoclave pressure to the side of the part opposite the mandrel The circumference of the outer fibers will decrease more than the inner fibers. This compaction will reduce the winding tension preferentially from the outside-in, giving an unbalanced residual stress profile and a new moment (spring-in when the part is cut).

Care was taken to develop equations to relate the spring-in to the residual strain profile through the thickness of a composite part. These equations were compared to experimental data, shown in Figures 2-38 and 2-39, where $\Delta\varphi$ is curvature change in units of cm^{-1}. Figure 2-38 is for 10 layer parts with the winding tension varied from 8.9 to 35.6 N. Figure 2-39, is for constant winding tension of 17.8 N while the part thickness is varied from 2 to 30 layers.

Using the 10 layer, 17.8 N winding tension sample, the experimental and analytical results were compared for the three theories:

a) Anisotropy with Initial Curvature:
    • The predicted curvature change due to anisotropy was less than 5% of the measured value.
    • Given the above result, it is assumed that this is not a significant factor in spring-in for the specimens.

b) Through Thickness Inhomogeneity:
    • The predicted curvature change due to anisotropy was less than 3% of the measured value.
    • This result suggests that this mechanism is not a significant factor in the specimens.

c) Part Compaction:
    • The predicted curvature change due to anisotropy was approximately 11% of the measured value for a worst case residual strain profile.
    • This mechanism is the only one that could have a significant contribution to the total spring-in for the specimens.

Because none of the above theories do not fully account for the spring-in of the specimens, experimental work and FE analysis was conducted to try to determine the residual stresses in the parts immediately after cure. Using an idealized strain profile, Figure 2-40 shows a comparison between the experimental and theoretical $\Delta\varphi$ values. The fit is very good. The primary contribution to the total spring-in is the CTE mismatch between the composite part and mandrel and the associated tension-lag. This conclusion should be more closely looked at, though. As it is not totally clear where this conclusion came from in the text of the paper.
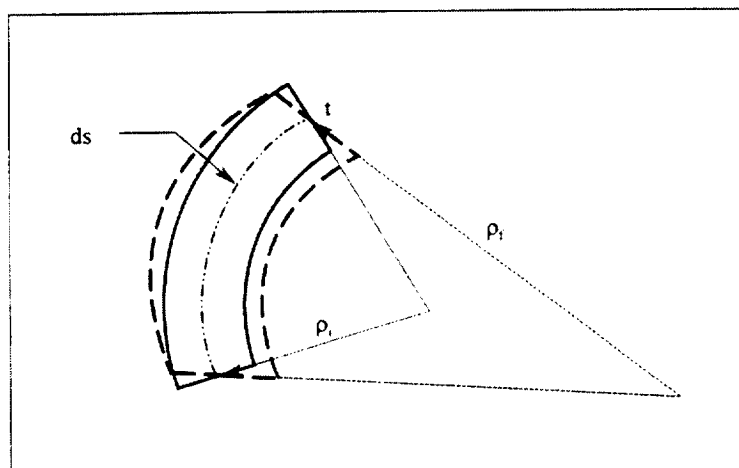

Figure 2-37: Differential element change in curvature due to anisotropy with initial curvature.
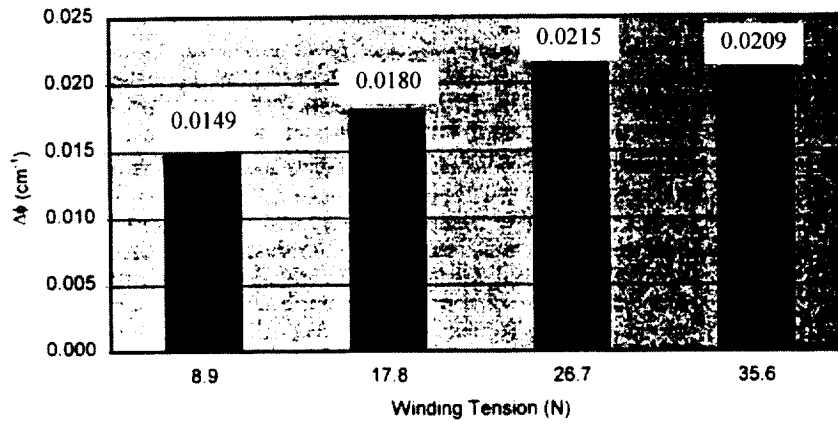
2-29

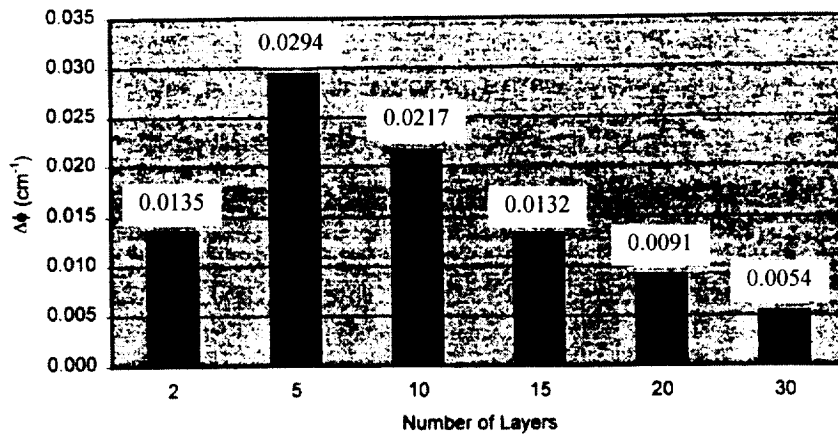**Figure 2-38: Curvature change vs. winding tension.**

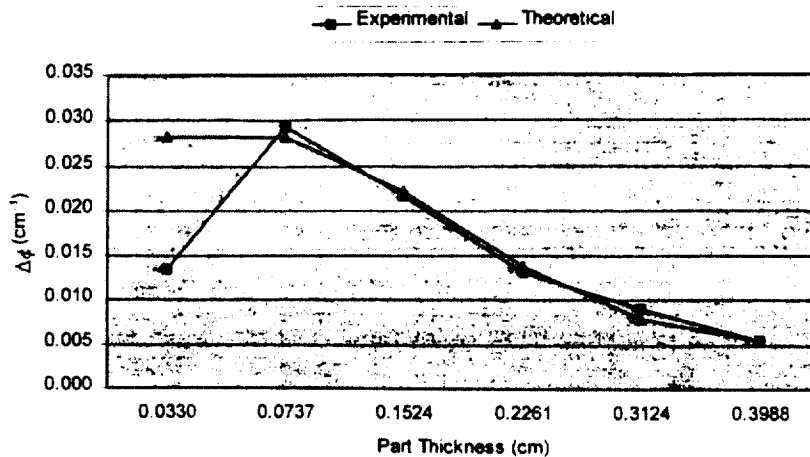**Figure 2-39: Curvature change vs. part thickness.**

Figure 2-40: Theoretical and Experimental $\Delta\varphi$ vs. part thickness.

CATEGORY

Analysis

REFERENCE

Huang, B. C., "Polar Woven Flywheel Rim Design," 44th International SAMPE Symposium, Vol. 2:2133-2144, 1999.

ABSTRACT

Although chemical batteries have been used extensively in spacecraft design, mechanical batteries such as flywheels offer significant weight and life benefits. Flywheel battery systems have the potential to store large amounts of energy for very little weight compared to chemical batteries and they can also be used as attitude control actuators to replace reaction wheel assemblies and control moment gyros. This dual function capability provides weight savings and an improvement in life and reliability of the total spacecraft system. Life expectancy of a flywheel is a least 10 years, during which it is expected to undergo 50,000 cycles (charge/discharge) while supplying 3 to 5 kW-h of usable energy. Two types of composite rotor construction include filament wound and polar woven architecture. Filament wound rotors are the most efficient, however, if rotor size is limited, a thin-walled filament wound rotor might not provide the required energy and therefore a shorter, thick-walled rotor is needed. Polar woven architecture offers superior radial stiffness and strength for a rotor design, which is required for the high radial stresses generated in a thick-wall rim section.

SUMMARY

Filament wound rims have fibers oriented in the hoop direction, where stresses are greatest. However, the wall thickness is limited due to the low radial strength and stiffness of this approach. This leads to flywheels with large diameters and thin walls. In cases where the rotor size is limited, a shorter, thick-walled rotor is needed to provide the same energy as a tall, thin-walled rotor. Bi-directional polar woven designs may offer an improvement because they have a higher radial stiffness and strength, which is required for the high radial stresses experienced by a thick walled rotor.

Isotropic rims were studied to obtain a good approximation of the rim dimension that would maximize the amount of storable energy. The maximum hoop stress occurs at the inner radius, and the maximum radials stress occurs at $r = (r_i r_o)^{0.5}$, where r_i is the inner radius and r_o is the outer radius.

Figure 2-41 shows a plot of rim thickness vs. radial stress. At 60,000 rpm, the polar woven (PW) flywheel rim thickness must be kept under 8 cm. However, a filament wound (FW) rim must be kept to a thickness of less than 4.5 cm. Figure 2-42 shows the energy plotted against rim thickness at different angular velocities. It is observed that the PW flywheel can provide more energy than an FW flywheel with the same outer radius. Energy density is inversely proportional

to rim thickness. Therefore, a thin rim design with a larger outer radius will yield the highest energy density, as seen in Figure 2-43.

Once the dimensions of the rim were determined in the isotropic study, a study of orthotropic rim sections was performed using material properties of the polar woven material. Figure 2-44 shows a plot of the radial stress vs. rim thickness. The proportionality given in the figure description was used to plot the results. The exact equation is proprietary, and not available.
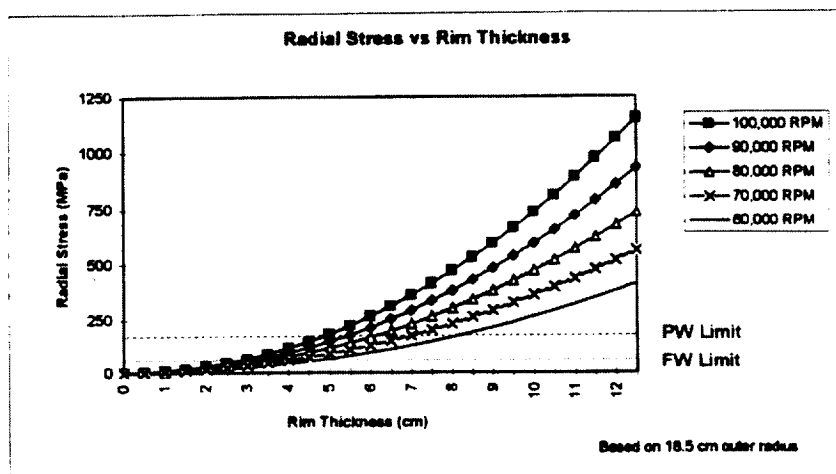
Figure 2-41: Radial stress vs. rim thickness for different angular velocities with a fixed outer radius of 18.5 cm.
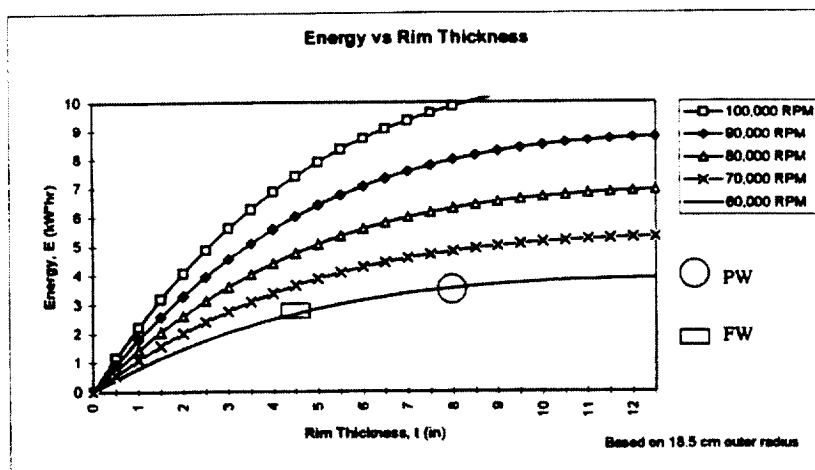
Figure 2-42: Energy vs. rim thickness at different angular velocities – Thicker rims provide more energy.

2-32
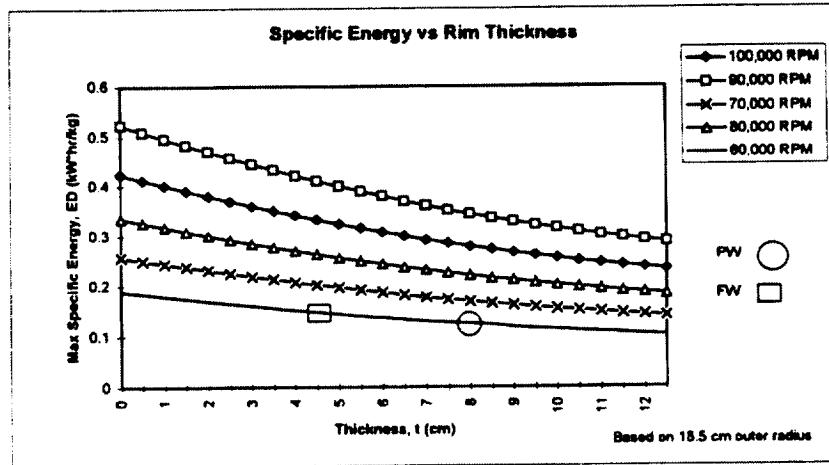
Figure 2-43: Specific energy vs. rim thickness at different angular velocities – Thinner rims are more efficient.
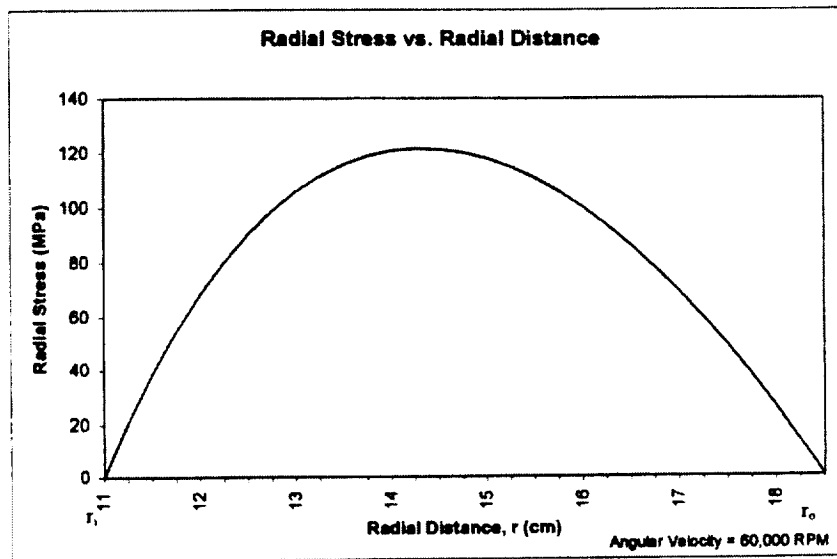
Figure 2-44: Radial stress distribution vs. rim thickness at a rotor speed of 60,000 rpm. Radial stress, σ_r, is proportional to $\rho\omega^2(r_i^2 + r_o^2 + r_i^2 r_o^2/r^2 - \{(1 + 3v)/(3 + v)\}r^2)$, where r_o is the outer radius, r_i is the inner radius, v is Poisson's ratio, and r is the radial distance bounded between r_i and r_o.

REFERENCE

Ha, S. K. and D. J. Kim, "Optimal Design of a Hybrid Composite Flywheel Rotor Using Finite Element Methods," *Proceedings of the 44th International SAMPE Symposium*, Vol. 2:2119-2132, 1999.

ABSTRACT

An optimum design has been performed to maximize the total stored energy (TSE) of a hybrid composite flywheel rotor with a permanent magnet attached inside the flywheel. The flywheel rotor consists of multiple rims of advanced composite materials. A four node axisymmetric finite element is thus developed which takes care of rim-by-rim variation of material properties and the rotating centrifugal forces. 3-dimensional intra-laminar quadratic Tsai-Wu criterion for the strength analysis is used yielding the failure index for each element. An optimum design is then performed maximizing TSE with the inner radius of the rotor and the thickness of each composite rim as design variables. Up to 4 material sequences are considered and their radial thickness and the size of the permanent magnet for each material sequence are calculated. The optimal design obtained in this study shows that TSE in a rotor can be significantly increased by properly fabricating the rotor using multiple rims of the optimal thickness.

SUMMARY

Design of a flywheel rotor that maximizes the TSE depends on several factors. Two in particular are investigated in this study: (a) properly designing a hybrid rotor with multiple rims of different materials in order to reduce the tensile stress in the radial direction, and (b) the method of attachment of the permanent magnet for the motor/generator to the hub that is connected to the flywheel rotor.

The overall objective of the study was to design a flywheel rotor that maximizes TSE without any material failure. The flywheel rotor should also induce the required voltage, V_o, with the given conditions of the geometry of the stator, the length of the rotor, and the rotating speed. Figure 2-45 shows the design variables for one of the optimization cases. The procedure followed for optimal design together with the structural analysis is shown in Figure 2-46.

Five materials were chosen, because of their availability, to combine for the investigation: (A) Glass/Epoxy, (B) Kevlar/Epoxy, (C) AS/H3501, (D) T300/N5208, and (E) IM6/Epoxy. The sequence is in the order of increasing circumferential Young's Modulus, E_θ.

Table 1 gives the results from the optimization procedure. The calculated design variables and calculated TSE are listed. Each thickness of composite rim and the inner and outer radii of the magnet are considered design variables. The rotation speed was set to 60,000 rpm.

From the investigation it was observed that the stress distributions are effected by the sequence of stiffness of the chosen materials. Softer materials were placed near the inside radius of the rotor which are easier to expand in the radial direction, and stiffer materials on the outer radius of the rotor which experience less radial displacement, This configuration eventually reduced the radial stresses.
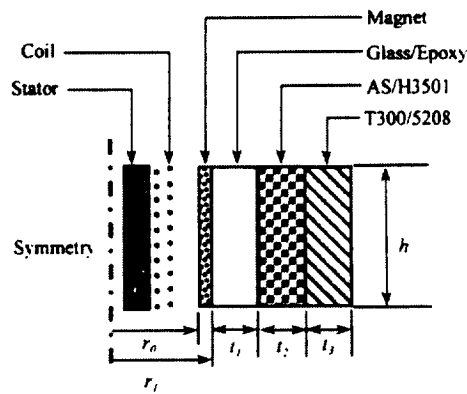
Figure 2-45: Cross sectional view of the hybrid composite flywheel rotor together with a stator and the permanent magnet; r_0, r_1 and t_m are design variables in the optimization.

Initial Design Variables
r_0, r_1, t_m ($m=1,2,....,M$)

Input Data
: Material Properties of Composites
: Rotation Speed ω

Pressure due to Magnet

Structural Analysis

3D Tsai-Wu Failure Criterion(R)

Update D.V.
r_0, r_1, t_m ($m=1,2,....,M$)

Optimum Design
Find $x_j = r_0, r_1, t_m$
($m=1,2,....,M$)
Maximize $E = \frac{1}{2}I\omega^2$
Subject to $Max\ R < 1$
& $V_u = \overline{V}_u$

No

Optimum

Yes

Find r_0, r_1, t_m ($m=1,2,....,M$)

Figure 2-46: The procedure of structural optimization for a hybrid composite flywheel rotor under the pressure due to a magnet using the structural analysis with r_0, r_1, and t_m as design variables.

CATEGORY

Analysis

REFERENCE

ABSTRACT

A simple theoretical/empirical hybrid method for the prediction of residual stresses in in-situ cured, thick hoop-wound, thermosetting composite rings is presented. The method avoids the need for complicated characterizations of resin and fiber properties that affect residual stress development during the manufacturing process. New results from a series of experiments with in-situ cured hoop-wound glass and carbon reinforced epoxy composites show that residual stresses due to non-thermal sources such as winding tension and resin shrinkage during cure are essentially constant for fixed manufacturing process parameters and resin system, regardless of ring geometry and fiber type. Also the combined effect of winding tension and resin shrinkage becomes progressively less important in comparison to thermal effects as the ID/OD ratio of a ring decreases. The analysis method is demonstrated by using the data acquired with a single ring to predict the residual stress in another ring with different fiber, ID, and OD. Equations for the thermal expansion of hoop-wound composite rings were corrected from the published version and verified for a range of ring geometries, two different types of fibers, and two resin systems. The analysis tools outlined in this paper aid the design and fabrication of multiple-concentric-ring structures subjected to varying temperature, such as composite flywheels for energy storage.

SUMMARY

Knowledge of the curing mechanism for flywheel rotors is needed for the following reasons, according to the paper:

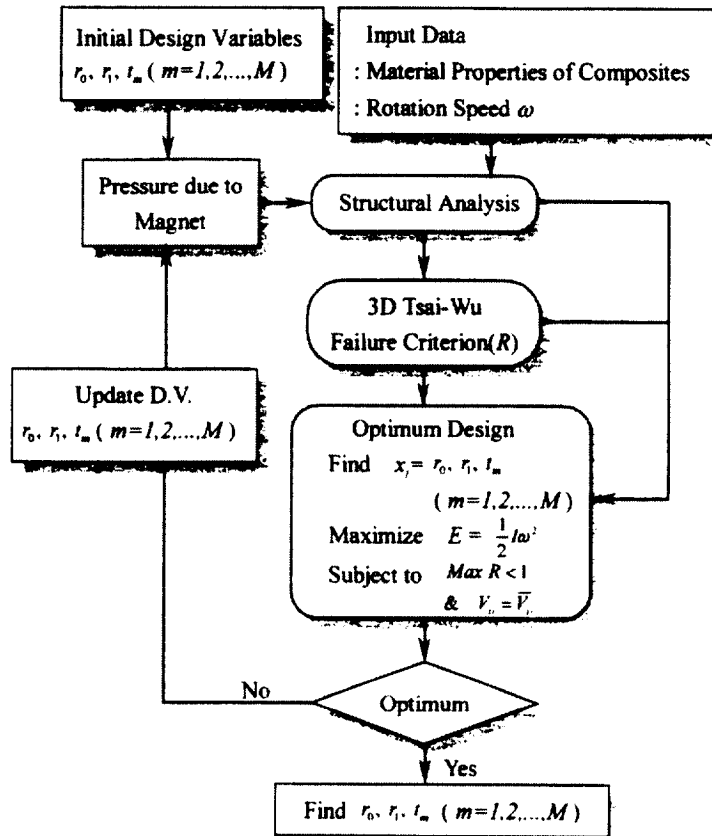a) The thermal expansions of the ID and OD of each ring (in multi-ring systems) are needed to predict interference pressures at different temperatures.

b) Knowing the residual stresses and thermal expansion coefficient of the ID of the ring is essential for net-shape manufacturing the ID of the ring.

c) The residual stresses incurred from the interactions of the winding tensions, matrix viscosity and stiffness, cure shrinkage, and thermal expansions can be large enough to cause matrix cracking.

The objectives of the project were to (a) experimentally characterize the residual stresses in in-situ-cured filament wound rings; (b) separate the components of these stresses due to non-thermal sources, such as winding tension and resin shrinkage, from those due to thermal expansion of the material; and (c) use this information to predict residual stresses in rings of arbitrary ID and OD made of the same resin system and under the same processing conditions.

The rotors shown in Figure 2-47 were those looked at in the paper. The β in the figure description refers to the ratio of inner radius to outer radius. The specimens were manufactured with typical volume fractions of 70% fiber and less than 2% voids.

Prior to the experiments the ID and OD ring coefficients of thermal expansion (RCTEs) for the rings was measured, as shown in Table 2-5. The experimental RCTE data given was compared to theoretical solutions from anisotropic thermoelasticity Equations 3-11, in paper). The comparison is given in Figure 2-48 for the carbon/epoxy rings. From the plots, it is verified that the ID and OD thermal expansions for rings of any β can be accurately found using the material properties and the solution for anisotropic thermoelasticity.

In order to measure the residual stresses in the composite rings, a wedge of material was cut and removed from each ring, while the hoop and axial strains at the ID and OD were recorded at room temperature. These mechanical strains were used to solve for the internal moments in the composite rings. Figure 2-49 shows a plot of the residual moments in the carbon and glass rings.

Figure 2-50 gives a plot of the radial residual stresses in the carbon and glass rings with β of 0.5 and 0.8 solved using Equation 18 in the paper. It can be seen that the radial residual stresses are significantly higher in carbon/epoxy rings than in glass/epoxy rings. More importantly, the maximum radial residual stresses in rings with β of 0.8 (typical for high speed flywheel rotors) are less than 2% and 8% of the radial strengths of typical glass and carbon composites, respectively.

Figures 2-51 and 2-52 show the relative contributions of temperature-induced and winding/cure-induced mechanical hoop strains at the IDs and ODs of the carbon rings. The winding/cure-induced mechanical strains are relatively constant for the entire range of β investigated. The major conclusion for this part of the study was that the winding/cure-induced residual strains are independent of β for in-situ cured, hoop wound rings.

Figure 2-53 shows a comparison between the calculated and predicted radial residual stress distributions in the carbon ring. It can be seen that the predicted radial stress is about 20% higher than the measured radial stress. This amounts to less than 1% of the radial strength of the composite, 74.6 MPa, shown on the plot for scale.

One conclusion reached from the experiments after separating out the thermal contribution to the residual strains, was that the calculated winding/cure induced hoop strains were found to be positive at the ID and negative at the OD of the rings. This suggests that cure shrinkage is the main cause of the non-thermal residual strain, since the outer layer of composite was originally wound with tension.
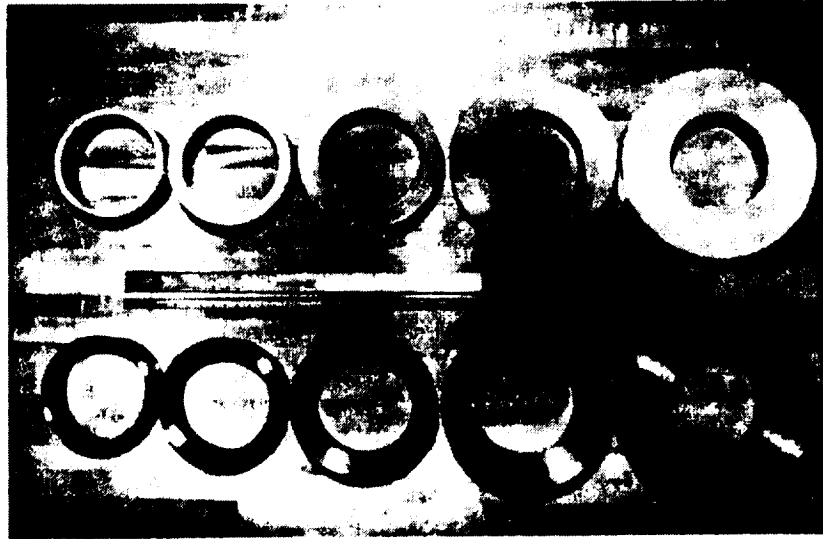
Figure 2-47: Photograph of *in-situ* cured carbon/epoxy and glass/epoxy rings with β = 0.5, 0.6, 0.7, 0.8, 0.9 after machining (14 in., 35.5 cm rule shown).

Table 2-5: Measured RCTE's of the Carbon Fiber/Epoxy and Glass Fiber/Epoxy Rings

	463 gl/ep		AS4C c/ep	
	ID RCTE	OD RCTE	ID RCTE	OD RCTE
β = 0.5	.030	7.06	−7.69	6.37
β = 0.6	.713	6.35	−6.39	5.69
β = 0.7	1.99	5.82	−4.45	4.98
β = 0.8	2.76	5.60	−2.97	3.49
β = 0.9	3.35	5.08	−1.61	2.28
β = 1 (Material Hoop CTE)	4.72	4.72	−.664	−.664
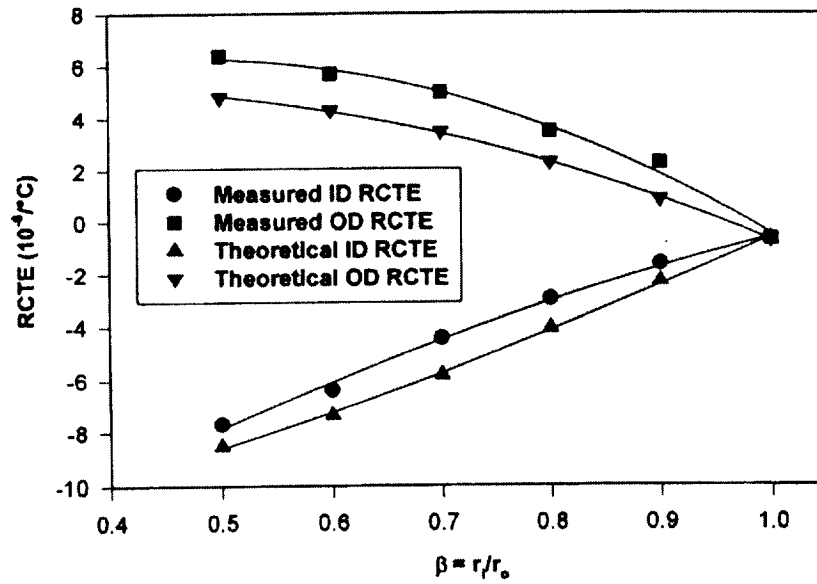
Figure 2-48: Measured and predicted ID and OD RCTEs vs. β for the fabricated carbon/epoxy rings.
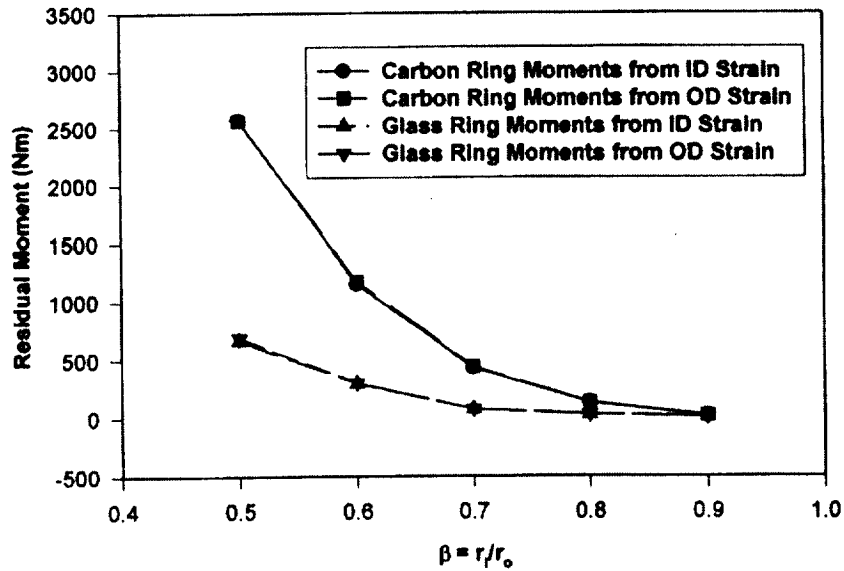
Figure 2-49: Residual moments in carbon/epoxy and glass/epoxy rings calculated from both ID and OD measured strains due to slicing rings.
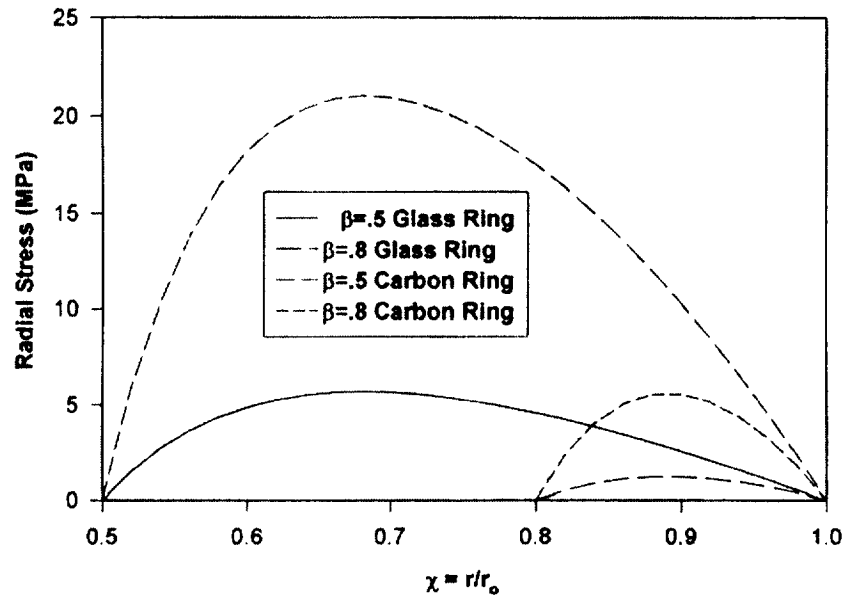
Figure 2-50: Radial residual stresses in carbon/epoxy and glass/epoxy rings with $\beta = 0.5$ and 0.8.
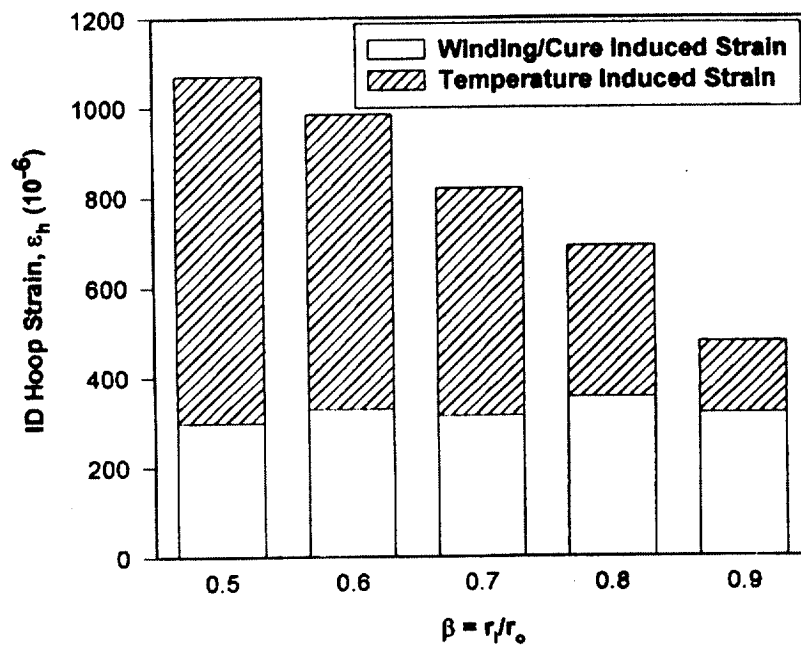
Figure 2-51: Components of the residual mechanical hoop strains at the ID of the carbon/epoxy rings.
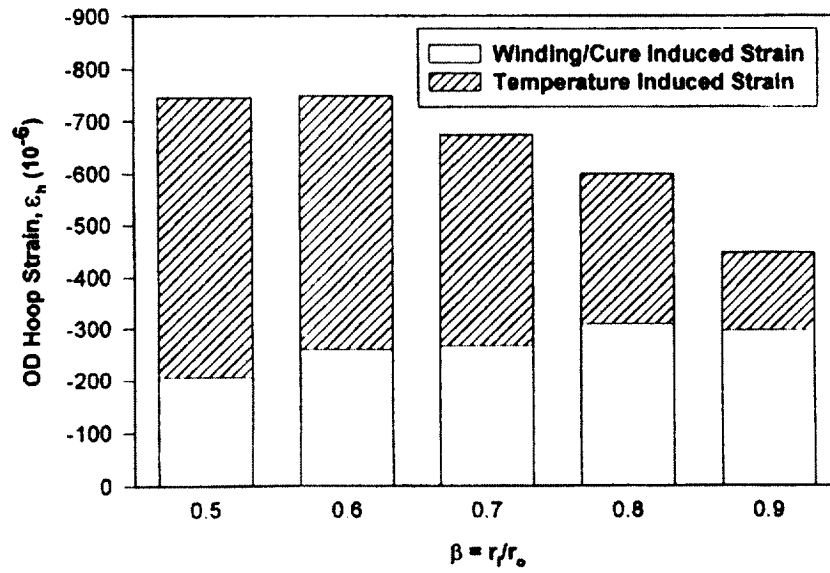
Figure 2-52: Components of the residual mechanical hoop strains at the OD of the carbon/epoxy rings.
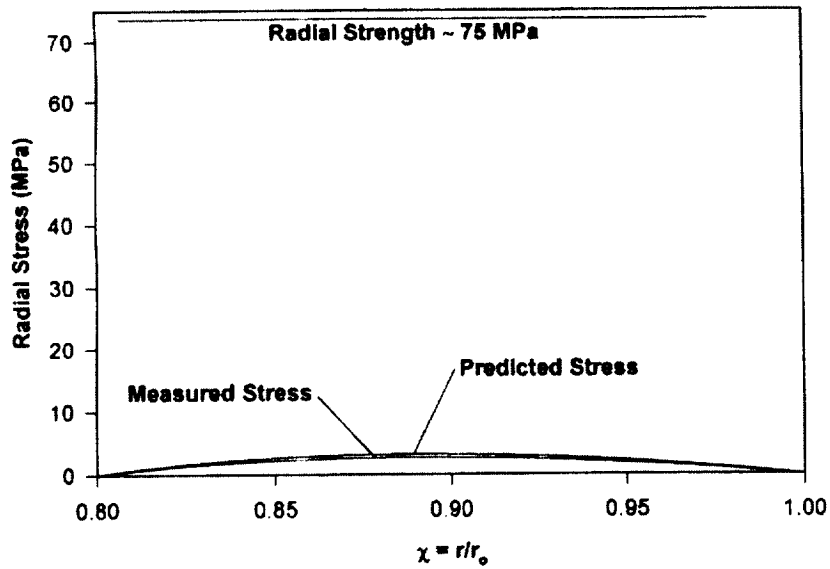
Figure 2-53: Measured and predicted radial residual stresses in a low temperature *in-situ* cured carbon/epoxy ring.

CATEGORY

Analysis

REFERENCE

ABSTRACT

The composite rotor of a pulsed-power machine is built with radial precompression to enhance mechanical performance; however, the preload might decrease due to the viscoelastic behavior of materials at elevated temperatures. In this investigation, an analytical solution is developed to study the viscoelastic problem of thick-walled cylinders. The analysis accounts for ply-by-ply variations of rotor structural properties, ply orientations, and temperature gradients through the thickness of rotors. Fiber-reinforced composite materials generally illustrate extreme anisotropy in viscoelastic behavior. The viscoelasticity exists mainly in matrix dominant properties, such as transverse and shear, while the fiber dominant properties behave more like elastic mediums. Accordingly, the viscoelastic characteristics of composite cylinders is quite different from those of isotropic cylinders. Currently, finite element packages such as ABAQUS, ANSYS, and DYNA3D are not very suitable for the viscoelastic analysis of composite cylinders because of the lack of anisotropic viscoelastic elements. The prestress in the hoop-wound fiber, which generates radial compression in the rotor, might decrease due to Poisson's effect alone from the creep behavior in the transverse properties of composite. The result also shows the effects of layup construction and fiber orientations on the anisotropic behavior of composite rotors.

SUMMARY

The objective of this study is to develop an analytical method to study the viscoelastic behavior of thick-walled composite cylinders. A thick, laminated composite cylinder with an elevated temperature is studied. The time-dependent thermal viscoelastic behavior of a 100 layer graphite epoxy composite cylinder subjected to a temperature increase $\Delta T = 150^\circ$ C is examined.

Figures 2-54 and 2-55 show radial displacement and radial stress profiles across the thickness of the cylinder at three instants in time. The shape of the radial stress plot is due to the discontinuity of material properties and various fiber orientations. The radial displacement reaches a steady state at 10^{12} minutes due to a long-term creep behavior. The radial displacement of most layers reaches a constant value, except at the innermost and outermost portions of the cylinder.

It is determined through the analysis that the stress relaxation in hoop-wound fiber layers results mainly from Poisson's effects of creep in the transverse direction since the properties are assumed to be elastic in the fiber direction. The reduction and redistribution of hoop stresses will cause a decrease of the radial compression in the cylinders over a long period.

Figure 2-54: Radial displacement profiles across the thickness of the cylinder at three different instants: t = 10^{-3} min, t = 10$^{4.5}$ min, t = 10^{12} min.
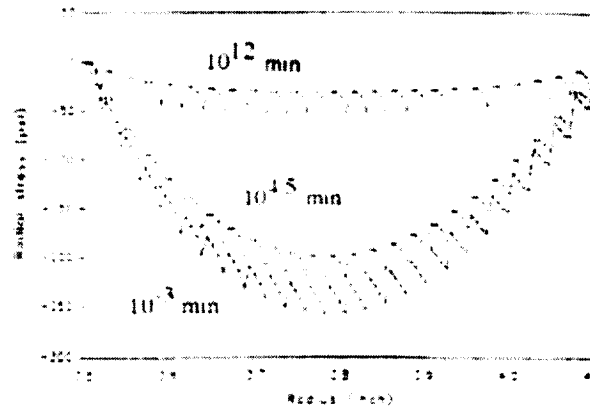
Figure 2-55: Radial stress profiles across the thickness of the cylinder at three different instants: t = 10^{-3} min, t = 10$^{4.5}$ min, t = 10^{12} min.

CATEGORY

Analysis

REFERENCE

ABSTRACT

Activation theory used in metals and polymers has been used to model creep of unidirectional composite and resin matrix, using the concept of internal stress. The model fits the experimental creep curves very well for a range of materials. The results obtained for a brittle epoxy and its carbon fibre-reinforced composite with two fibre orientations are reported. The model parameters, such as internal stress, activation volume and activation energy, have been measured experimentally and compared with model-fit values, and their influence on creep is discussed. Finally, an approach to predict the creep rupture of unidirectional composites using internal stress is presented.

SUMMARY

Most of the available models to simulate the visco-elastic behavior of polymers are broadly based on mechanical analogs, integral equations and power laws. One model extensively used in metals in understanding the plastic deformation mechanisms is based on an activation theory approach. In this analysis, the residual stresses are assumed to be small. This paper shows that the activation theory can be exclusively used to model the creep behavior of carbon fiber-reinforced polymer composites and the respective matrix resins. The internal stress measured experimentally can be used to predict creep rupture of unidirectional composites, which is the ultimate goal of this project.

The experimental tests conducted were constant-load creep tests repeated at different stress levels at room temperature.

The internal stress and creep curves at different stress levels up to 72% UTS are given in Figures 2-56 and 2-57 respectively for AS4/3501-6 $[10°]_8$ composite. In Figure 2-56, the solid line indicates the best-fit power law, at respective creep stresses. In Figure 2-57, the theoretical creep curves as predicted by activation theory are plotted with experimental results. The model simulates the experimental creep curves very well.

The internal stress, creep curve and activation volume plots for $[90]_{16}$ and 3501-6 composite are given in Figures 2-58 – 2-62. Solid lines in Figure 5 represent the best-fit power law for internal stress. From Figures 2-58 and 2-61, it can be inferred that the model prediction and experimental creep rate values are in good agreement. The observed deviation in the strain rate is thought to be due to temperature excursion.

Because the internal stress is defined to be due to elastic strain, a finite internal stress value will be measured immediately after loading as seen in Figures 2-56 and 2-60. The internal stress value at the start of creep depends on the rate of loading to a creep stress. The internal stress decreased with increasing loading rate. The rate of increase was high in the beginning but decreased with creep strain and time, as shown in Figure 2-60.

The relation of activation volume with effective stress is shown in Figures 2-59 and 2.62. They show clearly that activation volume decreases with increasing effective stress. The present model predicts the experimental creep curves very well.
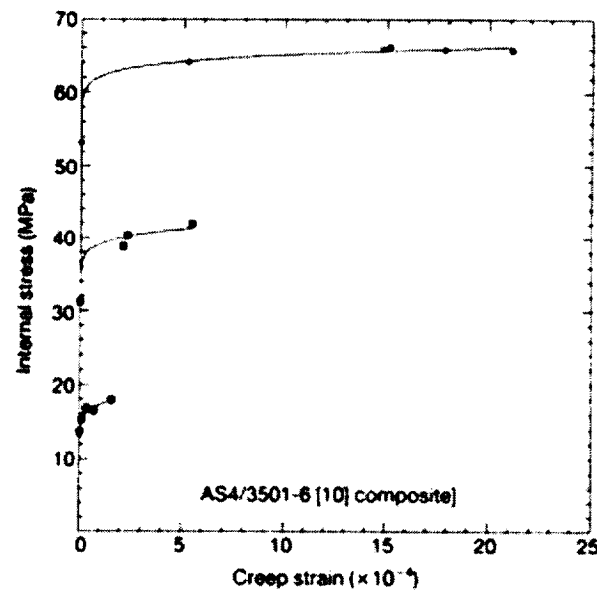
Figure 2-56: Internal stress as a function of creep strain at 295 K:
(◯) 18.55 MPa, (□) 41.96 MPa, (♦) 66.26 MPa, (------)
best fit.
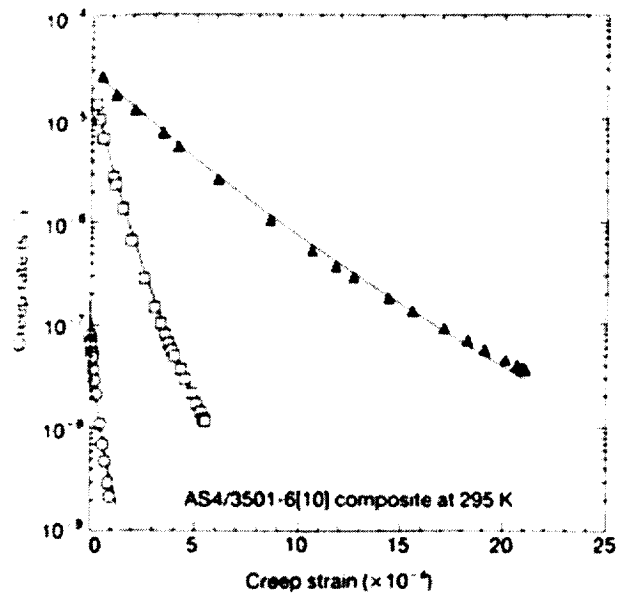
Figure 2-57: Comparison of (------) simulated and experimental creep
curves at 295 K: (=) 66.26 MPa, (□) 41.96 MPa, (*) 18.8 MPa.
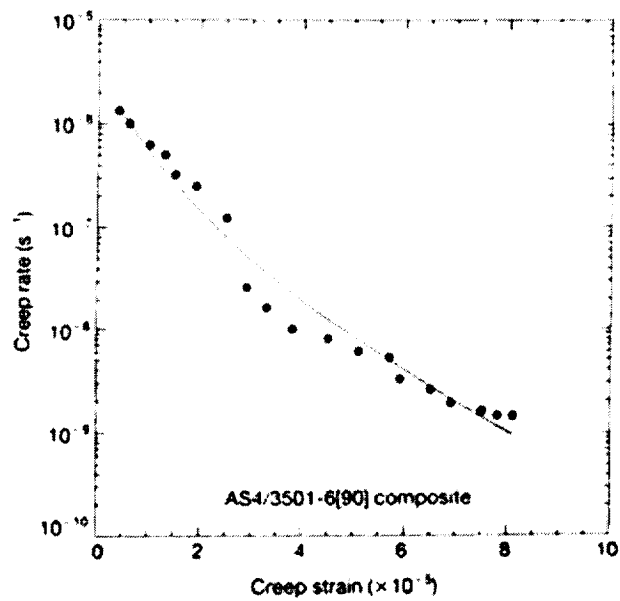
Figure 2-58: Comparison of (------) simulated and experimental
creep curves at 295 K: (() 31.02 MPa.
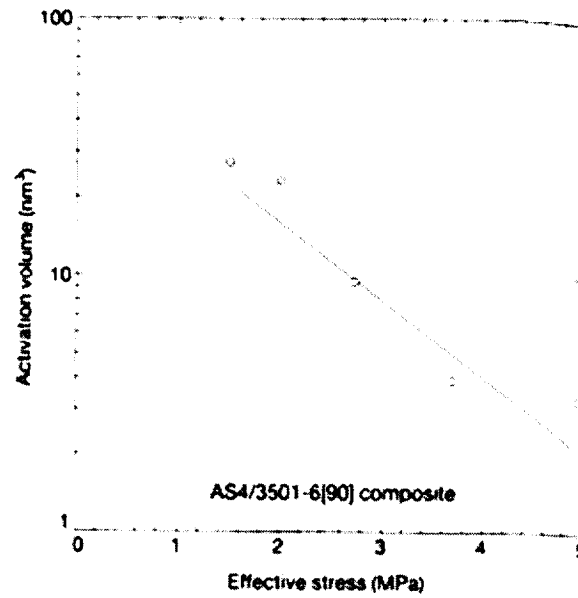
Figure 2-59: Comparison of (*) experimental and (------) model-fit
activation volume values at 295 K, for 31.02 MPa.
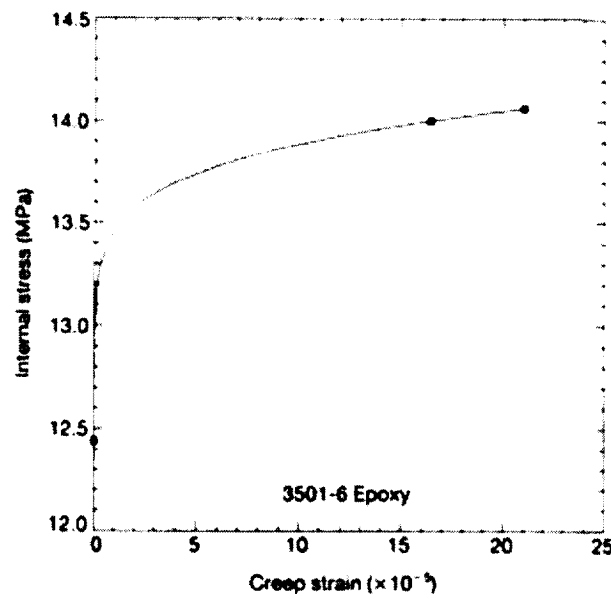
Figure 2-60: Internal stress as a function of creep strain at 295 K for
epoxy [3501-6]: (□) 14.13 MPa, (------) best fit.

2-48
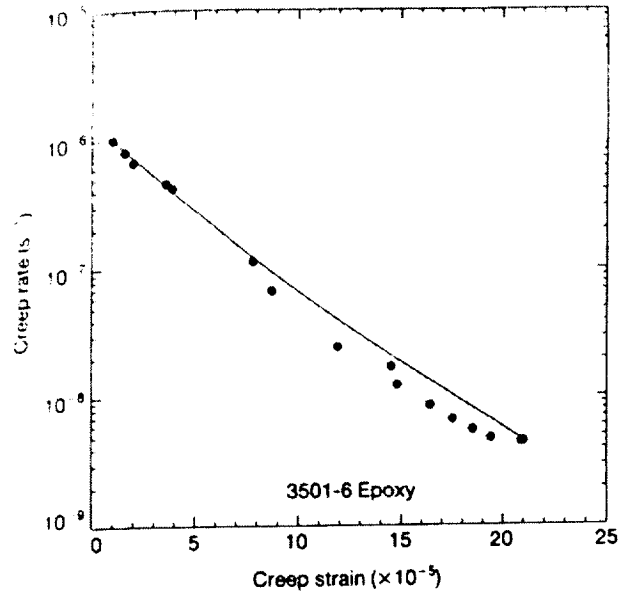
Figure 2-61: Comparison of (------) simulated (14.13 MPa and (() experimental creep curves at 295 K for epoxy [3501-6].
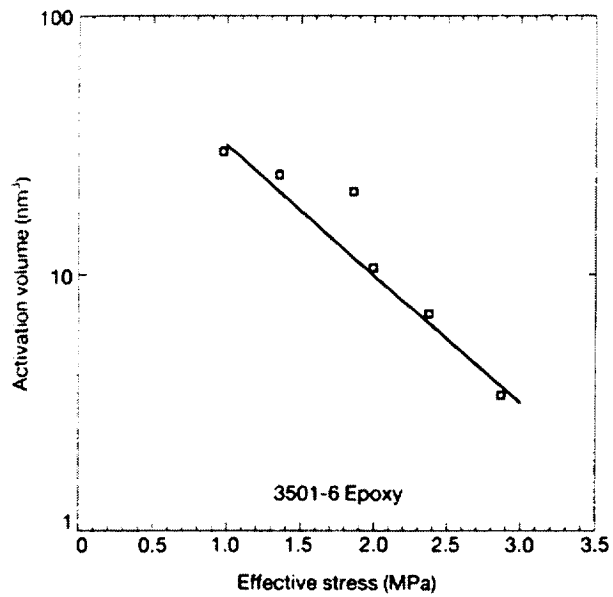
Figure 2-62: Comparison of (□) experimental and (------) model-fit activation volume values (14.13 MPa at 295 K for epoxy [3501-6].

CATEGORY

Analysis

REFERENCE

McCartney, L. N., "Analytical Micromechanical Models for the Prediction of Multiple Cracking in Composites," *Journal De Physique III*, Vol. 3:1637-1646, 1993.

ABSTRACT

Because of the wide variety of composite materials that are available, and the expense involved in testing to measure properties for design purposes (such as their damage tolerance), there is a need to develop predictive methods that can readily be utilized on desk-top computers. It is inevitable that such methods will be based on analytical rather than finite element techniques. A review is given of recent progress that is being made with the use of analytical micromechanical models for the prediction of the dependence of thermoelastic constants on crack density, and for the prediction of multiple cracking in both unidirectional and laminated composites.

Various stress transfer models for unidirectional and laminated composites are assessed for their quality by considering their ability (or otherwise) to satisfy the equations of equilibrium, stress-strain relations, interfacial boundary conditions, and external boundary conditions. Both shear-lag and variational models are considered. In addition, so-called complete solution models are described that provide *both* the stress and displacement distributions in a composite. The characteristics of the various models are briefly described.

A most important need is to be able to predict the dependence of the thermoelastic constants on the level of applied stress or strain rather than on crack density so that non-linear stress-strain behavior can be predicted. A recently developed energetic method of predicting multiple cracking in laminated composites is described showing how it can deal with both the simultaneous and progressive formation of cracks during loading for combined biaxial and shear modes of loading. It is pointed out that the fracture criterion can be derived from energetic principles or from the application of the generalized plane strain model of stress transfer, thus demonstrating energetic consistency. The fracture criterion depends only on macroscopic parameters, namely, the thermoelastic constants of cracked laminates and it follows that micromechanical models are only needed to determine the dependence of these constants on crack density.

COMMENTS

Discusses mathematical models to find stress transfer in unidirectional and laminated composites. Models that give displacement distributions are also discussed. Good overview of the fracture mechanics involved in cracked composites.

Analysis

SUMMARY

This text contains analytical methods for solving for stresses, strains, displacements, etc. for anisotropic plates.

First, consider the problem of the stress distribution in a composite curvilinear anisotropic ring. The plate is made of an arbitrary number of layers in a form of concentric rings of identical thickness h with cylindrical anisotropy. Each layer is assumed to be orthotropic, and all layers are rigidly connected as shown in Figure 2-63. The problem of the stress distribution in a many layer anisotropic pipe subjected to the internal and external pressures is analogous to this problem. The boundary conditions are as follows:

$$
\begin{array}{lll}
\text{when } r = a & \sigma_r^{(1)} = -p, & \tau_{r\theta}^{(1)} = 0; \\
\text{when } r = b & \sigma_r^{(n)} = -q, & \tau_{r\theta}^{(n)} = 0.
\end{array}
\qquad \textbf{Eq. 1}
$$
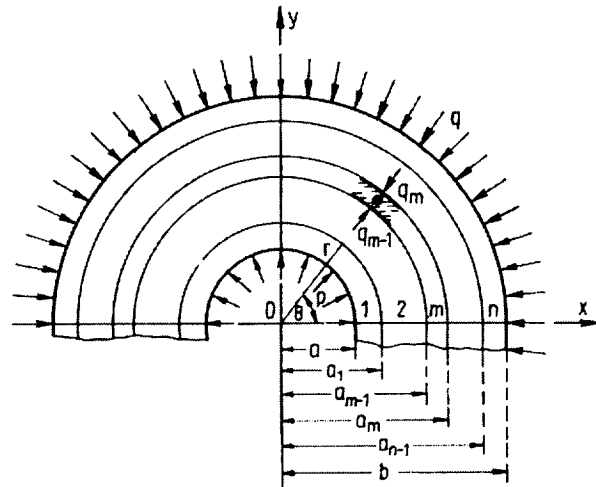
Figure 2-63: Plate with arbitrary number of layers in the form of concentric rings.

From this, we can calculate the hoop, radial, and shear stresses to be:

$$\sigma_r^{(m)} = \frac{q_{m-1}c_m^{k_m+1}}{1-c_m^{2k_m}}\left[\left(\frac{r}{a_m}\right)^{k_m-1} - \left(\frac{a_m}{r}\right)^{k_m+1}\right]$$

$$+ \frac{q_m}{1-c_m^{2k_m}}\left[-\left(\frac{r}{a_m}\right)^{k_m-1} + c_m^{2k_m}\left(\frac{a_m}{r}\right)^{k_m+1}\right],$$

$$\sigma_\theta^{(m)} = \frac{q_{m-1}c_m^{k_m+1}k_m}{1-c_m^{2k_m}}\left[\left(\frac{r}{a_m}\right)^{k_m-1} + \left(\frac{a_m}{r}\right)^{k_m+1}\right] \qquad \textbf{Eq. 2}$$

$$- \frac{q_m k_m}{1-c_m^{2k_m}}\left[\left(\frac{r}{a_m}\right)^{k_m-1} + c_m^{2k_m}\left(\frac{a_m}{r}\right)^{k_m+1}\right],$$

$$\tau_{r\theta}^{(m)} = 0;$$

The stress distribution in a rotating circular disk with cylindrical anisotropy can also be calculated. The disc shown in Figure 2-64 is assumed to possess cylindrical anisotropy and be orthotropic, so that any radial plane is an elastic symmetry plane. The stress distribution in such a disc, either solid or weakened by a circular opening at the center, is obtained by a stress function which depends only on distance r.
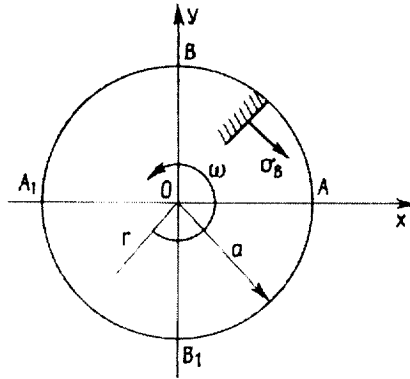
Figure 2-64: Rotating circular disk with cylindrical anisotropy.

The following are formulae for the components of stress:

$$\sigma_r = C(1+k)r^{k-1} + D(1-k)r^{-k-1} - \frac{\gamma\omega^2}{g}\cdot\frac{3+\nu_\theta}{9-k^2}r^2,$$

$$\sigma_\theta = C(1+k)kr^{k-1} - D(1-k)kr^{-k-1} - \frac{\gamma\omega^2}{g}\frac{k^2+3\nu_\theta}{9-k^2}r^2, \qquad \textbf{Eq. 3}$$

$$\tau_{r\theta} = 0;$$

Where

$$k = \sqrt{E_\theta \big/ E_r}$$

E_r and E_θ are Young's moduli for principal directions, radial r and tangential θ; v_r and v_θ are Poisson ratios; γ is the specific weight of the material; and ω is the angular velocity.

Constants C and D can be used to satisfy the required conditions at the plate and opening edges. The stresses in a solid disc are:

$$
\left.
\begin{aligned}
\sigma_r &= \frac{\gamma \omega^2 a^2}{g} \cdot \frac{3 + v_\theta}{9 - k^2} \left[\left(\frac{r}{a}\right)^{k-1} - \left(\frac{r}{a}\right)^2 \right], \\
\sigma_\theta &= \frac{\gamma \omega^2 a^2}{g} \cdot \frac{k}{9 - k^2} \left[(3 + v_\theta)\left(\frac{r}{a}\right)^{k-1} - k(1 + 3v_r)\left(\frac{r}{a}\right)^2 \right], \\
\tau_{r\theta} &= 0.
\end{aligned}
\right\}
\quad \textbf{Eq. 4}
$$

When $k = 1$, $v_r = v_\theta = v$, we have the stress distribution in an isotropic disc.

It is also possible to obtain the stress distribution in a rotating disc of several ring-shaped (concentric), welded or glued layers with cylindrical anisotropy but different elastic constants. The disc from Figure 2-63 is now assumed to be rotating with a constant angular velocity around its axis passing through the center. A circular opening is also assumed to be at the center of the disc. The external edge and edge of the opening are free from external load and their movements are not constrained, i.e., $p = q = 0$. An additional variable is introduced; γ_m ($m = 1, 2, ..., n$) which is the specific weight of the material in layer m. From this, we obtain the following formulae for stresses in the m-th layer:

$$\sigma_r^{(m)} = \frac{\gamma_m \omega^2}{g}\, a_m^2\, \frac{3 + \nu_\theta^{(m)}}{9 - k_m^2}\left[\frac{1 - c_m^{k_m+3}}{1 - c_m^{2k_m}}\left(\frac{r}{a_m}\right)^{k_m-1}\right.$$

$$+ \frac{1 - c_m^{k_m-3}}{1 - c_m^{2k_m}}\, c_m^{k_m+3}\left(\frac{a_m}{r}\right)^{k_m+1} - \left.\left(\frac{r}{a_m}\right)^2\right]$$

$$+ \frac{q_{m-1}c_m^{k_m+1}}{1 - c_m^{2k_m}}\left[\left(\frac{r}{a_m}\right)^{k_m-1} - \left(\frac{a_m}{r}\right)^{k_m+1}\right]$$

$$+ \frac{q_m}{1 - c_m^{2k_m}}\left[-\left(\frac{r}{a_m}\right)^{k_m-1} + c_m^{2k_m}\left(\frac{a_m}{r}\right)^{k_m+1}\right],$$

$$\sigma_\theta^{(m)} = \frac{\gamma_m \omega^2}{g} \cdot \frac{a_m^2}{9 - k_m^2}\left\{(3 + \nu_\theta^{(m)})\, k_m\left[\frac{1 - c_m^{k_m+3}}{1 - c_m^{2k_m}}\left(\frac{r}{a_m}\right)^{k_m-1}\right.\right.$$

$$- \frac{1 - c_m^{k_m-3}}{1 - c_m^{2k_m}}\, c_m^{k_m+3}\left(\frac{a_m}{r}\right)^{k_m+1}\left.\right] - (k_m^2 + 3\nu_\theta^{(m)})\left(\frac{r}{a_m}\right)^2\left.\right\}$$

$$+ \frac{q_{m-1}c_m^{k_m+1}k_m}{1 - c_m^{2k_m}}\left[\left(\frac{r}{a_m}\right)^{k_m-1} + \left(\frac{a_m}{r}\right)^{k_m+1}\right]$$

$$- \frac{q_m k_m}{1 - c_m^{2k_m}}\left[\left(\frac{r}{a_m}\right)^{k_m-1} + c_m^{2k_m}\left(\frac{a_m}{r}\right)^{k_m+1}\right],$$

$$\tau_{r\theta}^{(m)} = 0;$$

Eq. 5

The solution for a solid disc with a free external edge is:

$$\sigma_r = \frac{\gamma \omega^2 a^2}{g}\, \frac{3 + \nu_\theta - m}{9 - k^2 - (3 - \nu_\theta)m}\left[\left(\frac{r}{a}\right)^{n_1-1} - \left(\frac{r}{a}\right)^2\right],$$

$$\sigma_\theta = \frac{\gamma \omega^2 a^2}{g}\, \frac{1}{9 - k^2 - (3 - \nu_\theta)m} \times$$

$$\times \left[(3 + \nu_\theta - m)\, n_1\left(\frac{r}{a}\right)^{n_1-1} - (k^2 + 3\nu_\theta - \nu_\theta m)\left(\frac{r}{a}\right)^2\right],$$

$$\tau_{r\theta} = 0$$

Eq. 6

$$\left(k = \sqrt{\frac{E_{\theta m}}{E_{rm}}}, \quad n_1 = \frac{1}{2}\left[\sqrt{m^2 + 4(k^2 - \nu_\theta m)} + m\right]\right).$$

Eq. 7

3.0 Testing

This section contains the review summaries of the following articles:

- DeTeresa, S. J. and S. E. Groves, "Properties of Fiber Composites for Advanced Flywheel Energy Storage Devices," *Proceedings of the 46th International SAMPE Symposium*, Vol. 46, Book 2:1643-1655, 2001.
- DeTeresa, S. J., *et al.*, "Matrix-dominated Performance of Thick-section Fiber Composites for Flywheel Applications," *Proceedings of the 46th International SAMPE Symposium*, Vol. 46, Book 2:1631-1642, 2001.
- Shiue, F., *et al.*, "Condition Monitoring and Virtual Containment for Composite Flywheel," 42nd AIAA/ASME/ASCE/AHS/ASC Structures, Structural Dynamics, and Materials Conference and Exhibit, AIAA-2001-1441, 2001.
- Nagy, G., *et al.*, "The Evaluation and Testing of Graphite Fiber Composite Materials for High Speed Rotors," *IEEE Transactions on Magnetics*, Vol. 35, No. 1:289-293, 1999.
- Portnov, G. G., "Russian Experience in Composite Flywheels Spin-Tests," *Proceedings of the 44th International SAMPE Symposium*, Vol. 2:2155-2169, 1999.
- Shirey, C., *et al.*, "Tensile Behavior of Filament Wound Composites in Vacuum," 44th International SAMPE Symposium, Vol. 2:2110-2118, 1999.
- Emerson, R. P. and C. E. Bakis, "Relaxation of Press-fit Interference Pressure in Composite Flywheel Assemblies," *Proceedings of the 43rd International SAMPE Symposium*, Vol. 43, Book 2:1904-19152, 1998.
- *Polymer Matrix Composites, Vol. 1: Guidelines for Characterization of Structural Materials*, MIL-HDBK-17-1E, January 23, 1997.
- Martin, R. H., "Accelerated Methods of the Determination of Long Term Fatigue Properties of Glass Reinforced Plastics for Rotor Craft Applications," ADA340938, 1997.
- Martin, R. H., "Delamination Characterization of Woven Glass/Polyester Composites," *Journal of Composites Technology and Research*, Vol. 19, No. 1: 20-28, 1997.
- Vodicka, R., *Accelerated Environmental Testing of Composite Materials*, DSTO-TR-0657, DOD Australia, 1997.
- Sonnichsen, H. E., "Ensuring Spin Test Safety," *Mechanical Engineering*, Vol. 115, No. 5: 72-77, 1993.
- Demuts, E. and P. Shyprykevich, "Accelerated Environmental Testing of Composites," *Composites*, Vol. 15, No. 1: 25-31, 1984.
- Mohr, P. B. and C. E. Walter, *Flywheel Rotor and Containment Technology Development – Final Report*, Report No. UCRL-53448, 1983.
- Coppa, A. P. and S. V. Kulkarni, "Composite Flywheel Rotor Containment," *Progress in Science and Engineering of Composites*, ICCM-IV, 1982.
- Genta, G., "Spin Tests on Medium Energy Density Flywheels," *Composites*, Vol. 13, No. 1:38-46, 1982.
- Sapowith, A. D. and W. E. Handy, *A Composite-Flywheel Burst-Containment Study*, Report No. AVSD-0350-81-RR, 1982.
- Reedy, E. D. Jr. and H. K. Street, "Composite-rim Flywheels: Spin Tests," *SAMPE Quarterly*, Vol. 10:36-41, 1979.

- Parmley, P. A, *et al.*, "On the Accelerated Testing of Graphite/Epoxy Coupons," Report No. ADD116568, *Proceedings of the 1978 International Conference on Composite Materials (ICCM/2)*, pg. 1604-1619, 1978.

CATEGORY

Testing

REFERENCE

ABSTRACT

The performance of commercial high-performance fibers is examined for application to flywheel power supplies. It is shown that actual delivered performance depends on multiple factors such as inherent fiber strength, strength translation and stress-rupture lifetime. Experimental results for recent stress-rupture studies of carbon fibers will be presented and compared with other candidate reinforcement materials. Based on an evaluation of all of the performance factors, is it concluded that carbon fibers are preferred for highest performance and E-glass fibers for lowest cost. The inferior performance of the low-cost E-glass fibers can be improved to some extent by retarding the stress-corrosion of the material due to moisture and practical approaches to mitigating this corrosion are discussed. Many flywheel designs are limited not by fiber failure, but by matrix-dominated failure modes. Unfortunately, very few experimental results for stress-rupture under transverse tensile loading are available. As a consequence, significant efforts are made in flywheel design to avoid generating any transverse tensile stresses. Recent results for stress-rupture of a carbon fiber/epoxy composite under transverse tensile load reveal that these materials are surprisingly durable under the transverse loading condition and that some radial tensile stress could be tolerated in flywheel applications.

SUMMARY

The common feature of fiber composites is the combination of high-strength and/or high-modulus fibers bound together by a matrix material. This paper discusses the specific case of continuous fibers in a polymeric matrix, which offer the highest specific strengths. New experimental results are also presented for the stress-rupture lifetimes of a high-strength carbon fiber/epoxy composite loaded in both the longitudinal and transverse directions.

A summary of tensile properties for high-performance fibers is given in Table 3-1. These particular materials are commonly chosen for use in applications that require performance under long-term sustained or cyclic loading; applications such as flywheels and pressure vessels. The commercial fibers with the highest specific strength are the polybenzobisoxazole (PBO), extended-chain polyethylene (PE), and high-strength carbon fibers as shown in Figure 3-1. Translation of strength into composite structures, strength degradation under sustained loading, transverse tensile strengths, and creep are also important material concerns for durable rotor designs.

Typical 0° (fiber-direction) strength values for epoxy matrix composites are given in Table 3-2. These values have been normalized to 60% fiber volume fraction. The information reveals that only the carbon fiber composites exhibit more than 75% of the fiber strength. The glass fibers exhibit the lowest degree of intrinsic fiber strength translations, which is indicative of how sensitive their strengths are to processing and handling.

The degradation of composite strength under sustained load is due to both fiber and matrix contributions. It is unclear which dominates, but comparison of data for filaments and impregnated strands offers some clues. Single filaments of carbon appear to be much more resistant to stress-rupture than the strand counterpart. Dry bundles of E-glass also appear to be more resistant to stress-rupture than epoxy - and polyester - impregnated strands.

There is a large body of work on stress-rupture of fiber composites, but the work is mostly limited to fiber-direction (0°) loads. In thick flywheels, however, there are also significant radial tensile stresses, which act along the transverse (90°) direction of the composite. Because little data exists for the stress-rupture behavior in the transverse direction, most flywheel designs seek to minimize radial tensile stresses and avoid premature failure in this weak mode.

The preferred method of reducing high radial tensile stresses in thick flywheels is to maintain a compressive radial stress at maximum spinning speed. The following are some of the methods used to produce radial compressive stresses:

a) Programming tension during filament winding,
b) Interference fits between concentric cylinders,
c) Bonding the concentric cylinders using an adhesive that is pressurized during cure,
d) Mass-loading the inner diameter,
e) Building the flywheel using materials that provide a gradient in specific modulus from a low value at the inner diameter to a high value at the outer diameter.

All the proposed methods have limitations and drawbacks. Experimental results are presented for the transverse stress-rupture behavior of a high-strength carbon fiber and epoxy matrix.

Static strength tests were performed at quasi-static rates. All stress-rupture tests were performed at ambient conditions of temperature and humidity. The static or intrinsic strengths of the T1000G/1908 composite in the longitudinal and transverse directions are summarized in Table 3-3. Longitudinal stress-rupture data at stress levels of 92.2 and 87.1% (the percentage of the intrinsic strength) were collected over a period of nearly three years. The lifetime data for the two stress levels as well as the intrinsic strength data are given in Figure 3-2. A useful comparison is made with the stress-rupture behavior of other high-performance fibers in Figure 3-3. It is clear that carbon fibers are much more resistant to stress-rupture degradation than other high-performance fibers and that the higher strength T1000G carbon fiber is more durable than the AS4 carbon fiber.

The results for stress-rupture testing in the transverse direction for four stress levels up to nearly 20,000 hour duration are shown in Figure 3-4. The 50% failure line and the intrinsic strength results are also shown.

Based on the specific fiber tensile strength alone, the high-strength carbon and PBO fibers are the best candidates for high energy density flywheels. When strength translation into composite structures is considered, carbon fibers have the advantage. The cost of E-glass fiber composites is typically one to two orders of magnitude less than the other high-performance fibers. But this material and other glass composites suffer from inefficient fiber strength translation and degradation under stress-rupture conditions. The strength of glass is controlled by the corrosive effects of water acting at surface flaws. Because of this, both the strength and stress-rupture lifetimes are improved by either immobilizing the moisture at low temperature or eliminating the water in a dry environment. One way to improve the strength translation and the stress-rupture of glass fibers at ambient conditions is through the use of coatings.

Table 3-1: Tensile Properties of High-Performance Fibers

Fiber	Density (g/cc)	Tensile Modulus (GPa)	Tensile Strength (GPa)	Manufacturer
T700 Carbon	1.80	228	4.83	Toray
T1000G Carbon	1.80	297	6.38	Toray
E-Glass	2.58	72	3.45	OCF
R-Glass	2.55	85	4.33	Vetrotex
S2-Glass	2.49	87	4.59[1]	OCF
Hollex	1.80	67	3.45[1]	OCF
Fused Silica	2.20	69	3.45	J. P. Stevens
Kevlar 49	1.45	120	3.62	DuPont
Kevlar 29	1.44	58	3.62	DuPont
Twaron	1.44	80	3.15	ENKA
Twaron HM	1.45	124	3.15	ENKA
Technora	1.39	70	3.04	Teijin
Spectra 900	0.97	117	2.68	Allied-Signal
Spectra 1000	0.97	173	3.12	Allied-Signal
Dyneema	0.97	87	2.70	Dyneema VOF
Zylon-HM	1.56	269	5.80	Toyobo

[1] Measured using single filament test, all others using impregnated strand test.

Table 3-2: Typical 0° Tensile Strengths of Epoxy-based Fiber Composites

Fiber	0° Tensile Strength (GPa)	Fiber Strength Translation[1] (%)	Test Method	Reference
T700 Carbon	2.66	92	Coupon[2]	2
T1000G Carbon	3.03	79	Coupon	2
E-Glass	1.02	49	Coupon	3
E-Glass	1.03	50	ASTM D3039	4
E-Glass	0.80	39	NOL Hydro[3]	3
E-Glass	0.95	46	Rotor Spin[4]	3
S2-Glass	1.79	65	ASTM D3039	4
S2-Glass	1.81	66	ASTM D3039	5
S2-Glass	1.53	56	NOL Hydro	3
S2-Glass	1.63	59	Rotor Spin	3
Kevlar 49	1.38	64	Coupon	6
Kevlar 49	1.52	70	NOL Hydro	3
Kevlar 49	1.47	66	Rotor Spin	3
Spectra 900	1.09	68	Coupon	7
Spectra 1000	1.36	73	Coupon	7

[1] Ratio of strength of fiber in composite to values given in Table I.
[2] Test details not specified, presumably similar to ASTM D3039.
[3] Navy Ordinance Lab hydrostatic burst of rings test.
[4] Thin-rim flywheel rotor burst test.

Table 3-3: Intrinsic Longitudinal and Transverse Tensile Strengths of T1000G/1908

Test Direction	Average Strength (MPa)	Weibull Parameters		Number Tests
		Shape $\alpha\ (\sigma)$	Scale β (MPa)	
0°	3,735	14.73	3,870	25
90°	60.2 (CV = 7.7%)	—	—	8
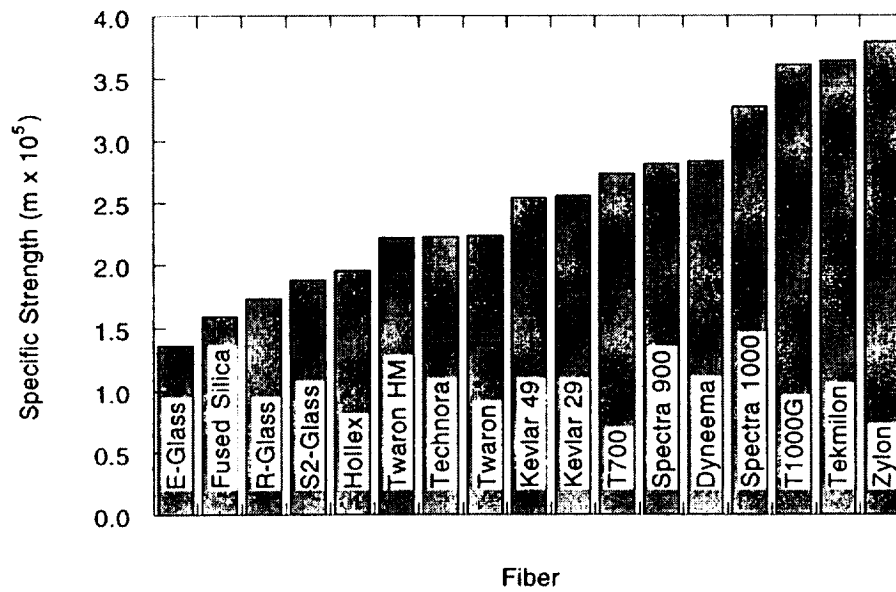
Figure 3-1: Specific strengths of high-performance fibers.
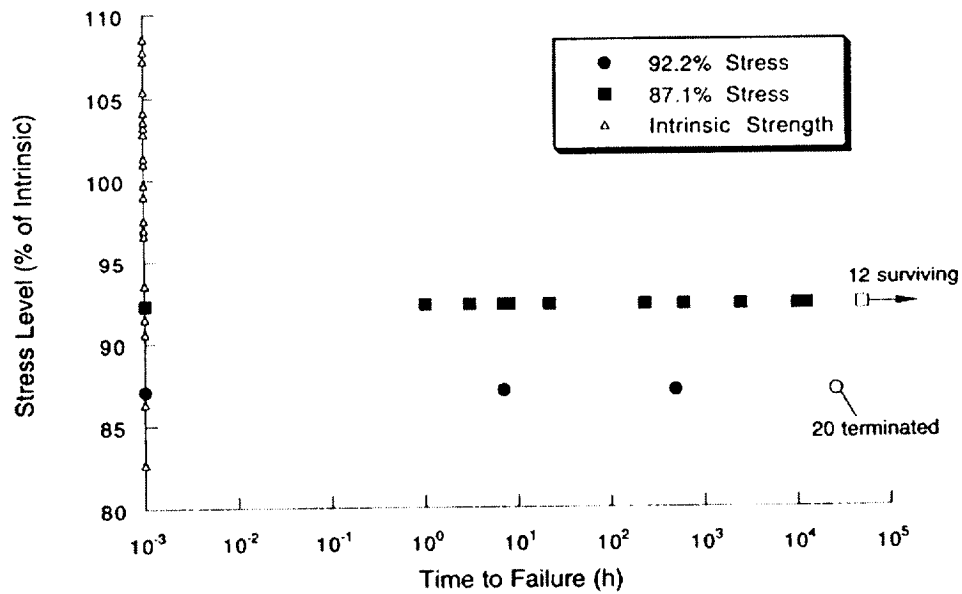
Figure 3-2: Stress-rupture lifetimes for longitudinal tension of T1000G/1908.
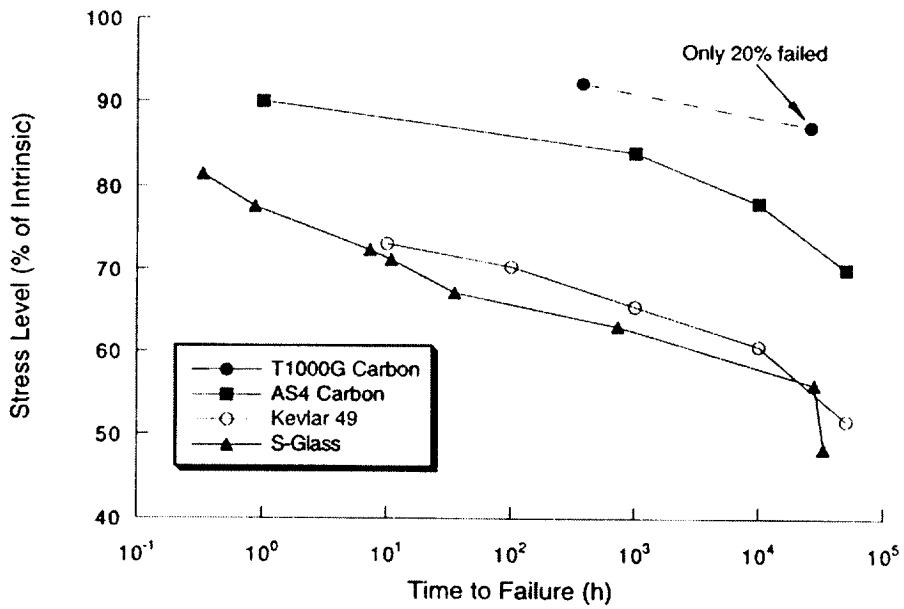
Figure 3-3: 50% probability lifetimes lines for stress-rupture of different high-performance fibers (16-20).
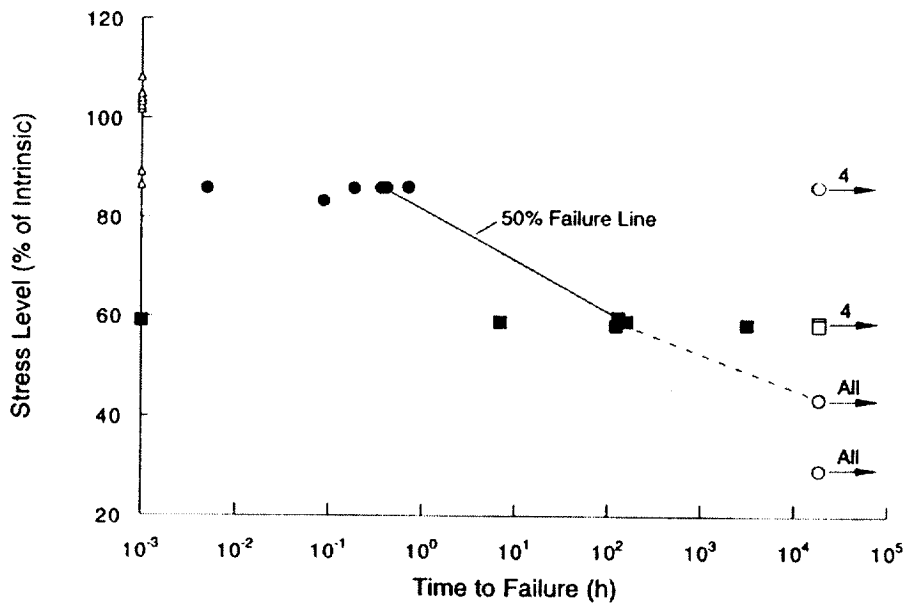
Figure 3-4: Stress-rupture lifetimes for transverse tension of T1000G/1908.

3-8

CATEGORY

Testing

ABSTRACT

An Achilles heel for the performance of thick-section, cylindrical fiber composite flywheels is the poor interlaminar properties of the material. Methods that have been used to minimize or eliminate radial tensile stresses include prestressing concentric cylinders and mass loading. There can also be significant interlaminar shear stresses at the edges of mass-loaded flywheels and in flywheels for high-power density applications where abrupt braking results in high torque levels. To specify adequate safety factors for thick-section flywheels used in these applications, the failure envelope and fatigue behavior under combined interlaminar stresses are required. Using a hollow cylindrical specimen, which was subjected to combined axial compression and torsion, results for fatigue and failure were generated for several flywheel material systems. Interlaminar compression resulted in significant enhancements to the interlaminar shear strength and results were compared to the predications of proposed three-dimensional composite failure models. The interlaminar shear fatigue behavior of a carbon/epoxy system was also studied and compression was found to greatly enhance fatigue life. The results demonstrate that radial compression stresses can yield improvements in the interlaminar shear strength and fatigue lifetimes of composite flywheel rotors.

SUMMARY

In most practical applications, the construction of the rotor is by filament winding or lamination where the fiber is oriented in the $z\theta$ plane. Consequently, the performance of these rotors is limited by the weaker, matrix-dominated, radial strength rather than the fiber-direction strength of the composite. Many different approaches have been proposed and utilized to minimize or completely eliminate radial tensile stress. Two such possibilities are: (1) a rotor with a gradient in specific modulus (modulus/density) from a low value at the inner diameter to higher values at the outer diameter; or (2) a thick-walled rotor made from concentric cylinders that are separated by a compliant material. These examples do not provide sufficient mitigation of the radial tensile stress for thick-walled composite rotors. In some cases, designers have added mass-loading to the inner diameter of the rotor to further alleviate the radial tensile stresses.

For high-power density applications such as the power source of electric armaments, the quick discharge of energy results in an abrupt reduction in angular velocity and this "braking" can subject thick-walled rotors to high interlaminar shear stresses. The study conducted looked at failure due to combined through-thickness compression and interlaminar shear under quasi-static

3-9

and fatigue loading conditions. The results for several composite materials are compared with the predictions of a few composite failure theories for three dimensional stress states.

The specimen used in the experiments to study fatigue and failure under combined interlaminar shear and compression is shown in Figure 3-5. Four different types of specimens were tested: a $[45/0/-45/90]_{XS}$ laminate of T300 carbon fiber with Hexcel F584 epoxy matrix, a $[0,90]_{XS}$ laminate of IM7 carbon fiber with Hexcel 8551-7 epoxy matrix, a liquid-molded E-glass, plain-weave fabric/vinyl ester laminate, and a filament-wound, $[90_2/\pm45]_{XS}$ panel of S2-glass/epoxy.

The shear stress-strain response, showed both enhanced strength and ductility under constant compression stress. Results of tests conducted at room temperature for all materials are shown in Figures 3-6 – 3-9. The T300-F584, E-glass/vinyl ester, and S2-glass/epoxy laminates appear to be elastic to failure under pure interlaminar shear. Cross-ply and quasi-isotropic laminates exhibit high interlaminar compression strengths, thereby allowing significant enhancement of the shear strength through large superimposed compression stresses.

The envelope for shear failure as a function of interlaminar compression for all materials is shown in Figure 3-10. The failure curves indicate that for the increase in shear strength up to the maximum value, the behavior is quadratic.

The biaxial strength results were also compared with the predictions of three-dimensional failure theories for fiber composites. All of the theories examined were derived for failure at the ply level and stresses were calculated for the plies. When the stress state is considered in all the failure theories, it is found that the effect on both of these shear stresses is identical. Thus is it not necessary to determine if failure of the specimens is due to either type of shearing stress for the purposes of failure theory comparison.

The predictions for failure of cross-ply or quasi-isotropic laminates of IM7/8551-7 under interlaminar compression are summarized in Table 3-4. Comparison of these predictions with the failure envelope in Figure 3-11 shows that almost all the theories predict failure at compression stresses less than those actually attained in the combined stress tests. Only Hashin theory appears to predict the observed high compression strength of the laminate. In this figure, all the data and predicted values have been normalized to the shear strength, S_L. Both the Christensen and Hashin theories do a somewhat better job of capturing the experimental results at low compression levels but depart significantly from these results when the compression stress is greater than four times the shear strength.

The shear fatigue studies were conducted to support the development of flywheel rotors for electric armaments. The thick-walled rotors are subjected to residual radial compression from manufacture combined with interlaminar shear from "braking" during energy discharge. The electrical self-heating also results in a rotor steady-state temperature of 93° C. Results for interlaminar shear fatigue of IM7/8551-7 at temperature under different interlaminar compression levels are summarized in Figure 3-12. The open symbols with arrows denote tests that were halted after reaching 10^6 cycles. Surprising results were obtained for fatigue tests under 103 MPa compression. No fatigue failure was observed up to shear stress levels of 96% of

the static failure stress. Thus, with only a moderate amount of compression, the mechanism for interlaminar shear fatigue failure was essentially eliminated.

Table 3-4: Predictions for Failure of Cross-ply or Quasi-isotropic Laminates of IM7/8551-7 Under Interlaminar Compression

Failure Theory	Compression Failure Stress (MPa)
Tsai-Wu (1)	183
Tsai-Wu (2)	146
Tsai-Wu (3)	261
Hashin	553
Christensen	392
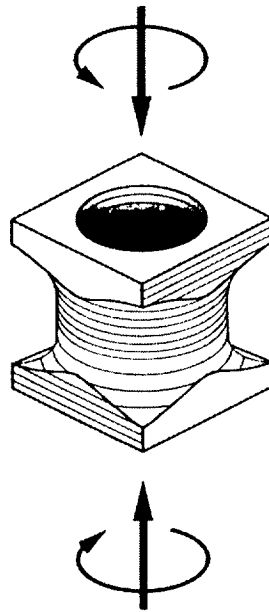
Figure 3-5: Hollow cylindrical specimen used for combined interlaminar shear and compression tests.
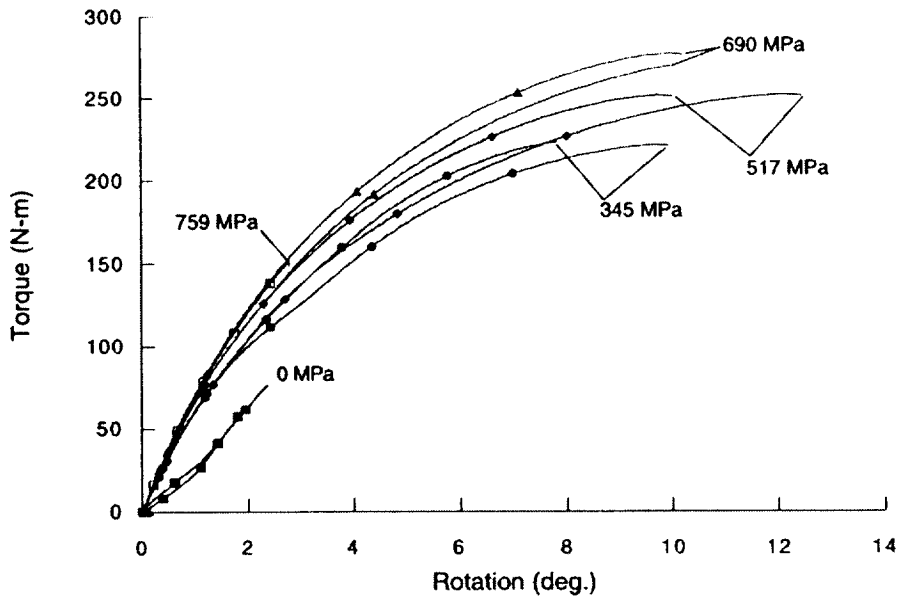
Figure 3-6: Interlaminar shear response of T300/F584 laminate under levels of interlaminar compression shown.
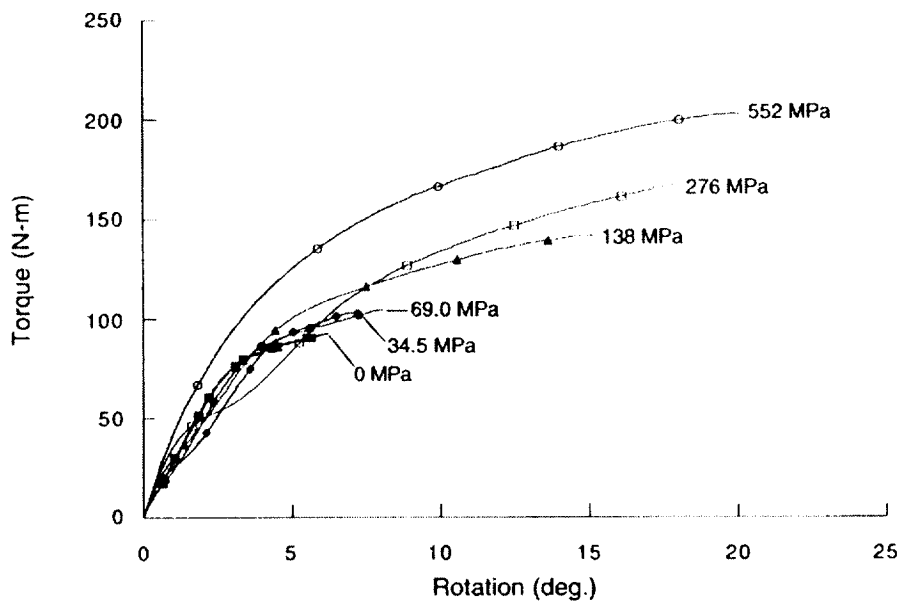
Figure 3-7: Interlaminar shear response of IM7/8551-7 laminate under levels of interlaminar compression shown.

3-12
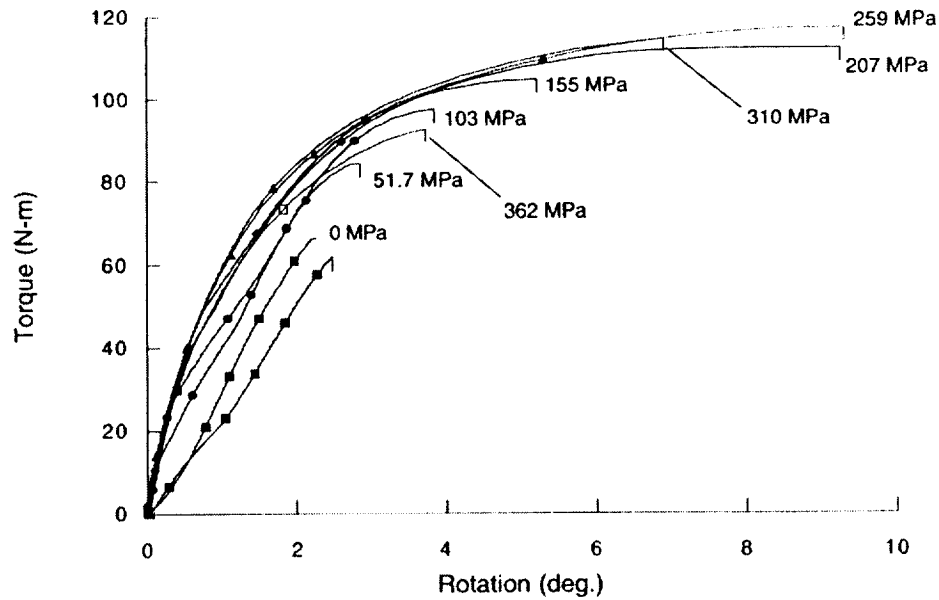
Figure 3-8: Interlaminar shear response of E-Glass/Vinylester fabric laminate under levels of interlaminar compression shown.
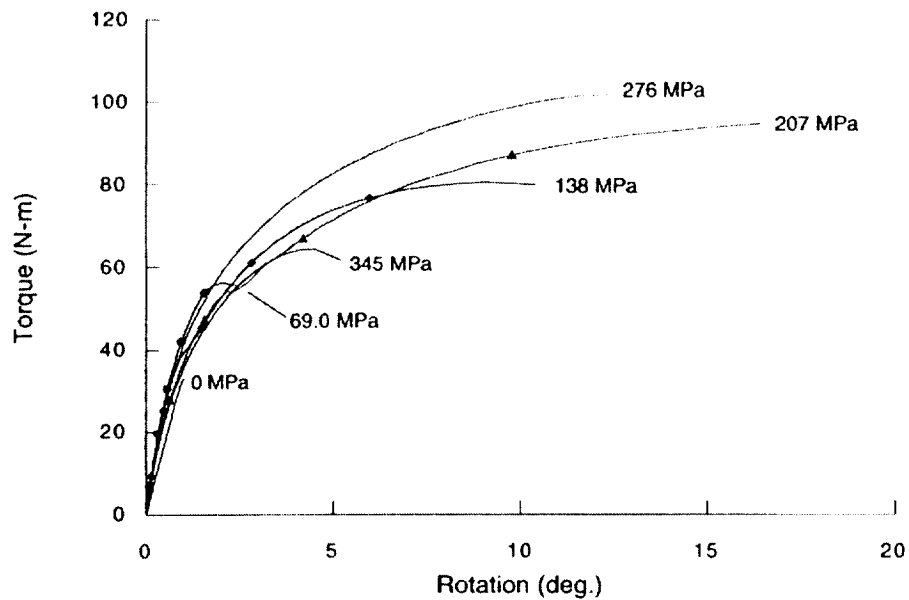
Figure 3-9: Interlaminar shear response of S2-Glass/epoxy laminate under levels of interlaminar compression shown.
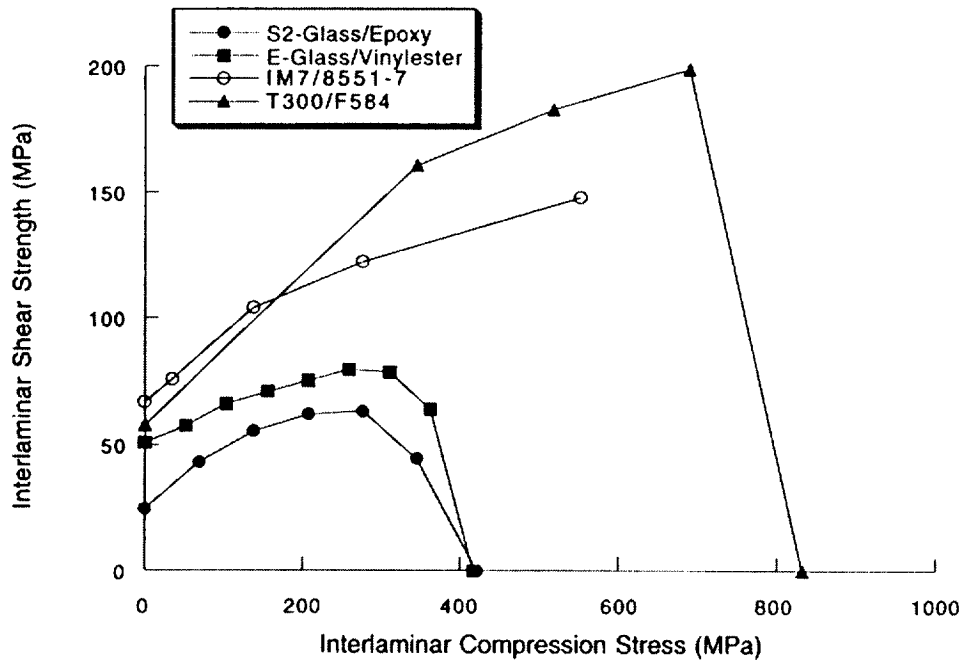
Figure 3-10: Failure envelope for laminates under combined interlaminar shear and compression stress.
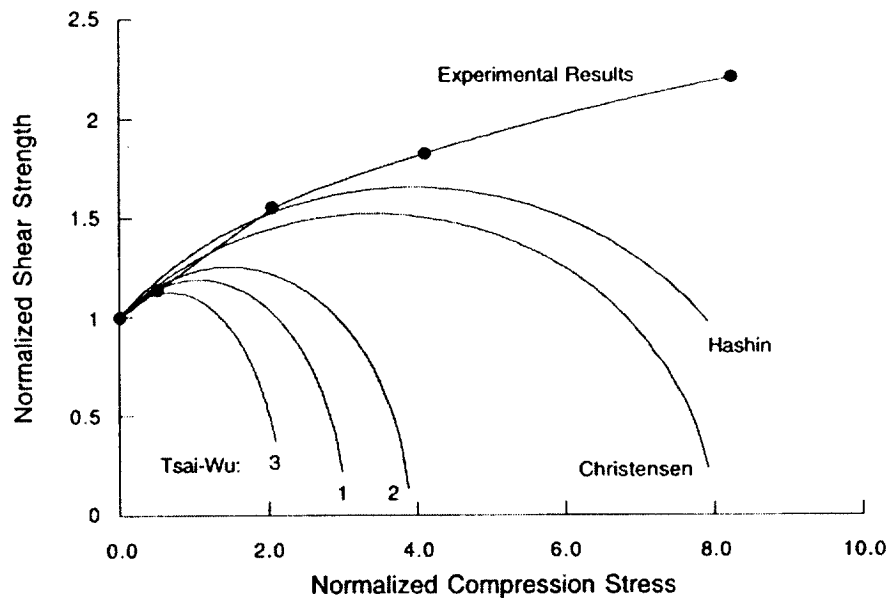
Figure 3-11: Comparison of predicted and observed failure envelopes for IM7/8551-7 cross-ply laminate under combined interlaminar shear and compression stress.
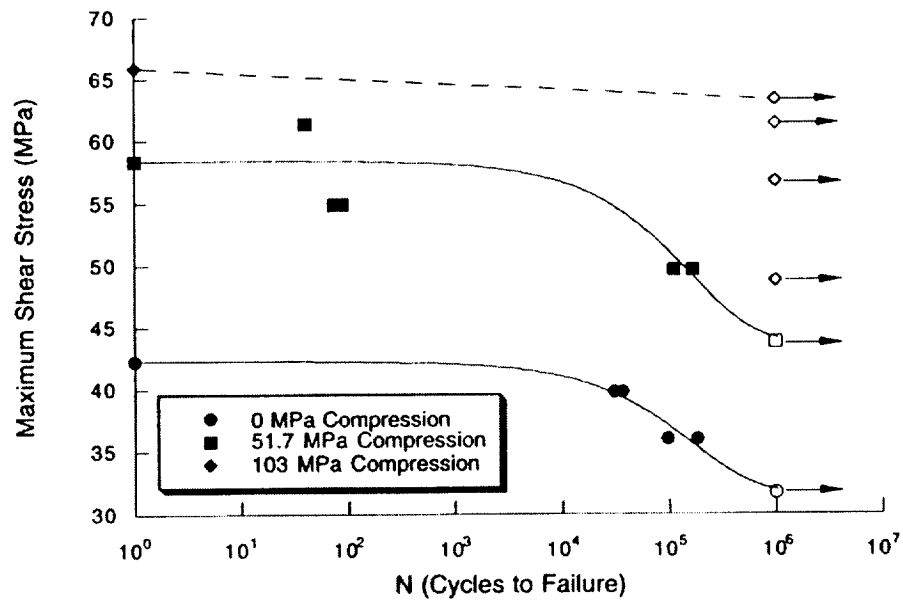
Figure 3-12: Interlaminar shear fatigue life of IM7/8551-7 at 93° C as a function of interlaminar compression stress.

CATEGORY

Testing

REFERENCE

ABSTRACT

This paper presents a health monitoring technique for advanced composite flywheels. Flaws of primary interest, such as delamination and debonding of interfaces, are those unique to composite flywheels. Such flaws change the balance state of a flywheel through small, but detectable, motion of the mass center and principal axes of inertia. The proposed technique determines the existence and the severity of such flaws by a method similar to the influence-coefficient rotor balancing method. Because of the speed-dependence of the imbalance caused by elastic flaws, normalized vibrations and imbalance change are defined. The normalized imbalance change not only permits the use of vibration readings at multiple speeds to increase the technique's accuracy, but also is a direct measure of the flaw severity. To account for the possibility that flaw growth could actually improve the balance state of a rotor, a new concept of "accumulated imbalance change" is also introduced. Laboratory tests show the proposed method is able to detect small simulated flaws that result in as little as 2-3 microns of mass center movement. Virtual containment software was also developed and demonstrated.

SUMMARY

In order to avoid the use of a heavy containment system, an integral health monitoring and "virtual containment" subsystem is suggested. The virtual containment concept uses sensors to monitor changes in a flywheel's operating condition, estimates the severity if the change is due to flaws, and then adjusts the operating condition accordingly to avoid further flaw growth or system failure.

The present study focuses on such flaws as circumferential delaminations or debonds. These flaws cause changes in the mass distribution of the rotating flywheel, thus affecting its balance state. The severity of rotor flaws can be better estimated by monitoring the balance state of a flywheel system.

A circumferential flaw causes a rotor to deform differently than when not flawed. This non-uniform deformation causes mass re-distribution, moving the system's center of mass away from its original location. Because it is difficult to accurately measure mass center movement experimentally, FEM is used to investigate the relationship between flaw sizes and the induced imbalances.

Figure 3-13 shows a two-dimensional axisymmetric model. For unexplained reasons, the steel portion was modeled with tria elements which are much more stiff than four noded quad elements used in the remainder of the model. Circumferential flaws were introduced at different radial locations. A through-the-thickness delamination was assumed. Figure 3-14a shows the motion of the mass center at three different speeds in a rotor with a delamination at the interface between the glass/epoxy and aluminum portion of the hub. Figure 3-14b shows the same information as Figure 3-14a, except that the vertical axis is in terms of ΔU_N, the normalized imbalance change $(\Delta U_N = \Delta U/\omega^2)$. In this case, ΔU_N is a possible measure of flaw severity.

Figure 3-15 shows the normalized imbalance change with respect to the flaw location, for three different flaw sizes. In the horizontal axis of the plot, 0 is the aluminum/composite interface, and 1 is the glass/carbon composite interface.

There are two types of imbalance for rigid rotors: static and dynamic. Static imbalance represents the mass center offset from the rotation axis. Dynamic imbalance does not change the overall mass center location of a rotor, but generates a transverse unbalance moment about the mass center of the rotor. For a two-dimensional disk rotor, only the mass center offset is required to quantify the state of balance. For a long, cylindrical rotor, both the mass center and principal axes could shift due to the existence of a flaw.

Tests were conducted with two different flywheel systems to validate the proposed condition monitoring technique. Both systems had simulated flaws induced by the addition of small pieces of brass to the OD of the flywheel at different locations. Flywheel system A has a disk-like rotor as shown in Figure 3-16. This system simulates the single-plane imbalance. This rotor consists of two rings plus a steel hub. Flywheel system B, Figure 3-17, is a cylindrical composite rotor. This is a one-piece cylindrical ring attached to the steel shaft through two solid hubs at the top and bottom of the cylinder. These solid hubs have outer glass/epoxy rings and aluminum inner hubs.

Table 3-5 shows the actual and calculated imbalances for three cases, each with a different number of measurements used in the calculation. In theory, one sensor reading should be enough to judge the extent of rotor imbalance. However, as shown in the table, the errors were very large. For this reason, the exact-point method in condition monitoring induced errors too large to make it useful. Table 3-6 shows the results for two-plane monitoring tests. The added imbalances were quite small. A 0.19 g mass attached to the rim results in a 25 g-mm imbalance of the flywheel. This is about 2-3 μm of mass center movement.

For the virtual containment portion of the project, the above monitoring method is used. The basic concept is that any change in monitored imbalance for a flywheel system is undesirable and should be avoided. A change in balance state usually indicates flaw growth or initiation. When a change is observed, the maximum speed is gradually reduced by an arbitrary, predetermined amount until no further change occurs. To simulate flaw growth, masses were released from the rotor at different instances during the test. After the release of each mass, the program slowed the flywheel accordingly. Figure 3-18 shows the movement of the mass center during the experiment.
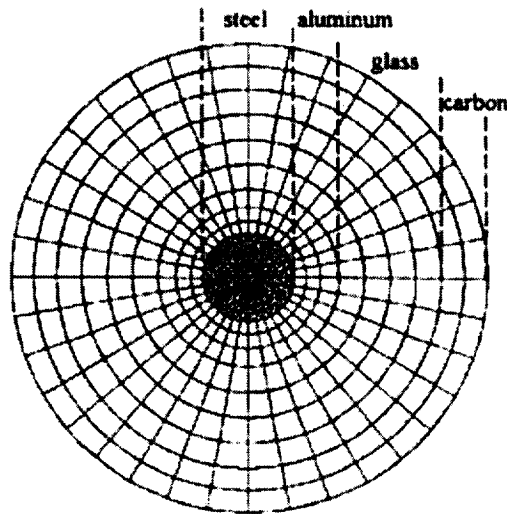
Figure 3-13: FEM mesh used for flaw simulation.

(a)

(b)
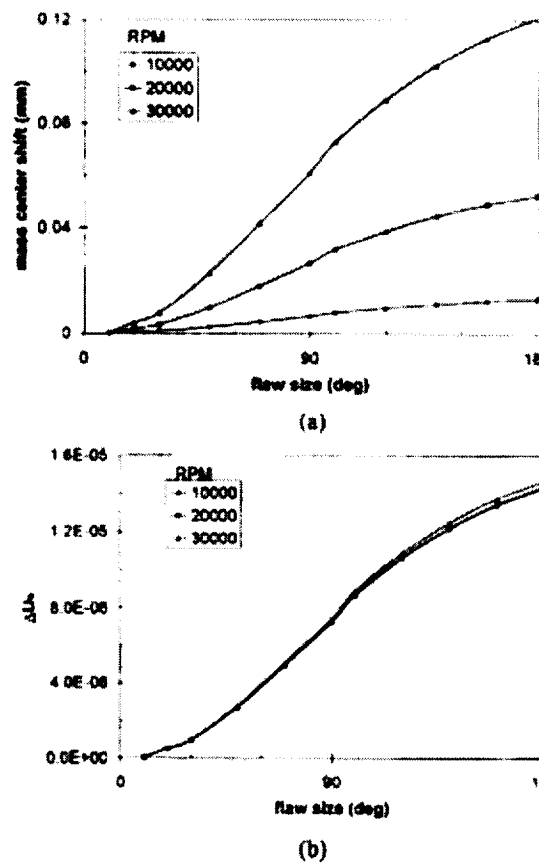
Figure 3-14: Mass center shift (a) and normalized imbalance change (b) with flaw size (debond at interface of glass and aluminum).
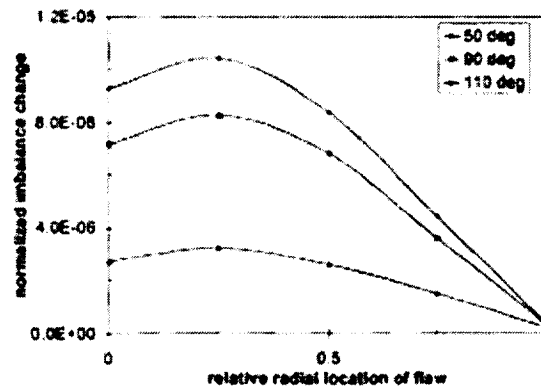
Figure 3-15: Normalized imbalance change for flaws at different radial locations in glass/epoxy hub.
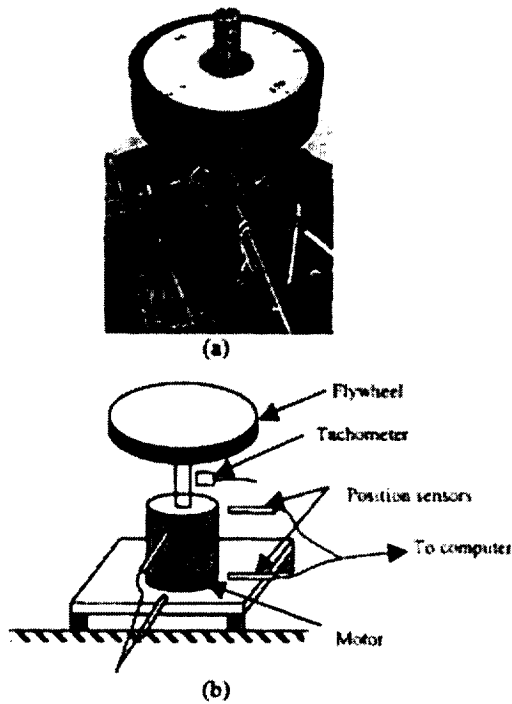
Figure 3-16: Flywheel system A(a) and schematic (b).
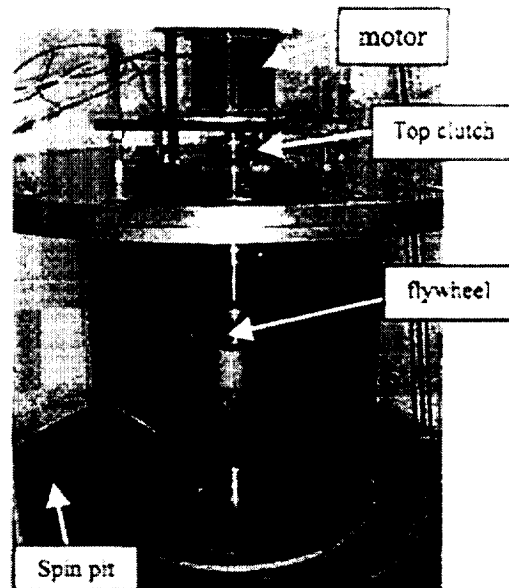
Figure 3-17: Flywheel system B.

Table 3-5: Test Results for Single Plane Monitoring

Added Imbalance (g-cm/ deg)	Detected imbalance (g-cm/ deg)		
	1 sensor 9 KRPM	4 sensors 9 KRPM	4 sensors 6 and 9 KRPM
2.93 / 0	1.89 / 95	2.61 / 12	2.75 / 0
2.91 / 180	4.10 / 165	3.08 / 166	2.84 / 190
1.81 / 93	2.32/ 254	1.96 / 115	1.80 / 96

Table 3-6: Test Results for Two-plane Monitoring

Speed (RPM)	Real imbalance (g-mm/deg)	Detected imbalance (g-mm/deg)
10250	43.4 / 0	51.6 / 1
10500	50.7 / 180	58.7 / 180
11000	25.0 / 60	20.8 / 59
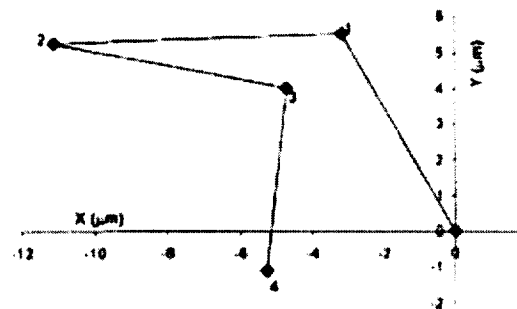
Figure 3-18: Mass center movement during flaw growth simulation experiment.

CATEGORY

Testing

REFERENCE

ABSTRACT

High speed rotating machine designs may depend on high strength, filament wound carbon fiber composite bands to contain discreet metal conductors in the spinning rotor. Both the failure strength and stiffness of these composite bands play a major role in determining the limiting speed and stored energy in the rotor. This paper describes the results of an investigation to evaluate the mechanical properties of several candidate advanced carbon fiber materials for composite rotors. An experimental technique utilizing a mass-loaded spinning composite ring (rotor) has been developed to provide a viable and cost-effective way to characterize, under relevant dynamic loading conditions, the delivered strength of candidate graphite fibers in filament wound constructions. The test concept and development are described, and the measured in-situ strengths of several representative candidate fibers (T650-42, IM7, M46J composite rotors) are compared to available data. Up to 40 percent reduction of delivered fiber strength in the filament wound rotors compared to vendor-supplied fiber tow strengths were observed.

SUMMARY

This paper points out that most material property data and strength information supplied by manufacturers for fiber/resin systems are obtained from flat coupon tests. Rotors, however, have very different geometries from the flat coupons, and the filament winding process causes its own degradation of the composite rotor. Another piece of information not given by manufacturers is an accounting for the effect of the dynamic stress state in the material. Testing and FE analysis were conducted and results compared to determine design allowables and a possible knock-down factor for the manufacturer provided material properties.

Figure 3-19 shows the test setup. A cylindrical composite specimen representing the rotor is placed on the elasto-plastic hub, and spun at increasing speeds until the ring bursts. In this way, the ring is loaded radially both by pressure due to mass-loading by the inner hub, and centrifugal forces due to the rotation.

Figure 3-20 shows the stress strain curve for the hub, Nylatron GSM, material used in the FE analysis. This and other properties were obtained from manufacturer's data as well as limited in-house tests.

Figure 3-21 shows the predicted and measured displacements for the IM7/epoxy rotor. Table 3-7, gives a summary of the test results and calculated knock-down factors. The knock-down factors average 60% of virgin fiber strengths, implying that the fabrication process and dynamic stress state may have a significant effect on the effective, delivered fiber strengths in composite rotor applications that should not be ignored during the design process.
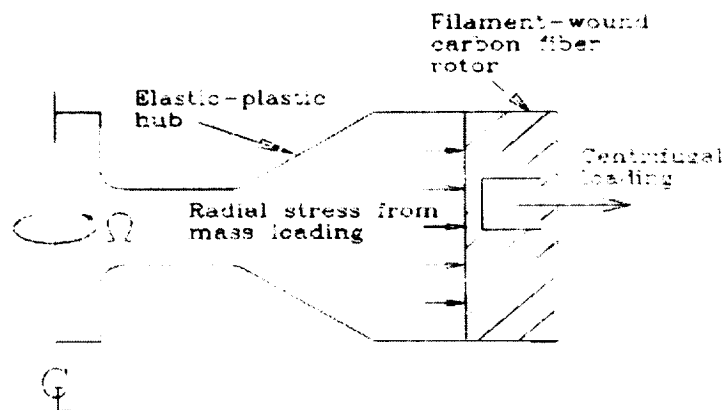
Figure 3-19: Concept for spin-burst test method.
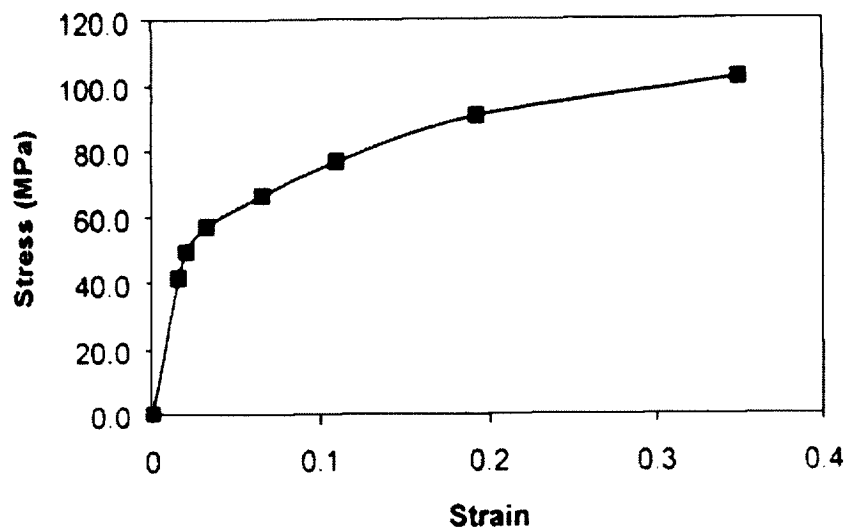
Figure 3-20: Stress-strain curve for Nylatron GSM material.
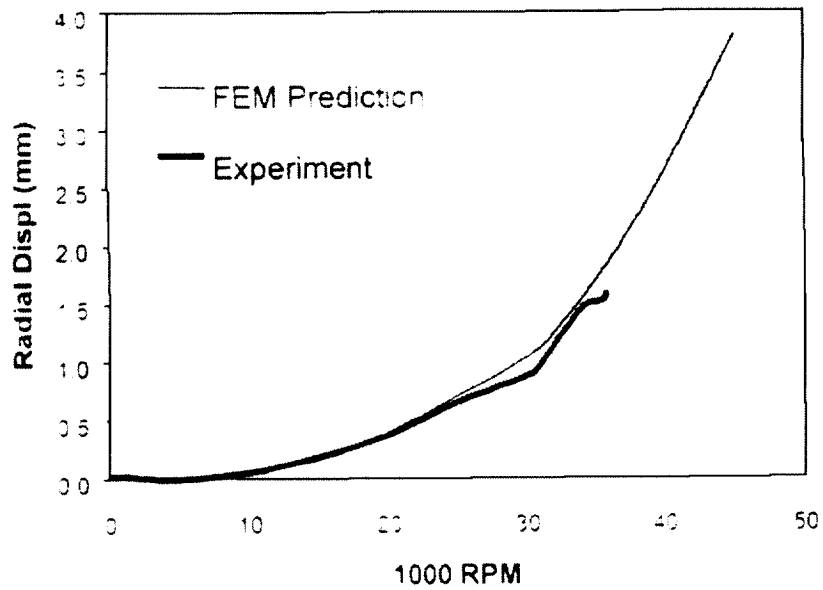
Figure 3-21: Predicted & measured displacements for IM7 Epoxy rotor.

Table 3-7: Summary of Preliminary Spin-burst Test Results

Fiber	Matrix	No. Tests	Virgin Fiber Strength Mpa (Ksi)	Fiber Modulus GPa (Msi)	Nom. Fiber Volume Fraction	RPM at Burst	Max. Fiber Stress at Burst Mpa (Ksi)	Apparent Fiber Strength Knock-down Factor
T650-42	Epoxy	1	5033 (730)	290 (42)	0.6	33,600	3185 (462)	0.63
IM7	Epoxy	1	5309 (770)	276 (40)	0.6	35,700	3337 (484)	0.63
IM7	Epoxy	2	5309 (770)	276 (40)	0.6	35,200	3289 (477)	0.62
M46J	Epoxy	1	4213 (611)	434 (63)	0.6	30,840	2344 (340)	0.56
M46J	Epoxy	2	4213 (611)	434 (63)	0.6	31,340	2386 (346)	0.57

CATEGORY

Testing

REFERENCE

Portnov, G. G., "Russian Experience in Composite Flywheels Spin-Tests," *Proceedings of the 44th International SAMPE Symposium*, Vol. 2:2155-2169, 1999.

ABSTRACT

Spin-test results are given for two types of composite flywheels, namely, molded disks and rim-type flywheels with chord-wise wrapping. The models differed in form, size, and material. Dynamic problems associated with flywheel speed-up, ultimate peripheral speeds, and the limiting energy storage capacities are described. Results are also given for full-scale flywheel tests. Dynamic problems were shown to be the governing factors for rim-type flywheels.

SUMMARY

The ultimate value of specific mass energy storage capacity, and the ability to operate over the working range of rotational speeds without resonance or rotational instability were evaluated. On the whole, the results of the tests couldn't be considered successful. The usefulness of these experiments is in the prevention of future mistakes. Figures 3-22 and 2-23 show schematics of the two types of flywheels tested; disks made by molding and those made by winding, respectively. Various types of spin-test stands were used.

The molded disk tests failure mode at ultimate speeds was instantaneous and accompanied by separation of the disks into three or four segments. Significant vibrations did not occur during testing of these types of disks.

Tests of rim-type flywheels showed that the specimens suffered from breakages of the threads of the overwrap long before the complete flywheel failure. The overwrap failure was accompanied by the generation of unbalance and enhancement of vibrations.
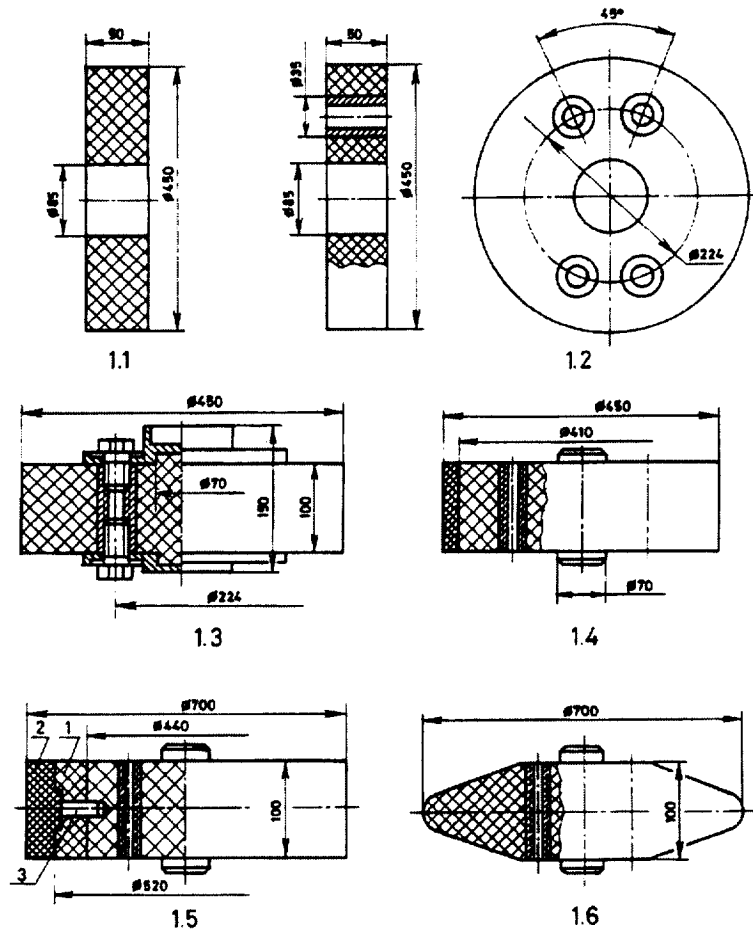
Figure 3-22: Flywheel models made by molding: 1.1 – disk with a central hole; 1.2 – disk with a central hole and four off-center holes with glued metal sleeves; 1.3 – solid disk with flanges jointed by 8 bolts screwed in the studs with internal thread, which are glued in the flange holes; the flanges are centered by means of shoulders of 70 mm in diameter; 1.4 – solid disk with a shroud from unidirectional GFRP (flanges are not shown; 1.5 – solid disk with a ballast from GFRP (1) and a shroud of GFRP (2) jointed to the disk by pins (3) made of GFRP (flanges are not shown); 1.6 – conic disk (flanges are not shown). All dimensions are given in millimeters.
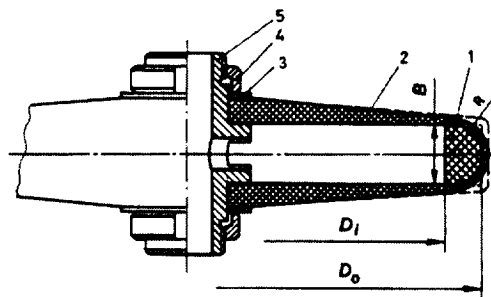
Figure 3-23: Chord-wise flywheel model: 1 – rim; 2 – overwrap; 3 – spacer; 4 – nuts; 5 – hub.

3-25

CATEGORY

Testing

REFERENCE

ABSTRACT

The tensile behavior of candidate filament wound composite materials for flywheel energy storage applications was evaluated. The materials were conditioned in a vacuum of 10-30 mtorr for at least 85 days prior to testing, and no appreciable weight losses were recorded during that period. Glass and carbon composites conditioned and fatigue tested in vacuum lost 10% to 12% of remaining strength per decade of logarithmic lifetime over the 10^2 to 10^5 range of cyclic lifetime. The ZenTron™ glass/epoxy and the S2-glass™/epoxy composites were noted to have more overall fatigue sensitivity than either E-glass/epoxy or T700S carbon/epoxy due to a steeper slope of the S-N curve at very low cyclic lifetimes. Typical fatigue failures were characterized as a longitudinal splintering mode growing inward from the lateral edges of the specimen. No significant differences in the ultimate tensile strength, Young's modulus, and ultimate strain were noted when vacuum-conditioned specimens were compared to as-received specimens.

SUMMARY

For space uses and the use of vacuums to minimize the inefficiencies associated with air drag, it is important to characterize the durability of composite rotor materials in vacuum environments. Flat coupon specimens were fabricated using a filament winding method similar to that used to make rotors.

Quasi-static tests were conducted in the lab. Since the test duration was only 30 minutes the use of a vacuum chamber was not needed. Table 3-8 shows the results from the quasi-static tests. The damage process was a progression of fiber fraying from the lateral edges of the specimen toward the centerline. Only the ZenTron showed a significant increase in projected failure strain with vacuum conditioning. However, no significant differences in material moduli or ultimate tensile strain when comparing specimens in the as-received state to the vacuum-conditioned state.

Figures 3-24 and 3-25 show the normalized S-N plots from the tests. ZenTron demonstrated the highest normalized S-N slope and E-glass the lowest at less than 10^2 cycles. At 10^5 cycles, S2-glass had the lowest normalized S-N slope, E-glass the highest, and ZenTron was in the middle level.

Table 3-8: Quasi-static Test Results

Material, Preparation, & Condit'g[a]	Fiber Vol. Fract.[b]	Quasi-Static Strength		No. Reps	Panel Nos. Used	Modulus (0.1-0.6% strain)		Theor. Mod.[c] (GPa)	Projected Ultimate Strain (%)	Transl. Factor (%)
		Mean (MPa)	CV (%)			Mean (GPa)	CV (%)			
E-glass(ar)	0.56	1280	8	5	2	44.3	8	42	2.89	80
E-glass(ep, c)		1110	7	5	1.4	38.3	6		2.84	79
S2-glass(ar)	0.74	1740	15	5	5	55.9	13	65	3.11	72
S2-glass(ep, c)		1740	3	5	3	62.9	13		2.80	65
ZenTron(ep,ar)	0.61	1710	4	4	6	53.1	1	59	3.23	77
ZenTron(ep, c)		1970	3	5	7	52.7	2		3.74	89
T700S(ep, ar)	0.62	2770	2	2	5	161	1	144	1.72	82
T700S(ep, c)		2280	18	5	2.4	153	8		1.48	70

Notes:

[a] As-received (ar); vacuum conditioning (c); edge prepared with epoxy (ep)

[b] Fiber volume fractions provided by manufacturer; panel number unknown

[c] Theoretical modulus based on rule of mixtures: $E = V_f E_f + (1-V_f-V_v) E_m$, where $E_m = 3$ GPa
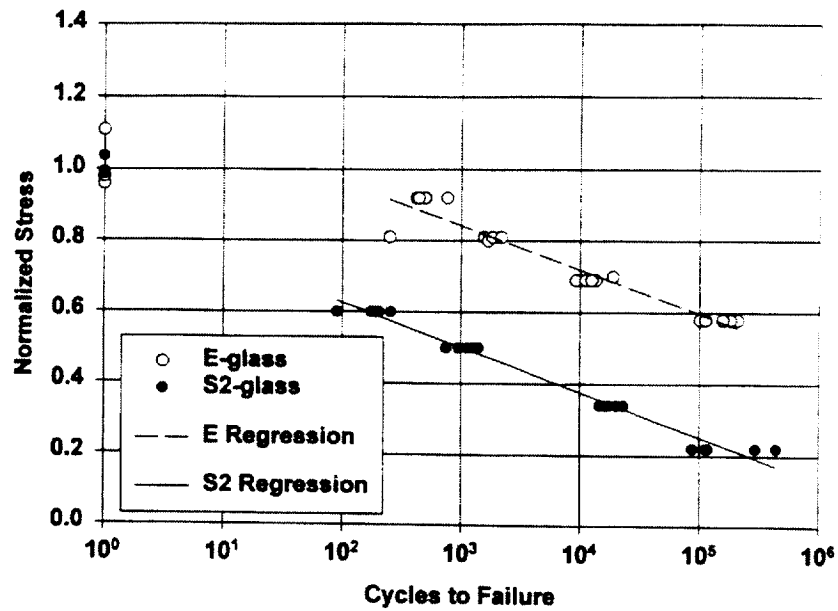
Figure 3-24: Stress-life curve for E-glass/epoxy and S2-glass/epoxy in vacuum.
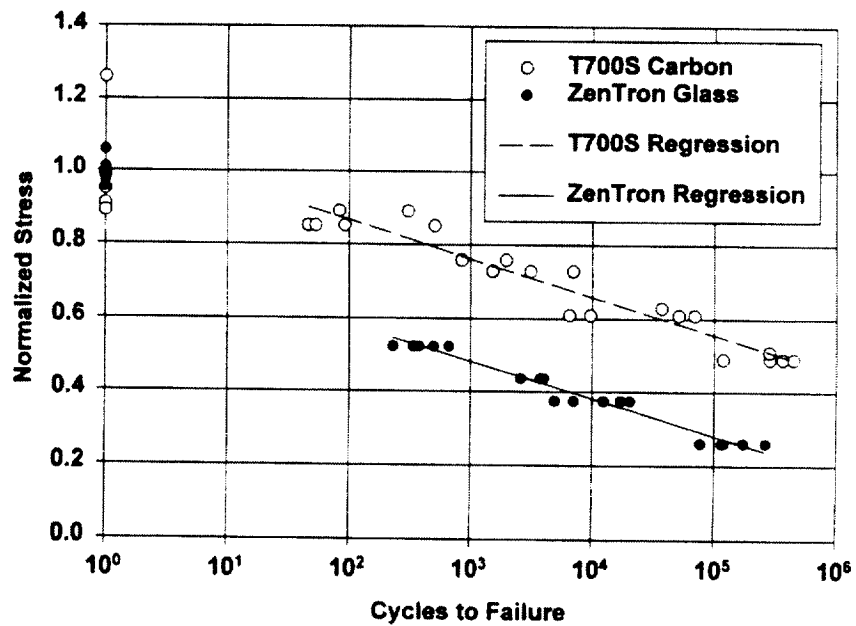
Figure 3-25: Stress-life curve for T700S/epoxy and ZenTron/epoxy in vacuum.

CATEGORY

Testing

REFERENCE

Emerson, R. P. and C. E. Bakis, "Relaxation of Press-fit Interference Pressure in Composite Flywheel Assemblies," *Proceedings of the 43rd International SAMPE Symposium*, Vol. 43, Book 2:1904-19152, 1998.

ABSTRACT

Relaxation of pressure in interference-fitted filament wound composite rings was experimentally investigated. The ring materials, shapes, and pressures were selected to be representative of typical rings for flywheel energy storage systems, where press-fitting and rotation cause long-term loadings that can lead to time-dependent deformation and stress redistribution. Two initial pressures and three interference-fitted ring pair configurations were used; carbon/epoxy on glass/epoxy, carbon/epoxy on aluminum, and aluminum on glass/epoxy. For the composite-on-composite assemblies a 3-4% pressure drop was observed, and for the assemblies with aluminum a 4-5% pressure drop was observed. Approximately steady-state pressures were realized within 500 hours after assembly of the ring pairs. The steady-state pressure losses are percentage-wise independent of the initial pressures, suggesting that a linear-viscoelastic model may apply to these materials.

SUMMARY

The paper represents short term relaxation of pressure in interference-fitted composite rings. The rings are observed under ambient conditions for up to one month. No accelerated testing methods were used to determine relaxation over a longer period of time.

The objective of the work was to use an interference fit to impose a biaxial stress state on a pair of concentric rings and to measure the resulting time-dependent deformation and pressure loss when one or more of the rings is made of a fiber reinforced plastic material. The outcome can be used to assess the relaxation of advantageous pre-stress, and to aid in the development of a viscoelastic model of multi-ring composite flywheel assemblies. This model could then be used to predict the long-term response of flywheels to more general loads such as combined rotation and interference-fitting.

Most flywheel designs employ a glass/epoxy composite inner ring and a stiffer, stronger, carbon/epoxy composite outer ring. This project uses glass/epoxy and carbon/epoxy under external and internal pressure loads, respectively. Some of the ring pairs used an aluminum ring in place of one of the other composite rings. This combination was chosen in order to isolate the time-dependent response of the composite, and provide a different pressure vs. time loading profile on the composite ring.

The ring pairs were first press-fitted and the instantaneous elastic strains of the free inside diameter and outside diameter surfaces were measured. These strains were used to calculate the initial interfacial pressure using a closed-form elasticity solution. After three weeks the rings were un-pressed, and the instantaneous strains were again recorded – yielding the corresponding relieved pressure. The difference between the initial and final pressures is the main parameter of interest.

The individual rings were wet-filament wound on an 80° C mandrel and kelp at the same constant temperature for an additional 30 hours after winding. Once the ODs were ground, the rings were kept at 100° C for an additional 48 hours for drying. During the experiments, the rings were stored in an ambient laboratory (10-40% humidity, 23-27° C).

Table 3-9 contains a listing of the ring pair configurations. Three designs were assembled with a "low" interface pressure of 27 MPa, and three with a "high" 54 MPa interface pressure. The abbreviations H, G, and C denote the hybrid (g/ep and c/ep), glass (g/ep and al), and carbon (c/ep and al) ring pairs, respectively.

The interference between the OD of the inner ring and the ID of the outer ring dictates pressure achieved upon assembly. Ring dimensions are given in Table 3-10. Target pressures and strains were calculated using a closed-form, plane-stress, orthotropic elasticity solution. Figure 3-26 is a schematic of the hybrid ring pair before pressing.

During the pressing operation, continuous comparison of the instantaneous hoop strains with the target strains indicated when the target pressure was achieved. Table 3-11 gives the results from the experiments. In the table, the following variables appear:

ε_0 = actual measured assembly strain
ε_r = measured strain just before disassembly
ε_F = strain measured just after disassembly

In most cases the pressure losses calculated by the inner and outer rings of a given pair do not agree, although by equilibrium they should. This could be attributed to changes in material properties not accounted for in the elasticity solution. To account for the different pressure losses provided by individual rings, the average pressure loss, Δp_{av}, was computed and listed in Table 3-11. All the experiments involving aluminum rings had approximately 4-5% average pressure loss, whereas the hybrid ring pairs had just under 3% loss.

Plots of normalized pressure vs. time for the low and high pressure G and C experiments are shown in Figures 3-27 and 3-28. Both of the low pressure curves show irregular behavior in the first 150 hours. This is likely due to the ambient differences between the room in which the rings were pressed and the room in which the ring pairs were immediately taken for moiré interferometry measurements.

Figures 3-29 and 3-30 show instantaneous and long-term hoop strain distributions through the radius of the LP-G gl/ep and LP-C c/ep rings respectively. In these figures, two different methods of analysis were used to calculated the different strain distributions. One method

3-30

achieves a high level of sensitivity to the local strain variations, and was used to generate the "Initially Assembled Strain" distributions. The other method is much simpler but not as sensitive to local variations in strain. This method was used to generate the "Strain After X Hours" and "Unloaded Strain" distributions. It can be concluded that while exhibiting significant local strain variations, the hoop strain distributions through the radius agree well with the elastically predicted strain distribution. Also, the hoop strain distributions while pressed do not significantly change with time, and the strains remaining after disassembly are rather small (less than 100 $\mu\varepsilon$).

Table 3-9: Ring Pair Configuration

	Ring Pair	Inner Ring	Outer Ring
Low Pressure (LP)	LP-H	g/ep	c/ep
	LP-G	g/ep	al
	LP-C	al	c/ep
High Pressure (HP)	HP-H	g/ep	c/ep
	HP-G	g/ep	al
	HP-C	al	c/ep

Table 3-10: Ring Dimensions

Ring Pair	Material	Inner Radius (cm)	Outer Radius (cm)	Radial Interference (cm)	Target Pressure (MPa)	Target Strain ($\mu\varepsilon$)
LP-H	g/ep	6.000	8.374	0.025	27	-2066
	c/ep	8.349	9.549			1098
LP-G	g/ep	6.000	8.374	0.025	27	-2066
	al	8.349	11.195			945
LP-C	al	6.604	8.374	0.025	27	-1949
	c/ep	8.349	9.549			1098
HP-H	g/ep	6.000	8.400	0.051	54	-4115
	c/ep	8.349	9.549			2202
HP-G	g/ep	6.000	8.400	0.051	54	-4115
	al	8.349	11.195			1853
HP-C	al	6.604	8.400	0.051	54	-3880
	c/ep	8.349	9.549			2202

Table 3-11: Elastic Strains for all Rings During Assembly and Disassembly

Ring	Target strain (10^{-6})	ε_0 (10^{-6})	ε_r (10^{-6})	ε_F (10^{-6})	Δp, (%)	Δp_{av} (%)	Assembly Duration (hours)
LP-H g/ep	-2066	-1707	-1631	10	3.9	2.9	713
LP-H c/ep	1098	956	908	-31	1.8		
LP-G g/ep	-2066	-1863	-1807	-12	3.7	5.1	692
LP-G al	945	739	692	1	6.4		
LP-C al	-1949	-1507	-1474	-73	2.3	4.2	620
LP-C c/ep	1098	1045	956	-25	6.1		
HP-H g/ep	-4115	-3810	-3626	13	4.5	2.7	595
HP-H c/ep	2202	1962	1880	-67	0.8		
HP-G g/ep	-4115	-3898	-3733	50	3.0	4.0	586
HP-G al	1853	1769	1715	661	4.9		
HP-C al	-3880	-4970	-4923	-1869	1.5	4.4	589
HP-C c/ep	2202	2015	1814	-55	7.2		
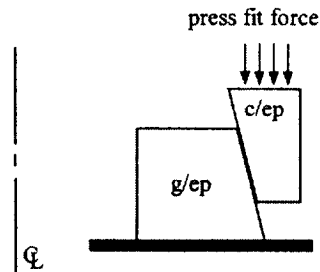
Figure 3-26: Cross-sectional illustration of ring pairs during pressing.
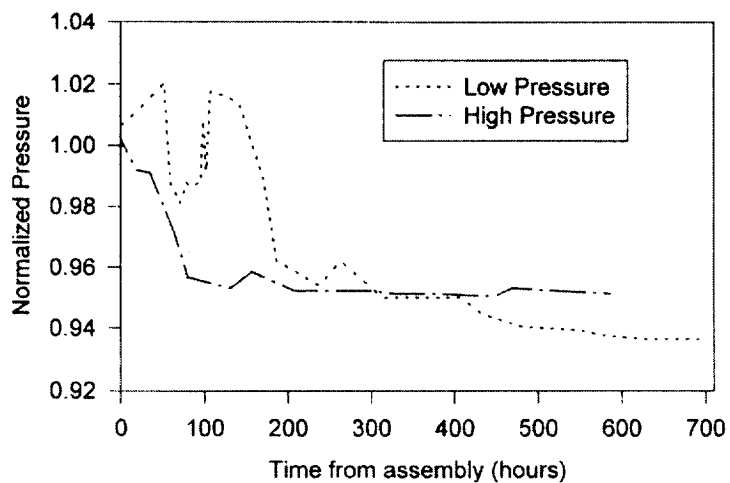
Figure 3-27: Normalized pressure vs. time for the LP-G and HP-G experiments, from aluminum strain

3-32
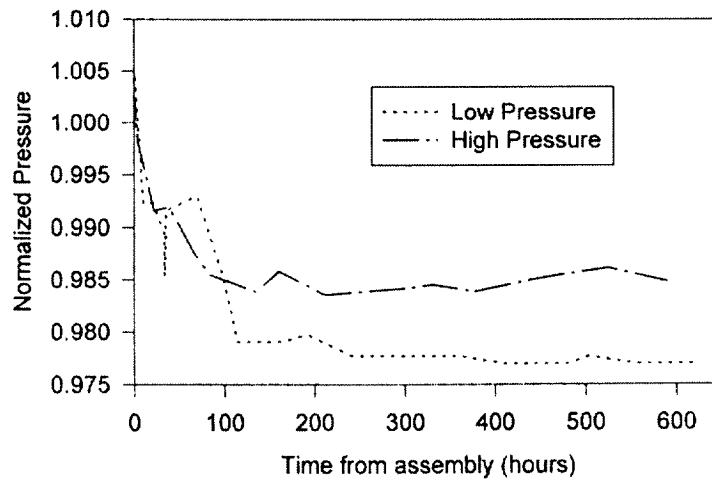
Figure 3-28: Normalized pressure vs. time for the LP-C and HP-C experiments, from aluminum strain measurements.
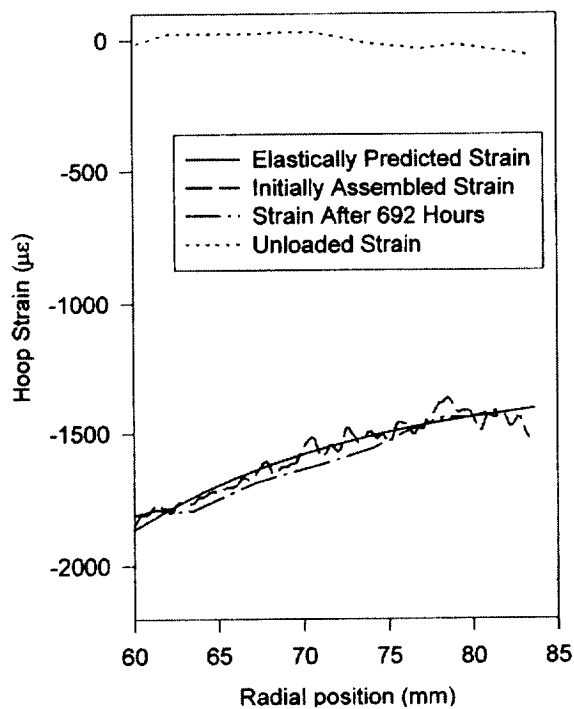
Figure 3-29: Predicted and measured strains in the LP-G gl/ep ring.
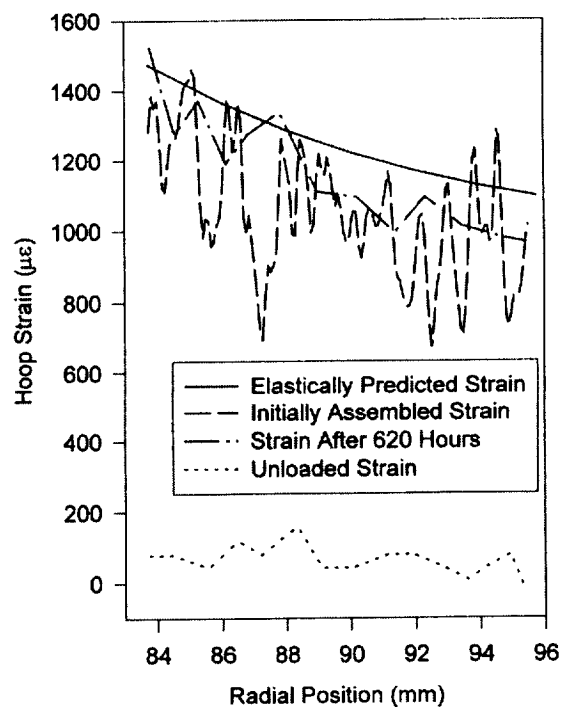
Figure 3-30: Predicted and measured strains in the LP-C c/ep ring.

Testing

Polymer Matrix Composites, Vol. 1: Guidelines for Characterization of Structural Materials, MIL-HDBK-17-1E, January 23, 1997.

This handbook is for guidance only. This handbook cannot be cited as a requirement. If it is, the contractor does not have to comply. This mandate is a DoD requirement only; it is not applicable to the Federal Aviation Administration (FAA) or other government agencies.

The three volumes of MIL-HDBK-17 serve as a general reference source for technical information on polymer matrix composites, including:

Volume 1: Guidelines for Characterization of Structural Materials

This volume contains guidelines for determining the properties of composite material systems, their constituents, and generic structural elements, including test planning, test matrices, sampling, conditioning, test procedure selection, data reporting, data reduction, statistical analysis, and other related topics. Special attention is given to the statistical treatment and analysis of data. Volume 1 contains guidelines for general development of material characterization data as well as specific requirements for publication of material data in MIL-HDBK-17.

It must be emphasized that this handbook differentiates between material basis values (material allowable) and design allowable values. Material basis values, being an intrinsic property of a composite material system, are the focus of this handbook. Design allowable values, while often rooted in material basis values, are application dependent, and consider and include specific additional considerations that may further affect the strength or stiffness of the structure. Also, when establishing application design values there may be additional certification or procurement agency requirements that go beyond MIL-HDBK-17.

Volume 2: Material Properties

Volume 2 contains statistically-based data meeting specific MIL-HDBK-17 population sampling and data documentation requirements, covering constituents and material systems of general interest. Data published in Volume 2 are under the jurisdiction of the Data Review Working Group and are approved by the overall Coordination Group (The MIL-HDBK-17 Coordination Group and Working Groups are discussed in Section 1.5). New material systems will be included and additional material data for existing systems will be added as data becomes available and are approved. Selected historical data from the MIL-HDBK-17A version of the

handbook that do not meet current data sampling, test methodology, or documentation requirements, but that still are of potential interest to the industry, are also documented in an appendix to this volume.

The material properties in Volume 2 are defined over a range of potential use conditions, focusing, when possible, on the upper and lower material environmental limits so that application-specific environments do not limit use of the data. Data at intermediate environmental conditions, when available, provide additional definition of the relation between material response and environment.

While the process of establishing structural design values for specific applications can begin with the data contained in Volume 2, most applications require collection of additional data, especially if there are requirements for data from the laminate or higher structural complexity levels (structural complexity level is discussed in 2.1.2.1). Also, the ability to manufacture material equivalent to that from which the data in Volume 2 were obtained typically must be proven to the procuring or certifying agency, which usually involves limited testing and data comparison. General guidelines for such material/process equivalence evaluation are presented in Volume 1; however, many of the details of such an evaluation remain at the discretion of the procuring or certifying agency.

Volume 3: Materials Usage, and Analysis Guidelines

Volume 3 provides methodologies and lessons learned for the design, manufacture, analysis, and supportability of composite structures, and for utilization of the material data provided in Volume 2 consistent with the guidance provided in Volume 1. Topics discussed in Volume 3 include materials and processing, quality control, design and analysis, joints, reliability, thick composites, and supportability.

SUMMARY

Section 6.7 covers uni-axial mechanical property tests. Several tables are relevant to the tests conducted on composite rotors.

Table 3-12: Tension Test Methods for MIL-HDBK-17 Data

	Symbols	Fully Approved, Interim and Screening Data
Lamina Properties		
0° In-Plane Strength	$F_1^{tu}, \varepsilon_1^{tu}$	ASTM-D3039, SRM4, SRM9 (crossply only)
0° In-Plane Modulus, Poisson's Ratio	E_1^t, ν_{12}^t	ASTM-D3039, SRM4
90° In-Plane Strength	$F_2^{tu}, \varepsilon_2^{tu}$	ASTM-D3039, SRM4, ASTM-D5450
90° In-Plane Modulus	E_2^t	ASTM-D3039, SRM4, ASTM-D5450
Out-of-Plane Strength	$F_3^{tu}, \varepsilon_3^{tu}$	(no recommendation)
Out-of-Plane Modulus, Poisson's Ratios	$E_3^t, \nu_{31}^t, \nu_{32}^t$	(no recommendation)
Laminate Properties		
x In-Plane Strength	$F_x^{tu}, \varepsilon_x^{tu}$	ASTM-D3039
x In-Plane Modulus, Poisson's Ratio	E_x^t, ν_{xy}^t	ASTM-D3039
y In-Plane Strength	$F_y^{tu}, \varepsilon_y^{tu}$	ASTM-D3039
y In-Plane Modulus	E_y^t	ASTM-D3039
Out-of-Plane Strength	$F_z^{tu}, \varepsilon_z^{tu}$	(no recommendation)
Out-of-Plane Modulus, Poisson's Ratios	$E_z^t, \nu_{zx}^t, \nu_{zy}^t$	(no recommendation)

Table 3-13: Shear Test Methods for MIL-HDBK-17 Data

Property	Symbols	Fully Approved, Interim and Screening Data	Screening Data Only
In-Plane Shear Strength	$F_{12}^{su}, \varepsilon_{12}^{su}$	ASTM-D3518, SRM7-88, ASTM-D5379, ASTM-D5448, MIL-STD-375	--
In-Plane Shear Modulus	G_{12}	ASTM-D3518, SRM7-88, ASTM-D5379, ASTM-D4255, ASTM-D5448, MIL-STD-375	--
Out-of Plane Strength	$F_{13}^{su}/\varepsilon_{13}^{su}, F_{23}^{su}/\varepsilon_{23}^{su}$	ASTM-D5379	--
Out-of Plane Shear Modulus	G_{13}, G_{23}	ASTM-D5379	--
Short Beam Strength	F^{SBS}	--	D2344, SRM8-88

Table 3-14: Fracture Toughness Test Methods for MIL-HDBK-17 Data

Property	Symbols	Fully Approved, Interim and Screening Data	Screening Data Only
Mode I Toughness	G_{IC}	ASTM-D5528	--
Mode II Toughness	G_{IIC}	ENF	--
Mode III Toughness	G_{IIIC}	--	--
Mixed Mode I, II, Fracture	f_c	--	MMB

3-36

CATEGORY

Testing

REFERENCE

Martin, R. H., "Accelerated Methods of the Determination of Long Term Fatigue Properties of Glass Reinforced Plastics for Rotor Craft Applications," ADA340938, 1997.

ABSTRACT

The U.S. Army Vehicle Technology Centre (VTC) at NASA Langley, has successfully used interlaminar fracture mechanics analysis on rotor craft structures to predict delamination initiation. The structure was analyzed to determine the values of strain energy release rate (G) at critical locations in the structure. These predictions were compared with structural test data running out to 10^7 cycles. However, in reality these structures may experience between 10^8 and 10^9 cycles in service at a frequency of 5 Hz. Hence, the aim of this work was to develop an accelerated and cost effective method of generating these long term fracture data for the analysis. Two materials were used in this project. These were S2/8552 and S2/F584, both glass epoxy systems. Delamination onset was monitored at both 5 Hz and 20 Hz and no difference in cycles to delamination onset was identified. It was concluded that longer term tests could be run at between 15 and 20 Hz to represent structural tests at 5 Hz. A multi-station fatigue machine was modified to allow up to six composite DCB test pieces to be tested. Each station had its own instrumentation to monitor individual specimens for compliance changes. This machine operates electro-mechanically and hence is less expensive to run than the conventional servo-hydraulic fatigue machines. The multi-station machine was used to generate delamination onset data up to 10^8 cycles at 17 Hz for both materials. For both materials a consistent decrease in the values of G between 10^0 and 10^8 cycles was observed. It is estimated that the increase in frequency and the use of an electro-mechanical multi-station fatigue machine, reduces the cost of generating long term fatigue data to under 5% of that using conventional testing approaches. This allows additional data to be generated giving greater confidence.

SUMMARY

Table 3-15 contains information about the fatigue tests conducted. The tests were conducted at different frequencies and amplitudes for different durations to determine temperature changes in the specimens. A thermal camera was utilized to determine if the effects of high strain on the laminates produced significant changes in the temperature of the specimens at frequencies up to 30 Hz. In all the tests, no significant increase in temperature was found. No increase in temperature was found in the delamination tip region.

The figures shown give results for the following laminates:

Figures 3-31 – 3-33: S2/E7T1 (with fabric layer)
Figures 3-34 – 3-36: S2/F584

Figures 3-37 – 3-39: S2/8552

Load displacement curves, pictures of the failure surface, and R-curves are included. Figure 3-40 gives the G-N curves for the three tested materials. The quasi-static test results are shown in the 10^0 part of the plot.

The work strove to create criteria for the generation of Mode I interlaminar fatigue up to 10^8 cycles in order to gain the ability to make predictions of fatigue loaded structural parts with lives up to the same number of cycles.

Table 3-15: Summary of Heat Build up Tests

δ_{max}	Frequency (Hz)	Cycles (000s)	Time Elapsed (mins)	Specimen Temperature (°C)
1.75	5	12	40	25.2-25.3
2.5	5	20	67	25.6-26.2
3.5	5	60	200	25.6-25.9
3.5	10	50	83	25.0-25.6
3.5	20	250	50	25.4-25.6
3.5	30	59	140	25.1-25.2
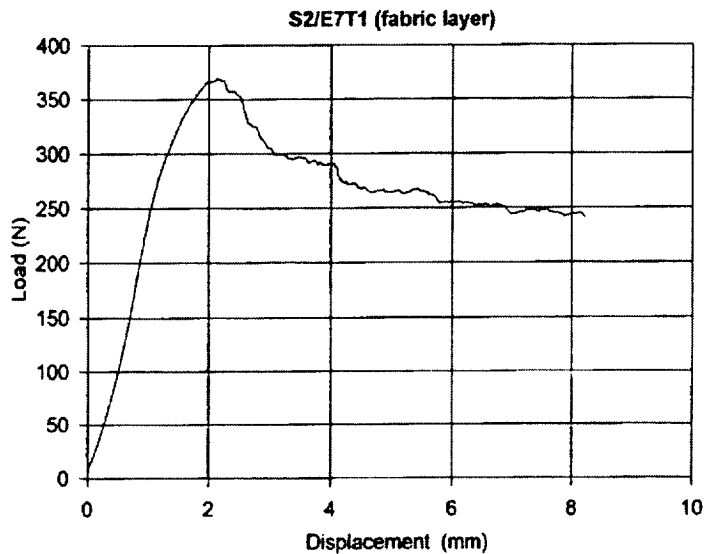
Figure 3-31: Typical load displacement curve for S2/E7T1 with a fabric layer.
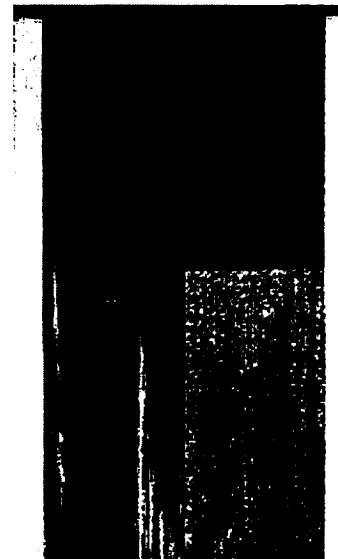
Figure 3-32: Digital scan of failure surface.

S2/E7T1 (fabric layer)

3-38
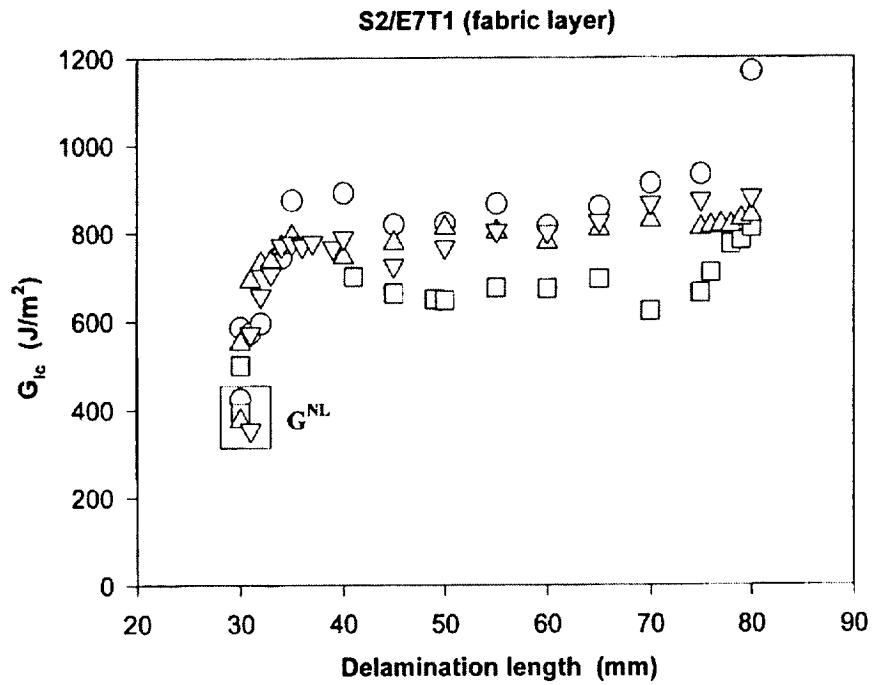
Figure 3-33: R-curve for S2/E7T1 material (with fabric layer).
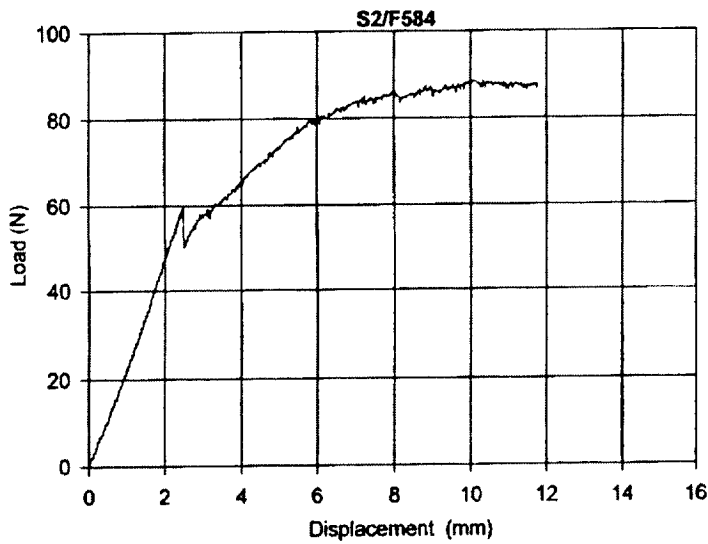
Figure 3-34: Typical load displacement curve for S2/F584.

Figure 3-35: Digital scan of failure surface.

Figure 3-36: R-curve for S2/F584 material.

Figure 3-37: Typical load displacement curve for S2/F584.

Figure 3-38: Digital scan of failure surface.
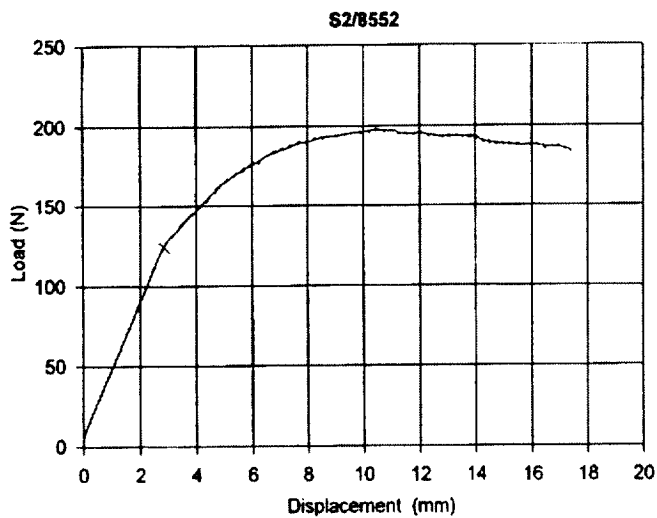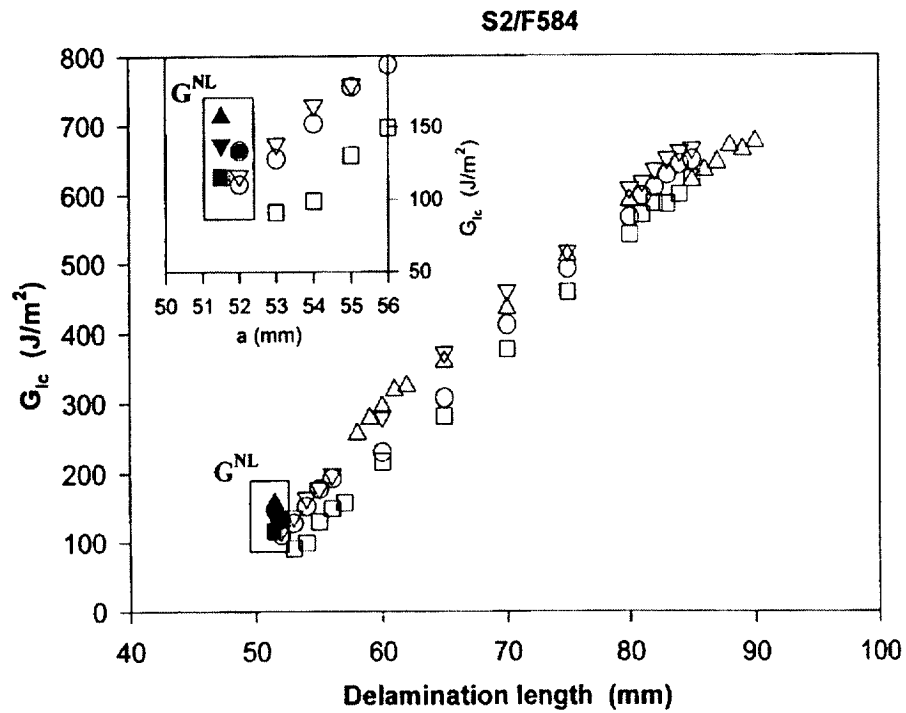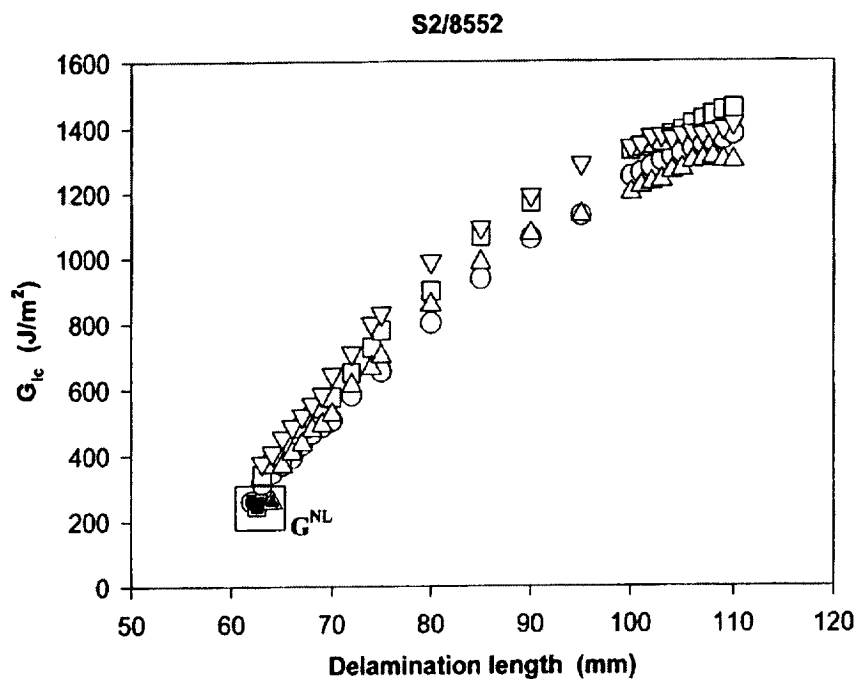
S2/8552

Figure 3-39: R-curve for S2/8552 material.
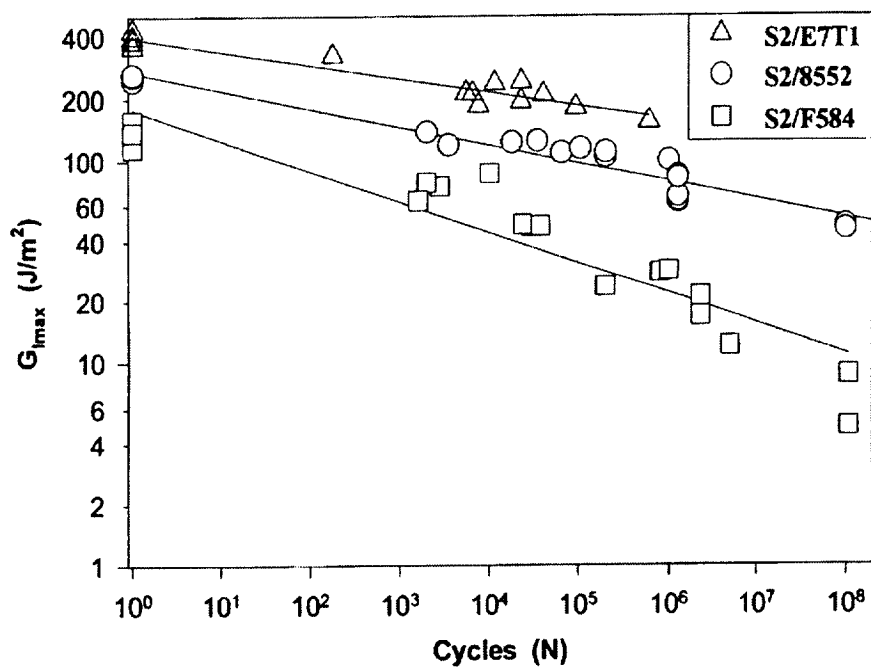
Figure 3-40: Comparison of delamination onset.

CATEGORY

Testing

REFERENCE

ABSTRACT

The test methods to determine interlaminar fracture toughness of composite materials require values to be determined at delamination initiation from the thin insert. In woven composites, the location of the insert relative to the yarns will vary which may effect the toughness values at initiation. This work determined the effect of the location of the insert relative to the yarns interlaminar fracture toughness using the double cantilever beam (DCB) and end-notch flexure (ENF) specimens under quasi-static and fatigue loads. The specimens were configured so that the insert end was placed at the edge of and in the center of a yarn and in a mixed position where the insert was at edge in one ply above and in the center of the ply below. Quasi-static and fatigue tests were conducted for each configuration. The static tests on the DCB resulted in "stick-slip" type fracture, where the delamination grew rapidly across a transverse yarn to the beginning of the next transverse yarn and stopped until the load increased sufficiently to cause further stick-slip fracture. As the delamination propagated down the beam, the crack branched either side of the transverse yarns eventually resulting in the complete ply bridging the delamination. This resulted in an increase in G_{Ic} values. Delamination growth in the ENF static tests also produced crack branching and ply bridging that resulted in stable delamination growth. For both specimen types, the lowest values of G_c were obtained in the specimens with the insert in the center of the yarn and the highest G_c with the insert at the edge of a yarn. The scatter in the fatigue data prevented a clear indication of which insert position resulted in the lowest number of cycles to delamination onset with the applied G_{max}.

SUMMARY

It is important to determine the effect of the different material configurations ahead of the delamination front on the initiation values of toughness, and to determine if woven materials can be incorporated into existing standard test methods. The materials used for the study were the double cantilever beam (DCB) for Mode I and the end-notched flexure (ENF) for Mode II (Figure 3-41). 2-D, plain weave, S2 glass fiber and American Cyanamid 4102 polyester resin composite specimens were used. The tests involved visually and electronically monitoring the onset of delamination growth. By testing several specimens at different loads, and different cyclic strain energy release rates, G_{max}, a G-N curve can be generated where N is the number of cycles to delamination onset. To simulate the delamination, a 13 μm Teflon® insert was placed between two plys during lay-up. The insert was positioned to give the three different configurations shown in Figure 3-42.

DCB Testing

At a displacement rate of 0.3 mm/min, the DCB specimens were statically loaded. At certain intervals, delamination length was measured visually and entered into the computer at the corresponding load and displacement. The static tests resulted in a linear loading curve until initiation from the insert. Once the delamination began to grow, it grew in a "stick-slip" fashion, where the delamination would grow rapidly across the top of a transverse yarn to the beginning of the next yarn and stop until the load increased further. When the delamination propagated, it did so unstably to the next yarn position resulting in a load drop. See Figure 3-43 for a comparison of the different insert set-ups. As the delamination propagated down the beam, the delamination front was observed from the edge to be branching or growing on different sides of a yarn so that as the delamination grew the complete ply eventually bridged the delamination, resulting in a significant increase in G_{Ic} as shown in Figure 3-44.

Fatigue tests were also conducted at 5 Hz and 8 Hz frequencies. During these tests, significant delamination did not occur. A typical load versus cycles curve is given in Figure 3-47. Unlike the results shown in the figure, in most tests there was no period of constant load, and the delamination began to grow immediately causing the maximum cyclic load to decrease immediately. All configurations show a significant reduction in toughness in fatigue compared to the quasi-static tests.

ENF Testing

Delamination growth in the ENF static tests also produced crack branching and ply bridging. Fiber bridging, however, does not occur in ENF specimens fabricated from unidirectional tape. Crack branching was apparent in the static tests by causing stable delamination growth as observed in the load-displacement curve shown in Figure 3-45. "Ratcheting" was observed in these specimens, as well. The cause of the stable delamination growth is that the increase in interlaminar fracture toughness caused by the crack branching and ply bridging, occurs at a greater rate than the decrease of the strain energy release rate with crack length. The R-curve for the ENF specimen is shown in Figure 3-46.

In the ENF fatigue tests, the load vs. fatigue cycle plots, either decreased early in the tests, indicating delamination growth, or initially increased and then decreased. The initial increase was believed to be caused by the settling of the specimen in the fixture.

Conclusions

Because of crack branching and ply bridging, structures made from woven materials may be inherently more damage tolerant in the presence of a delamination. The material may experience minor cracking or delamination very soon in service, but because of its woven nature, the material has a resistance to delamination growth. It was found that the position of the insert did have an effect on the initiation toughness values.

Double Cantilever Beam Specimen

25
10

Dimensions in mm
Drawings not to scale

25
65
140

End Notched Flexure Specimen

25

25 25
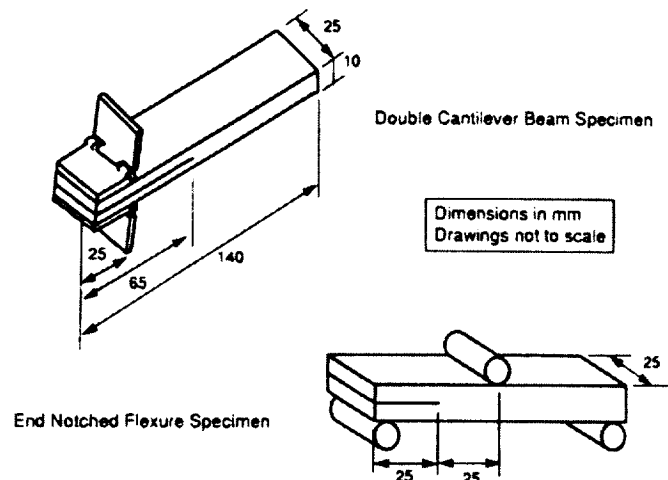
Figure 3-41: Schematics of double cantilever beam and end notched flexure specimens.

Transverse yarn

Edge Configuration
Longitudinal yarns directly
above each other across width

Longitudinal yarn

Centre Configuration
Longitudinal yarns directly
above each other across width

Insert

Branched crack

Mixed Configuration
Longitudinal yarns not directly
above each other across width
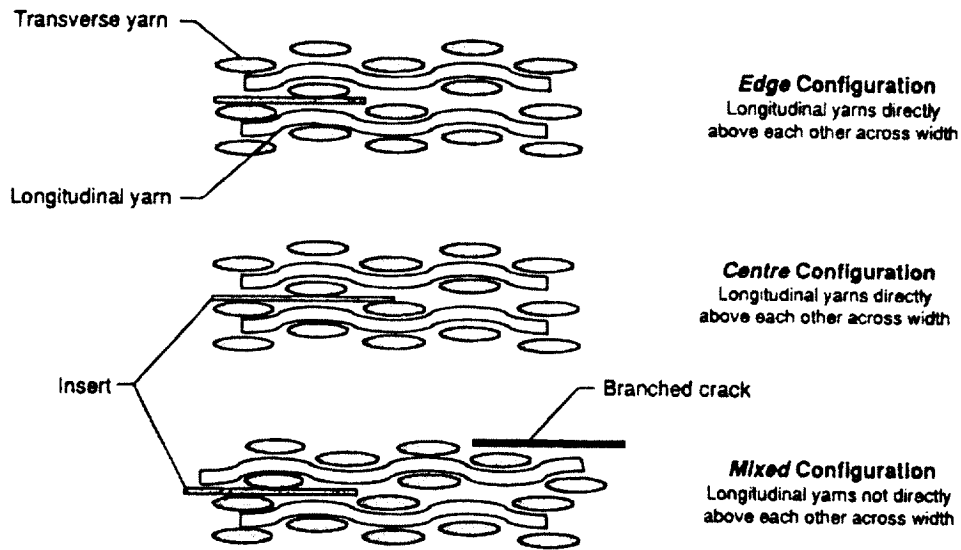
Figure 3-42: Insert configurations.
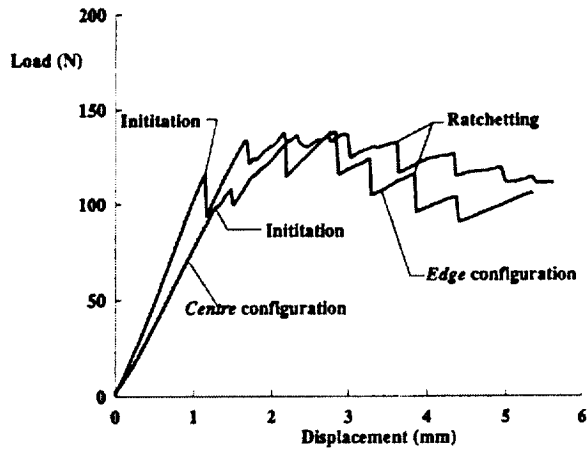
Figure 3-43: Load displacement data for DCB specimens.
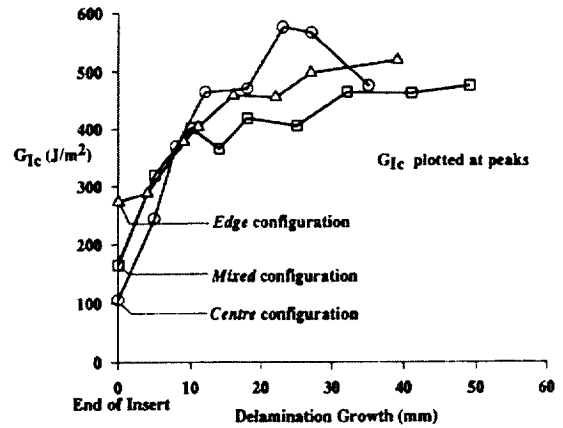
Figure 3-44: DCB R-curves.
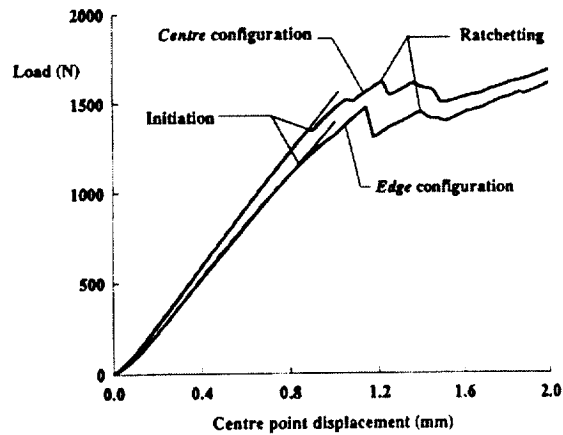
Figure 3-45: Load displacement data for ENF specimens.

Figure 3-46: ENF R-curves.

DCB - Delamination growth
1%   = 0.15mm
5%   = 0.80mm

ENF - Delamination growth
0.2%   = 0.15mm
1%   = 0.80mm
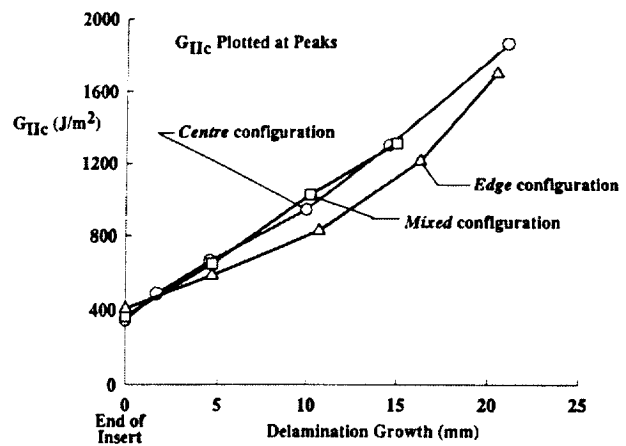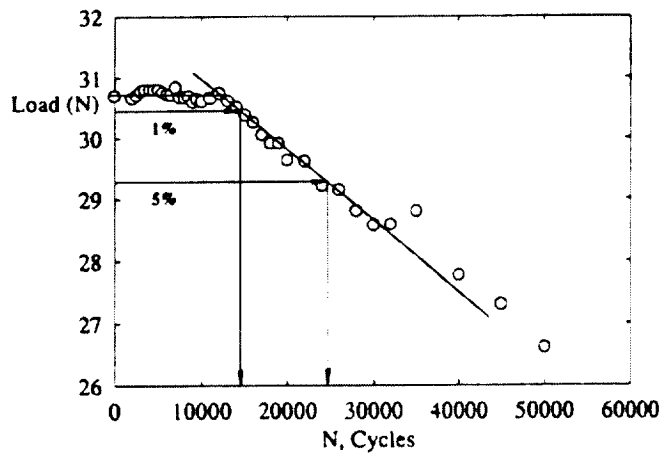
Figure 3-47: Load drop in DCB fatigue test.

CATEGORY

Testing

ABSTRACT

Composite materials are found to lose mechanical durability and strength on exposure to aircraft operating environments. This is mainly due to absorption of moisture from humid air by the matrix material. Composite materials are extensively used in the RAAF for both major structural components on the F/A-18 and for bonded repairs and doublers. The performance of these materials under long-term environmental exposure is an important aspect of both aircraft certification and in the understanding of how the components will age. This report provides a broad overview of environmental effects on composite materials and methods which may be used to predict their long-term behavior. The use of accelerated testing environments in the laboratory is an attractive proposition as it enables tests to be carried out in reduced time frames. A number of accelerated testing methodologies and the implications are outlined here. Accelerated testing can be carried out with confidence if the exposure conditions are representative and the failure modes of the material during mechanical tests reflect those seen in service.

SUMMARY & COMMENTS

This report pertains mostly to aircraft exposure to moisture and humidity. However, the report does describe accelerated testing methods and their complexities.

Table 3-16 lists a variety of high-performance resins and their maximum moisture uptake when exposed to high humidity. The moisture uptake in composites will be lower due to the presence of fibers. The immediate effect of moisture on the mechanical properties of a composite is the reduction of both modulus and glass-transition temperature, T_g. Figure 3-48 shows a plot of T_g versus moisture content for neat 3501-5 resin.

The environmental fatigue behavior of composites is as important as static tests. The effect of moisture on both the static and fatigue response of a number of composite systems has shown that the interlaminar shear strength of a carbon fiber reinforced plastic material is modestly higher than dry specimens. This effect can be attributed to plasticisation of the matrix and a relaxation of some residual thermal stress during processing. In some cases, conditioning specimens to levels of moisture commonly found during service may have a beneficial effect.

When exposed to moisture, the surface layers of the composite change their moisture concentration much quicker than the bulk. When thermal spiking is present, the effect of the

3-46

moisture content in the composite may be detrimental. Spiking is thought to create matrix damage which allows greater levels of moisture to absorb into the composite. Figure 3-49 suggests that there is a critical moisture level above which thermal spiking will cause permanent damage to the composite matrix.

Water trapped in voids or cracks within composite materials may freeze when exposed to extremely cold conditions found in service. Water expands by 8.3% in volume upon freezing, and has a bulk modulus that is three to four times that of epoxy resin. This trapped frozen water will put pressure on the surrounding material which may result in permanent matrix damage.

Ultraviolet damage in composites is usually characterized by erosion of exposed layers of the matrix materials. Such damage can be minimized by application of UV resistant coatings.

A number of methods exist for accelerated testing of environmental conditions:

a) Intensify the exposure results: This techniques uses increased levels of exposure to indicate long-term material degradation. This will also increase the severity of the degradation and may cause the mode of degradation to alter. The variables that may be intensified include the temperature, moisture levels, UV radiation levels and any other conditions present in the operating environment. It is necessary to identify the relationship between the increase in exposure intensity and the property that is to be measured. Therefore, it is difficult to determine the results of an accelerated test without first making a comparison to other long-term exposure data.

b) Increase to frequency of exposure to degrading conditions: This scheme attempts to replicate the conditions of real conditions and then increase the frequency of exposure to the most damaging conditions. The decision must also be made whether to cycle between two extreme climatic conditions or to expose materials to long periods of each.

c) Simulation of environmental conditions by load enhancement: This involves using load enhancement factors or intensifying another material testing parameter. For example, the effects of a hot/wet environment may be simulated by testing a dry structure at higher loads. The mode of failure is important in this case and must be identical for the load enhanced test and the hot/wet test in order for the results to remain valid.

The ENSTAFF method of accelerated testing works on a similar principle to FALSTAFF (Fighter Aircraft Loading Standard for Fatigue evaluation); the mechanical equivalent. ENSTAFF combines mission profiles, cyclic loads, environment and associated temperature excursions during typical combat aircraft usage. This allows many "flights" to be performed within relatively short time-frames, and allows the prediction of the part performance over an extended period. It is designed specifically for testing of composite materials for wing structure of combat aircraft operating under European conditions. A similar technique could possibly be developed for use in testing components for space flight conditions. Although ENSTAFF represents the most "realistic" way of accelerated testing it must be noted that long-term degradation mechanisms (if present) may not be adequately represented by this method. This includes mechanisms such as UV exposure, erosion or chemical reactions which may change the material properties.

Table 3-16: Maximum Moisture Uptake of Selected Resins in Composite Materials

Name	Maximum Moisture Uptake of resin in % by weight
3501-6 Graphite/Epoxy (Hercules) [1]	4.5
FM-73 Epoxy Adhesive [2] (Cytec)	4
MR-45 Bismaleimide (Amoco) [3]	3.1
V398 Bismaleimide (US Polymeric) [3]	5.3
PMR-15 Polyimide (US Polymeric) [3]	4.0
PEEK Thermoplastic (ICI) [3]	0.7
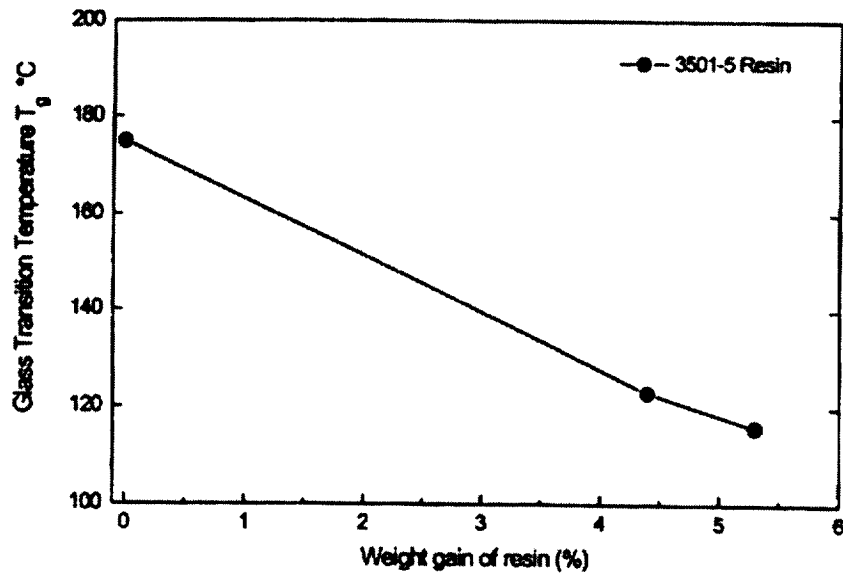
Figure 3-48: Plot of T_g versus Temperature for neat 3501-5 Epoxy Resin cured at 177° C.

3-48
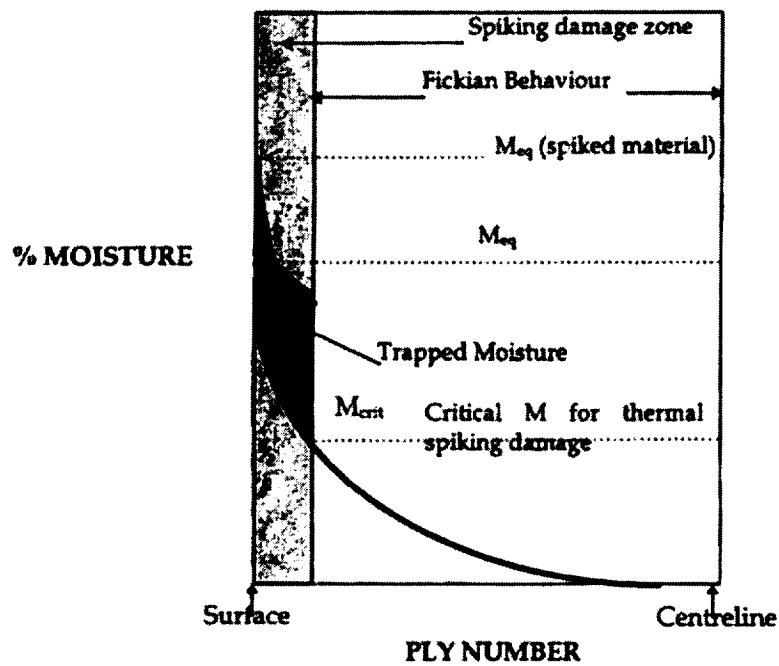
Figure 3-49: The effects of thermal spikes on the moisture absorption behavior of a graphite epoxy laminate.

CATEGORY

Testing

REFERENCE

Sonnichsen, H. E., "Ensuring Spin Test Safety," *Mechanical Engineering*, Vol. 115, No. 5: 72-77, 1993.

ABSTRACT

Because many of the hazards associated with centrifugal stress testing of rotating components (spin test systems) are not known, users must take precautions. The kinetic energy of typical turbomachinery components is very high at burst speed, and the fragments of a disk can do serious damage to structures and people.

SUMMARY

Various examples of spin test facility failures are laid out in the article. See Figure 3-50 for an explanation of the components in a proper spin test system. Spin test systems must be designed to contain the fragments of high-speed rotors at burst, protect the users from potential injury, and save the burst fragments intact for analysis if possible. The kinetic energy of typical turbomachinery components is very high at burst speed, and the fragments of a disk can do serious damage to structures and people if containment is inadequate. For example, a steel disk 14 inches in diameter and 3 inches thick, spinning at 27,000 rpm has kinetic energy of about 3 million lb-ft, the equivalent of five full-size automobiles traveling together at 60 miles per hour.

Rotors made with composite materials, however, store substantial energies in relatively small form factors (small size). Spinning them in some existing spin pits may cause containment problems that did not previously exist. Additionally, composites generate large amounts of dust during a burst, which can ignite an explosion when an oxidizing agent and a spark are present.

The total angular momentum of a spinning disk is not changed when it bursts. The momentum is transferred to the containment structure by the impact of the burst fragments. In the late 1970's, the angular impulse caused by the destruction of a spinning epoxy-glass composite rotor tore a spin pit from its attachment bolts and twisted it around in place, tearing away all the service lines including the vacuum pipe. The vacuum pipe failure admitted air to the chamber, allowing the explosive ignition of epoxy dust, causing failure of the cover bolts and ejection of rotor fragments into the surrounding test cell area. Fortunately, the incident occurred in a concrete test cell and no injuries occurred.

When these rotors burst, the angular momentum is transferred to the containment structure over a period of milliseconds. If the containment cylinder were rigidly attached to the test chamber, it can be predicted that the burst of a heavy rotor would tear the chamber from its mounting bolts, as in the above example. Properly designed spin test chambers include a separate internal burst-

containment cylinder that is not attached to the chamber but is free to rotate under the angular impulse of burst fragments. The chamber mounting bolts are therefore subject to forces not exceeding the friction drag of the containment liner as it slides.

In order to preserve pieces of broken disks for analysis, many spin test chambers are lined with lead blocks or other relatively soft material to cushion the impact of burst fragments. The soft liner is also helpful in reducing the formation of metal dust as the burst fragments strike the inner surface of the containment cylinder. In some instances, the lead bricks typically used as an inner liner can transfer very large forces to the chamber cover when impacted by rotor burst fragments. This impact force is significantly larger than the typical cover flange bolt strength, and can easily blow the cover off the chamber. To prevent this, it is necessary to add a steel brick retention ledge to the inside of the containment cylinder at both ends.

Some known hazards involving kinetic energy include burst fragment translational energy, test article angular momentum, cushion liner extrusion, drive turbine burst energy, and drive spindle ejection. Hazards involving chemical energy include oil and metal dust deflagration.

Oil deflagration in spin chambers is probably the most common accident in the testing process, but the incidents, with few exceptions, have been mild. It is likely that the relatively low explosion pressures observed are the result of the typically slow venting rates of the chamber. If the oil mist is ignited before the absolute pressure in the chamber reaches atmospheric, the resulting peak pressure will be directly reduced by the ratio of pressure at ignition to atmospheric pressure.

The following rules are recommended for safe spin testing:

a) Primary issues are retention of the lid, the strength of the cover, and the ability of the liner and vessel to contain a burst.
b) Enclose spin pits in a test cell (usually with concrete walls) and do not allow anyone inside the cell when tests are being run. Test cells are important because all the potential causes of accidents during spin testing are not known.
c) Fill sight glasses with appropriate steel plugs. These glasses allow shrapnel to escape out of the spin pit and oxygen to enter easily.
d) Vent the vacuum pump exhaust line outside the building and use an oil mist coalescing filter to eliminate the discharge of excessive amounts of oil into the air.
e) Install a reliable and safe lid elevator to prevent damage to hands and fingers while operating the spin pit.
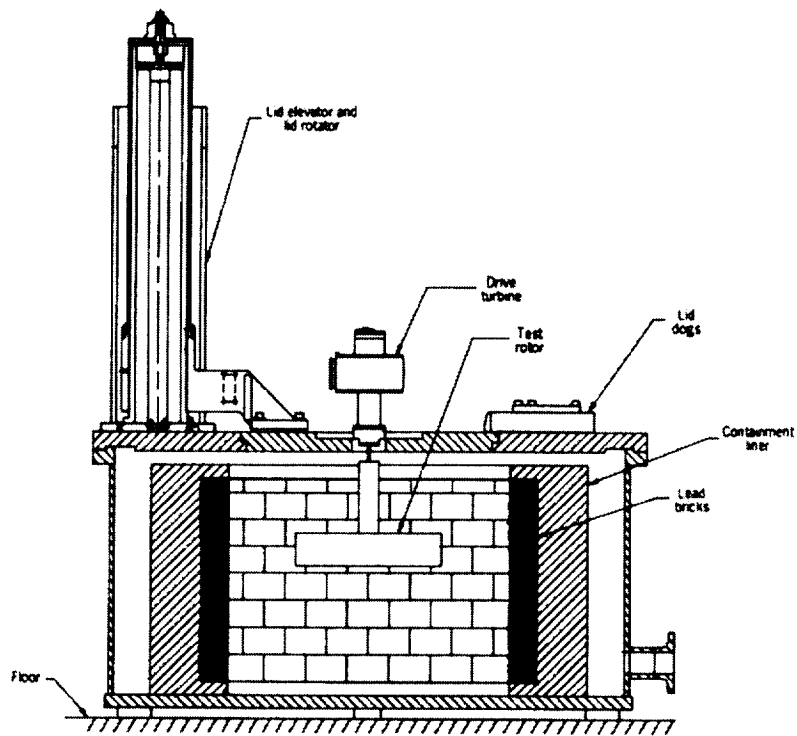
Figure 3-50: Spin test systems much be designed to contain the fragments of high-speed rotors at burst, protect users from potential injury, and save the burst fragments intact for analysis. Shown is a typical spin pit lay out.

CATEGORY

Testing

REFERENCE

ABSTRACT

The strengths and absorbed moisture obtained from eight different accelerated environmental test methods are presented and compared with static, ambient fatigue and environmentally exposed real time data. The test parameters included 0.52% and 1.17% moisture targets, the presence and absence of 127° C thermal spikes, moisture preconditioning and concurrent conditioning, six life times of spectrum loading and four types of graphite/epoxy specimens. Compression strength is reduced by increased moisture and elevated temperature, but is not significantly affected by moisture conditioning method or spectrum loading. Accelerated environmental testing, subject to the limitations of test variable severities, can determine the effects of real time environmental testing. If temperatures above glass transition temperatures cannot be avoided, their potentially detrimental effect must be accounted for in accelerated simulations.

SUMMARY

The specimens tested were divided into eight accelerated environmental test groups. All of the specimens in the accelerated environmental tests were flat, coupon-type specimens with a 25.4 mm central test section, as shown in Figure 3-51. These groups were subjected to six aircraft life times (LT) or 7680 flights to an accelerated spectrum loading representative of the baseline aircraft horizontal stabilizer. Table 3-17 shows the pertinent conditioning parameters and the final moisture contents of the test specimens.

The environmental effects in this study were assessed by noting changes, if any, in two quantities between various accelerated environmental test methods – test specimen residual strengths at room temperature (RT) and their corresponding amounts of absorbed moisture. Figures 3-52 and 3-53 plot the probability of survival for residual strength of Groups 4 and 6, and 5 and 6, respectively. The average moisture and strength values are listed in Table 3-18 and plotted in Figures 3-54 and 3-55. Figures 3-54 and 3-55 also show bands of reduced data from real time tests without flight mechanical loads. The worst scatter was observed for the thinner (8-ply) specimens. Such scatter is likely due to the thin specimens in compression being subject to the local buckling mode of failure that typically is associated with higher scatter than other failure modes. The results substantiate the theory that fiber dominated tension is not significantly affected, whereas matrix dominated compression is reduced by increasing the moisture content (M). Elevated temperature reduces tensile strength slightly and compressive strength more significantly. Real time tests have demonstrated that the absorptivity and thus the equilibrium

moisture content of epoxies are increased if such material is exposed to thermal excursions exceeding its glass transition temperature, T_g.

Both 8- and 16-ply tension specimens failed in the same mode – net tension across the fastener hole. Compression specimens, on the other hand, produced two dominant failure modes. The typical failure mode of the 8-ply specimens, as mentioned before, was that of local instability away from the hole. For the 16-ply specimens, the predominant failure mode was compressive laminate crushing failure characterized by extensive brooming across the hole.

Neither compressive nor tensile strengths were significantly affected by a mechanical spectrum loading whose peak load magnitude is 53% of hot wet static B allowable strength and occurs once in 100 flights. The greatest reduction in strength of about 10%, due to thermal spiking, belongs to the thinner compression specimens while the strengths of the other preconditioned specimen types are practically unaffected.

On the whole, the accelerated environmental testing methods examined were able to reproduce real time data within reasonable bounds, and thus qualify as valid schemes for simulating actual conditions while reducing test time considerably.

Table 3-17: Environmental Conditioning of Test Specimens

Group No	Type of environmental conditioning	Ground storage environment	Goal (%)	Actual (%)	RH	Temp (°C)	He[4] (%)	Cycle (h)	Duration (days)	Goal (%)	Actual (%)
1	Concurrent	Average	—	0.10			Var	1	60	0.52	0.52
2	Preconditioned	Average	0.52	0.53			Var	1	55	0.52	0.46
3	Concurrent	Tropical	—	0.18			85	1.5	60	1.17	1.17
4	Preconditioned	Tropical	1.17	1.09			85	1.5	48	1.17	1.21
5	Concurrent	Tropical	—	0.15			35 to 85	3	71	1.17	1.16
6	Preconditioned	Tropical	1.17	1.04			50 to 75	3	73	1.17	1.03
7	Concurrent	Average	—	0.22			67	3	71	—	0.89
8	Concurrent	Tropical	—	0.26			85	3	62	—	1.32

[1]Continuous moisture conditioning at 77°C and various relative humidity (RH) levels for 'preconditioned' specimens only
[2]No moisture conditioning
[3]On-off steam cycle moisture conditioning at 60°C
[4]Equivalent average relative humidity

Figure 3-51: Test specimen geometry and lay-up. Fiber
orientation and loading: Type I [0/±45/90]$_S$
tension; Type II [0/±45/0]$_S$ compression; Type III
[0/±45/90$_2$/45/0]$_S$ tension; Type IV [0/±45/0$_2$/45/0]$_S$
compression.

Figure 3-52: Thermal spike effect on residual strength –
preconditioning in tropical environment.
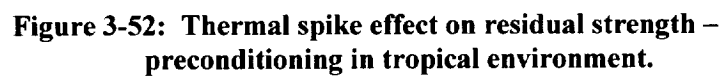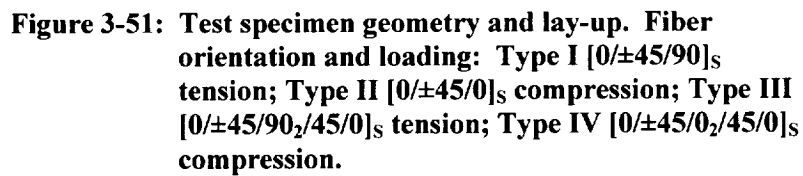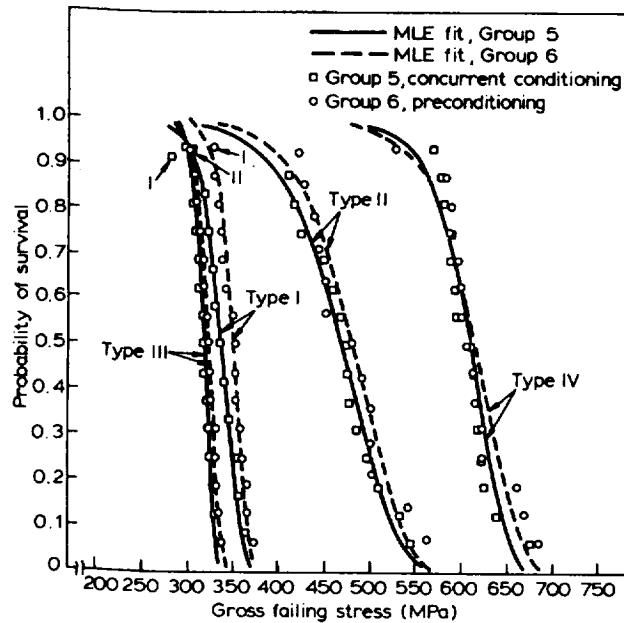
Figure 3-53: Concurrent conditioning vs. preconditioning - tropical environment, thermal spiking.

Table 3-18: Moisture Content and Room Temperature Strength

Type of test, conditioning/environment	8-ply specimens				18-ply specimens			
	Tension (Type I)		Compression (Type II)		Tension (Type III)		Compression (Type IV)	
	$\bar{M}$ (%)	$\bar{F}$ (MPa)	$\bar{M}$ (%)	$\bar{F}$ (MPa)	$\bar{M}$ (%)	$\bar{F}$ (MPa)	$\bar{M}$ (%)	$\bar{F}$ (MPa)
Static/ambient[4]	0	344	0	590[2]	0	317	0	688
Static, preconditioned/average[4]	0.61	344	0.56	597	0.56	321	0.56	676
Static, preconditioned/tropical[4]	1.17	345	1.18	565	1.20	320	1.16	655
Nominal fatigue, 6 LT/ambient[4]	0.56	355	0.43	576	0.36	328	0.30[3]	684[3]
Gp 1 concurrent/average	0.63	361	0.60	532	0.37	328	0.39	642
Gp 2 preconditioned/average	0.43	369	0.61[3]	564[3]	0.62	332	0.50	649
Gp 3 concurrent/tropical	1.12	359	1.05	560	1.05	337	0.88	628
Gp 4 preconditioned/tropical	1.13	359	1.04	528	1.30	314	1.23	616
Gp 5 concurrent/tropical	1.18[1]	338[1]	1.05	466	1.02	320	1.12	615
Gp 6 preconditioned/tropical	1.04	351	1.09[2]	480[2]	1.20	324	1.16	616
Gp 7 concurrent/67%	0.84	359	1.08	524	1.02	325	0.94	609
Gp 8 concurrent/85%	1.29	342[3]	1.29	552	1.33	315	1.32	613

$\bar{M}$ – Average value of moisture gain, % by weight, $\bar{F}$ – average value of gross failure stress, MPa
Each group had 15 specimens except as noted:
(1) 11 specimens, (2) 13 specimens, (3) 14 specimens, (4) data from another study
End of test moisture gain goals: average environment 0.52%, tropical environment 1.17%

3-56
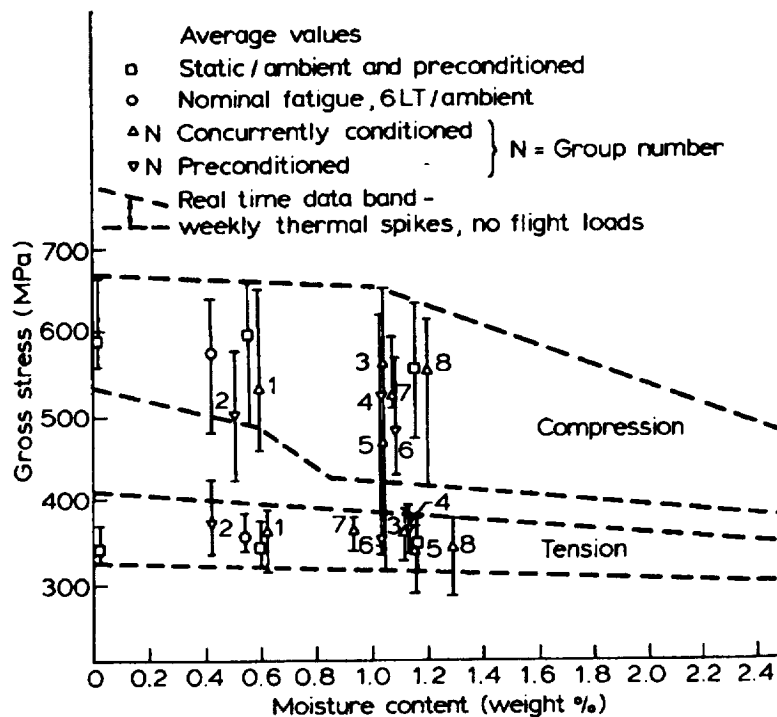
Figure 3-54: Residual strength at room temperature for 8-ply specimens.
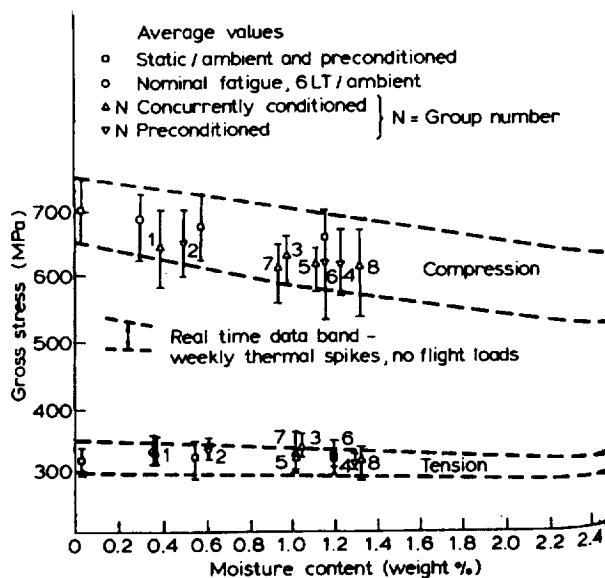
Figure 3-55: Residual strength at room temperature for 16-ply specimens.

3-57

CATEGORY

Testing

REFERENCE

Mohr, P. B., Walter, C. E., *Flywheel Rotor and Containment Technology Development – Final Report*, Report No. UCRL-53448, 1983.

ABSTRACT

A program to develop energy storage systems based on high-performance flywheels, which has been carried on by LLNL under DOE sponsorship since 1975, has been terminated with the 1983 fiscal year. This final report summarizes the accomplishments of that program, with emphasis on the work of the terminal year and orderly closeout of the program. Activities of the terminal year included fabrication, quality assurance inspection, and spin-test evaluation of rotor and containment structures. Peak stored energies approaching 0.7 kWh were consistently attained in 10-kg rotors, yielding material-average stored energy densities exceeding 70 Wh/kg. Flywheel rotors were tested by cycling them between full design speed and half speed for 10,000 cycles without rotor failure. The initial test of a lightweight containment structure indicated need for a better understanding of the rotor failure process and for additional development. In complementary studies, production cost estimates were made for three flywheel designs. In a cooperative program with the University of Wisconsin, construction began on a second-generation hybrid automobile combining a flywheel, a continuously variable transmission, and a conventional heat engine – a combination which promises fuel economy improvements up to 100% in urban use. Suggestions are made for direction of future work when interest in flywheel systems reappears.

SUMMARY

The objective of the project was the development of energy technology that can reduce or make more effective the expenditure of limited energy resources. The implementation of this objective has taken the following technological forms:

a) To develop new material forms that promise improved and predictable performance and benign failure characteristics.
b) To develop high-performance flywheels that are reliable and practical.
c) To develop flywheel-containment systems that are fail-safe, light in weight, and inexpensive.
d) To exhaustively test various designs (in both the ultimate performance and practical lifetime sense) and to identify those that are the most promising for development and use in favorable applications.

For flywheel rotors, the strain energy and stored energy under any rotational condition can be related to two material properties, strength and density, by the following formula

$$\text{Energy Density} = \frac{E}{m} = K\frac{\sigma}{\rho}$$

K is a factor which is dependent on rotor shape whose value is always less than or equal to unity, σ is the maximum stress, and ρ is the mass density of the rotor. Examples of shape factors for composite materials are shown in Figure 3-56.

In the early stages of the program, the characteristics of various composite arrangements were explored. Thin rims proved to be the most energy-effective way to arrange continuous fibers. But thin rims were inefficient in the use of space. Thick rims gave rise to radial stresses resulting from strain differences.

The following is a comparison of some of the fiber options looked at in the program:

a) E-glass is the primary reinforcement material for reinforced plastic applications. It has moderate strength and is low in cost.
b) S2-glass is stronger and costs more than E-glass; it is used either when higher strength is designed or in a hybrid form with graphite to reduce cost and improve impact resistance.
c) Aramids include Kevlar-49 and Kevlar-29. They are high-cost reinforcements that have high tensile and low compressive strength. They can be used in a hybrid form with graphite to improve impact resistance.
d) Graphite fibers are high in strength, modulus, and cost. They have superior fatigue resistance.

The designs shown in Figure 3-57 were favored because of performance and practicability. They consist of wound rims, cross-ply disks, and woven rings – used singly or in combination. The designs chosen for development were: (1) a hybrid rotor consisting of a wound rim of graphite filament attached to a disk hub structure made of cross-ply glass filaments (as well as a simple rotor consisting of the disk hub structure alone), (2) a wound rim of glass and Kevlar filament with a spoked hub of composite materials and metal, and (3) a bi-directional-weave ring of glass filament or Kevlar, fully machine-woven.

The test plan consisted of performing spin testing of the cross-ply disk and wound rim rotors. The cyclic spin testing was performed on one of the GE hybrid rotors and one of the simple disk rotors. One of the GE ultimate burst tests was also performed within a containment housing. It was the first such test ever performed under the entire DOE flywheel development program. Table 3-19 lists the GE rotors that were tested. For five rotors, the common failure mode was separation of the rotor from the hub. All of these rotors separated at speeds from 89% to 116% of the design ultimate values. From the rotors that were recovered intact, it was observed that the hubs separated from the rotors by tearing off the glass/epoxy surface ply to which they were bonded.

From Table 3-19, only D2 and H8 rotors bust under purely rotationally induced forces. Rotor D2 was the only one to experience a disk burst, whereas H8 failed in the circumferential ring failure

(CRF) mode. Following ring burst events, the disks of these rotors separated from the hub and then were destroyed by collision with the test chamber and containment housing.

Figure 3-58 shows the Garrett flywheel design which comprises a rim of composite material joined to a hub with four rigid spokes. Two problems with rim-type flywheel designs are: (1) matching spoke growth with radial growth of the rim with increasing speed while maintaining an adequate connection to the rim, but not adversely affecting the time; and (2) the limitation on rim radial width imposed by the low radial strength of circumferentially wound composite rims.

The rim is subjected to tangential (hoop) stresses, bending stresses, and shear stresses during operation. High centrifugal forces are the cause of the hoop stresses, and the change in curvature of the rim over the spoke tips during operation induces the bending stresses. Table 3-20 shows a similar summary for a nine-ring rim with a maximum operating speed of 2500 ft/s. From the tests conducted on the Garrett design, this type of flywheel demonstrated the highest energy capability (~80 Wh/kg).

AVCO's "constant-stress" composite flywheel concept (Figure 3-59) incorporates fibers in the two principal stress directions – radial and circumferential. This is done by forming a circular or spiral weave in which the warp yarns become the circumferentials and the picks become the radials. Figure 3-60 shows the hub design based on spin-growth compatibility, strength, and spindle-mount resonance criteria. The hub material was Nylon II, and the cross-section was tapered.

The testing program also included the characterization of three types of fibers (Kevlar-49, S2-glass, and E-glass) composited with the same epoxy. In the case of static tensile properties, 75° C temperature or vacuum, either alone or in combination, has little significant effect on the Kevlar-49 composite. However, at 100° C the drop-off in the failure stress of the Kevlar-49 composite is more pronounced. This is caused because of strength degradation of the Kevlar fiber at the elevated temperature. Figures 3-61 – 3-63 show the fatigue data for different test conditions with the Kevlar-49 fiber. No failures were observed up to 10^6 cycles.

The stress rupture and dynamic fatigue of Kevlar-49/epoxy strands were also tested. The results of the tests are shown in Figures 3-64 – 3-67, the following conclusions were drawn:

a) At a constant applied stress, cyclic loading is much more severe than sustained loading in damaging (i.e., drastically reducing the lifetime of) the longitudinal Kevlar-49/epoxy composite (see Figures 3-64 and 3-65).
b) The length of the rest periods in cyclic fatigue may also have a significant effect on the lifetime of the longitudinal Kevlar composite (see Figures 3-65 – 3-67).
c) Dynamic fatigue of longitudinal Kevlar composites cannot be predicted by such conventional theories as Miner's rule (see Figures 3-66 and 3-67).

Figure 3-68 shows a plot of specific mechanical properties which compare several composite and metal options.

Flywheel containment is a very important issue to consider when designing a flywheel assembly. In order to design an appropriate containment system, one must understand the failure modes the system is containing. It has been observed, that upon failure, composite rotors break up into much smaller fragments than metallic rotors giving them a much lower capability to inflict damage to surrounding structures. Some studies reported that when composite rotors burst they can produce impressive damage in heavy containment, although still well below that produced by comparable metal rotors. Figures 3-69 and 3-70 show schematics of two containment designs. The momentum transformation is accomplished by engagement with a close-fitting ring of high-strength steel which serves a double function: (1) It deforms to contain the impulse of radial momentum, and (2) it combines with the tangential (rotational) momentum to effect a sudden slowing of rotational speed.

When a rotor was spun to failure in the containment system of Figure 3-70, the rotor dropped free from the hub, breached the containment, and destroyed both itself and the containment housing. A substantial amount of the residual energy remained to be absorbed by the spin test enclosure. From this test, the following conclusions were made:

a) The containment volume and possibly the strength need to be increased. Venting, on failure, could be considered as a partial alternative to increased volume.

b) Mechanisms for early-time, high-rate energy release (by ablation or deflagration reactions) need to be reassessed. The amount of stored energy that must be absorbed by the containment in the first moments after failure appears to have been underestimated.

c) The graphite-epoxy debris from the test should be analyzed chemically for evidence of high-rate reactions or physical heating.

d) The containment ring should be reconfigured to increase its stability and to redirect or vent any hydrodynamic impulse (blast) resulting from interaction between the flywheel containment ring.

The application of flywheel technology to hybrid vehicle research is also discussed. Figure 3-71 shows a stored-energy bus that Garrett developed for the Urban Mass Transit Administration (circa 1983) of the Department of Transportation. This system utilized a rotor with multiple Kevlar/epoxy rings on an aluminum hub. This flywheel stored 16 kWh of energy. Table 3-21 gives a summary of other specialized flywheel applications.
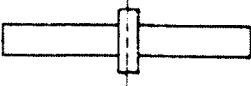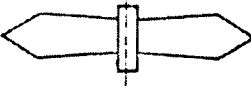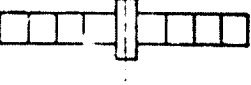
Description	Shape factor K
Circumferentially wrapped flat disk	0.43
Circumferentially wrapped flared disk	0.47
Tape overwrap	0.35
Multi-rim	0.45

Figure 3-56: Flywheel rotor configurations and shape factors for fiber-composite materials.
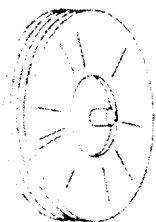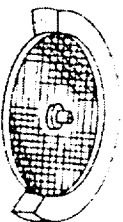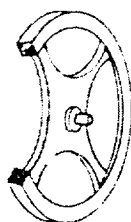
Wound in single operation   9 or 15 layers

	Bi directionally woven ring with nylon hub (AVCO)	Cross ply disk and wound rim (GE)	Layered wound rim with spoked hub (Garrett)
Wt (lb)	24.6	23.30	22.3
Dia (in.)	18.8	16.10	23.0
Ip (in. lb, sec^2)	3.0	1.80	4.3
Thickness (in.)	1.6	1.75	2.1

Figure 3-57: The three advanced composite flywheel designs evaluated in FY 1983.

3-62

Table 3-19: Summary of Spin Tests Performed on GE Rotors

Rotor No.	ORNL No.	Rotor type	Test type[a]	Results
D1-3M1	GE-C	Disk	U	Hub separated from rotor after arbor rubbed above design ultimate speed, recovered intact
D2-3M2	GE-D	Disk	F, U	Successfully passed 10,000-cycle test, later burst at above design ultimate speed
D5-3M5	GE-L	Disk	U	Hub tore loose from disk above design ultimate speed and burst
H3-3M17-R9	GE-H	Hybrid	U	Hub tore loose from disk at 89% of design ultimate speed, rotor recovered intact
H9-3M16-R15	GE-I	Hybrid	U	Hub tore loose from disk at 94% of design ultimate speed, rotor recovered intact
H3-3M18-R7	GE-G	Hybrid	U	Hub tore loose from disk above design ultimate speed, rotor recovered intact
H8-3M6-R14	GE-F	Hybrid	F, U	Successfully passed 10,000-cycle test, later burst at above design ultimate speed
H6-3M12-R12	GE-J	Hybrid	C, U	Burst at above design ultimate speed, apparently after separating from hub

[a] U = ultimate burst, F = cyclic fatigue, C = containment.

Figure 3-58: Garrett flywheel with a nine-ring rotor.

3-63

Table 3-20: Summary of Garrett Nine-Ring Rim's Operating Stresses

| Ring No. | Bending stress (ksi) | | | Hoop stress (ksi) | | | Fiber material |
	At rest	2500 ft/s[a]	Allowable	At rest	2500 ft/s	Allowable	
1 (outer)	21.9	3.8	36	0.3	114.3	150[b]	Kevlar-49
2	22.6	3.9	36	0.3	116.7	150	Kevlar-49
3	23.4	4.1	36	0.3	119.2	150	Kevlar-49
4	24.2	4.2	36	0.3	121.8	150	Kevlar-49
5	25.0	4.3	36	0.3	124.5	150	Kevlar-49
6	23.1	4.0	36	0.2	87.2	140[d]	Kevlar-29
7	24.2	4.2	36	0.2	90.0	140	Kevlar-29
8	25.4	4.4	36	0.2	92.8	140	Kevlar-29
9 (inner)	26.0	4.5	36	0.2	90.6	100[e]	S2-glass

[a] Maximum operational speed.

[b] Based on 40% of Du Pont Kevlar-49 manual value.

[c] Based on Du Pont Kevlar-49 manual value for 10^6-cycle fatigue (R = 0.1).

[d] Based on 94% of Kevlar-49 manual value.

[e] Based on STP497 data increased by 1.67 factor for vacuum environment.
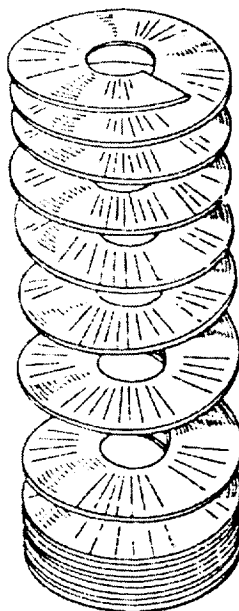
Figure 3-59: Details of the AVCO bi-directional weave.
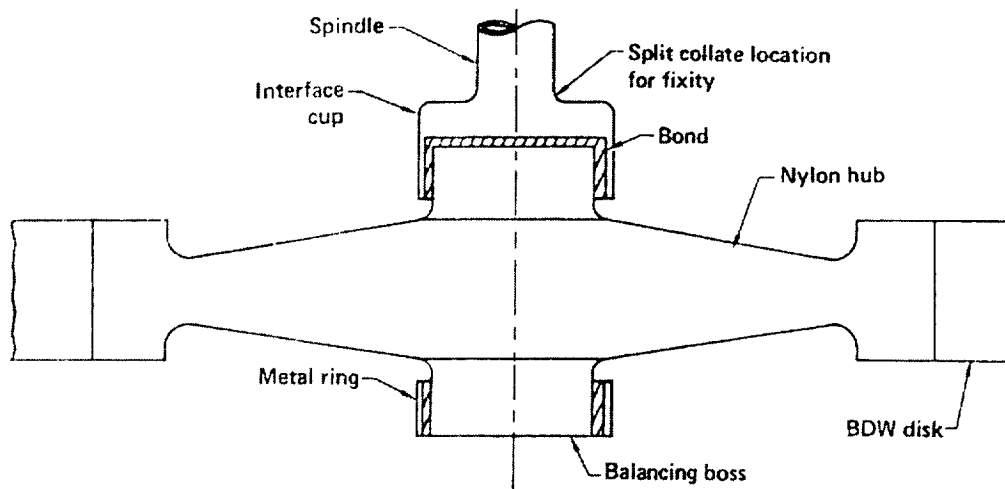
Figure 3-60: Details of hub and spindle of AVCO flywheel.
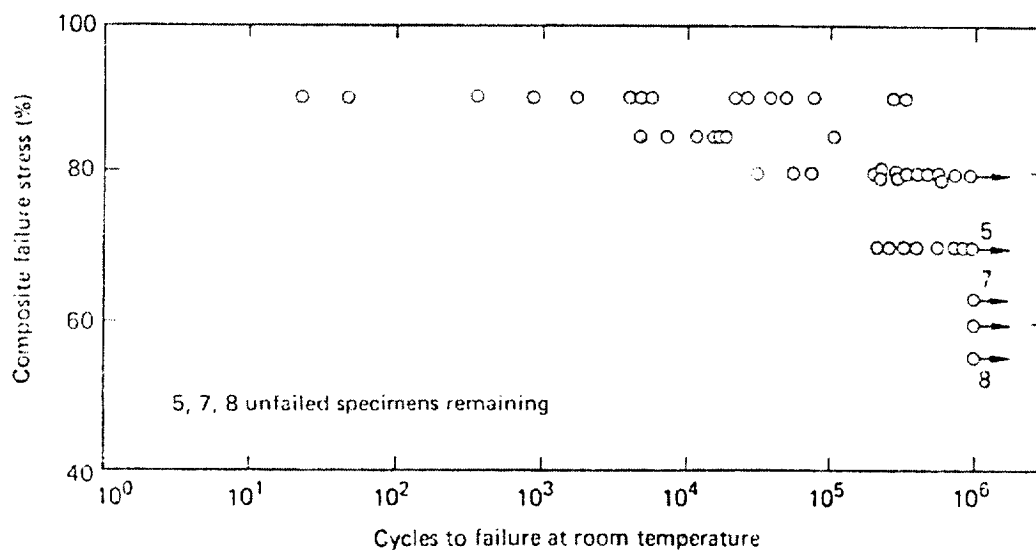
Figure 6-61: Fatigue data on a Kevlar-49/epoxy composite tested at room temperature.
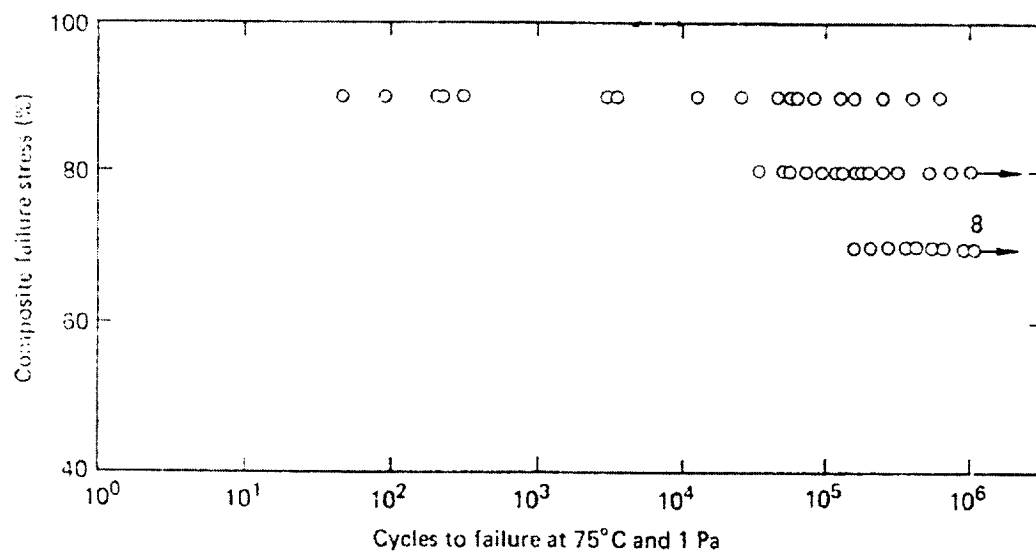
Figure 3-62: Fatigue data on a Kevlar-49/epoxy composite tested at 75° C in vacuum.
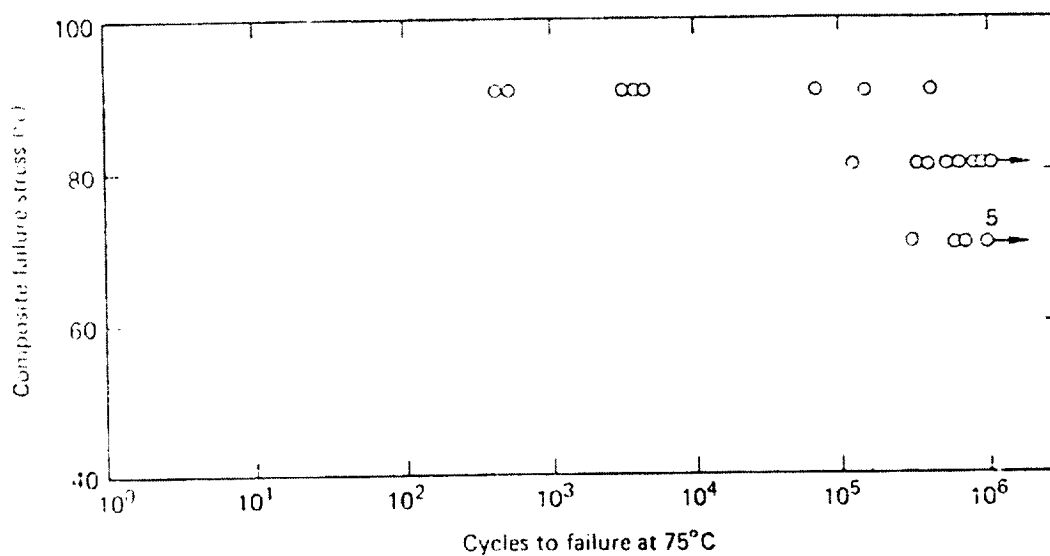
Figure 3-63: Fatigue data on a Kevlar-49/epoxy composite tested at 75° C in air.
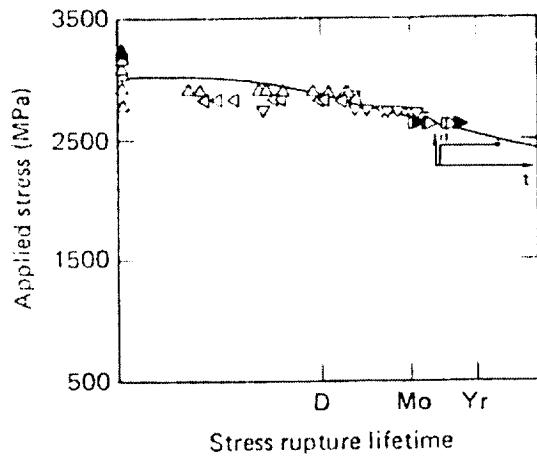
Figure 3-64: Lifetime of Kevlar-49/epoxy strands under sustained load.
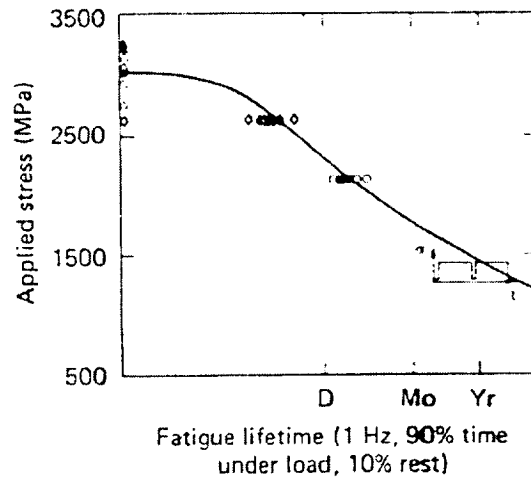
Figure 3-66: Lifetime of Kevlar-49/epoxy strands under 90/10 cyclic loading.
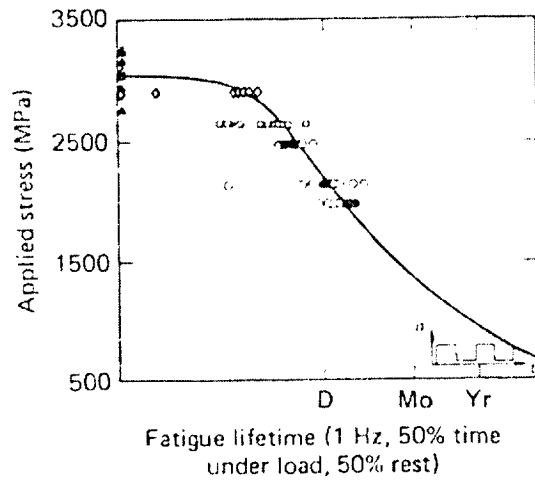
Figure 3-65: Lifetime of Kevlar-49/epoxy strands under 50/50 cyclic loading.
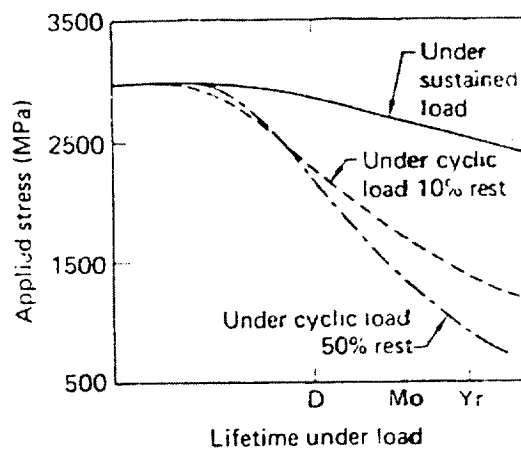
Figure 3-67: Lifetime of Kevlar-49/epoxy strands under various load conditions (summary).
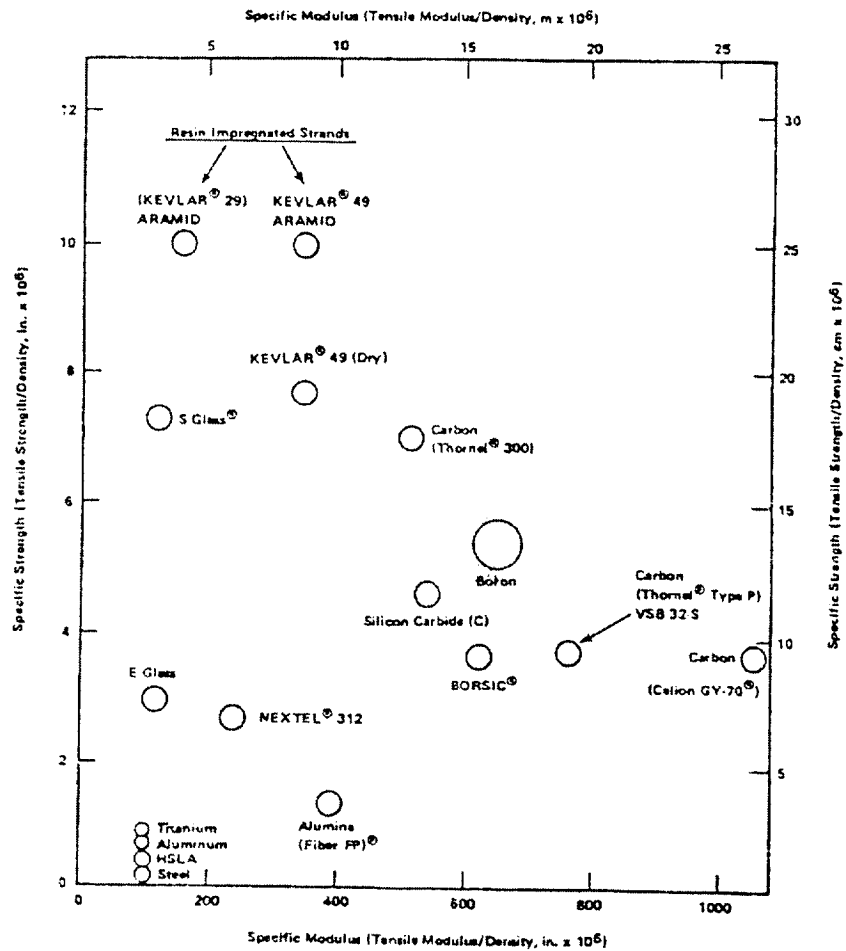
Figure 3-68: Comparison of the specific mechanical properties of selected reinforcing fibers with those of several metals (circle size indicates approximate diameter of fibers).
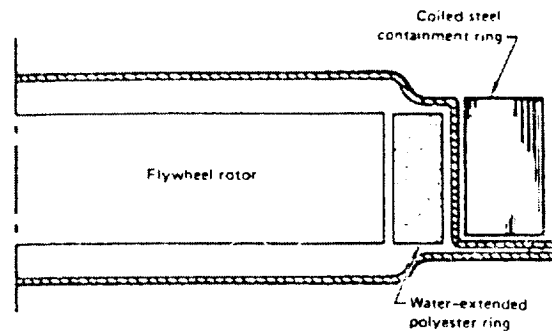
Figure 3-69: AVCO containment design.
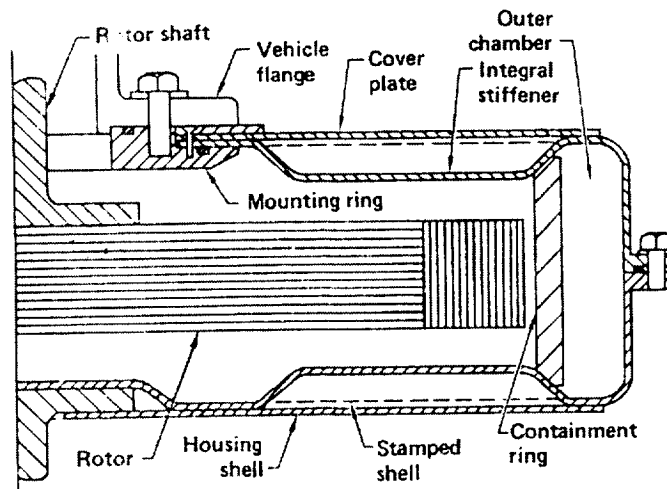
Figure 3-70: GE containment design.
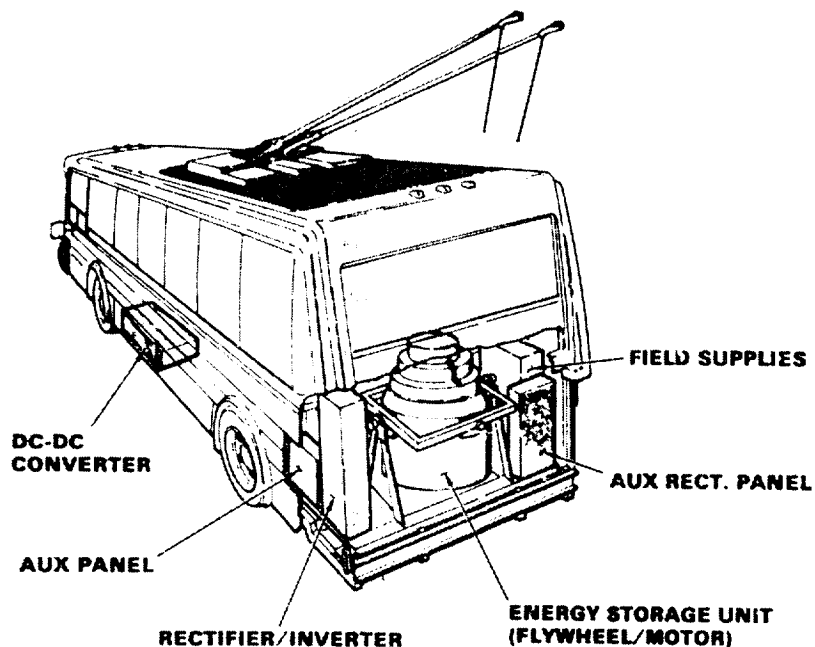
Figure 3-71: Electric-powered version of flywheel-assisted bus being developed by Garrett Corporation.

Table 3-21: Typical Flywheel Applications

Application	Attributes
Aircraft power supply	Excellent low-mass power source; minimum size and mass essential
Spacecraft power supply	Minimum size and mass, inertial stabilization
Portable power supply	For remote equipment requiring high power (e.g., for x-ray machines, welders, etc.)
Emergency power supply	Uninterrupted power (e.g., for computers, hospital equipment, etc.)
"Pulse" power supply	For anything requiring high power for short duration
Forklift, crane etc.	For lifting and energy recovery, propulsion power; no sparks, no fumes
Momentum wheel	To absorb vibratory or jerk motions of motor-driven or rotary machinery
Spacecraft stabilization	To provide positioning forces for orientation and stabilization

3-70

CATEGORY

Testing

REFERENCE

Coppa, A. P. and S. V. Kulkarni, "Composite Flywheel Rotor Containment," *Progress in Science and Engineering of Composites*, ICCM-IV, 1982.

ABSTRACT

Composite construction has been increasingly applied to the development of efficient flywheel rotors for vehicular energy storage systems. New developments in understanding and quantifying composite rotor burst containment behavior are contributing to advancing the practicality of such systems. The paper briefly discusses some of these developments, summarizes overall design requirements for containment housings, and presents a novel analysis of composite rotor containment action. The analysis considers fragmentation released from a failed composite rotor as undergoing a progressive crushing process during containment. The process is characterized by a constant parameter called the apparent fragment crushing strength, which is the ability of initially released fragmentation to resist progressive breakdown under the applied containment forces. The analysis has been successfully applied to correlating the containment test behavior of a variety of high performance composite rotors. Burst-containment weight estimates based on the analysis are also presented for several containment ring constructions. Containment considerations for a loose rotor spinning on the housing interior are also discussed.

SUMMARY

Table 3-22 lists several types of composite rotor construction and the materials used. Three types of rotor design are listed – rim, disk, and rim/disk hybrid. One of the major reasons for using flywheels as energy storage devices, is the high specific power they possess (more than 500 W/kg). As shown in Figure 3-72, they can supply sudden power demands better than conventional storage batteries. Composite flywheels, because of their high momentum-to-weight ratio, are used in many spacecraft for attitude control. Composite materials, have a higher specific strength than steel, and flywheels made from them can store two to three times as much energy per kilogram as steel flywheels. Another thing that makes composite rotors an attractive option, are the relatively benign containment processes that are associated with rotor burst compared to that of steel rotors. The flywheel housing must also handle a loose rotor condition that can occur in the even of rotor break-away from the shaft.

The basis of composite rotor containment is the assumption that failure of a composite rotor is not as catastrophic as that of a metallic rotor. Composite fragments, because of their relatively low transverse and interlaminar strengths, cannot exert high contact pressures on their housing. When pressures induced in the fragment exceed these strength limits, the matrix can be expected to break-up, thereby releasing fibers or ribbons of fibers or local delamination and crushing.

3-71

Rapid heating at the fragment/ring interface due to high pressure and high speed sliding also contributes to rapid fragment break-up. An analysis, called the crushing fragment containment analysis (CFCA) was developed to calculate the containment ring response to such a loading process. The analysis assumes that at failure the rotor releases an axially symmetric distribution of fragments which contacts the containment ring after moving through the radial clearance space that initially exists between the rotor and ring. The containment is considered adequate when the final radial growth of the ring is within allowable limits.

Figure 3-73 shows that fragments having low strength can transmit substantial deformation to the ring even when the initial radial clearance is zero. The CFCA was used to analyze the containment behavior of a variety of rotor types. The resulting values of fragment crushing strength, p_o, which are dependent on the composite material and construction and the radial impact speed are shown in Table 3-23. In the table, C is the radial clearance and V_R is the radial fragment speed at initial contact. Containment ring weights, W_c, are shown in Figure 3-74 for several ring materials plotted against the maximum radial growth. The estimates are based on p_o. The plot indicates that designs with very small growth may be obtained by employing moderately heavier rings.

The requirements for burst-containment of composite rotors can be determined by the following steps:

a) Definition of the rotor failure modes based on composite strength analysis.
b) Computation of containment ring dimensions vs. ring growth, based on rotor failure modes and given material and operational properties, using an analysis such as described in the paper.
c) Selection of a specific ring design (ring thickness, growth, material) that satisfies such constraints as integration into the overall housing design and rotor/housing system weight, volume, and cost.

**Table 3-22: Description of Flywheel Rotors
Involved in the Data Correlation**

Rotor Description	d_o in.	W_R lb.	KE_B kwh	ω_B rpm	Failure Mode	W_F lb.
Hybrid Rotor: FW Graphite/Epoxy Ring; Laminated S-2 Glass/Epoxy Disk (General Electric)	17.68	23.3	0.459	35,040	Outer ring Rupture	6.34
Disk Rotor: Laminates D-2 Glass/ Epoxy Disk (LLNL)	15.00	5.2	0.156	49,320	Complete Disk Burst	5.2
Hybrid Rotor: FW Graphite/Epoxy Outer Ring; Molded Chopped Glass/ SMC Disk (Owens Corning)	24.00	28.5	0.414	21,620	Complete Burst of Rim and Disk	28.5
Wound-Rim Rotor: FW Kevlar 49/ Epoxy, Glass/Epoxy (Brobeck)	13.76	24.5	0.608	48,120	Rupture of 70% of Kevlar 49/Epoxy Rim	6.76
Disk Rotor: Varying Thickness, Laminated Graphite/Epoxy	24.00	11.8	0.306	34,940	Complete Disk Burst	11.8

d_o, OD, W_R, rotor weight; KE_B, energy at burst, ω_B, burst speed, W_F, total fragment weight.

Table 3-23: Values of p_0, Fragment Crushing Strength as Obtained from Data Analysis of APL Flywheel Rotor Burst Tests

Material	Form	Impact Direction	P_0 (psi)	C (in.)	V_R (in/sec)
Graphite/ Epoxy	Filament Wound Ring	Transverse	20,000	4.62	22,900
	Laminate	Longitudinal	45,000	1.50	15,790
S-2 Glass/ Epoxy	Laminate	Longitudinal	0	1.50	16,470
Kevlar 49/ Epoxy	Filament Wound Ring	Transverse	0	2.12	21,540
Chopped Glass/ SMC	Molding	Longitudinal	5,000	1.50	9,880
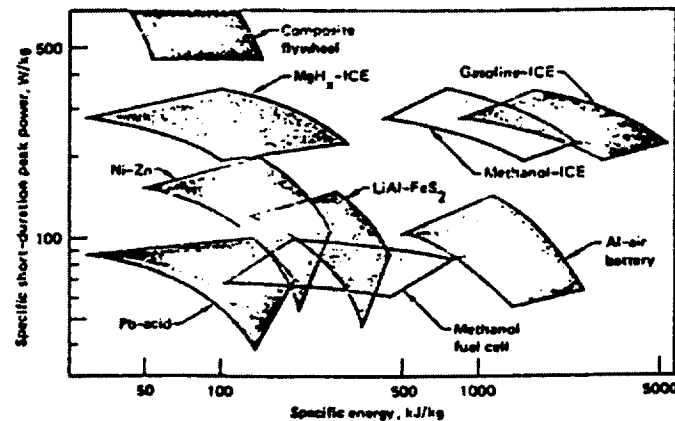
Figure 3-72: Performance comparison of various energy storage systems.
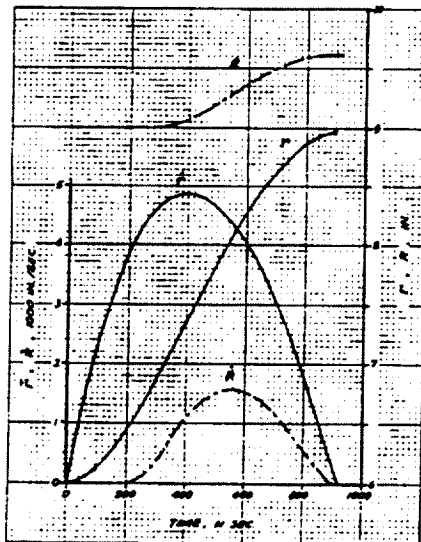
Figure 3-73: Calculated fragment and containment ring motions vs. time for complete burst of a 0.25 kwh laminated S-Glass/Epoxy disk rotor; p_0 = 6000 psi; radial clearance, C = 0; 4130 Steel ring (σ = 158 ksi).
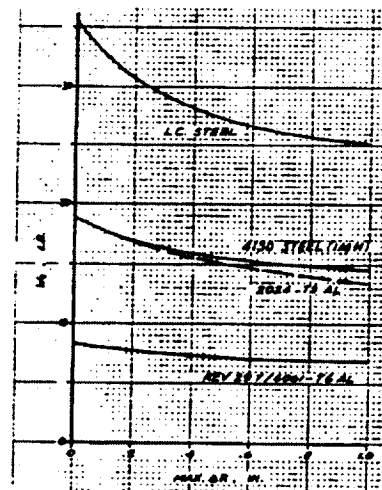
Figure 3-74: Containment design curves: W_C vs. ΔR_{max} for complete burst of an 18 in. OD, 0.25 kwh laminated S-Glass/Epoxy disk rotor for several containment ring materials.

3-73

CATEGORY

Testing

REFERENCE

Genta, G., "Spin Tests on Medium Energy Density Flywheels," *Composites*, Vol. 13, No. 1:38-46, January 1982.

ABSTRACT

Results of spin tests performed during theoretical and experimental research aimed at developing advanced flywheels, are reported. The main objective of the work was to develop some prototypes of low cost advanced flywheels which could operate safely in the medium-energy density range. Composite material rotors, both disc and rim shaped, and quasi-circular ones were tested. The results obtained with bare steel wire quasi-circular flywheels allowed design of prototypes with 2 and 5 kWh operating energy capacities which are now being evaluated.

SUMMARY

The main focus of the project was on evaluating the possibility of building low-cost rims without aiming for a very high energy density. During the spin test program, no deep study of laminate discs as kinetic energy accumulators was undertaken. High cost fibers such as carbon or Kevlar were not seriously considered and E-glass was chiefly used as the reinforcement. One of the rotor designs tested was two constant thickness pierced discs built using fiberglass/epoxy laminates. Two types of rotors made from wood were also tested. Since this design is not applicable to space applications, these results will not be summarized.

Spin tests play an important role in the development of advanced flywheels. A burst spin test gives valuable information about the speed range in which the flywheel maintains its structural integrity and the way failure takes place. This information is valuable for verifying the stress analysis and design choices and giving some input data for the design of the containment structure. However, no data on fatigue or creep behavior can be obtained in this way and the practice of accelerating the rotor with a stepped velocity/time law which is sometimes prescribed cannot be of advantage.

Flywheel failures can be due to several reasons, such as:

- overspeed;
- decay of material properties due to overheating or other reasons and;
- fatigue or creep.

Overspeed is not always the most dangerous situation, although it is the failure mode with the greatest energy.

The paper gives the results from 73 spin tests conducted on 56 flywheels. A schematic of one of the spin test setups is shown in Figure 3-75. The flywheels can be divided into four groups:

a) constant thickness discs built in laminate;
b) variable thickness discs built in laminate;
c) composite material rim flywheels;
d) quasi-circular flywheels.

Table 3-24 lists the results of 16 tests performed on laminated discs. In the table ω_{max} is the maximum angular velocity of the rotor, V is burst peripheral velocity, e is the stored energy at angular velocity (nominal), and e/m is the energy density produced. Tables 3-25 and 3-26 give some of the characteristics of the rotors tested. The aims of the discs of this type were:

- To test the operation of the facility and to establish the test procedures.
- To evaluate the possibility of measuring the aerodynamic drag torque acting on the flywheel through spindown tests. Flywheels 1-7, 1-8, 2-3, and 2-4 were built for this purpose and, after the successful completion of the "aerodynamic" tests, were also spin tested.
- To assess the possibility of using low cost laminates to build the hubs for rim flywheels.

Failure of the laminate rotors was benign, giving way to a great number of very thin laminae, each one extending for a great part of the circumference or even more than 360°. The kinetic energy of the fragments is almost all rotational, see Figure 3-76. During the spin tests, in four cases the test was interrupted because of strong vibrations due to asymmetrical displacements following local delaminations. These were attributed to manufacturing flaws.

Burst containment was not one of the main objectives of the tests, but some observations were recorded:

a) After admission of air into the test chamber following a test on the elastometric rotor, some burning was initiated by high temperature spots.
It was very difficult to prevent the containment structure from rotating under the impact loads when failure occurred.
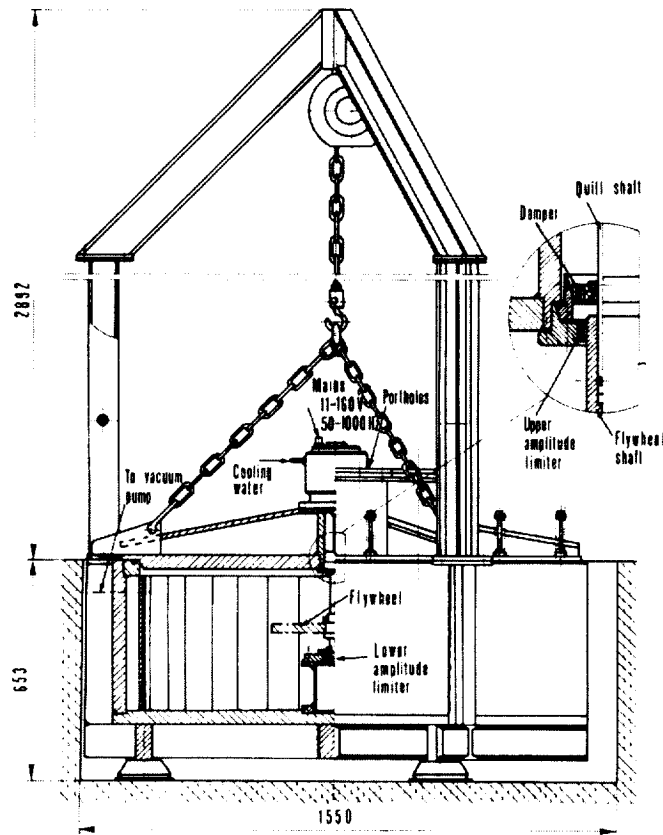
Figure 3-75: Spin test facility at the Instituto della Motorizzazione – Politecnico di Torino (Dimensions in mm).

Table 3-24: Results of Spin Tests on Laminate Discs

Disc number	Test number	ω_{max} (rpm)	V (m s^{-1})	e (Wh)	e/m (Wh/kg)
1-1	1	26 000	408	11.78	11.77
1-2	2 3 4	27 000	424	12.30	12.72
1-3	26	12 360	162	3.03	1.85
1-4	28	12 807	168	3.25	1.99
1-5	25 29 34	24 400	319	11.80	7.22
1-6	27	26 100	342	13.51	8.26
1-7	43	17 760	421	7.91	12.30
1-8	48	15 800	410	7.07	11.67
2-1	47	14 138	296	12.82	3.40
2-2	52	25 400	400	12.23	8.13
2-3	58	14 300	299	11.98	3.37
2-4	59	18 081	377	21.75	5.74

Table 3-25: Characteristics of Laminated Disc Rotors

Material	Disc number	m (kg)	d_e (mm)	d_i (mm)	t (mm)
Constant thickness laminate discs					
Fibreglass (Vetrotessile X1 glass cloth) Epoxy (Araldite LY 560 - HY 560) (57.1 weight % fibre)	1-1	1.001	300	38	10
	1-2	0.975	300	38	10
Unidirectional beech wood laminate (Rexilon 16)	1-3	1.635	250	35	25
	1-4	1.635	250	35	25
[0/90°] beech wood laminate (Rexilon 18TS)	1-5	1.635	250	35	25
	1-6	1.635	250	35	25
[0/90°] birch plywood (3 layers/mm)	1-7	0.643	510	–	5
	1-8	0.606	495	–	5
Variable thickness laminate discs					t_{max}
[0/±45°/90°] quasi isotropic beech wood laminate (Rexilon 20 M) Constant stress disc	2-1	3.769	400	–	50
	2-3	3.554	400	–	60
	2-4	3.792	400	–	60
Hyperbolic	2-2	1.505	301	51	46

Note:

m = mass d_i = inner diameter

d_e = outer diameter t = thickness
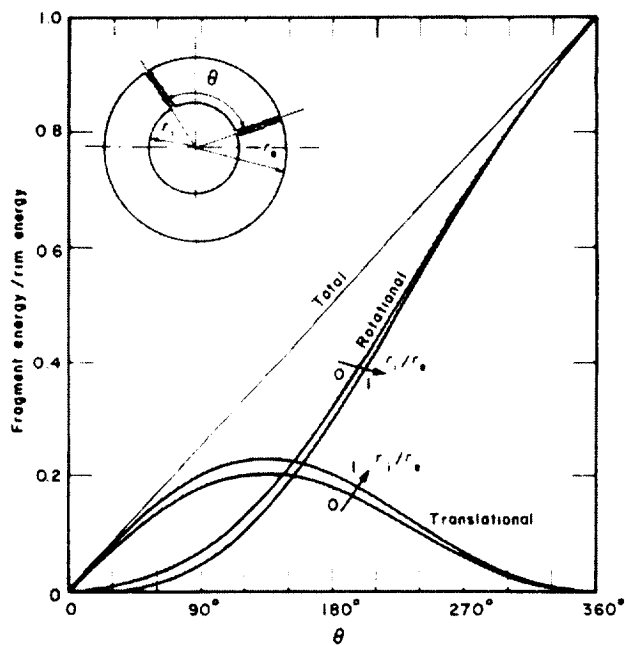
Figure 3-76: Rotational, translational and total energy of a rim fragment as a function of angle θ.

Table 3-26: Characteristics of Composite Material Filament Wound Flywheels

Material	Rotor number	m (kg)	d_e (mm)	d_i (mm)	t_r (mm)
Composite material rim flywheels					
Rim: Fibreglass/epoxy	3-1	4.46	400	—	30
Hub: Polyamidic resin (Ertalon 6)	3-2	4.512	400	—	30
constant stress disc	3-3	4.827	400	—	30
	3-4	4.309	403	—	30
	3-5	4.381	398	—	30
	3-6	4.29	398	—	30
Rim: Fibreglass/epoxy					
Hub: [0/±45°/90°] beech wood	3-7	4.68	403	51	30
laminate (Rexilon 20 M)	3-8	4.254	400	51	30
Hyperbolic profile disc	3-9	4.598	400	51	30
Rayon (SA 1843) with elastomeric matrix wound with variable angle and fibre content	3-10-P	4.65	246.7	102	98
Kevlar T950 with elastomeric	3-11-P	10.595	367.6	30	87
matrix, wound as 3-10-P	3-12-P	6.80	300	29.8	86
Composite material multi-rim flywheels					
Hub: Rexilon 20 conical disc with central hole Inner-rim: Kevlar/epoxy Outer rim: Carbon/epoxy	3-13-N	5.935	500	51	25
Hub: Polyamidic (Ertalon 6) constant stress disc Inner rim: Fibreglass/epoxy Outer rim: Kevlar/epoxy	3-14-C	5.22	500	—	23
Hub: as 3-13-N, inner rim: as 3-14-C, outer rim: as 3-13-N	3-15-N	5.84	470	51	25
Hub: as 3-13-N, inner rim: as 3-14-C,	3-16-N	6.95	500	51	25
outer rim: as 3-14-C	3-17-N	6.09	501	51	25
Hub: as 3-13-N, inner rim: as 3-13-N, outer rim: as 3-13-N	3-18-N	5.85	470	51	25
Hub: as 3-14-C but with bolt holes, inner rim: as 3-14-C, outer rim: as 3-14-C	3-19-C	7.025	510	—	25
Hub: as 3-19-C, inner rim: as 3-14-C, outer rim: as 3-13-N	3-20-C	5.145	480	—	24

CATEGORY

Testing

REFERENCE

Sapowith, A. D., Handy, W. E., *A Composite-Flywheel Burst-Containment Study*, Report No. AVSD-0350-81-RR, 1982.

ABSTRACT

This report has been prepared under Subcontract No. 1121401 for Lawrence Livermore National Laboratories. Work accomplished herein is part of the Flywheel Rotor and Containment Technology tasks of the Mechanical Energy Storage Project. It covers work performed from September 1980 to August 1981. It continues the work performed on the state-of-the-art burst containment under Subcontract No. 6692009. It evaluates the likely failure modes of disk and rim-type flywheels and establishes design criteria for containment of these composite flywheels. In addition to design criteria, containment designs are described and sized and containment weight estimates are made.

SUMMARY

The failure mode investigated in this report is that of slow growth "benign" disk failure. If the flywheel were to grow radially to interfere with the containment ring, then a frictional torque would be applied to the rim of the flywheel, stopping it quickly. The flywheel energy would be contained torsionally with little or no radial component of kinetic energy, resulting in a very lightweight containment design. A flywheel rotor was instrumented and spun to failure to test this hypothesis. The progressive failure occurred over a 0.2 second period. The strain gages functioned as failure wires, providing a sequence of pulses over the flywheel. A plot of the time of these pulses versus gage location and, more particularly, the distance of these gage locations from an assumed failure location on the ID is shown in Figure 3-77. The flywheel speed is superimposed on the plot. It shows that the slowdown covers the same 0.2 second period as the failure wire data.

The slowdown can be explained by a conservation of momentum of a change in moment of inertia of the flywheel. Figure 3-78 shows this type of change as a radius change versus time and in Figure 3-79 as a radial growth velocity versus time. During the initial slow growth period, the radial velocity is in terms of only inches per second.

One thing to consider from this mode of containment is that while stopping a flywheel by this method may seem mechanically easy, an amount of energy as small as 1 kWh equals 3400 Btu of heat. That amount of heat must be dissipated somehow. Coating the inside of the vacuum housing with traditional brake shoe material is one consideration. However, the heat caused by friction would cause ablation or charring of the epoxy and the phenolic. The ablation, in turn would result in the generation of a large amount of heated, toxic gas in the vacuum housing. Venting the housing to reduce the pressure could cause self-ignition of the gas at these

temperatures when mixed with air. A brake shoe material that provides cooling and dilution of the gases produced is recommended.
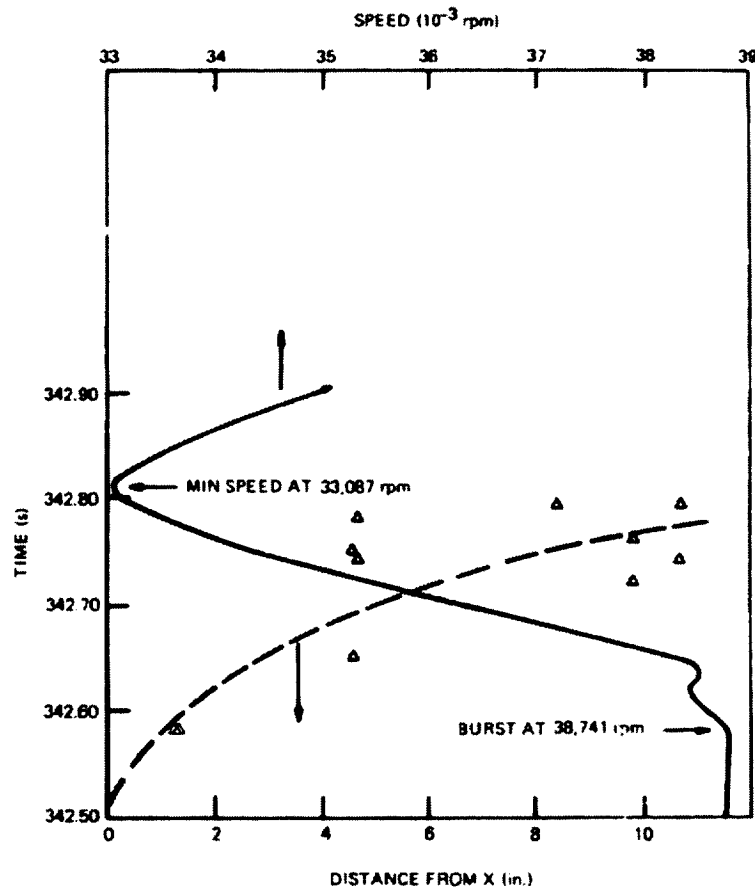
Figure 3-77: Distance/time path from suggested failure point (X on ID at 90°).
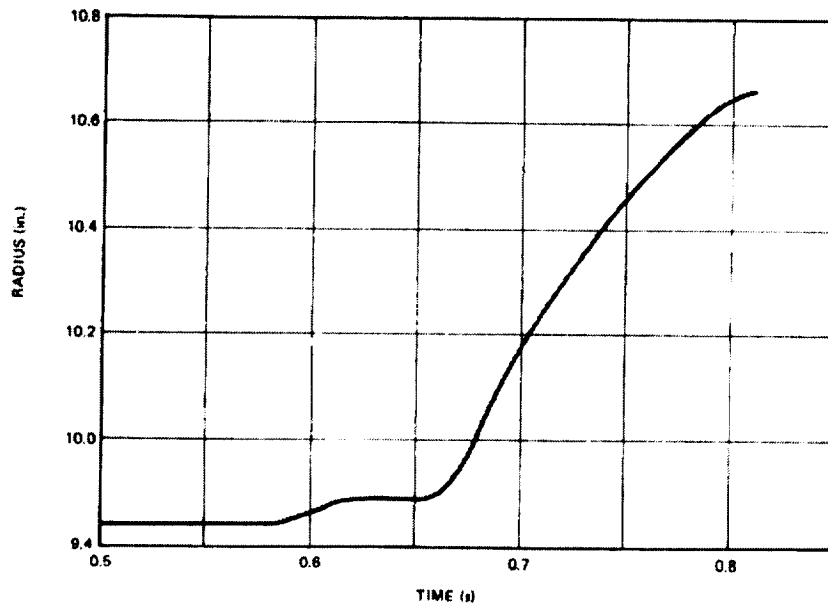
Figure 3-78: Outside radius versus time (conservation of momentum uniform strain).
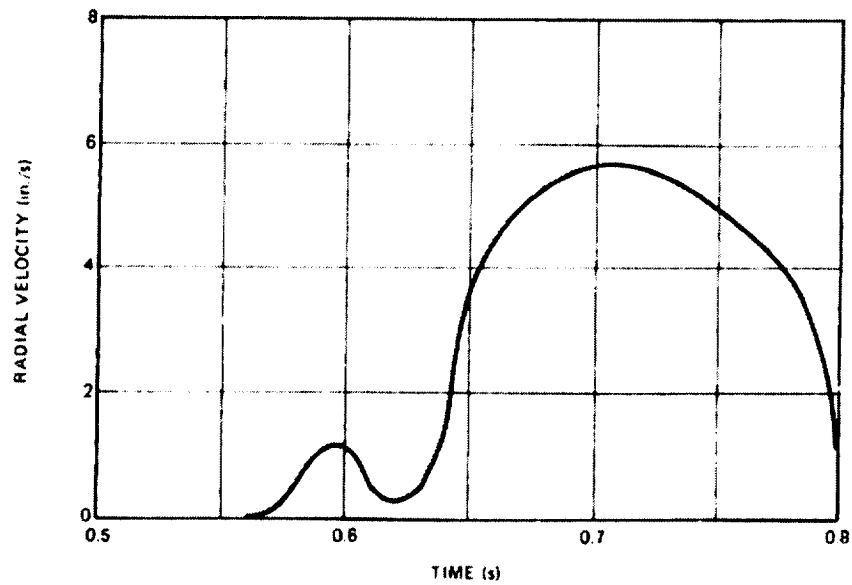
Figure 3-79: Radial velocity of rim versus time.

CATEGORY

Testing

REFERENCE

Reedy, E. D. Jr. and H. K. Street, "Composite-rim Flywheels: Spin Tests," *SAMPE Quarterly*, Vol. 10:36-41, April 1979.

ABSTRACT

Two composite-rim flywheels of a size appropriate for use in a hybrid vehicle were designed. Each design employed a different method of utilizing Kevlar 49/epoxy bands to attach the rim to an aluminum hub. Four prototype flywheels, two of each design, have been fabricated and spin tested.

SUMMARY

Though these flywheel rotor designs are not suitable for aerospace applications, the spin test method should be reviewed.

The flywheels were designed for energy storage of up to 0.56 kWh at their maximum operating speed. The rotor total weight was required to be less than 25 lb for use in a hybrid vehicle. The rim cross-section is semi-elliptical with its flat edge facing the hub. Kevlar 49/epoxy was chosen for the band material since rotating bands of this material tend to match the rim displacement. In addition, its low density and high strength allows the bands to operate at a high tip speed. Two rotors were produced incorporating a pin-wrapped hub connection, as shown in Figure 3-80. Two rotors were also produced which utilize six over-wrapped bands to connect rim and hub as shown in Figure 3-81.

Spin tests were conducted to assess the rotor's energy storage capacity, dynamic behavior, and failure mode. The two rotors with the Pin-Wrapped hub design achieved higher rotational speeds (29,000 to 30,100 rpm) than those rotors with the Wagon Wheel hub design (17,900 and 22,000 rpm). The graphite/epoxy rims of the Wagon Wheel rotors, however, had pre-existing flaws which would have lowered their maximum speed.

Some tests were terminated due to excessive shaft runout. This runout could have been induced by (1) an increasing rotor imbalance due to either a structural failure or a migration of the balancing weights, (2) a gyroscopic forcing moment introduced by a pre-existing rim tile, (3) approaching a critical speed, or perhaps (4) a combination of the above.
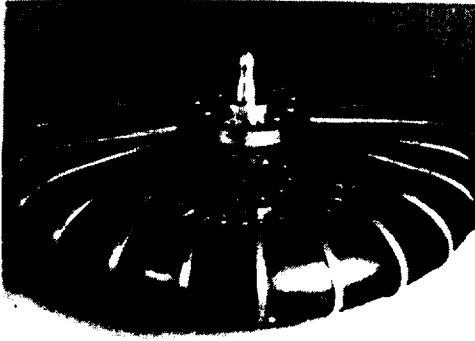
Figure 3-80: Pin-wrapped flywheel.
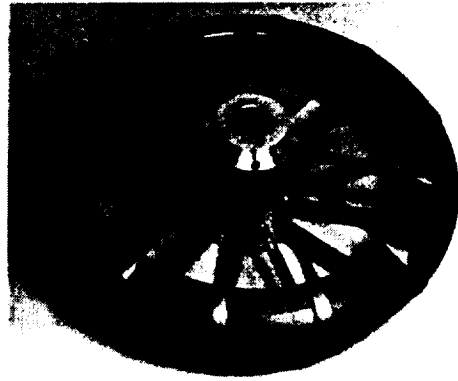
Figure 3-81: Wagon wheel flywheel.

CATEGORY

Testing

REFERENCE

Parmley, P. A, et al., "On the Accelerated Testing of Graphite/Epoxy Coupons," Report No. ADD116568, *Proceedings of the 1978 International Conference on Composite Materials (ICCM/2)*, pg. 1604-1619, 1978.

ABSTRACT

Aircraft structures should be designed to be damage tolerant and durable. In order to meet these goals for advanced composite structures, it is essential to determine the damage growth rate and related residual strengths for structures undergoing a service environment (i.e., spectrum loading, temperature, humidity, chemical degradation). Realistic testing of the coupled behavior of the components of the environment is impractical since the test duration would be the lifetime of the aircraft. In addition, the random nature of the environment precludes attainment of any degree of certainty unless an "expected worst" case is used.

In order to assure structural serviceability, integrity, and durability, it is therefore necessary to develop a rational accelerated testing procedure for graphite/epoxy. One of the objectives of this paper is to present such a rational and to discuss qualitatively its limitations.

SUMMARY

The main emphasis was given to how the real time environmental matrix of load, temperature, and moisture was reduced and compressed in order to permit an accelerated one life simulation test to be conducted in 24 hours. An attempt was made to bound the problem by developing a realistic but yet an "expected worst case" set of test conditions.

The main objective was to design an accelerated test program and procedure that would induce flaw damage growth in the coupon closely representative of that incurred by a real structure under a real time "expected worst case" environment so that residual strength values can be obtained. A second objective was the evaluation of two selected NDE techniques (pulse-echo ultrasonics and acoustic emission) on their capability of monitoring flaw growth, and to characterize the flaw in size, shape, and volumetric location.

The two laminates selected were a quasi-isotropic (0/±45/90) and a (0$_2$/+45) fiber orientation. The absorbed moisture level and through-the-thickness distribution to be used results from many years of aircraft operation at a severe state-side basing and then one year of basing on a South Pacific Island demonstrated to be the worst, worst-case. All wet coupons were preconditioned to this worst case before testing. The loading environment utilizes a vertical tail (VT) spectrum that sees fully reversed load and, hence, a stress ratio (R) of −1.0. The maximum load applied is the limit design load, where limit load is 2/3 of ultimate allowable.

Three types of coupons, shown in Figure 3-82, were selected to represent tension, compression, and bolted structures. The test matrix shown in Table 3-27 begins with a screening of four flaw types at one flaw size followed by further screening of the two most critical flaws at a second flaw size. Based on these results, an in-depth evaluation of the critical flaw type was made. Combinations of room temperature (RT) and elevated test temperature (Hot) with dry and wet moisture conditioned coupons are to be made, with the greatest emphasis being placed on elevated temperature wet. Some -65° F residual strength tests are also planned in order to gain some insight into the effect that very low temperatures have on degradation. In addition, a more realistic stacking sequence specimen and a scaled specimen with increased width was tested.

A typical random spectrum of the load and temperature history for the VT of a supersonic aircraft is shown in Figure 3-83. It was derived from a metal VT spectrum. The load is presented as a load factor (L.F.) in terms of a ratio to limit load (or stress). To create the worst case, which would encompass fighters, bombers, and transports, the maximum load to be expected in a lifetime was raised to full limit load for these composite tests. All the other loads in the load spectrum were raised proportionally.

The accelerated load and temperature spectrum finally adopted for a simulated one life is shown in Figure 3-84. In this spectrum approximately 500,000 total load cycles are compressed into 127,500 cycles and nearly 4000 low-high-low temperature excursions are compressed into six cycles per lifetime. In order to put the coupons through the proper number of heat-up and cool-down excursions alone, 90 hours would be required per lifetime test. In order to reduce this time, two compromises were made: (1) rearranging the temperature sequences in a mission, and (2) revising the 1% of the time temperature events to include the 9% temperature events, wherein the temperatures are adjusted to compensate. The first compromise was made by reordering the mission temperature histories into monotonically increasing sequence from low to high to low as shown in Figure 3-85.

For the multi-life tests, the sequence of segments are as shown in Figure 3-86. The –65 to 270° F cycle is only repeated at the beginning of the third lifetime. Residual strength tests for the various test series are made at the end of one, two and four lifetimes as shown by the symbol ↑. At the times shown by the symbol |, an ultrasonic NDE is made to track the flaw growth. To complete the description of the test condition, the coupons are preconditioned at 165° F and 98% relative humidity to an average 1.29% moisture content. During multi-lifetime tests, whenever the moisture levels fall below 80% of the initial value, the coupons are reconditioned.

Figure 3-87 summarizes the compromises made in developing the accelerated environmental test condition. Figure 3-88 shows the more significant of the flaws defined by an industry survey, classified by the manufacturing sequence in which they occur. Because of the limited size of the coupon test specimen, concern was raised for the amount of influence the tabs and edges would have on the state-of-stress in the area of the flaw. Moiré fringes were produced on two of the flawed tension coupons at a stress level approaching ultimate. It was determined from these fringes that the influence of the tab is considered negligible at the area of the flaw.

For future work, the author outlines the following technical aspects that require clarification: (1) further expanding the time at temperature to elucidate any creep effects on flaw growth; (2) investigation of the coupling of the freeze-thaw-hot cycle induced damage with flaw growth; and (3) improved definition of the minimum size flaws that could grow to catastrophic proportions within a specified number of lifetimes and require NDE detection.
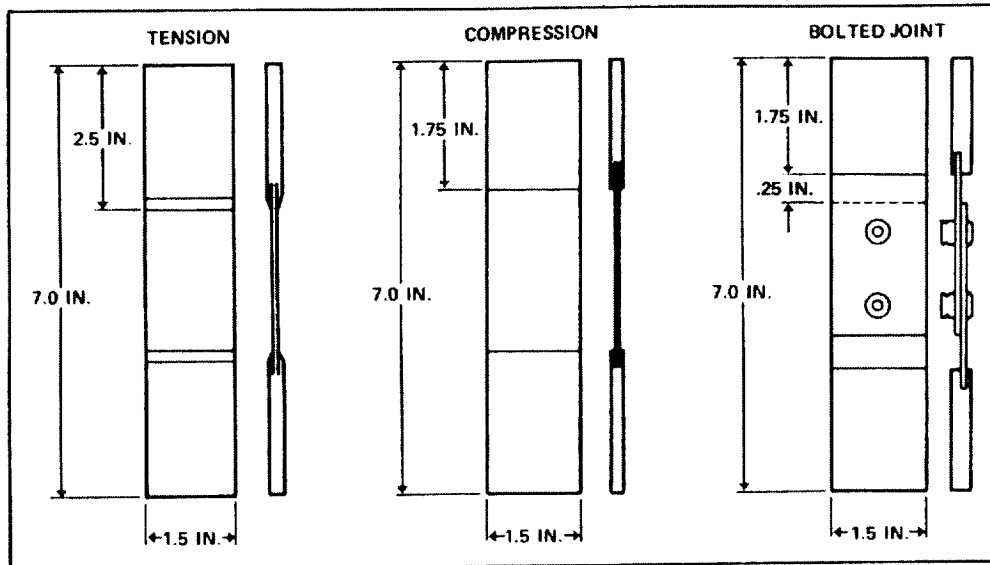
Figure 3-82: Coupon configurations.

Table 3-27: Coupon Test Matrix

TEST SERIES	MATERIAL	LAMINATE	FLAW TYPE	FLAW SIZE	TEST CONDITION			LIFE TIMES				TOTAL SPECIMENS	NOTES
					MOISTURE	FATIGUE TEMP	RESIDUAL TEMP	0	1	2	4[1]		
T_1/C_1	A	1,2	0,1,2,3,4	A	DRY	RT	RT	3		3[2]		60 + 60	
T_2/C_2		1,2	0,1,2,3,4	A	WET	REAL	HOT	3		3[2]		60 + 60	
T_3/C_3		1,2	C_1 & C_2	B	DRY	RT	RT	3		3		24 + 24	
T_4/C_4		1,2	C_1 & C_2	B	WET	REAL	HOT	3		3		24 + 24	
T_5/C_5		1	0		DRY		65	3				3 + 3	
			C_1 & C_2	C	DRY	REAL	65	3		3		12 + 12	
T_6/C_6			0		WET		65	3				3 + 3	
			C_1 & C_2	C	WET	REAL	65	3		3		12 + 12	
T_7/C_7			CRITICAL	A	DRY	RT	RT	2			5	7 + 7	
				B				2			5	7 + 7	
				C				5	5	5		15 + 15	
T_8/C_8				CRITICAL	DRY	REAL	NOT	3		5		8 + 8	
T_9/C_9				CRITICAL	WET		RT	3				3 + 3	
T_{10}/C_{10}				A	WET	REAL	HOT	2		2	5	9 + 9	
				B				2	5	2	5	14 + 14	
				C				5	10	10		25 + 25	
T_{11}/C_{11}	B	1	CRITICAL	CRITICAL	WET	REAL	HOT	5		5		10 + 10	
T_{12}/C_{12}	A	1	CRITICAL	CRITICAL	WET	REAL	HOT	3	3	5		11 + 11	2ND STACKING SEQUENCE
$T_{13}*/C_{13}*$	A	1	CRITICAL	CRITICAL	WET	REAL	HOT	3		3		6 + 6	INCREASE WIDTH TO 6 INCHES
T_{14}/C_{14}	A	1	0	0	WET	RT	RT	3		3		6 + 6	CONTROL FOR ELEMENT TESTS
T_{15}/C_{15}	A	1	0	0	DRY		HOT	3				3 + 3	CONTROL FOR ELEMENT TESTS
B_1	A	1	0,1,2,3	A	DRY	RT	RT	3		3[2]		24	
B_2		1	0,1,2,3	A	WET	REAL	HOT	3		3[2]		24	
B_3		1	C_1 & C_2	B	DRY	RT	RT	3		3		12	
B_4		1	C_1 & C_2	B	WET	REAL	HOT	3		3		12	
B_5			CRITICAL	A	DRY	RT	RT	2			5	7	
				B				2			6	7	
				C				5	5	5		13	
B_6				CRITICAL	DRY	REAL	HOT	3		5	5	8	
B_7				CRITICAL	WET		RT	3				3	
B_8		1	CRITICAL	A	WET	REAL	HOT	2		2	5	9	
				B				2	5	2	6	14	
				C				5	10	10		25	
B_{10}		1	CRITICAL	CRITICAL	WET	REAL	HOT	3	3	5		11	2ND STACKING SEQUENCE
$B_{11}*$		1	CRITICAL	CRITICAL	WET	REAL	HOT	3		3		6	INCREASE THICKNESS
B_{12}		1	0	0	WET	RT	RT	3		3		6	CONTROL FOR ELEMENT TESTS

*TEST CONDUCTED BY ROCKWELL

[1] OR UNTIL CRITICAL DAMAGE SIZE IS REACHED

[2] OR UNTIL DAMAGE GROWTH IS DISCERNIBLE BUT NOT GREATER THAN 4 LIFE TIMES

MATERIAL

A = AS3501 5A GRAPHITE EPOXY

B = T300/5208 GRAPHITE EPOXY

C_1 AND C_2 ARE THE TWO MOST CRITICAL FLAWS FROM SCREENING TESTS

ORIENTATION

$1 = [[0/\pm45/90]_s]_2$

$2 = [[0/\pm45/0]_s]_2$

3-87

LOAD FACTORS

ARCTIC RUNWAY STORAGE
ARCTIC BASE TAKEOFF

.203 LF
.510

-80°F,   1% OF THE TIME
-65°F,   1% OF THE TIME
0 TO 100°F,   99% OF THE TIME

SUBSONIC CRUISE

.351
.194
.090
.382, 0.1 TIMES

10°F,   90% OF THE TIME
80°F,   90% OF THE TIME
-20°F,   1% OF THE TIME

SUPERSONIC CRUISE

.377 0.01 TIMES
.295, 0.1 TIMES
.218
.166
.166

270°F,   10% OF THE TIME
235°F,   90% OF THE TIME

SUBSONIC REFUELING

.351

10°F,   90% OF THE TIME
50°F,   10% OF THE TIME

LOW LEVEL PENETRATION
TERRAIN FOLLOWING

.748 LF
.612
.612
.612
.612

130°F,   90% OF THE TIME
175°F,   10% OF THE TIME

.449
.299
.720, 0.1 TIMES
.578
1.000 0.01 TIMES
.650
.347

DASH-OUT ESCAPE
TERRAIN FOLLOWING

.930 0.01 TIMES
.715, 0.1 TIMES
.538
.417
.298
.315
.285
.676 0.01 TIMES
.534 0.1 TIMES
.415
.296

110°F,   90% OF THE TIME
190°F,   10% OF THE TIME

SUBSONIC CRUISE

.351

10°F,   90% OF THE TIME
60°F,   9% OF THE TIME
-20°F,   1% OF THE TIME

PRE-LANDING LOITER
(ARCTIC BASE VICINITY)

.230 0.10 TIMES
.203
.182
.673, 0.01 TIMES
.771, 0.1 TIMES
.510
.392
.295

-45°F,   1% OF THE TIME
0°F,   9% OF THE TIME
25°F,   90% OF THE TIME

FLY-AROUND AND
LANDING

.203
.510
.350
.203
.510
.203 0.1 TIMES
.510, 0.1 TIMES
.350 0.1 TIMES
.703 0.1 TIMES
.510, 0.1 TIMES

-45°F,   1% OF THE TIME
0 TO 100°F,   99% OF THE TIME

UNIFORM DISTRIBUTION
PROBABILITY   50% OF THE TIME
TIME AT 30°F   49% OF THE TIME
TIME AT 70°F
1200 MISSIONS/LIFE

NOTE: TOTAL LOAD CYCLES PER LIFE TIME = 500,000   FIGURE 5   SKIN TENSILE STRESS HISTORY

Note: Total load cycles per lifetime = 500,000

Figure 3-83: Skin tensile stress history.
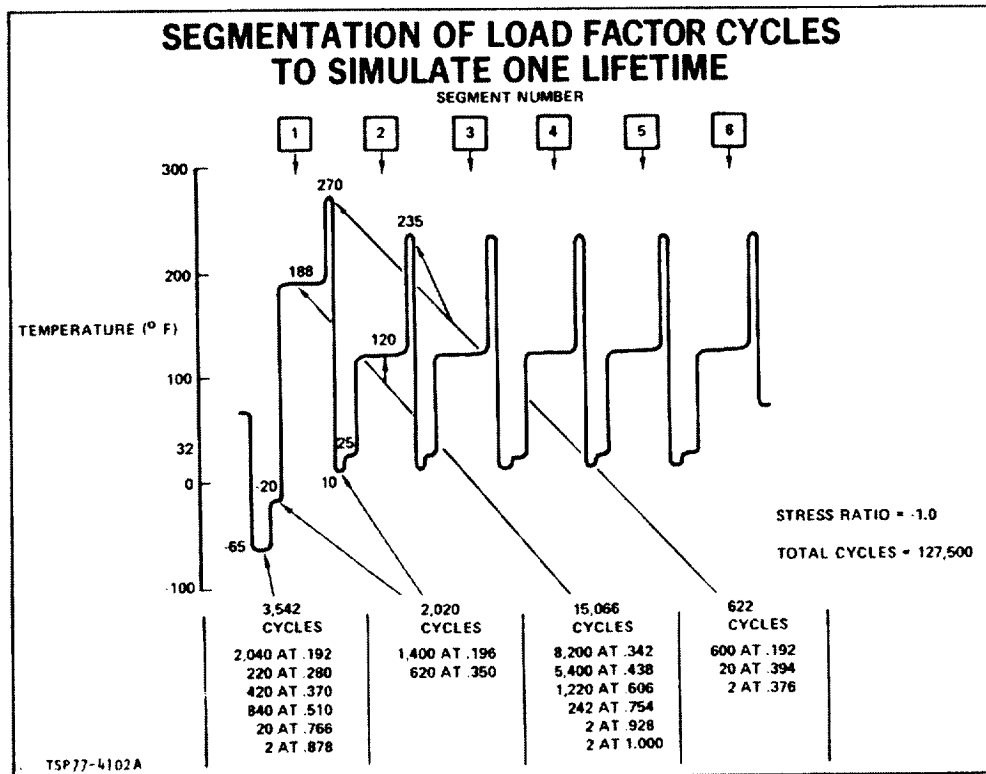
Figure 3-84: Segmentation of load/temperature cycles.
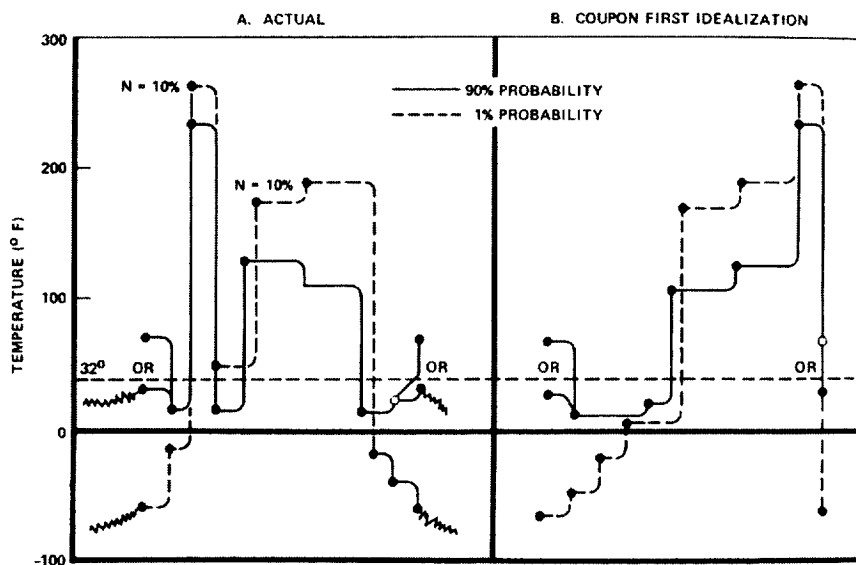
Figure 3-85: Temperature histories expected in a mission and first rearrangement.
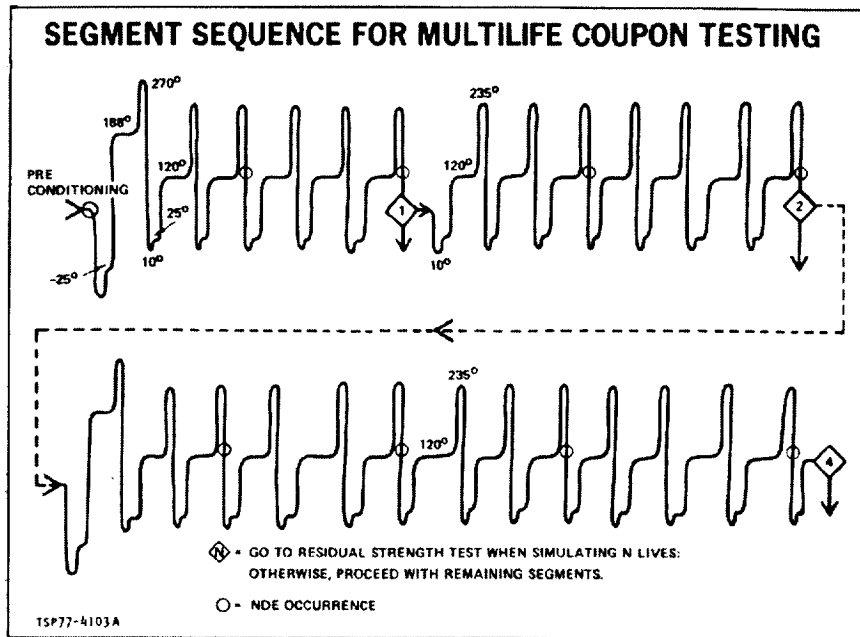
Figure 3-86: Multi-life coupon testing.

COMPROMISES

- 500,000 CYCLES ——► 127,500 CYCLES

    EFFECT: CLIPPING OF LOWER STRESS EXCURSIONS

- MONOTONICALLY ARRANGE TEMPERATURE EXCURSION

    EFFECTS: REDUCES FREEZE-THAW OR LIQUID-STEAM CYCLES;
    REORDERS STRESS/TEMPERATURE EXCURSIONS

- REDUCE SEGMENTS FROM 100 TO 6

    EFFECT: REDUCES FREEZE-THAW OR LIQUID-STEAM CYCLES

- REDUCED DWELL TIME AT TEMPERATURE

    EFFECT: MAY BE SIGNIFICANT (CREEP/RELAXATION)

NOTE: FREEZE-THAW CYCLES REDUCED FROM 10,000 TO 6
LIQUID-STEAM CYCLES REDUCED FROM 1,300 TO 6

Figure 3-87: Compromises in developing the accelerated environmental test condition.

3-90

3-91

```
CATEGORIZED FLAWS BY OCCURRENCE
IN MANUFACTURING SEQUENCE
```

- FIBER & PREPREG GENERATION
  - PREPREG VARABILITY EXCEEDS SPEC
  - RESIN STARVED
  - RESIN RICH
  - FOREIGN PARTICLES
  - PILLS OR FUZZ BALLS
  - (CONT)

- BASIC LAMINATE LAYUP
  - BLISTERS, DELAMINATIONS
  - EXCESS POROSITY
  - SCRATCHES FIBER BREAKAGE
  - SPLIT TOW
  - REWORKED AREAS
  - FOREIGN PARTICLES
  - DROPPED PLY
  - VARIABLE CURE
  - TOOL IMPRESSION
  - (CONT)

- MACHINE LAMINATE
  - OVERSIZED HOLE
  - BREAKOUT
  - PULL THROUGH, COUNTERSINKS
  - OVERTORQUED FASTENER
  - (CONT)

- BOLTING, FASTENER & ATTACHMENT
  - OVERSIZE HOLE
  - OUT OF ROUND HOLE
  - EDGE NOTCH
  - (CONT)

- BONDING & ADHESIVE PROCESSES
  - ADHESIVE STARVED
  - EXCESS POROSITY
  - FOREIGN PARTICLES
  - (CONT)

- FINAL ASSEMBLY & PAINTING
  - PAINT POROSITY, VOIDS
  - ETC

Figure 3-88: Flaws defined by an industry survey.

3-91

4.0 NDE

This section contains the review summaries of the following articles.

- Bakis, C. E. and R. P. Emerson, "Optoelectronic Radial Displacement Measurement on Rotors," *Proceedings of the SEM Annual Conference on Experimental and Applied Mechanics*, 2001.
- Baaklini, G. Y., *et al.*, *NDE Methodologies for Composite Flywheels Certification*, NASA TM-2000-210473, 2000.
- Madaras, E. I., *et al.*, "Ultrasonic Studies of Composites Undergoing Thermal and Fatigue Loading," 24th Annual Review of Progress in Quantitative Nondestructive Evaluation, San Diego, California, July 27-August 1, 1997, AIAA-2000-1759, 2000.
- Johnson, E. C. and J. P. Nokes, , *Nondestructive Evaluation (NDE) Techniques Assessment for Graphite/Epoxy (Gr/Ep) Composite Overwrapped Pressure Vessels*, Report No. TR-98(8504)-3, The Aerospace Corporation, 1998.

CATEGORY

NDE

REFERENCE

ABSTRACT

An improved method of measuring radial displacements at discrete points on the axial surface of rotating rotors is presented. The method uses optoelectronic devices to determine the position of a reflective pattern placed on the rotor. The radial displacements are separated into components due to run-out and axisymmetric deformation. The pattern maximizes displacement sensitivity at a finite number of measurement points across the surface of the rotor while also providing data for compensation for the intensity of reflected light and sensor stand-off distance. Displacement measurements recorded at rotor speeds of up to 10 krpm were repeatable to within $\pm$ 1 μm. Hoop strains were within 100 $\mu\varepsilon$ of theoretical predictions, provided a proper accounting was made for thermal strains. Since overall strains in the rotor were rather low, the measured strains differed from theoretical strains by up to 25%.

SUMMARY

The objective of the project was to devise an improved optoelectronic system and data analysis algorithm for determining radial displacements on an axial face of an axisymmetric rotor. The proposed optical pattern allows the separation of radial run-out and axisymmetric deformations and permits, within defined limits, the correction of measurement errors caused by changes in the intensity of optical illumination.

Several methods exist for measuring stress or strain on the axial surface of high-speed rotating machinery, such as: electrical resistance strain gages, X-ray diffraction, and speckle interferometry. For the purposes of the current paper, these methods were ruled out due to either limited speed capability, lack of long term stability, high expense, difficulty of making multi-point measurements, insufficient sensitivity, or excessive susceptibility to misalignment and vibrations. This system is completely non-contact, low-cost, amenable to multi-point measurements, and not overly sensitive to misalignment and vibration.

Figure 4-1 shows one of the lobes used in the experiment to measure the hoop strain distribution on a uniform disk. The figure identifies triangular patches for measuring displacement, wedge-shaped patches for compensation of the sensor data, and concentric rings for assuring good alignment of the four independently generated lobes.

Variability in IR LED intensity, IR detector sensitivity, and sensor standoff distance during spin testing can each cause erroneous angle measurements on the compensation patches as well as the displacement patches. These must be compensated for in order to get accurate strain measurements and radii displacements. In order to compensate for the inevitable imperfection in pattern shape (in Figure 4-1), calibration experiments are carried out at a very low rotor speed to determine the relationship between duty cycle, φ, and undeformed radial position on each reflective patch. Figure 4-2 shows an example of the algorithm's ability to compensate for differences in LED intensity.

Figure 4-3 shows how the axisymmetric radial deformation at the 70.7 mm radial measurement position on an aluminum rotor varies with speed, minus the effect of any temperature changes measured on the rotor with three radially spaced IR thermocouples. The individual lobe measurements or radial deformations are shown along with the average for all four lobes.

Figure 4-4 shows a summary of the average axisymmetric radial deformations during a spin test of the aluminum rotor. The difference between theory and experiment is greatest near the 3 krpm resonance.
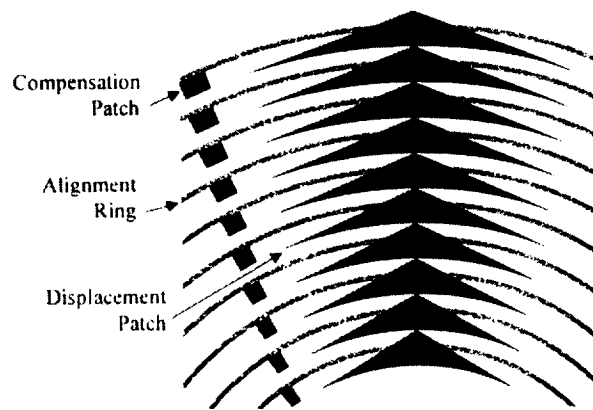
Figure 4-1: One of four lobes, each having 10 annuli.
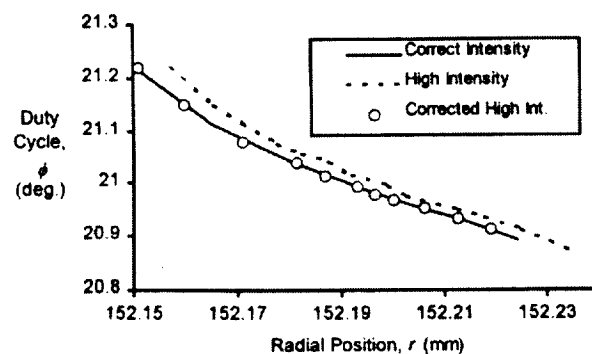
Figure 4-2: Demonstration of compensation for LED intensity.

4-3
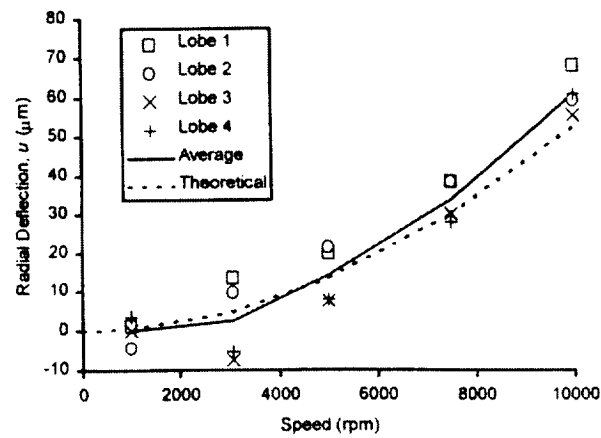
Figure 4-3: Axisymmetric radial deformation from one sensor at the 70.7 mm position on the aluminum rotor.
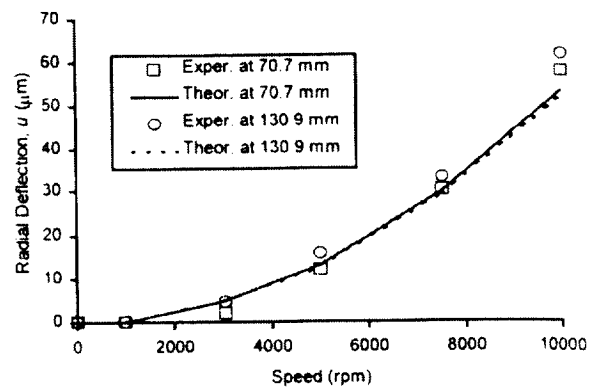
Figure 4-4: Axisymmetric radial deformation from four sensors at two positions on the aluminum rotor.

CATEGORY

NDE

REFERENCE

Baaklini, G. Y., *et al.*, *NDE Methodologies for Composite Flywheels Certification*, NASA TM-2000-210473, 2000.

ABSTRACT

Manufacturing readiness of composite rotors and certification of flywheels depend in part on the maturity of nondestructive evaluation (NDE) technology for process optimization and quality assurance, respectively. Capabilities and limitations of x-ray-computed tomography and radiography, as well as advanced ultrasonics were established on NDE ring and rotor standards with EDM notches and drilled holes. Also intentionally seeded delamination, tow break, and insert bagging material were introduced in hydroburst-rings to study the NDE detection capabilities of such anomalies and their effect on the damage tolerance and safe life margins of subscale rings and rotors. Examples of possible occurring flaws or anomalies in composite rings as detected by NDE and validated by destructive metallography are shown. The general NDE approach to ensure quality of composite rotors and to help in the certification of flywheels is briefly outlined.

SUMMARY

Several ultrasonic methods were used to look for damage to a composite flywheel rotor (Figure 4-5). Through-transmission (TT) and pulse-echo (PE) were used for flaw detection. X-ray computed tomography and radiography were also performed on the rotors.

X-ray microfocus radiography, x-ray computed tomography, and pulse echo ultrasonic scans were able to detect EDM notches down to 125 by 125 μm and drilled holes down to 300 μm in diameter in the multi-layered rotor. The ultrasonic pulse echo method easily detected intentionally seeded delamination, tow break, and insert of bagging material in hydroburst rings.

The NDE plan, based on the findings in the paper, is:

a) Perform flaw/damage detection on 100% of the rings with pulse echo ultrasonics and real-time microfocus radiography and selected slices with computed tomography.
b) Perform flaw/damage detection on 100% of the rotor with thick computed tomography slices and 100% of the outer shells with 5 MHz pulse echo ultrasonic down to 4.5 cm deep from the OD of the rotor.

Figures 4-6 and 4-7 below show examples of the ultrasonics and tomography methods used.
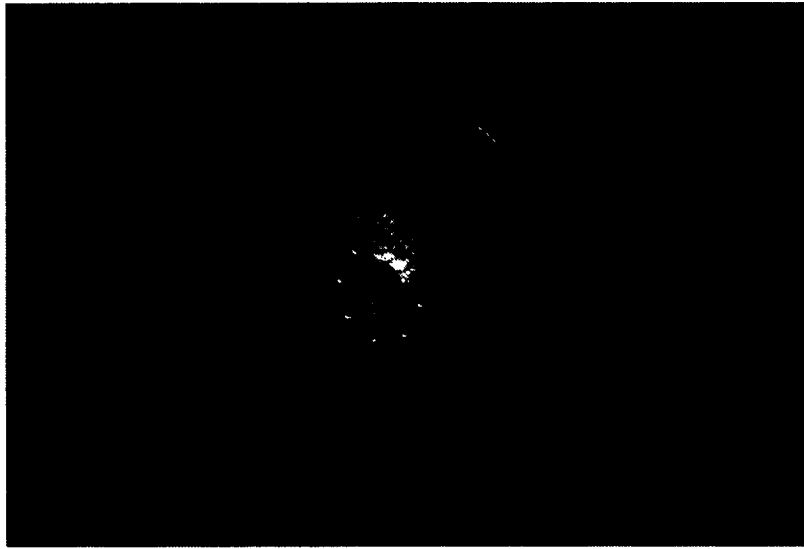
Figure 4-5: Preloaded composite rotor for the flywheel energy storage
system targeting the replacement of chemical batteries on the
international space station.
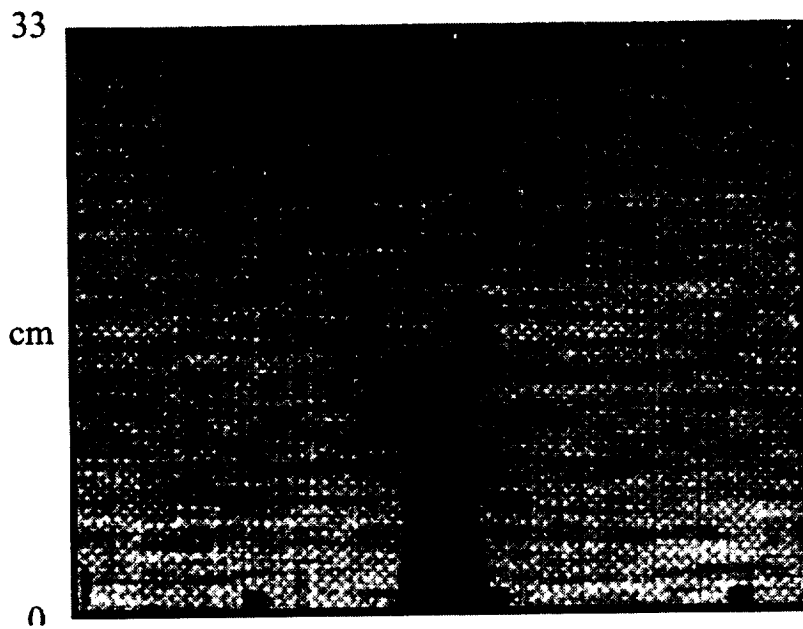
Figure 4-6: Ultrasonic scan showing a large delamination in one of
the rings.

4-6
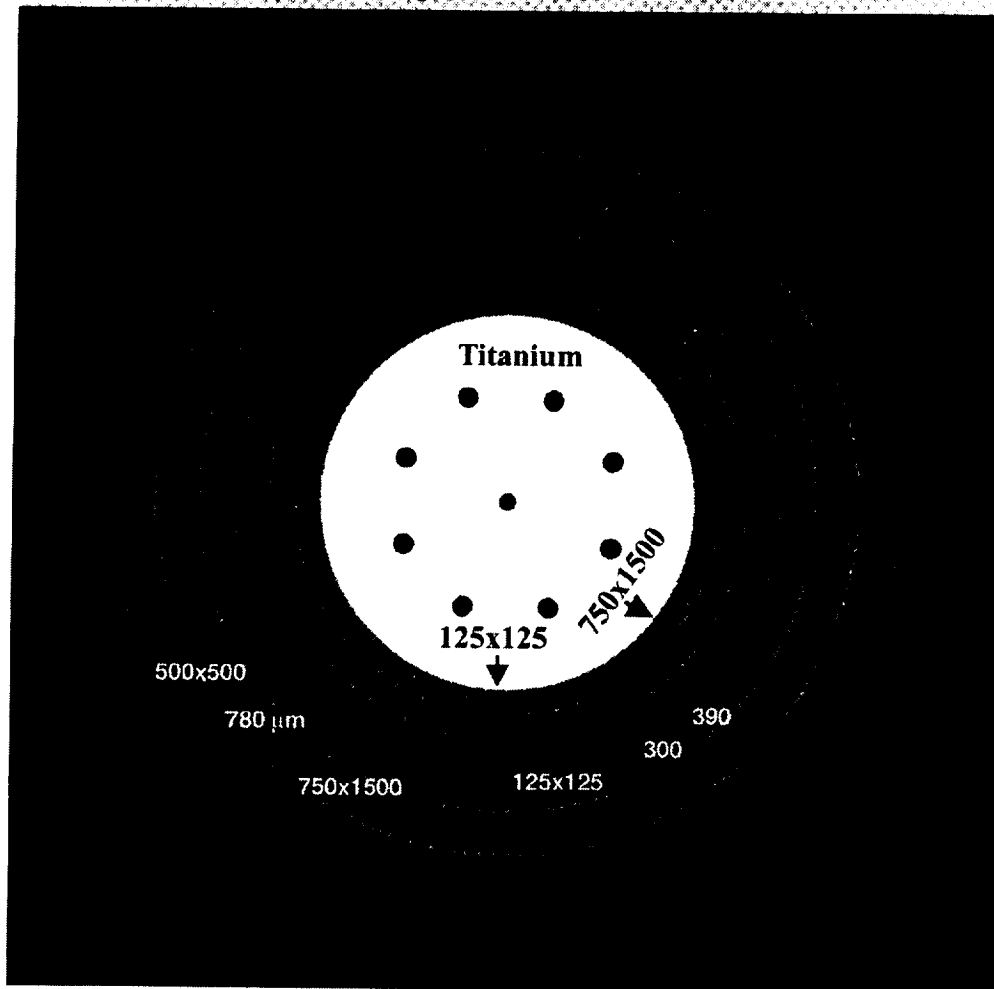
Figure 4-7: Computed tomography slice of a multi-layered rotor standard with EDM notches and drilled holes set (125 x 125, 300, 390, 500 x 500, 780, and 750 x 1500 μm) in each layer. This set was duplicated in a spiral fashion starting at the innermost ring near the ID and finishing at the outermost ring near the OD.

CATEGORY

NDE

REFERENCE

ABSTRACT

New composite materials possess attractive properties for use in advanced aircraft. A necessary requirement for their introduction into aeronautic use is an accurate understanding of their long term aging processes so that proper design criteria can be established. In order to understand those properties, these composites must be exposed to thermal and load cycles that are characteristic of flight conditions. Additionally, airline companies will require nondestructive evaluation (NDE) methods that can be used in the field to assess the condition of these new materials as they age.

As part of an effort to obtain the required information about new composites for aviation use, we are performing ultrasonic measurements both in the NDE laboratory and in the materials testing laboratory at NASA. The materials testing laboratory is equipped with environmental chambers mounted on load frames so that composite samples can be exposed to thermal and loading cycles representative of flight protocols. Applying both temperature and load simultaneously will help to highlight temperature and load interactions during the aging of these composite materials.

This study reports on our initial ultrasonic attenuation results from thermoset and thermoplastic composite samples. Ultrasonic attenuation measurements have been used reliably to assess the effects of material degradation. For example, recently, researchers have shown that by using frequencies of ultrasound on the order of 24 MHz, they could obtain adequate contrast in the evaluation of thermal degradation in these composites. [ref. 1, in paper] This paper will present data that shows results at a lower frequency range. In addition, we report results on the frequency dependence of attenuation as the slope of attenuation with respect to frequency, $\beta = \Delta\alpha(f)/ \Delta f$. The slope of attenuation is an attractive parameter since it is quantitative, yet does not require interface corrections like conventional quantitative attenuation measurements. This is a consequence of the assumption that interface correction terms are frequency independent. Uncertainty in those correction terms compromises the value of conventional quantitative attenuation data. [ref. 2, 3 from paper]

SUMMARY

Environmental testing was conducted on 16 and 32 ply thick dog bone shaped panels. NDE was conducted with two different ultrasonic pulse echo systems. Figure 4-8 gives one of the flight load and temperature profiles to which the samples were exposed. Figure 4-9 shows the

thermoset panels at several steps in the aging process. These panels were loaded with high strain load/thermal protocol. The thermoplastic panels, shown in Figure 4-10, were subjected to high strain/thermal protocol. These panels show a large increase in attenuation (~ 400%) after only 5,000 hours. The circled areas suggest local damage. Similar damage is seen in the low strain loading/thermal protocol in Figure 4-11. Figure 4-12 shows a correlation between slope and attenuation vs. composite age.
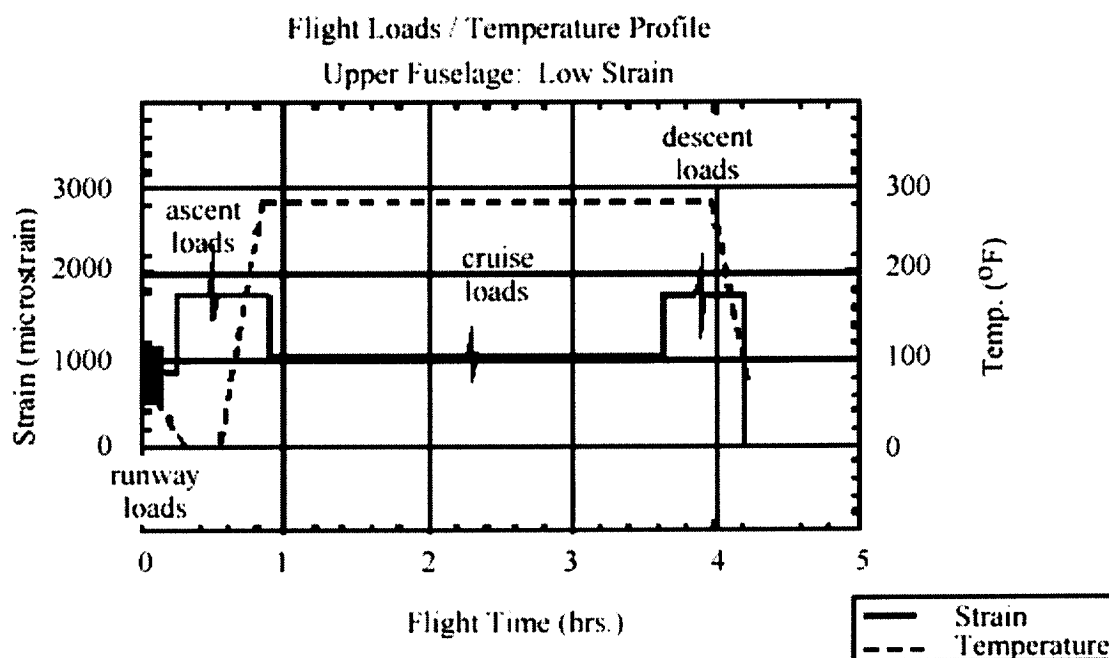
Figure 4-8: Representative flight strain loads and thermal loads that are used to study the aging process in composites. The strain levels are indicated on the left axis and shown as a solid line. The temperature levels are indicated on the right axis and shown as a dashed line. The horizontal axis shows the flight time in hours.

a) Age = 0 hours
   <α> = 0.28 ± 0.22 Np/cm

b) Age = 0 hours
   <α> = 0.26 ± 0.12 Np/cm

1.8 Np/cm

c) Age = 5,000 hours
   <α> = 0.35 ± 0.08 Np/cm

d) Age = 10,000 hours
   <α> = 0.40 ± 0.26 Np/cm

0 Np/cm
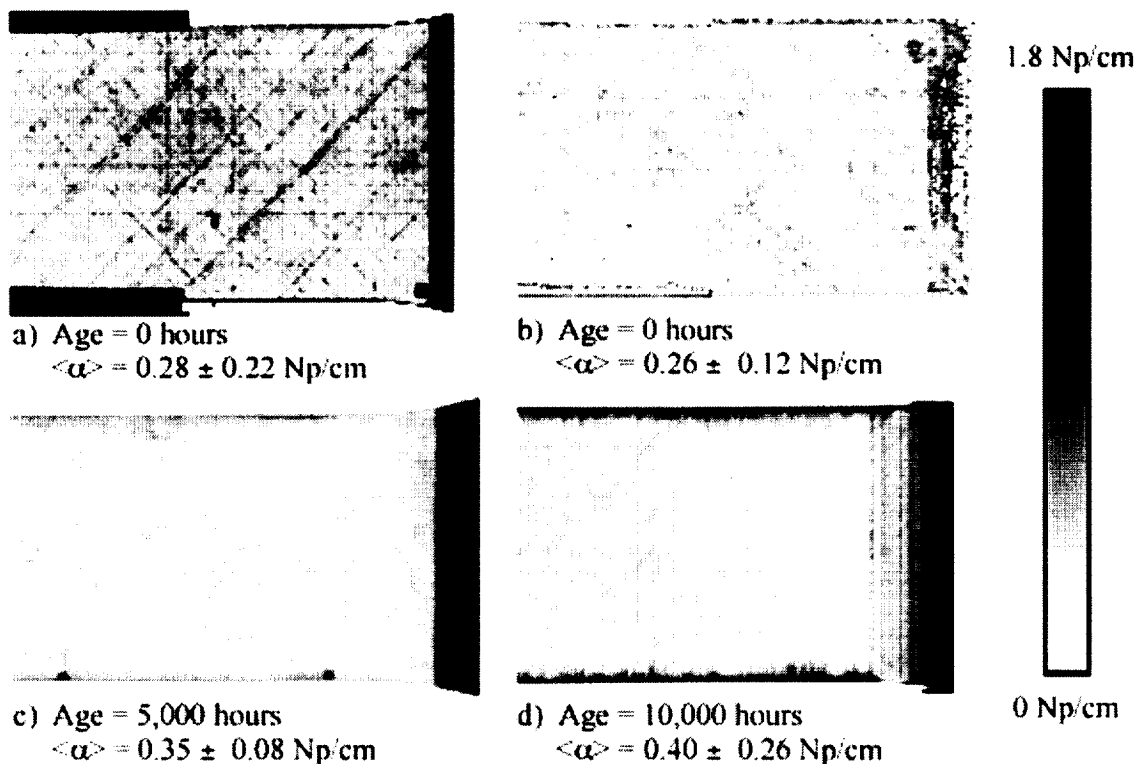
Figure 4-9: Ultrasonic attenuation images panels of IM7/5260, 32 ply, at different ages subjected to the high strain protocol. Each figure shows the detail for half a panel and the age, average attenuation, <α>, and standard deviation are listed below each figure. The figures are scaled from 0 (white) to 1.8 Np/cm (black).

a) Age = 0 hours
   <α> = 0.21 ± 0.07 Np/cm

b) Age = 5,000 hours
   <α> = 1.22 ± 0.41 Np/cm

5.6 Np/cm

0 Np/cm
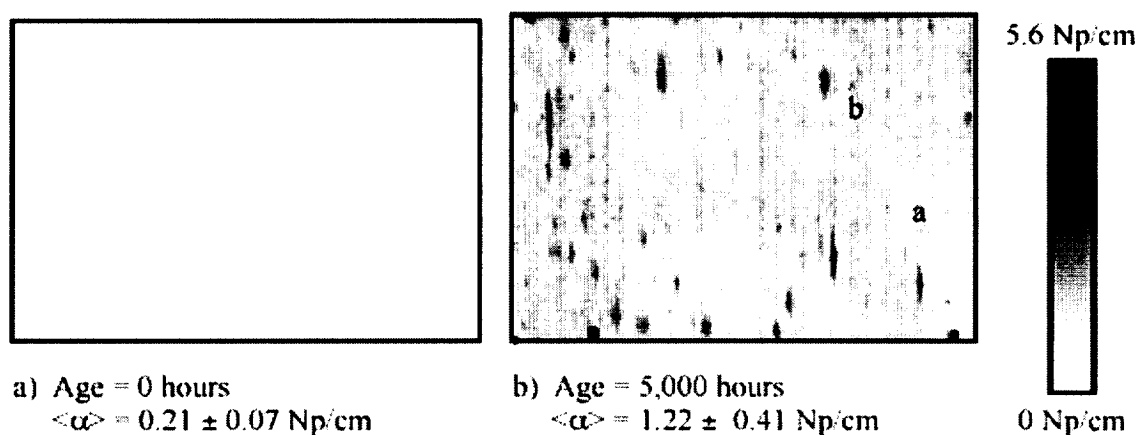
Figure 4-10: Ultrasonic images of a IM7/K3B, 16 ply panel undergoing high strain and thermal aging. Each figure shows the detail for half a panel and the age, average attenuation, <α>, and standard deviation are listed below each figure. The circled areas are addressed in figure 6 [not included in summary]. The figures are scaled from 0 (white) to 5.6 Np/cm (black).

a) Age = 3,000 hours
   <β> = 0.91 ± 0.32 Np/MHz-cm

b) Age = 6,000 hours
   <β> = 1.40 ± 0.46 Np/MHz-cm

8 Np/MHz-cm

0 Np/MHz-cm
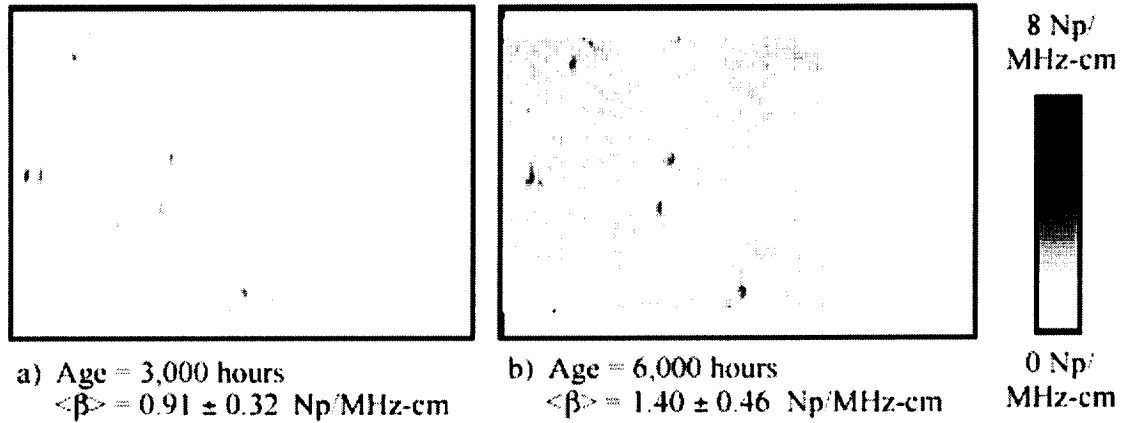
Figure 4-11: Ultrasonic slope of attenuation, b, images of an IM7/K3B, 16 ply panel which has undergone a low strain load/thermal protocol. Each figure shows the scanned region for half a panel and the age, average slope of attenuation, <β>, and standard deviation are listed below each figure. The figures are scaled from 0 (white) to 8 Np/MHz-cm (black).
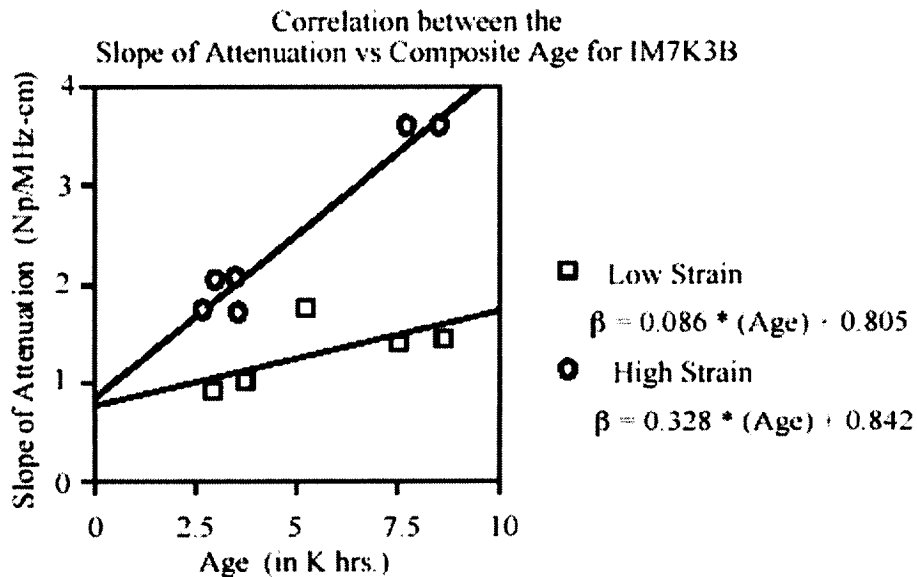
Figure 4-12: Correlation between slope of attenuation vs. composite age for IM7/K3B composites. The open squares represent data taken with the low strain levels. The open circles represent data taken with the high strain levels.

CATEGORY

NDE

REFERENCE

ABSTRACT

NDE methods evaluated included eddy current measurements, ultrasonics, radiography, acoustic emission monitoring, acousto-ultrasonics, and interferometric (e.g., shearography) methods. The major interest was in the detection of damage to COPVs caused by impacts at energy levels that would leave no visible scar on the COPV surface. Each of the above-mentioned NDE methods was assessed with regards to its utility for the detection of impact damage to COPVs and its applicability in the field.

Three COPVs were impacted at various energies and then inspected using each of the NDE methods. The results for each method are presented, followed by a summary comparing the advantages and disadvantages.

Several NDE techniques were shown to be effective for detecting impact damage sites on graphite/epoxy overwrapped pressure vessels even if the impact energy was below the threshold for creating visible surface damage. These techniques (ultrasound, radiography, thermography shearography, and eddy current testing) are sensitive because a small dent is left in the liner following the impact.

The impact damage detection thresholds for the various NDE techniques employed depend of the size and shape of the vessel. The tup characteristics and the internal pressure of the vessel during impact also affect the degree of damage and , hence, the detectability of the impact site. The size of the indication associated with a flaw is also dependent on the technique used. Visual inspection can lead to an underestimate or lack of detection of the damage. For both thermography and shearography, consistent sizing could be accomplished through the use of calibration standards and a consistent test set-up. The ultrasonic and eddy current results are most likely accurate measures of how much of the liner was debonded.

SUMMARY

One subtask to the Enhanced Technology for Composite Overwrapped Pressure Vessels Program, a nondestrucutvie evaluation (NDE) techniques assessment was conducted. Three different size composite overwrapped pressure vessels (COPVs) were used to assess several NDE techniques with regards to utility for detection of impact damage to COPVs and applicability in the field.

Several techniques for performing NDE to locate the presence of impact damage on a composite structure are discussed:

1) Visual Inspection

Visual inspection is the easiest way to inspect for mechanical damage such as that caused by impact. There is, however, no quantitative reliability and confidence level associated with visual inspection capability.

Means are available, however, to help in the visual detection of damage. The capability of visual inspection can be enhanced by the use of magnification loupes. The use of dye penetrant (or alcohol wipe) can also be used to accentuate indications of damage. A borescope can be utilized to visually inspect the inside liner of the COPV for dents caused by impact.

Most visual inspection options are hampered by any limitations to visual access of the surface in question and the poor surface contrast of most graphite/epoxy components.

2) Ultrasonic Inspection

This technique has been used in the aerospace industry for several years for detecting delamination or debonding in composite structures. Two options exist for ultrasonic inspection: through-transmission and pulse-echo. In the through-transmission technique, a sound pulse generated by one transducer is received by a second after passing completely through the pressure vessel. For the pulse-echo technique, a reflection rod is inserted into the center of a COPV. Figure 4-13 shows a pulse-echo C-scan representation of a COPV after a 10 J impact. The impact left no visible indication on the surface of the COPV; so a visual inspection would not have found the damage. However, in the figure the impact site is clearly identified by the dark region in the scan.

In order to conduct this technique, the COPV will need to be fully immersed in water. This will likely not be tolerated for flight hardware. Performing a reliable handheld ultrasonic scan of the outside surface might be hindered if access to the vessel is limited or if the outside has a rough texture. In addition, a liquid or gel might be required to couple the sound into the vessel.

3) Shearography

Electronic shearography is a noncontact interferometric method for measuring changes in the out-of-plane slope of a surface. The technique requires an initial or baseline image of the component that is stored for later use. After storing the initial image, a small load is applied to the part. This load is best applied by pressurization by a small amount. A second image under load is taken. This image is then subtracted from the baseline image. The result is a family of high contrast fringes indicative of the deformation due to the pressure differential. Mechanical damage can cause subtle changes in load carrying characteristics and, hence, the contours of the vessel that are effectively detected using shearography.

This technique is particularly effective for detecting impact in spherical COPVs because of the relatively uniform stress field, as shown in Figures 4-14a and 4-14b. Figure 4-14a represents the nominal deformation of the spherical COPV under 40 psi pressure load. The fringes in Figure 4-14b clearly indicate the presence of a 20 J impact with a 25 mm diameter impactor.

One drawback of shearography is the need for a matted surface to scatter the laser creating the necessary speckle pattern. The surface of the composite may need to be prepared using either a strippable paint or a spray powder.

4) Radiography
The materials and thicknessess associated with typical COVPs provide little impediment to the passage of X-rays of standard inspection energies. The detection of an impact site requires a tangential shot that manifests the dent in the liner, and a full inspection would require several tangential shots about the circumference using film or a real-time scanner. Computer-aided tomography could also be employed. This may prove reasonable prior to and after COPV shipment, but would be impractical once the COPV has been installed.

5) Thermography
Thermography is an NDE technique for measuring the surface temperature of an object based on the emission of infrared (IR) radiation. Using an IR camera, the complete temperature profile of a target can be recorded at video frame rates (30 Hz). Internal discontinuity caused by flaws can lead to variations in the surface temperature profile of the hardware. Flaws that produce localized variation in the thermal properties of a composite, such as a delamination or porosity, can often be easily detected via thermography.

For a COPV, one consequence of an impact event is the possible creation of a disbond between the liner and overwrap of the impact site. In the damage area, significantly higher thermal impedance could be formed. The location of surface hot spots can then be mapped using an IR camera. Evaluation of IR data showed a bruised area to be as much as 2° C higher temperature than surrounding areas shortly after transient heating with a quartz lamp. Figure 4-15 shows an image obtained during the thermography inspection of a cylindrical COPV with both 15 and 20 J impact sites.

6) Eddy Current
Eddy current inspection is commonly used to detect cracks in metallic parts of hardware. While the metal liners of COPVs are conductive, Gr/Ep overwraps are essentially transparent to eddy current probes at standard inspection frequencies (less than 1 MHz). Within the COPV with composite overwrap and metal liner, the overwrap acts as a spacer between the probe and the metal liner. Eddy currents that are very sensitive to the gap between the probe and the liner can be used to detect impact-induced dents in the liner. Figure 4-16 shows a simple eddy current image of a COPV with various impact locations.

7) Acoustic Emission
Loaded structures typically produce sound as the materials and components within the structure respond to the load. For composite hardware, matrix cracking and fiber breaking

both produce sound that can be detected. Acoustic emission (AE) monitoring is a method for evaluating the structural integrity of a structure based on the generation of sound during structural loading.

A pressurized vessel can be subjected to an initial AE screening and then be pressurized again after being subjected to an impact. The COPV exhibits significantly more AE after impact that exceeds a particular threshold. The energy threshold required for AE monitoring to detect impact varied significantly between COPV types. Figure 4-17 demonstrates the change activity that occurs after a 35 J impact on a cylindrical COPV.

AE monitoring does not provide a quantitative mans for ascertaining the severity of the impact damage. Instead, AE methods appear to offer potential as an impact screening technique.

Other techniques that were evaluated during the program were a microwave technique and acousto-ultrasonics. The microwaves were unable to penetrate the Gr/Ep, which is a conductive medium. The acousto-ultrasonic technique was found to offer little advantage over standard ultrasonic techniques used for detecting delaminations.

Summary

Several examples of the NDE techniques are presented for composite overwrapped pressure vessels (COPVs). These NDE techniques have been shown to be effective for detecting impact damage sites of Gr/Ep composite components even if the impact energy is below the visual damage threshold (VDT). Selection of the most appropriate technique(s) depends on a number of factors including:

- Specific type (size, shape, material thickness, coatings, etc.) of COPV to be inspected
- Accessibility constraints during inspection
- Required sensitivity
- Tup characteristics
- Internal pressure of the vessel during impact

A quick guide for selecting an appropriate NDE technique is presented in Figure 4-18. The "Whole Field" column relates how the data is taken, point-by-point as in a scan versus whole field as in a grabbed image. "Flaw Characterization" is an assessment of how well the flaw is sized. "COPV Preparation" includes what must be done to the vessel in order to be able to inspect it (coating the surface, etc.). "Field Use" relates to how field deployable the technique is.
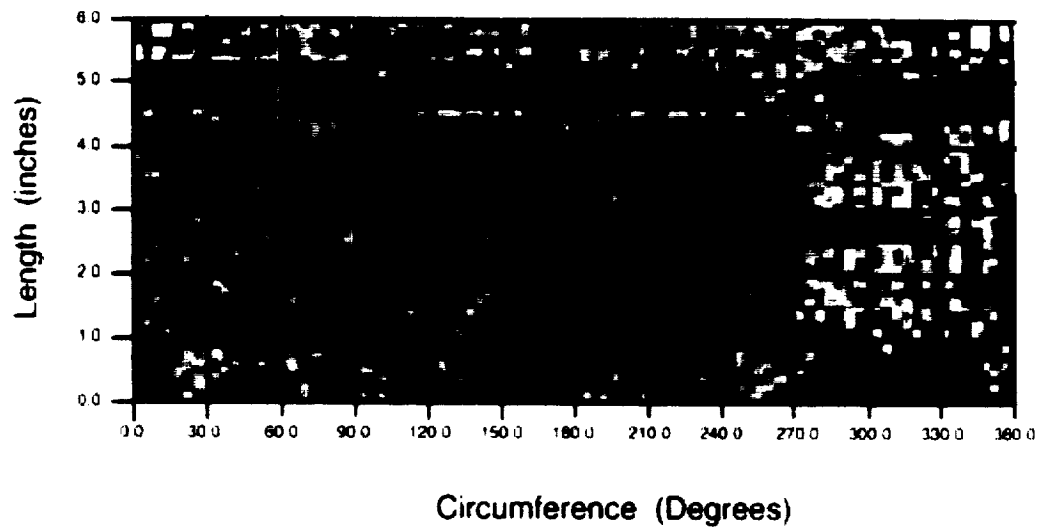
Figure 4-13: Pulse-echo C-scan of a COPV subjected to a 10 J impact.

Figure 4-14a: Initial shearographic image.
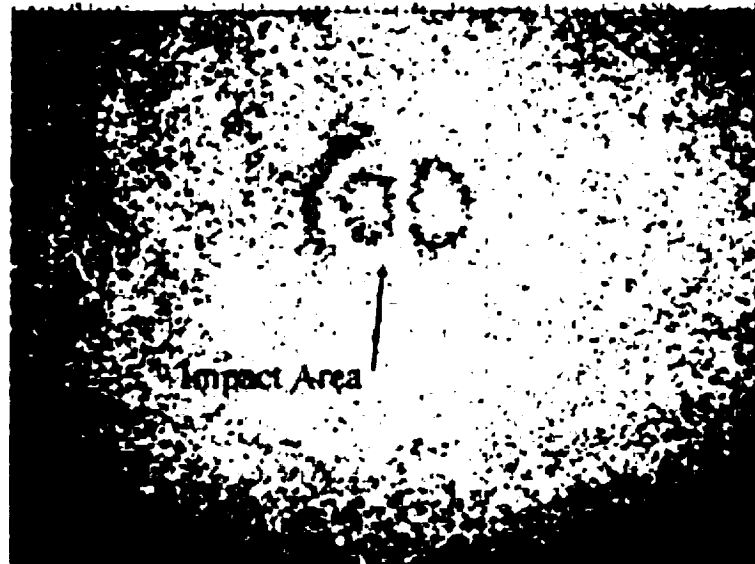
Figure 4-14b: Post-impact shearographic image.

13 J impact using a 25mm tup

20 J impact using a 25mm tup
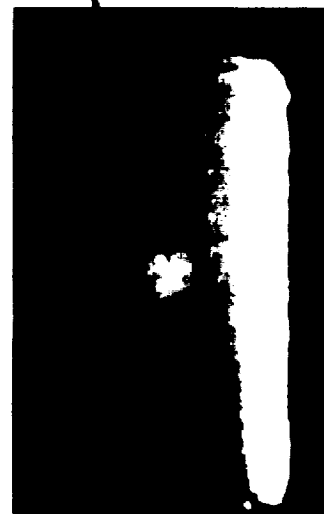
Figure 4-15: Thermography indications on a COPV subjected to two impact levels.
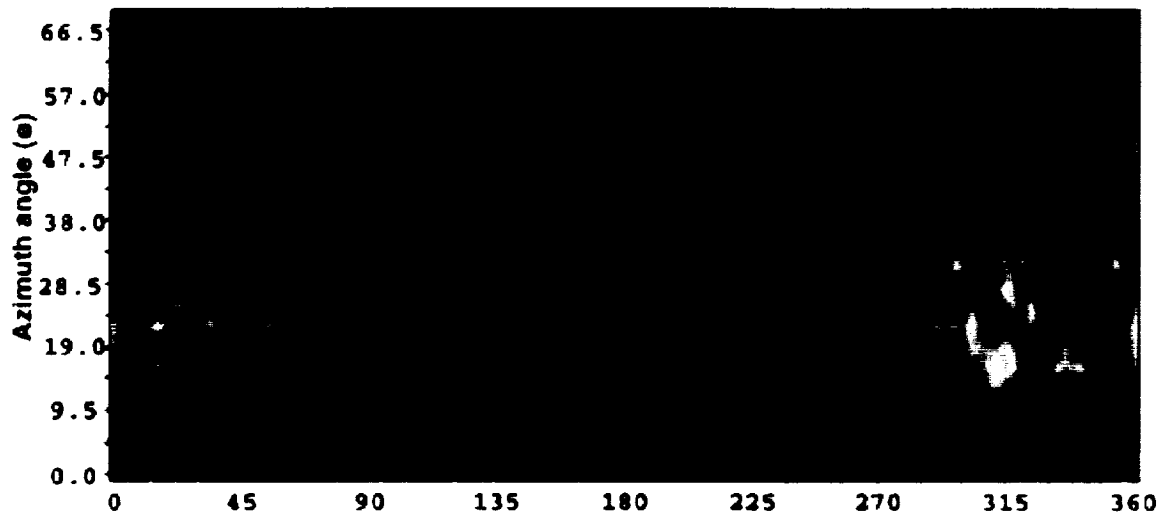
Figure 4-16: Eddy current images of a COPV subjected to various levels of impact.
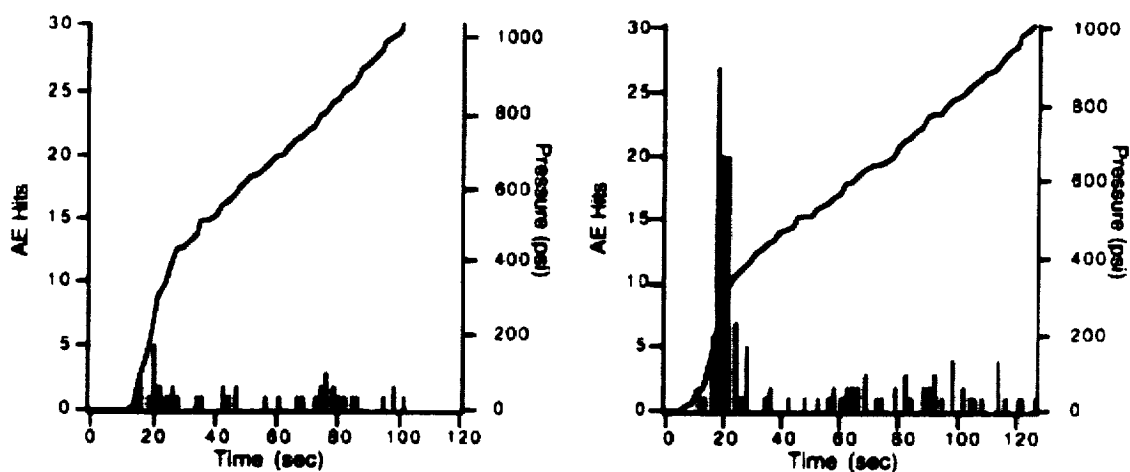
Figure 4-17: Acoustic emission data – (a) Before impact and (b) After impact.

Legend:
- ● - Better
- ◓ - Average
- ○ - Weak

	Whole Field	Flaw Characterization	Inspection Time	Simplicity	Data Evaluation	Sensitivity	COPV Preparation	Field Use
Acoustic Emission	○	◓	●	◓	○	○	◓	●
Acousto-Ultrasonics	○	○	◓	○	○	○	◓	○
Eddy Currents	○	◓	◓	●	◓	◓	●	●
Interferometry	●	◓	●	◓	◓	◓	○	◓
Ultrasonics	○	◓	◓	●	◓	◓	●	●
Radiography	○	○	◓	◓	◓	○	●	○
Thermography	●	◓	●	●	◓	◓	●	●
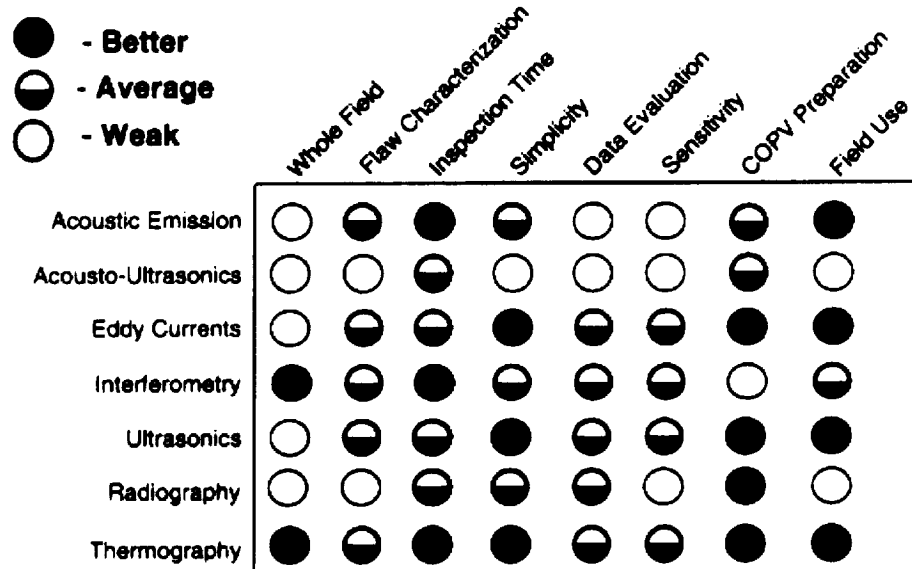
Figure 4-18: Features of various NDE techniques for the inspection of Gr/Ep COPVs.

5.0 FATIGUE

This section contains the review summaries of the following articles:

- Minnetyan, L. and C. C. Chamis, "Computational Simulation of Composite Fatigue Life," 41st AIAA/ASME/ASCE/AHS/ASC Structures, Structural Dynamics, and Materials Conference and Exhibit, AIAA-2000-1759, 2000.
- Bledzki, A.K., *et al.*, "The Accumulated Dissipated Energy of Composites Under Cyclic-dynamic Stress," *Experimental Mechanics*, Vol. 37, No. 3: 324-327, 1997.
- Ding, Y.Q., *et al.*, "Comparison of the Fatigue Behaviour of 2-D and 3-D Woven Fabric Reinforced Composites," *Journal of Materials Processing Technology*, Vol. 55: 171-177, 1995.

CATEGORY

Fatigue

REFERENCE

ABSTRACT

Fatigue life/durability of composites is evaluated via computational simulation. A computer model is utilized for the assessment of structural response, progressive fracture, and defect/damage tolerance characteristics. Critical locations for damage initiation are identified. Constituent material properties, stress and strain limits are scaled up to the structure level to evaluate the overall damage and its respective propagation. Damage initiation, growth, accumulation, and propagation to fracture due to cyclic fatigue are included in the simulations. Fatigue life results are shown for polymer and metal matrix composites and for metals. Results show the damage progression sequence and the changes in the structural response characteristics during different degradation stages. A procedure is outlined for use of computational simulation data in the assessment of damage tolerance, determination of sensitive parameters affecting fracture, and interpretation of experimental results with insight for design decisions.

SUMMARY

Three computational techniques were utilized to conduct the simulations: composite mechanics, finite element analysis, and damage progression tracking. The overall durability of the composite is evaluated in the damage progression module. Figure 5-1 shows the fatigue life simulation for composites under thermal cycling. In the equation, N_T is the number of thermal fatigue cycles to fracture, B_T is the degradation coefficient, σ_{lcyc} is the thermal stress, S_{lo} is the reference stress and T is the current temperature. T_0, T_{GD} and T_{GW} are reference, dry and wet temperatures, respectively for polymer composites. Figure 5-2 is a schematic of the steps taken in the study

The assumptions made in the models are the following: (1) Fatigue degrades all ply strengths at approximately the same rate. (2) All types of fatigue degrade laminate strength linearly on the semi-log plot including: (a) mechanical (tension, compression, shear, and bending); (b) thermal (elevated to cryogenic temperature); (c) hygral (moisture); and (d) combinations (mechanical, thermal, hygral, and reverse-tension compression). (3) Laminated composites generally exhibit linear behavior to initial damage under uniaxial and combined loading. (4) All ply stresses (mechanical, thermal and hygral) are predictable by using linear laminate theory.

Figures 5-3 and 5-4 show some of the results from the study conducted on an airfoil made of AS-4 graphite fibers and a high-modulus, high strength epoxy matrix and a woven fabric ceramic

5-2

matrix composite respectively. Figure 5-3 shows the damage progression with increasing time duration for the four different cyclic pressure amplitudes. It indicates that for the first three lowest load amplitudes, the airfoil endures a significant number of cycles after damage initiation without additional damage. Figure 5-4 shows strength and stress evolutions versus fatigue cycles. From this, it can be seen that the laminate will only survive with 0.01 probability and won't survive with 0.001 probability.

From this study, the following conclusions were drawn: (1) Composite fatigue life can be simulated using available methods. (2) Computational simulation, with the use of established composite mechanics and FEA, can be used to predict the influence of composite geometry as well as loading and material properties on the durability of composite structures. (3) The fatigue life procedure is flexible and applicable to all types of constituent materials, structural geometry, and loading.

- CRITERIA: FIRST PLY INITIAL TRANSVERSE CRACKING

$$\text{THERMAL CYCLES} \quad \text{Log } N_T = \frac{1}{B_T}\left[\left(\frac{T_{GW}-T}{T_{GD}-T_0}\right)^{1/2} - \frac{\sigma_{cyc}}{S_{A_0}}\right]$$

σ_{cyc} = MAX. TRANSVERSE PLY STRESS AT ΔT TO YIELD MAX. (σ_{cyc}/S_{A_0}) RATIO
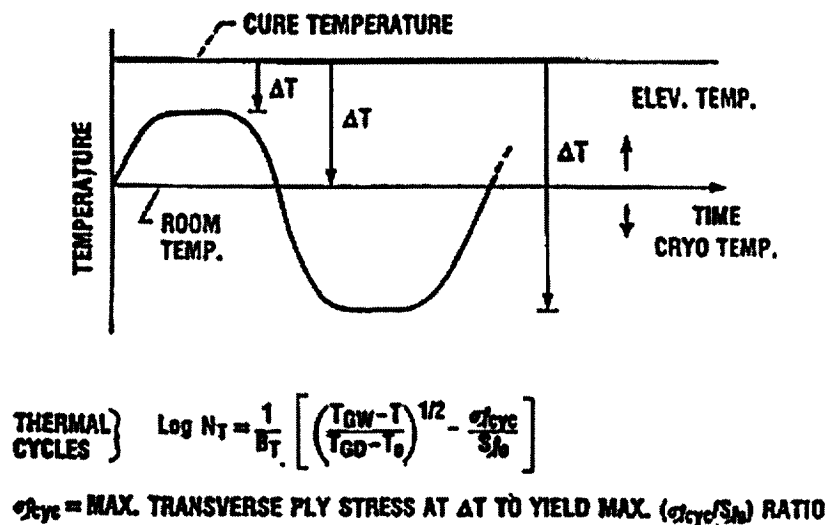
Figure 5-1: Thermal fatigue and cycles to initial cracking.
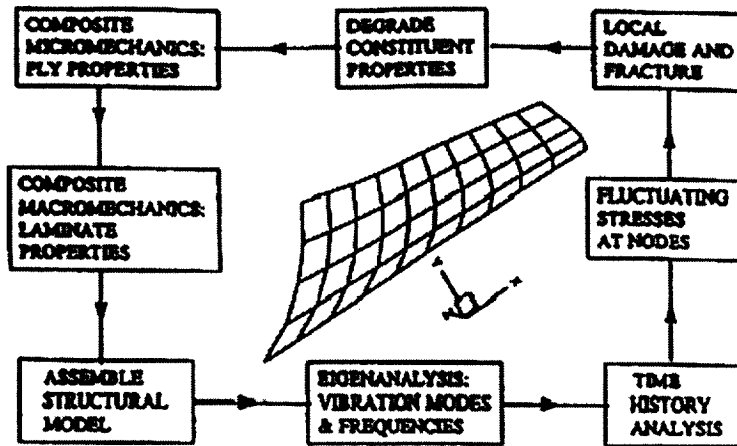
Figure 5-2: Computational simulation cycle.
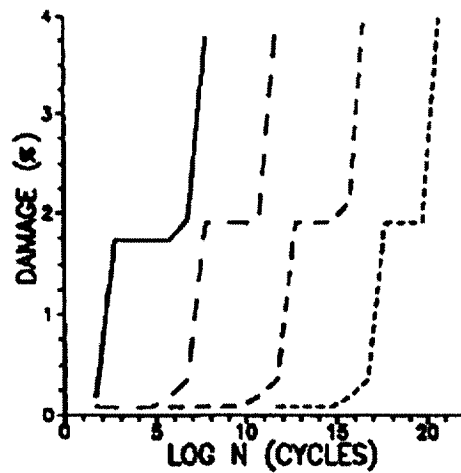
AS-4/HMHS: 16 plies [±45/0/90/ ∓ 45/90/0]ₛ, Loading frequency = 50 Hz
Short dashed line: cyclic load amplitude = 11.83 N
Medium dashed line: cylic load amplitude = 13.52 N
Long dashed line: cyclic load amplitude 15.21 N
Solid line: cyclic load amplitude = 16.90 N

Figure 5-3: Damage progression under cyclic loading.

5-4

Subjected to High Cycle Fatigue Environment
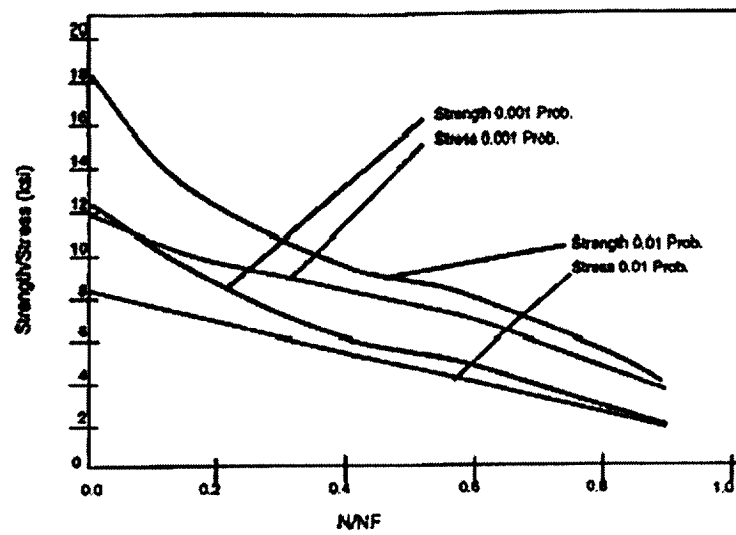
Figure 5-4: Ceramic matrix composite.

CATEGORY

Fatigue

REFERENCE

ABSTRACT

This paper presents a method for the estimation of the vibratory fatigue strength of composite materials, which is based on the accumulated dissipated energy. The accumulated dissipated energy was measured with a special measuring technique that is able to catch quasi-continuously the mechanical properties of the tested samples. The samples were made of glass-fiber epoxy foams reinforced with pretreated woven fabrics. The curves of the accumulated dissipated energy were approximated by an equation that includes several parameters. These parameters were identified for experiments with different types of load and for samples with different contents of micropores. In the equation for samples that reach more than 10^6 load cycles, the accumulated dissipated energy in one load stage test turns out to be a linear function. With this function the fatigue limit of the samples can be predicted.

SUMMARY

The testing frequency was chosen to be only 10 Hz because at this frequency the warming up of the samples during the first 1500 load cycles is no more than 3° C. The InDyMat system (intelligent dynamic material testing) was used to determine the dissipated energy during the experiments. The system is able to catch and evaluate mechanical properties quasi-continuously during a cyclic-dynamic stress.

The curves for the accumulated dissipated energy can be approximated with mathematical functions containing several variables. The variables were determined by comparing the calculated curves with the measured values of the loss energy. As shown in Figure 5-5, the correlation between curves is greater than 95%. Figure 5-6 shows the accumulated dissipated energy calculated with different numbers of measured values.

In Figure 5-7 is it observed that the curve of the accumulated dissipated energy is a linear function for samples that reach more than 10^6 load cycles. However, samples that did not reach the fatigue limit show a strongly nonlinear curve.
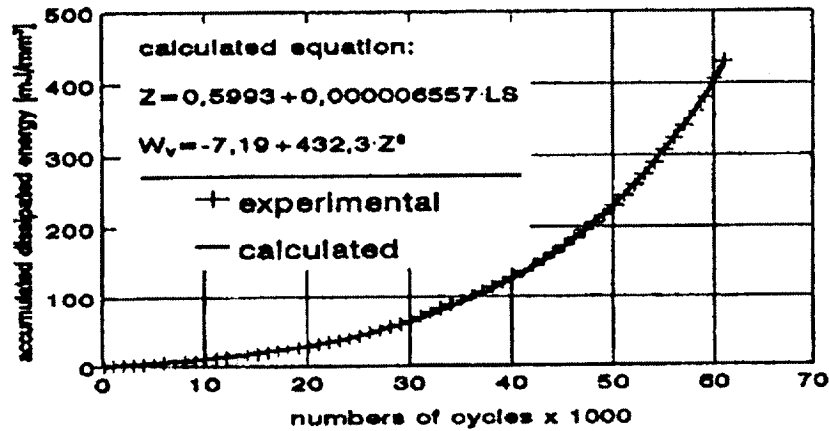
Figure 5-5: Comparison of a measured and a calculated accumulated dissipated energy.
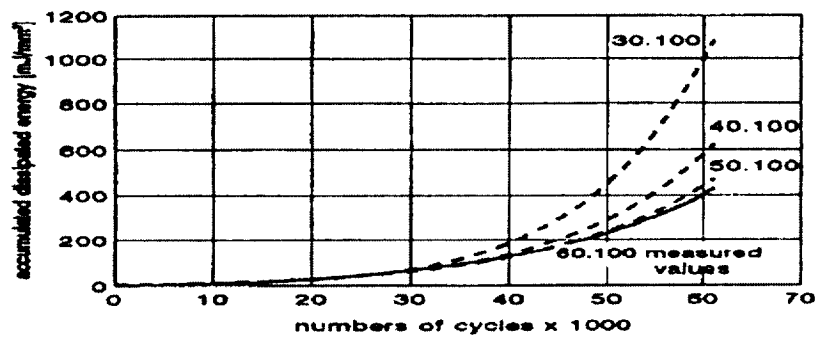
Figure 5-6: Calculations of the accumulated dissipated energy for different numbers of measured values.
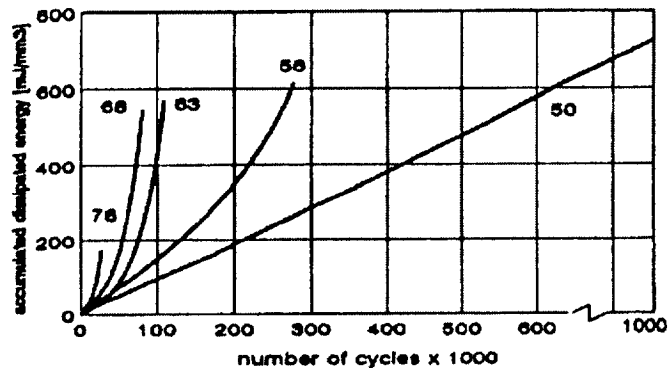
Figure 5-7: Accumulated dissipated energy as a function of the number of load cycles in the fatigue test with a single load stage (stress ratio = 0.1, f_{test} = 10 Hz, stress values in N/mm^2).

5-7

CATEGORY

Fatigue

REFERENCE

ABSTRACT

Some of the earliest investigations concluded that the basic mechanism of fatigue in composites differs greatly due to the different reinforcements. The variety of damage modes, the complexity of their interactions, and the subsequent effect on engineering properties make it difficult to interpret fatigue failure and lifetime for composite materials.

This paper reports the mechanical properties of 3-D T300 carbon fabric reinforced epoxy composite with a 52% fibre volume fraction, these results being compared to those of a standard 2-D fabric laminate containing the same fibre volume fraction. The static tensile and fatigue behaviour of these two types of composites were examined. Due to the greater amount of fibre aligned in the principal-stress direction, the in-plane static tensile properties of the 2-D fabric reinforced composite are better than those of the 3-D fabric reinforced composite.

SUMMARY

One way to control delamination is the introduction of the third directional reinforcement by weaving, braiding, or stitching. The through thickness fibers, in this case, would increase the interlaminar shear strength of the composite and hence inhibit delamination. The additional third-directional fibers can also provide additional stiffness and strength to the thickness direction.

Tensile and fatigue tests were performed to determine the material response and failure modes. The following conclusions were drawn:

a) The in-plane static tensile properties of the 2-D composite are better than those of the 3-D composite (see Figure 5-8). The initial tensile modulus and strength being 14.3% and 23.6% greater than that of the 3-D composite, depending on the percentage of fibers used for the through-the-thickness reinforcement.

b) Under tensile fatigue loading (see Figure 5-9), the residual strength and modulus of both the 2-D and 3-D composites show a sharp reduction initially, due to the localized flaws in the early part of the fatigue cycling, followed by a more gradual decrease. Under some applied stress levels, increasing the number of load cycles decreased the residual strength and modulus.

c) Due to the through-thickness reinforcement , the 3-D composite has significantly better fatigue performance than the corresponding 2-D composite.

d) From Figure 5-10, it is observed that the fatigue residual stiffness reduction of the 2-D and 3-D composites correlate reasonably well with the theoretical predictions.
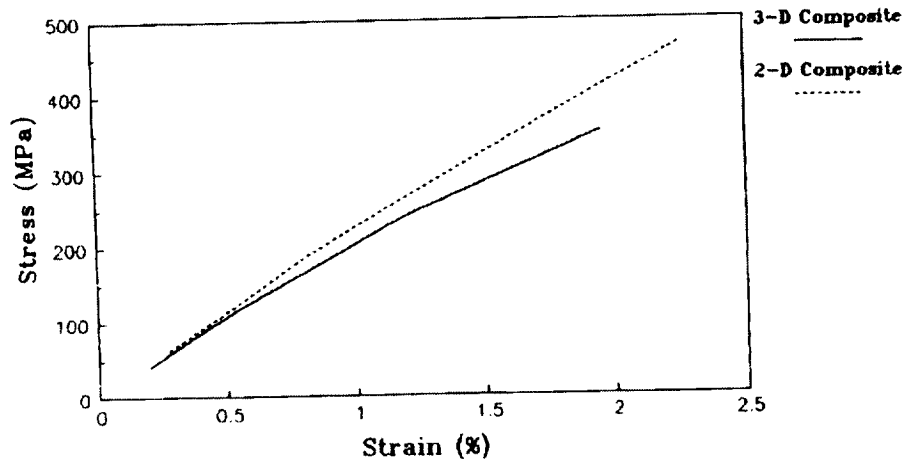
Figure 5-8: Representative stress-strain curves for the tensile tests.
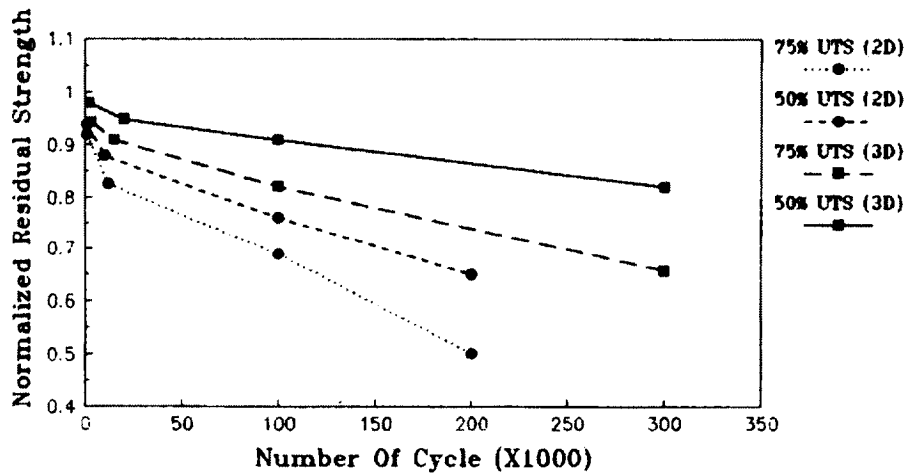
Figure 5-9: Residual-stiffness comparison of 2-D and 3-D composites under tensile fatigue loading.
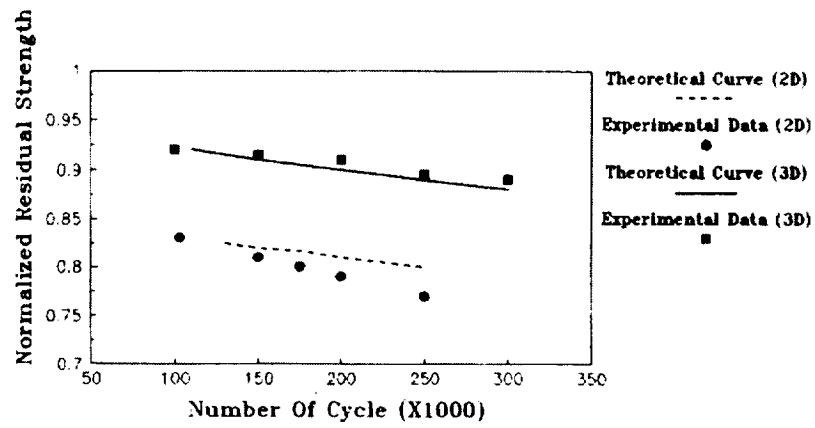
Figure 5-10: Comparison of the theoretical and experimental, results of residual stiffness of 2-D and 3-D woven composites under tensile fatigue loading.

6.0   Composite Damage Tolerance

This section contains the review summaries of the following articles.

- Chang, J. B., S.T. Chiu, and L. C. -P. Huang, "Damage Control of Space-Flight Composite Overwrapped Pressure Vessels" 51st International Astronautical Congress, IAF-00-I.3.10, 2000.
- Mahler, M., *et al.*, "Propagation and Control of Crack-like Damage in Curved Composite Panels Under Combined Loads," 41st AIAA/ASME/ASCE/AHS/ASC Structures, Structural Dynamics, and Materials Conference and Exhibit, AIAA-2000-1759, 2000.
- Fisher, C. and G. Lesieutre, "Health Monitoring of High Energy Density Rotor for Use in Spacecraft Applications," *Proceedings of the 44th International SAMPE Symposium*, Vol. 2:2145-2154, 1999.
- O'Brien, T. K., *Towards a Damage Tolerance Philosophy for Composite Materials and Structures*, NASA TM-100548, 1988.
- Chamis, C. C and C. A. Ginty, *Fiber Composite Structural Durability and Damage Tolerance: Simplified Predictive Methods*, NASA-TM-10079, 1987.
- Sollars, T. A., *Shuttle/Centaur G-Prime Composite Adapters Damage Tolerance/Repair Test Program*, NASA 87-0792, 1987.
- Demuts, E., *et al.*, "Assessment of Damage Tolerance in Composites," *Composite Structures*, Vol. 4: 45-58, 1985.

CATEGORY

Composite Damage Tolerance

REFERENCE

Chang, J. B., S.T. Chiu, and L. C. –P. Huang, "Damage Control of Space-Flight Composite Overwrapped Pressure Vessels," 51st International Astronautical Congress, IAF-00-I.3.10, 2000.

ABSTRACT

This paper describes an impact damage test program performed on space-flight composite overwrapped pressure vessels (COPVs). The primary purpose of the testing was to determine the critical variables that have the most effect on the burst strength after impact of a specific COPV design. The test variables included impact energy level, impactor size, internal pressure level, and medium used for pressurization (e.g., gas or liquid). The test results have motivated the AIAA Pressure Vessel Standard Working Group to introduce a new set of damage control require-ments for this class of pressure vessel in a recently developed AIAA pressure vessel standard. The highlights of the damage control requirements including system threat analysis, damage protection and/or indication system, and damage tolerance (residual strength) demon-stration testing are presented in this paper.

SUMMARY

Impact Damage Study

To study the effect of impact damage, an experimental program was conducted at the National Aeronautics and Space Administration/White Sands Test Facility (NASAWSTF). The study involved measurement of the burst strength after impact (BAI) as a function of the following major variables:

- Impact energy level
- Impactor geometry
- Vessel geometry/size
- Impact location
- Internal pressure level during impact
- Pressure media (gas or liquid)

Impact Damage Test Results

The impact damage test results showed the effect of various conditions and variables to the BAIs of tested COPVs. Table 6-1 shows that, for the small spherical (Type 2) COPVs, the applied impact energy (IE) levels ranged from 25 to 50 ft-lb with the majority of the tests conducted at

35 ft-lb. Since in one test case (S/N B-64), damage generated by 35 ft-lb was not detected visually by all the three inspectors, 35 ft-lb is determined as the visible damage threshold (VDT) for Type 2 vessels.

The test results showed that in general, BAIs decreased as the IE increased. It also showed that the BAI had a large scatter for a specific IE level compared to the undamaged vessels, which had only ±3% variations. The internal pressure levels were shown to significantly affect the BAI. When the vessels were pressurized at their MEOP level of 6,000 psi during impact, BAIs were higher than those impacted while empty. The choice of pressurizing fluid, either gas or water, had no significant effect on the BAI.

Table 6-2 shows the test results for the small cylindrical (Type 3) COPVs; the IE level applied ranged from 5 to 20 ft-lb. The VDT was determined as 15 ft-lb. At this IE level, inspectors could not visually detect the damage sites of two test specimens (S/N S-08 and S-04).

Again, the general trend was that the BAIs decreased as the IE increased. The scatters for damaged COPVs were also higher than those for undamaged ones.

The most significant result was the effect of the pressure levels during impact. When the cylindrical vessels were pressurized with water to 0.5 x MEOP (3,000 psi) and then subjected to the VDT level (15 ft-lb) impact, the BAIs were higher than those vessels that were empty during impact. The trend was the same as that observed in the spherical COPV tests. However, at the same IE level (15 ft-lb), when the water pressure was increased to MEOP (6,000 psi), the BAIs decrease significantly. The BAIs decreased even more when gas was used as pressurization fluid instead of water. At the VDT level (15 ft-lb), one test specimen (S-33) exploded 0.7 sec after impact. The end result of the failure for this COPV was dramatic. Many loose pieces were found in the test chamber. Figure 6-1 shows the vessel remnants from this impact test. Compared to the result of a typical hydraulic burst test as shown in Figure 6-2, the potential safety threat of an unexpected impact event for an unprotected COPV charged with gas during transportation or ground handling is obvious.

Impact test results for the large spherical (Type 1) COPVs and the large cylindrical (Type 4) COPVs are shown in Table 6-3. It can be seen that, compared to the BAI of the small COPVs, the large cylindrical COPVs in general degraded more as the IE increased.

Significant Findings

The following are the significant finding obtained from this task:

The test results revealed the high variability in the strength degradation as a function of various influencing variables, including vessel geometry, impact energy, internal pressurization level, impactor shape and impact location.

- The effect of impact locations was most discernable for the cylindrical COPVs. For the small cylindrical COPV, impacts in the center of the hoop region were more severe than impacts near the transition zone. However, for the large cylindrical COPVs, impact in the dome showed more damage than impact in the hoop region.

- The statistical spread in the BAI standard deviation was relatively large. This made it difficult to determine distinct variable effects or to predict with any degree of confidence the burst pressure based on visual or NDI of the impact-damaged region.

Figure 6-1: Vessel remnants after pneumatic burst at impact.
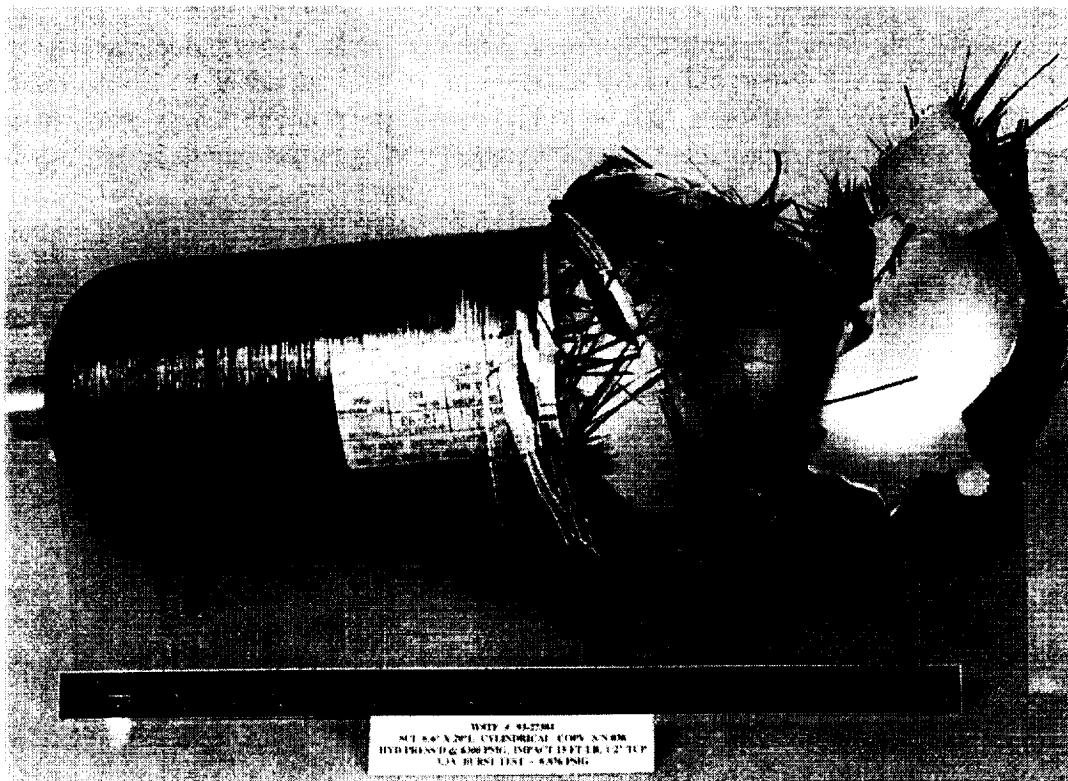
Figure 6-2: A typical vessel remnant after hydroburst test.

6-4

Table 6-1: Small Spherical (Type 2) COPVs Impact Test Results

S/N	IE (ft-lb)	Pressure Level at Impact (psi) and Test Fluid	BAI (psi)	Degrad, %	Remarks
	N/A	N/A	10,600	N/A	Average Baseline
B-77	25	Empty	11,106	>Baseline	Impact @ boss/0.5 in. tup
B-58	25	Empty	10,243	3	Norm Condition[1]
B-57	35	Empty	8,415	21	Norm Condition
B-61	35	Empty	7,136	37	Norm Condition
B-62	35	Empty	7,816	26	Impact @ Equater/0.5 in tup
B-69	35	Empty	8,920	16	1-in. tup
B-64	35	Empty	8,707	18	1-in. tup, not detected[2]
B-73	35	Empty	9,294	12	1-in. tup
B-72	35	Empty	9,826	7	Norm Condition/50 cyc
B-70	35	Empty	8,159	21	Norm Condition/50 cyc
B-84	35	Empty	9,113	14	Norm Condition/50cyc
B-85	35	Empty	8,894	16	Norm Condition
B-68	35	6,500(W)	9,924	12	Norm Condition
B-96	35	6,500(W)	9,914	6	Norm Condition
B-71	35	6,500(W)	9,417	11	Norm Condition
B-81	35	6,500(G)	10,496	1	Norm Condition
B-82	35	6,500(G)	9,294	12	Norm Condition
B-83	35	6,500(G)	9,396	11	Norm Condition
B-86	40	Empty	8,145	23	Norm Condition
B-78	50	Empty	7,399	30	Norm Condition

Nomenclature: BAI = burst strength after impact, IE = impact energy level, G = N_2 gas, W = water.

Notes:
1. Impacted at membrane section with 0.5-in. tup.
2. One out of three inspector missed visually.

Table 6-2: Small Cylindrical (Type 3) COPVs Impact Test Result

S/N	IE (ft-lb)	Pressure Level at Impact (psi) and Test Fluid	BAI (psi)	Degrad, %	Remarks
	N/A	N/A	10,700	N/A	Average Baseline
S-18	5	Empty	9,800	8	Norm condition[1]
S-06	10	Empty	8,884	17	Norm condition
S-32	15	Empty	8,246	23	Norm condition
S-05	15	Empty	8,377	22	Norm condition
S-30	15	Empty	9,257	14	Norm condition
S-08	15	Empty	10,123	5	Impact @ transition[2]
S-20	20	Empty	7,764	28	Norm condition
S-13	15	3,000[3](W)	9,892	8	Norm condition
S-09	15	3,000(W)	9,425	12	Norm condition
S-04	15	3,000(W)	9,776	9	Norm condition[5]
S-29	15	6,000[4](W)	7,510	30	Norm condition
S-22	15	6,000(W)	7,950	26	Norm condition
S-38	15	6,000(W)	8,877	17	Norm condition
S-31	15	6,000(G)	7,569	29	Norm condition
S-33	15	6,000(G)	N/A	N/A	Exploded[6]
S-37	15	6,000(G)	7,724	28	Norm condition

Nomenclature: BAI = burst strength after impact, IE = impact energy level, W = water, G = N_2 gas

Notes:
1. Impact at membrane section with a 0.5-in. tup.
2. One out of three inspectors missed visually.
3. 0.5 x MEOP
4. MEOP
5. All three inspectors missed visually.
6. The COPV exploded on the test stand 0.7 sec after impact.

Table 6-3: Large Cylindrical and Spherical COPVs Impact Test Results

S/N	IE (ft-lb)	Pressure Level at Impact (psi) and Test Fluid	BAI (psi)	Degrad, %	Remarks
Type 4					
	N/A	N/A	7,774	N/A	Average Baseline
93-27662	25	Empty	7,263	7.5	Impact @ Hoop[2]
93-27666	30	Empty	6,482	17.4	Impact @ Hoop
93-27661	35	Empty	5,953	24.2	Impact @ Hoop
93-27668	35	Empty	5,126	34.7	Impact @ Dome
93-27670	35	Empty	5,309	32.4	Impact @ Dome
93-27663	35	4,500[2](W)	5,877	25.1	Impact @ Hoop
93-27664	35	4,500(W)	6,010	23.4	Impact @ Hoop
93-27660	50	Empty	5,401	31.2	Impact @ Hoop
93-27658	65	Empty	5,185	33.9	Impact @ Hoop
Type 1					
	N/A	N/A	7,280	N/A	Average Baseline
93-27681	35	Empty	7,054	3.1	Impact @Membrane-Inlet
93-27671	65	Empty	7,256	0.3	Impact @ Membrane-Boss
93-27672	100	Empty	6,256	14.1	Impact @Membrane-Boss
93-27673	100	4,725[3](G)	6,228	14.5	Impact @Membrane-Boss
93-27674	100	4,725(G)	5,987	17.8	Impact @Membrane-Inlet
93-27675	100	4,725(G)	6,235	14.6	Impact @Membrane-Inlet
93-27676	100	Empty	6,294	13.5	Impact @Membrane-Inlet
93-27679	100	Empty	6,941	4.7	Impact @Membrane-Inlet
93-27681	100	Empty	7,054	3.1	Impact @Membrane-Inlet

Nomenclature: BAI = burst strength after impact, IE = impact energy level, W = water, G = N_2 gas

Notes:
1. Impact with a 0.5-in. tup
2. MEOP
3. 1.05 x MEOP

CATEGORY

Composite Damage Tolerance

REFERENCE

Mahler, M., *et al.*, "Propagation and Control of Crack-like Damage in Curved Composite Panels Under Combined Loads," 41st AIAA/ASME/ASCE/AHS/ASC Structures, Structural Dynamics, and Materials Conference and Exhibit, AIAA-2000-1759, 2000.

ABSTRACT

Certification and damage tolerance criteria are critical technologies for the advancement of composites structures on commercial aircraft. Understanding and predicting the path and propagation load of crack-like damage in these anisotropic structures is necessary to meet certain requirements. Under the NASA High Speed Research program, the behavior of these cracks were investigated using honeycomb core-stiffened panels. The work was complimented by previous work using flat laminated panels. The panels were designed with integral straps that contained a majority of the 0° plies in the laminate. The difference in stiffness of the base panel and tear strap region was designed to change the direction of crack propagation. The panels were tested under combined loads typical of those experienced on an aircraft. Finite element analysis was used to predict the strain distribution around the crack tip. The cracks were analyzed as ideal cracks and the strain around the crack was interrogated in an R-θ coordinate system. The method developed facilitated prediction of the direction that the crack would propagate and the initial failure load. The cracks in both panels propagated as predicted.

SUMMARY

Demonstration of damage tolerance and fail safety in composites through control of the damage as it evolves, along with an understanding of the control mechanism, represent major steps forward in the development of damage tolerant composite structures. Two sizes of panels were tested - one a curved, 4-ft square composite honeycomb panel and one a curved 10-ft by 6-ft panel, both containing a centrally located circumferential sawcut. See Figures 6-3 – 6-5 for the setup of the tear strap and layout of a typical panel.

The panels were subjected to combined loads. The models were run in MSC/NASTRAN to compare with test results. See Figure 6-8 for the models. The correlation between predicted and measured strains proved to be within 10%. Figures 6-4 – 6-7 highlight the predicted versus observed path of damage for the 4-ft panel.

The study demonstrated the ability to control and contain catastrophic damage growth in composite sandwich panels. From the comparison of FEA and test results, the damage progression path in curved panels subjected to combined loads can be accurately predicted by following the orientation of the dominant notch tip laminate strain failure index profile.

Figure 6-3: Failure of tension-loaded flat tear strap panels.

Figure 6-4: Longitudinal tear strap design.

Figure 6-5: Basic 10-ft by 6-ft panel design.

6-9
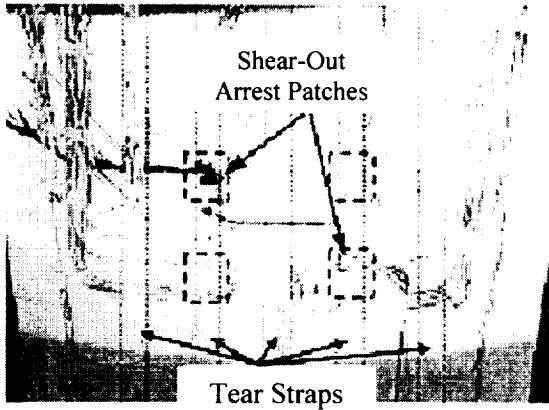
Figure 6-6: Photograph of failed 4-ft panel.
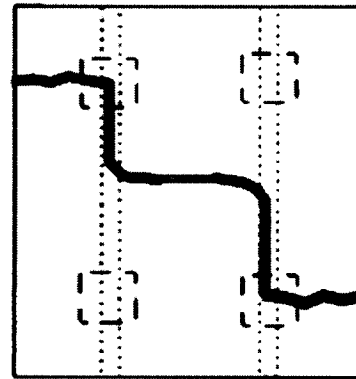
Figure 6-7: Predicted damage progression in 4-ft panel.
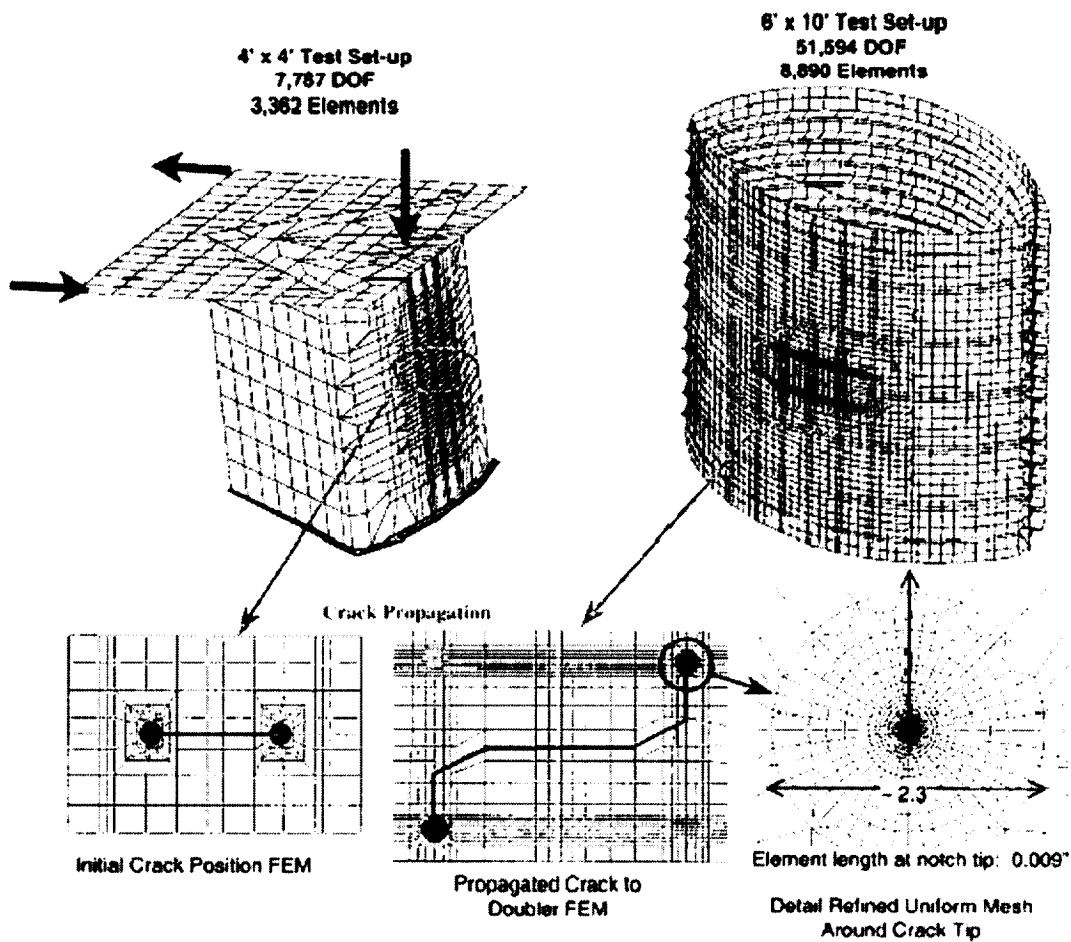
Figure 6-8: Panel and test fixture finite element model.

CATEGORY

Composite Damage Tolerance

REFERENCE

Fisher, C. and G. Lesieutre, "Health Monitoring of High Energy Density Rotor for Use in Spacecraft Applications," *Proceedings of the 44th International SAMPE Symposium*, Vol. 2:2145-2154, 1999.

ABSTRACT

Flywheel energy storage (FES) systems have demonstrated the potential to store very high amounts of energy with minimum weight when compared to chemical battery systems. A high energy density flywheel is needed in order to achieve a lightweight design that is competitive with chemical battery systems, however, there are major concerns regarding the safety of operation and the structural integrity of critical components, such as the rim, hub, and shaft. The stresses at high speeds (up to 80,000 rpm) can be very high and cause fiber breakage, matrix microcracking, debonding, and delamination, which lead to premature failure of the rotor design. The consequences of failures of the rotor are a major concern regarding the implementation of a flywheel energy storage system for a spacecraft system and therefore a design approach that includes the use of health monitoring is necessary in order to ensure fail-safe operation.

SUMMARY

By monitoring the radial motion of the rotor or shaft relative to the fixed housing for changes in the center of mass, it is anticipated that one can identity growing flaws. Analyses found that a delamination moves the center of mass between 1 and 10 microns depending of the speed and size of the flaw.

The author contends that ensuring full containment of the flywheel in case of catastrophic failure using a high strength structure is too heavy and costly. For this reason, a system that prevents catastrophic failure of the rotor is necessary. Figure 6-9 shows an FE model of a typical rotor. The rim is filament wound with T1000 fibers and a unidirectional glass epoxy composite is used for the hub.

Two specific failure modes occur in a fiber reinforced composite: (a) debonding, the separation of fibers from the matrix, and (b) delamination, the separation of the individual plys. Table 6-4 shows the possible failure modes of each component. It is important to characterize each type of failure mode in order to identify control strategies for de-rating the system and/or shutting it down completely.

The rotor dynamics will be monitored by the health monitoring system shown in Figure 6-10. Sensors that monitor radial motion will be placed on the shaft and rim of the rotor. Any changes in the mass properties of the rotor, caused by a flaw, will result in balance changes of the rotor.

The balance changes will cause a change in the rotor motion and the sensors will then detect the changes in radial position. By the changes in the rotor motion, the failure mode of the flaw along with its size and severity can be determined.

Tests with masses being released from a spinning rotor, simulating a rotor imbalance have been performed. Another test with tape being released from a spinning rotor to simulate the formation of a delamination were also conducted. These tests proved successful in characterizing flaws and their severity. Future tests are planned with sub-scale rotors manufactured with different types of imbedded flaws, and some without.

FE analyses indicated that a delamination moves the mass center on the order of 1 to 10 microns depending on the speed and size of the flaw. A rotodynamic model is also being developed to account for growing flaws. The connections between the rigid rotor and the flexible ring are continuous radial springs.
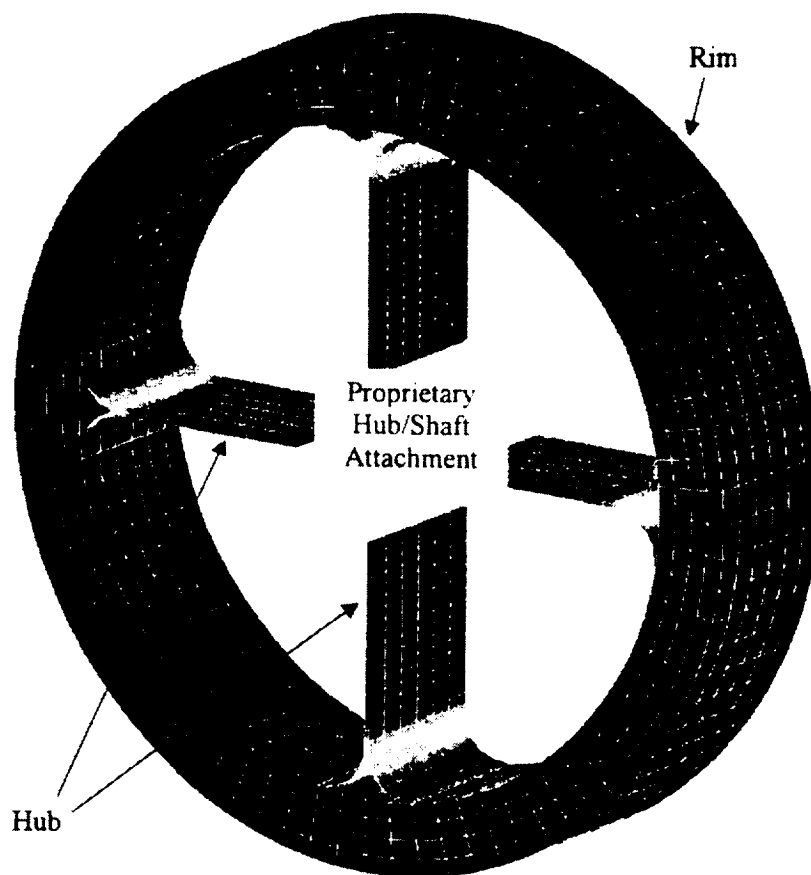
Figure 6-9: Components of a typical rotor.
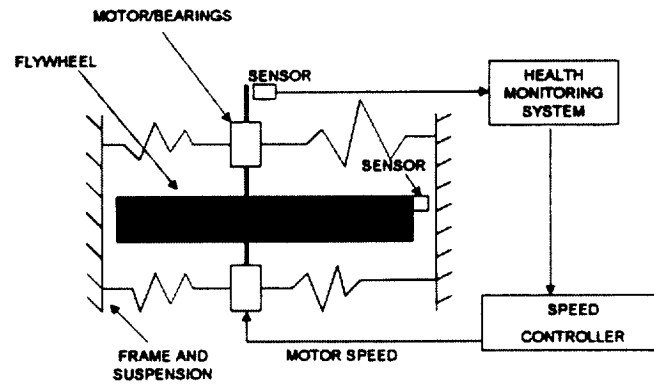
Figure 6-10: Components of health monitoring system.

Table 6-4: Possible Failure Modes for Rotor Components

	Interface of Hub/Rim	Hub	Rim
Breaking of Fibers		Compression Causes Microbuckling	High Hoop Stresses
Microcracking of the Matrix	Compression Stresses	High Compression Stresses	Low Radial/Shear Strength
Debonding			Low Radial/Shear Strength
Delamination	Weak Link		

CATEGORY

Composite Damage Tolerance

REFERENCE

O'Brien, T. K., *Towards a Damage Tolerance Philosophy for Composite Materials and Structures*, NASA TM-100548, 1988.

SCOPE

A Damage-threshold/Fail-safety approach is proposed for ensuring that composite structures are both sufficiently durable for economy of operation, as well as adequately fail-safe or damage tolerant for flight safety. Matrix cracks are assumed to exist throughout the off-axis plies. Delamination onset is predicted using a strain energy release rate characterization. Delamination growth is accounted for in one of three ways: either analytically, using delamination growth laws in conjunction with strain energy release rate analyses incorporating delamination resistance curves; experimentally, using measured stiffness loss; or conservatively, assuming delamination onset corresponds to catastrophic delamination growth. Fail-safety is assessed by accounting for the accumulation of delaminations through the thickness. A tension fatigue life prediction for composite laminates is presented as a case study to illustrate how this approach may be implemented. Suggestions are made for applying the Damage-threshold/Fail-safety approach to compression fatigue, tension/compression fatigue, and compression strength following low velocity impact.

SUMMARY

The purpose of the paper is to demonstrate how a Damage-threshold/Fail-safety approach may be used to predict the tension fatigue life of composite laminates, and then illustrate the similarities between this application and the use of the same philosophy for predicting compression fatigue life and compression strength after low velocity impact.

Several methods for improving the performance of impacted composite panels and components have been proposed. One approach is to increase the inherent toughness of the composites by using tougher resin matrices, such as toughened epoxies and thermoplastics, or to modify the form of the material by adding tough adhesive layers during the layup or as interleaves in the prepreg. For wing skin design, the application referenced in this article, the goal has been to increase the compression failure strain after impact above the strength of a comparable laminate with an open hole. Although compression strength is greatly reduced after low velocity impact, any further reduction with subsequent fatigue cycles is minimal; giving impacted composite panels very flat compression S-N curves. However, the compression S-N curve for composite laminates with an open hole is not flat, even for toughened matrix composites, because the interlaminar stresses at the hole boundary cause delaminations that form in fatigue and grow with increased cycles.

Many papers have been published that propose a fracture mechanics characterization of composite materials based on the rate of delamination growth with fatigue cycles, da/dN in terms of the strain energy release rate, G. This characterization is analogous to fatigue crack growth in metallic structures. Unlike metals, where the rate of crack growth with cycles is correlated with the stress intensity factor at the crack tip, delamination growth in composites occurs much more rapidly. This growth rate is often over barely one order of magnitude in G. For this reason, small uncertainties in applied load may yield large uncertainties in delamination growth rates.

The most common technique for characterizing delamination onset in composite materials is to run cyclic tests on composite specimens, where G for delamination growth is known, at maximum load or strain levels below that required to create a delamination under monotonic loading.

A previous Damage-threshold/Fail-safety approach for composite fatigue analysis involved the following steps:

a) Predict delamination onset thresholds using fracture mechanics.
b) Assume complete propagation occurs immediately after the delamination threshold is exceeded.
c) Determine the remaining load carrying capability of the composite with delamination present using composite mechanics (i.e., check for fail safety).
d) Iterate on steps 1-3 to account for multiple sources of delamination.

Step 2 is a conservative approach. One alternative discussed in the paper is to monitor stiffness loss in real time, and hence reflect the consequence of delamination growth, and other damage mechanisms, as they occur.

Figure 6-11 shows the number of cycles at a given maximum cyclic stress for edge delaminations to form (solid symbols), for the first local delamination to form at the ±45° interface (brackets), and for fatigue failure to occur (open symbols). In order to predict the ultimate fatigue failure of these laminates, the onset and growth of the damage observed must be characterized, and the influence of this damage on laminate stiffness and strength must be determined. Once these relationships are known, fatigue life may be predicted using the Damage-threshold/Fail-safety approach.

Figure 6-14 shows the influence of damage on laminate stiffness. As matrix cracks accumulate, and as delaminations form and grow, the stiffness of the laminate decreases. Laminate stiffness is the ratio of the remote stress to the global strain in the laminate. The amount of stiffness loss due to delamination also depends on the laminate layup and the relative moduli of the fiber and the matrix, as well as the location and extent of the delamination. Delaminations starting from matrix cracks will affect laminate stiffness differently than delaminations growing from the straight edge.

Figure 6-12 shows the steps that would be required to predict stiffness loss as a function of fatigue cycles using a G characterization of damage onset and growth. In Part (a), plots of G versus log N are generated to characterize the onset of delamination. Power law relationships

between G and the rate of growth of delamination with fatigue cycles are needed to characterize damage growth. Part (b) uses these material characterizations, to predict the decrease in matrix crack spacing, 2s, and the increase in delamination size, a, with fatigue cycles. This information can then be used to predict the decrease in modulus with cycles, which for a constant stress amplitude test is tantamount to predicting the increase in global strain with cycles (Part (c)). Some examples of G versus log N curves for several are shown in Figure 6-14.

Even if one could achieve a truly generic description of damage accumulation with cycles, the resulting stiffness loss prediction, and hence the prediction of increasing global strain with cycles, is necessary, but not sufficient, to predict fatigue life. The final failure of the laminate is governed not only by loss in stiffness, but also by the local strain concentrations that develop in the primary load bearing plies, which in most laminates are zero degree plies. Figure 6-13a shows that fatigue failures typically occur after the global strain has increased because of the fatigue damage growth, but before this global strain reaches the global strain at failure, ε_F, measured during a static strength test. This implies that local strain concentrations must be present in the zero degree plies that control the laminate strength. Once delaminations initiate at matrix ply cracks anywhere through the laminate thickness, the local strain will increase significantly in all of the remaining uncracked plies. If several delaminations form at matrix cracks throughout the laminate thickness at one location, then the local strain on the zero degree plies at that location may reach the static failure strain, resulting in the observed fatigue failure (Figure 6-13b).

Based on the Damage-threshold/Fail-safety approach, fatigue failure of the composite would correspond to the number of cycles where the damage growth increased the global maximum cyclic strain, ε_{max}, to the current value of the effective global failure strain $(\varepsilon_F)_i$. This approach does not require a prediction of damage growth with fatigue cycles if the laminate stiffness loss can be monitored in real time. When this is possible, only the incremental decrease in the effective failure strain needs to be predicted to predict fatigue life. This may be accomplished by assuming that matrix cracks exist in all of the off-axis plies. This assumption is analogous to assuming the existence of the smallest flaw in a metal that could be detected by NDE to assess damage tolerance. Then, the number of fatigue cycles to onset of each local delamination through the thickness may be predicted using delamination onset criteria (Figure 6-12a) along with strain energy release rate analyses for local delamination.

The Damage-threshold/Fail-safety approach was used to predict the fatigue life of $(45/-45/0/90)_s$ E-glass epoxy laminates. The strain energy release rate, G, is plotted versus log N in Figure 6-15. Significant scatter is observed in G_c, potentially due to the interaction that occurred between the edge delamination as it formed and the 90° ply cracks that were extensive before edge delamination onset. These values may be artificially elevated if extensive 90° cracking is present in the laminate.

Many factors may affect delamination onset and growth. For example, the toughness of the matrix will have a very strong effect on G_c but very little influence on delamination onset at 10^6 cycles (see Figure 6-14). Therefore, the slope, m, as measured by fitting the delamination onset data with the equation $G = m \log N + G_c$ will be lower for a brittle matrix composite than a tougher matrix composite (Figure 6-16a). Assuming that the brittle and tough matrix composites

6-16

eventually reach a common G threshold for delamination onset at $N \geq 10^6$ cycle, then the exponent, n, in a delamination growth law would be lower for the tougher matrix composite (Figure 6-16b).

The significance of accumulated delaminations on compression strength has been documented previously by comparing the strength of laminates with one, two, or three implanted delaminations through the thickness to identical laminates with either barely visible or visible impact damage as shown in Figure 6-17. Lower compression strengths were observed for the impacted laminates, which typically contain delaminations in nearly every interface. Figure 6-18 shows a plot of cycles to failure as a function of stress amplitude for $(0/90/0/45/-45/0)_s$ graphite epoxy laminates subjected to fully reversed cyclic loading, either in the initially undamaged state or following an impact. The data indicate that the compression strength after impact is very low compared to the fatigue behavior of the virgin laminate. Most of the strength reduction occurs after the impact, with very little degradation due to subsequent cyclic loading.

For composites loaded in compression, final failure is not necessarily determined by the local strain concentration in the zero degree plies, but often results from a global instability that occurs after delaminations accumulate through the thickness and become locally unstable. In these situations, where the accumulation of delamination through the thickness occurs rapidly, prediction of the initial delamination onset may provide a reasonable estimate of fatigue life in addition to establishing the delamination durability of the composite.
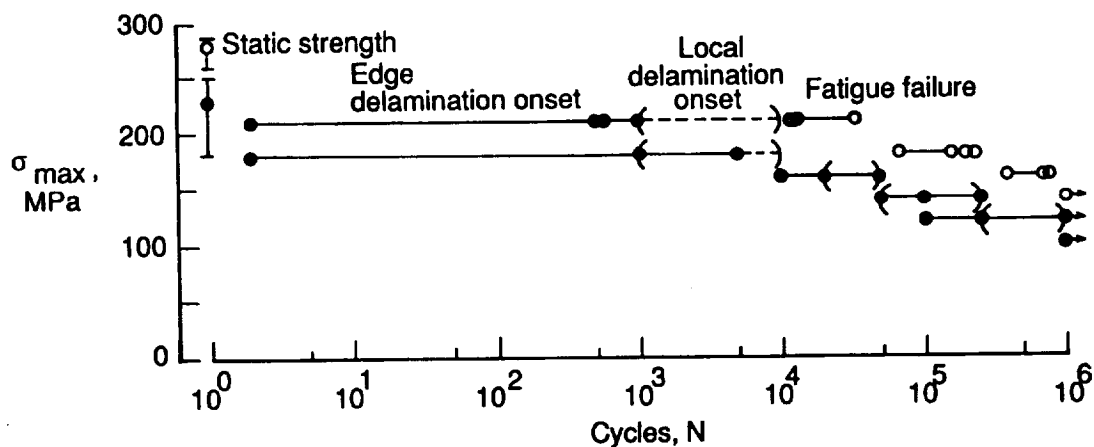
Figure 6-11: Tension fatigue behavior of $(45/-45/0/90)_s$ X751/50 E-glass epoxy laminates.

6-17

(a) Characterization of damage onset and growth

(b) Prediction of matrix cracking and delamination with fatigue cycle

(c) Prediction of stiffness loss with fatigue cycles
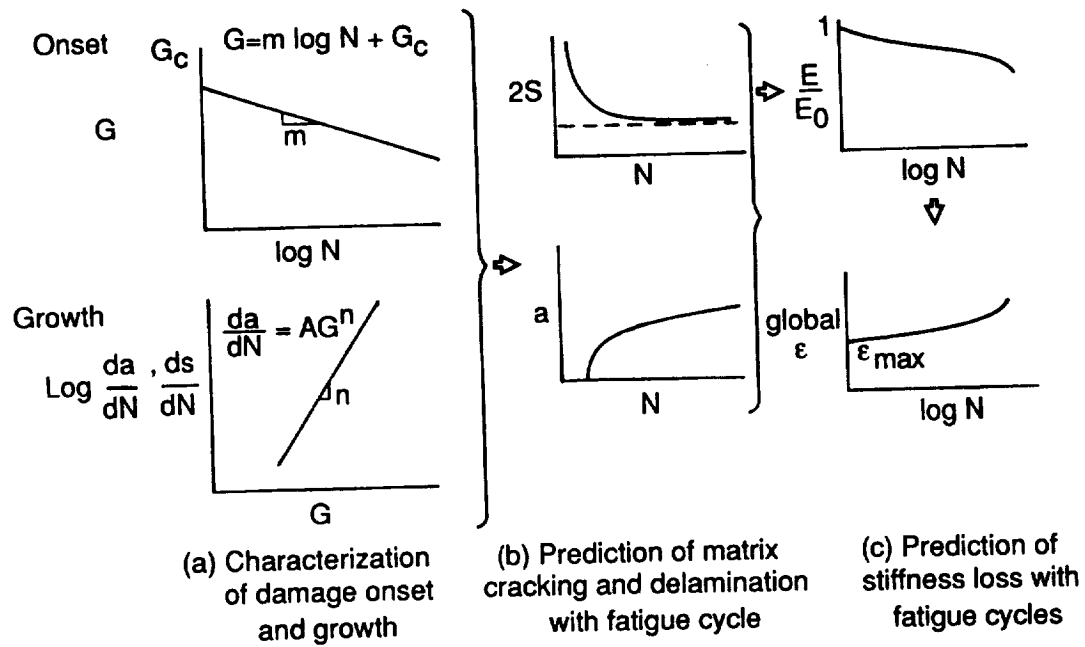
Figure 6-12: Prediction of stiffness loss in composite laminates.

ε_F = strain at failure in static test

(a)

(b)
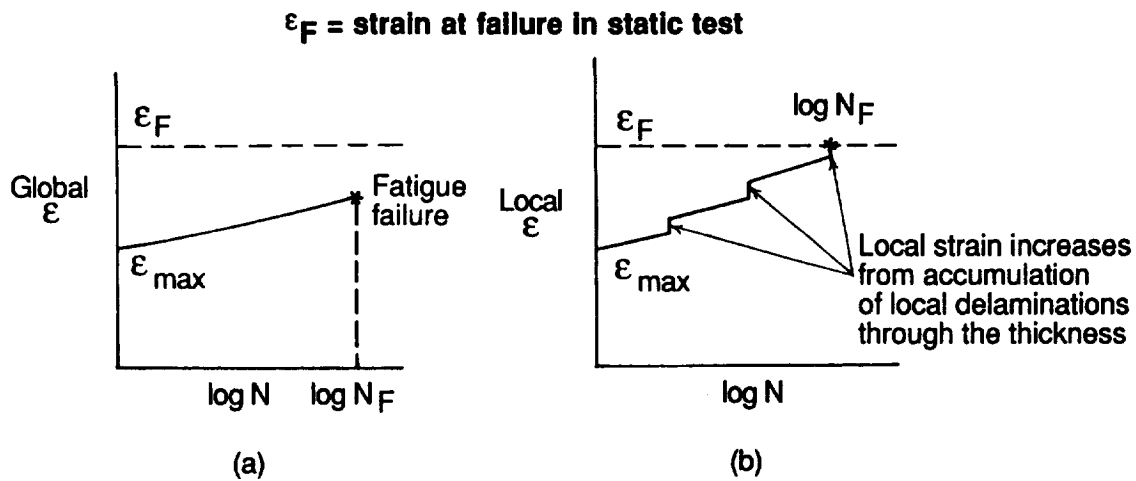
Figure 6-13: Increase in global versus local strain in zero degree plies.

6-18
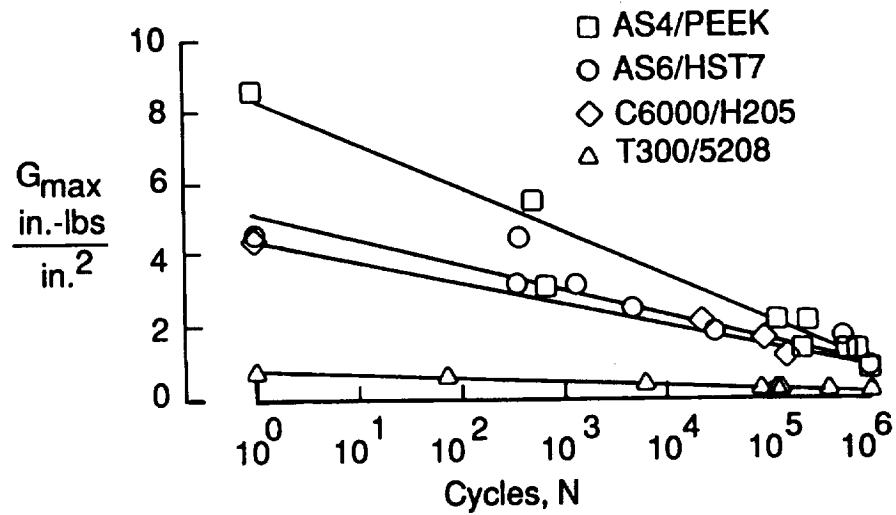
Figure 6-14: Mechanical strain energy release rate in delamination onset as a function of fatigue cycles.
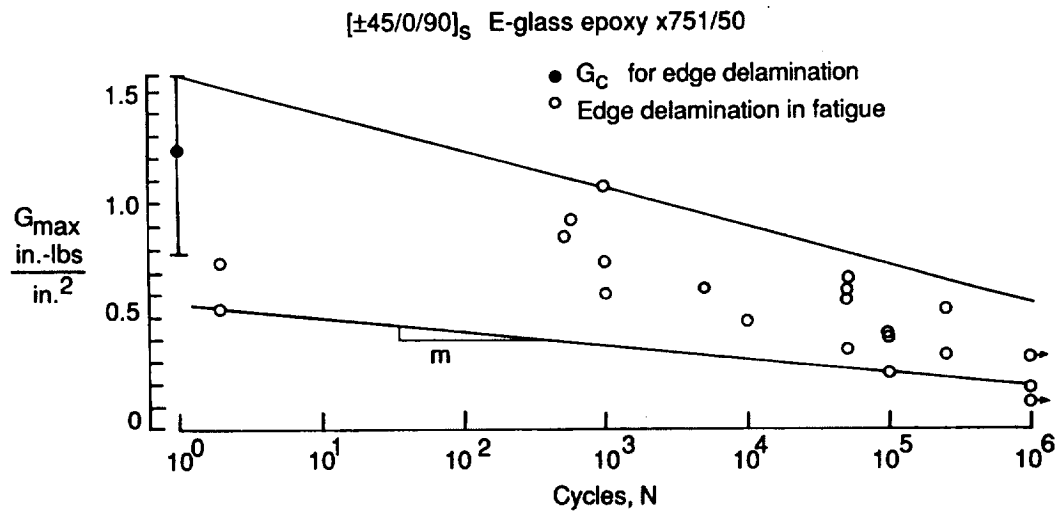
Figure 6-15: Delamination onset criterion.

$$\frac{da}{dN} = AG_{max}^{n}$$
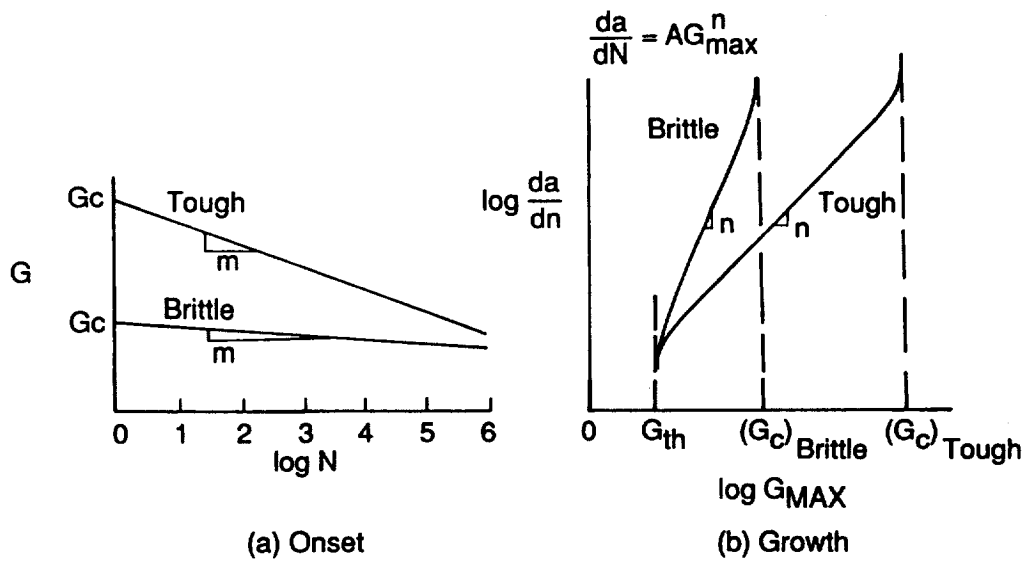
(a) Onset

(b) Growth

Figure 6-16: Effect of matrix toughness on delamination onset and growth.
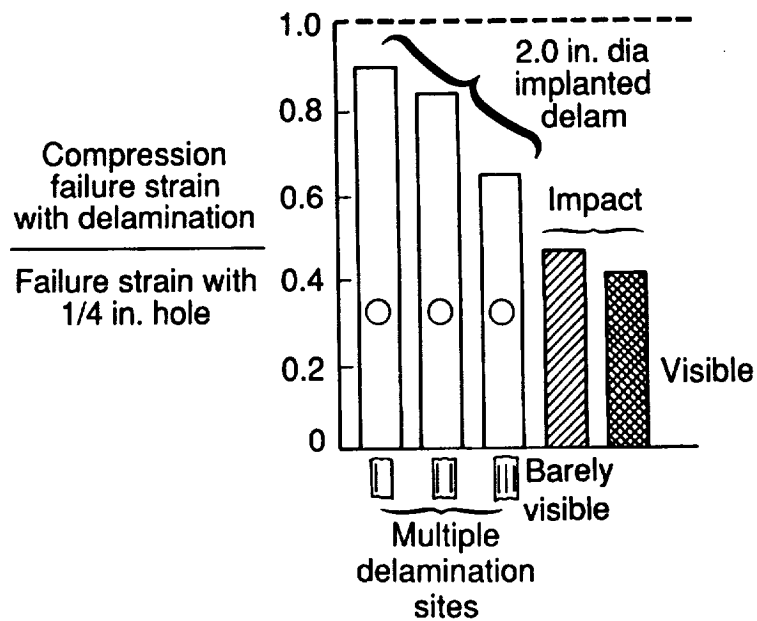
Figure 6-17: Normalized compression failure strain reduction for laminates with implanted delaminations or impact damage.
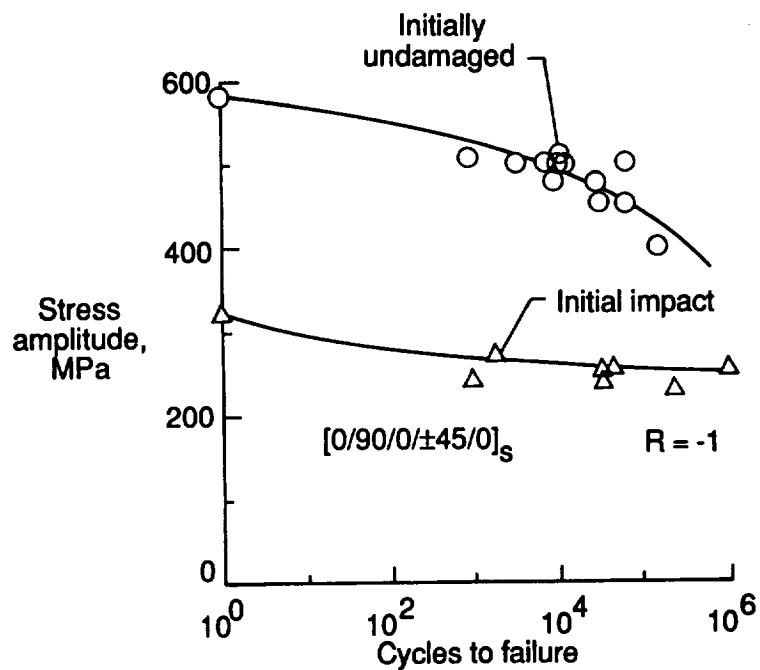
Figure 6-18: Fatigue behavior of initially undamaged and impacted graphite epoxy laminates under fully reversed cyclic loading.

CATEGORY

Composite Damage Tolerance

REFERENCE

Chamis, C. C and C. A. Ginty, *Fiber Composite Structural Durability and Damage Tolerance: Simplified Predictive Methods*, NASA-TM-10079, 1987.

ABSTRACT

Simplified predictive methods and models ("theory") to evaluate fiber/polymer-matrix composite material for determining structural durability and damage tolerance are presented and described. This "theory" includes equations for (1) fatigue and fracture of composites without and with defects, (2) impact resistance and residual strength after impact, (3) thermal fatigue, and (4) combined stress fatigue. Several examples are included to illustrate applications of the "theory" and to identify significant parameters and sensitivities. Comparisons with limited experimental data are made.

SUMMARY

The numerical models presented are based on composite micromechanics and ply-stress influence coefficients. They are, therefore, generic and applicable to all types of fiber/polymer-matrix composites including intra- and interply hybrids.

The following are the fundamental aspects underlying the development of the predictive methods in the paper:

a) Holes, slits, and impact damage (defects) induce similar strength degradation in fiber-composite laminates where the characteristic dimensions of these defects are negligible compared to the dimensions of the laminate, see Figure 6-19.
b) Fatigue degrades all ply strengths at approximately the same rate, see Figure 6-20.
c) All types of fatigue degrade laminate strength linearly on a semilog plot including: (a) mechanical; (b) thermal; (c) hygral (moisture); (d) combinations of mechanical, thermal, hygral, and reverse-tension compression.
d) Laminates generally exhibit linear behavior to initial damage under uniaxial or combined loading including hygrothermal effects.
e) All ply stresses (mechanical, thermal, and hygral) are predictable by using linear laminate theory.
f) Stress concentration factors for circular holes are available.

In the section on thermal fatigue it was noted that the factors which contribute to the transverse ply stress will also contribute significantly to the number of thermal cycles to initial transply cracking. The most prominent of these factors, and the most difficult to quantify accurately

include: (1) temperature profile through the laminate thickness, (2) thermal cyclic degradation coefficients, and (3) in-situ ply-transverse strength.

Figure 6-21 shows the comparison for composites with defects under reverse fatigue loading. The two predicted curves show the difference between the static fracture stresses for tension and compression. As can be seen the experimental data are approximately between the two predicted curves.

The predictive equation derived for combined hygrothermo-mechanical cyclic loading was used to estimate the number of cycles for various conditions for three different laminates, as shown Table 6-5.
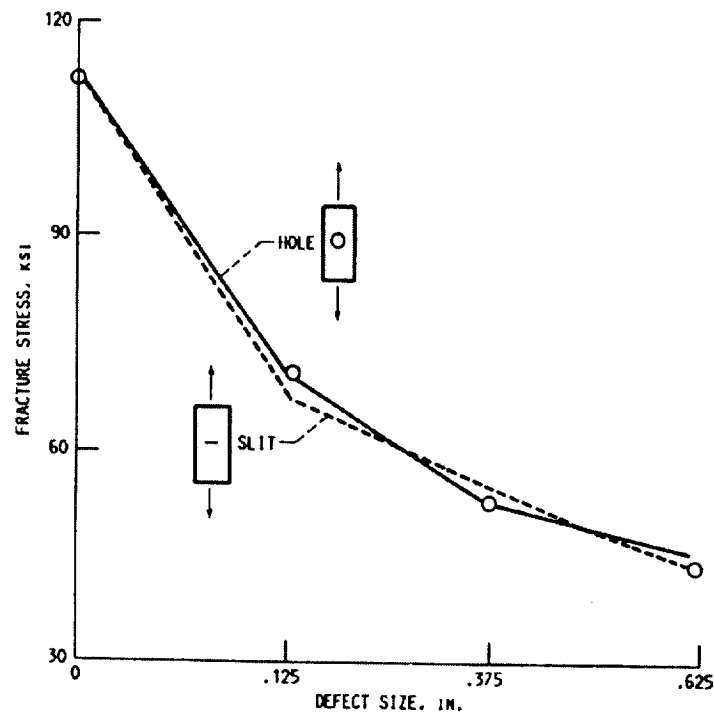
Figure 6-19: Laminate static fracture data ([0/±45/90]$_{2S}$, T300/E).

FATIGUE

○ LONGITUDINAL, 0°
□ TRANSVERSE, 90°
△ INTERLAMINAR SHEAR, ±45°

OPEN SYMBOLS DENOTE ROOM TEMPERATURE, WET
SOLID SYMBOLS DENOTE ROOM TEMPERATURE, DRY

ROOM TEMPER-
ATURE, WET

ROOM TEMPER-
ATURE, DRY

$$\frac{S}{S_0} = \left\{ \left[\frac{T_{GW} - T_T}{T_{Go} - T_{To}} \right]^{1/2} - 0.10 \; LOG \; N \right\}$$

STRESS (CYCLIC/STATIC), S/S_0

LOG, FATIGUE CYCLES
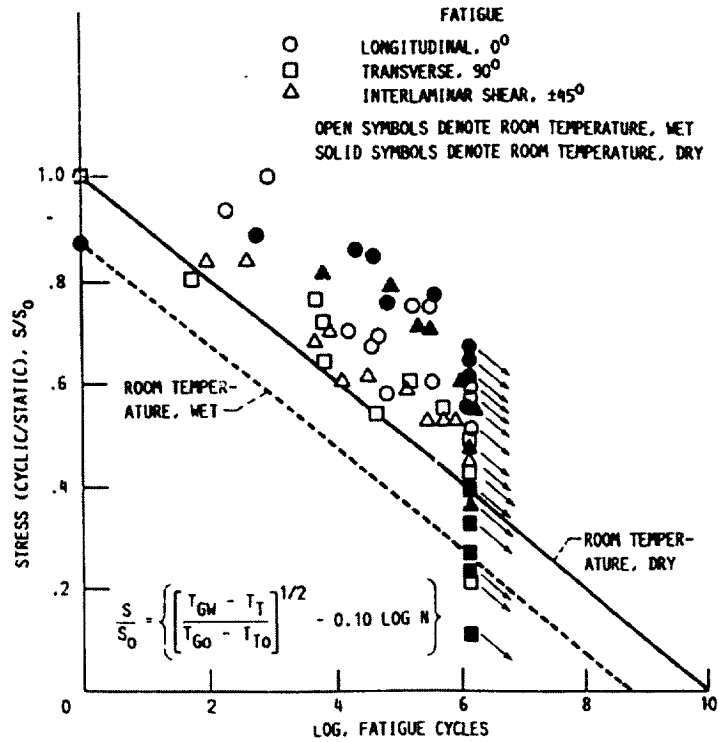
Figure 6-20: Compressive life and durability as graphite-fiber/epoxy.

TENSION-TENSION

R = -1

COMPRESSION-
COMPRESSION

DATA (REF. 3)

$$\frac{2S_{CCYC}}{S_{CO}} = 1 - 0.05 \; LOG \; N \quad \begin{cases} S_{CXXT} = 110 \; KSI \\ S_{CXXC} = 80 \; KSI \end{cases}$$

CYCLIC STRESS, KSI

LOG FATIGUE CYCLES
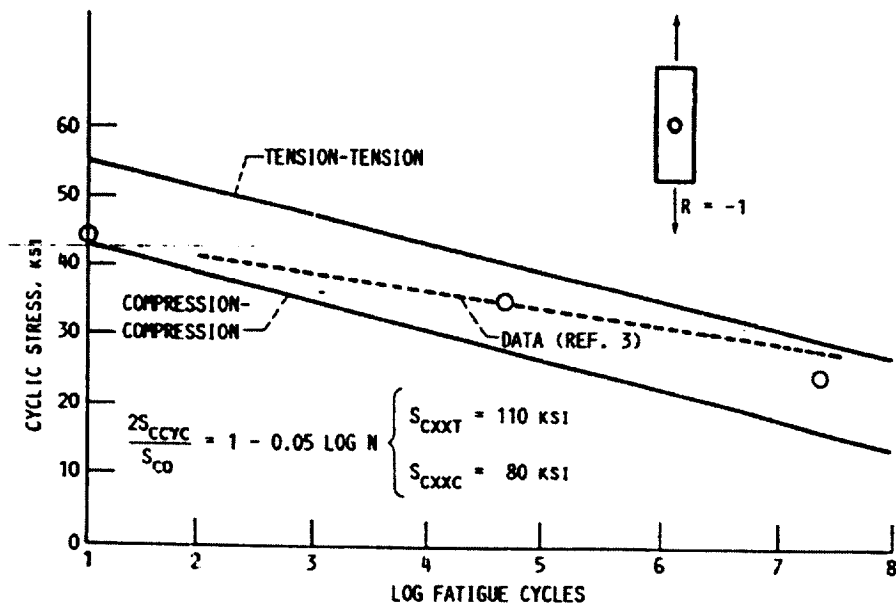
Figure 6-21: Comparisons of predicted fatigue strength with data ([0/±45/90]$_{2S}$, T300/E laminate).

Table 6-5: Cycles to Initiate Transply Cracks Depend on Laminate Configuration and Type of Loading Conditions (as Graphite Fiber/epoxy at 0.62 FVR)

[Fatigue degradation coefficients are assumed to be $B_H = B_T = B_L = 0.1$.]

(a) Ply-transverse stress influence coefficients

Loading condition	Laminate configuration		
	$[\pm45/0/90]_s$	$[90_2/\pm10]_s$	$[\pm30/0_3]_s$
Stress along 0° ply direction, σ_{cxx} Use temperture, T^a Use moisture, M Transverse ply-strength tension/compression, $S_{\ell22T}/S_{\ell22C}$, ksi	0.145 −16.681 −1298.265 8/20	0.170 −12.280 −1170.719 8/20	−0.022 −7.698 −571.146 8/20

(b) Cycles to failure

Loading condition	Laminate configuration			Comments
	$[\pm45/0/90]_s$	$[90_2/\pm10]_s$	$[\pm30/0_3]_s$	
Applied stress, N_L	36 500	4220	>100x10^6	σ_{cxx} = 30 ksi
Applied stress and residual stress, N_L	1	1	>100x10^6	σ_{cxx} = 30 ksi + σ_R
Elevated temperature cycling[b], N_T	76 620	234 060	987 000	T = 250 °F
Cryogenic temperature cycling[b], N_T	180	275 260	>100x10^6	T = 300 °F
Moisture cycling[c], N_M	>100x10^6	>100x10^6	>100x10^6	M = 1 percent

[a]Cure temperature, 350 °F.
[b]Cyclic temperatures are from room temperature to T.
[c]Cyclic moisture is from dry to M.

CATEGORY

Composite Damage Tolerance

REFERENCE

Sollars, T. A., *Shuttle/Centaur G-Prime Composite Adapters Damage Tolerance/Repair Test Program*, NASA 87-0792, 1987.

ABSTRACT

One major question involved in selection of a composite material system for structural applications is, "How damage-tolerant is it?" While this is a valid concern, the term "damage-tolerant" must be better defined. The purpose of our program was to answer that question for one particular application and also to define clearly "damage tolerance" with respect to the Shuttle/Centaur G-Prime composite corrugated adapters.

There were three main objectives in the Composite Adapters Damage Tolerance/Repair (DT/R) Test program. The first was to determine the effects of likely-to-occur and potentially critical defects or damages on the adapters' strength and stability. The second was to determine the adequacy of repairs on significantly damaged areas, and the third was to generate enough nondestructive investigation (NDI) damage data to upgrade C-SCAN acceptance criteria for production parts.

Justification for the program's existence was based on three premises: (1) defects and damage would occur. It was imperative to develop a sound rationale for accepting or rejecting discrepant parts. (2) Competent repair methods had to be developed to deal with significantly damaged areas, and most important was (3) the need to determine the structural effects of nonvisible damage that could accidentally occur subsequent to final ultrasonic inspection during assembly, shipment, or in service. The benefits to be realized were many. Rational accept/reject criteria and repair methods would reduce both engineering liaison costs and any unnecessary scrappage of parts. Most importantly, a successful "damage-tolerant" design would ensure that degradations of strength and stability due to the presence of undetected defects or damage would not be catastrophic.

SUMMARY

The integration of the Centaur high performance upper stage vehicle into the Space Shuttle offered a significant increase in the performance capability of the Space Transportation System (STS). The vehicle is shown in Figure 6-22. The vehicle was designed with minimum weight as a primary goal; thus, the aluminum sheet-stringer cylindrical forward and aft adapters were replaced with corrugated graphite/epoxy composite adapters. The corrugation design, shown in Figure 6-23, was chosen because the adapters had to carry loads between two metal rings, one at cryogenic temperatures and the other relatively warm. The corrugation was ideal in

6-26

accommodating the severe reduction in diameter of the cold ring without buckling in the hoop direction.

The structural efficiency of a graphite/epoxy adapter and its relatively low thermal conductivity (K) compared to an aluminum or titanium adapter offered a substantial weight savings for the applied loads in the cryogenic environment of the LO_2 and LH_2 tanks.

In order to develop accept/reject criteria for the Shuttle/Centaur G-Prime composite adapters, it was necessary first to identify the potential threats that existed during fabrication, assembly, and service life. Some of these threats are shown in Figure 6-24. As an example of the effect of a flaw, a hole that was accidentally drilled in an improper location would result in a stress concentration that ultimately could cause premature failure. In generating damage tolerance/repair test requirements for the Shuttle/Centaur composite adapters, loading and environmental conditions were considered as well as critical damages and defects. The basic test plan is presented in Figure 6-25.

The first phase in the defect and threshold impact damage investigation was producing and detecting flaws. In order to duplicate manufacturing defects, panel lay-up deliberately included voids or disbonds in the radii regions that were large enough to show up during NDI. Impact damage from foreign objects was induced by dropping a weighted impactor on corrugation radii as well as on corrugation flat regions. The goal was to obtain maximum internal damage without any external visual signs of damage.

Fatigue effects were considered in the test plan preparation. Published data on the potential fatigue threshold of the chosen composite material indicated that fatigue at the main fasteners and fittings would not cause failure. Coupon data from the literature also showed that fatigue should not be a problem for the basic laminates of the G-prime composite adapters. For these reasons, fatigue was included primarily to evaluate its influence on growth of imposed damages.

The objective of the in-house test program was to determine the effects of defects/damages and repaired areas on the compression strength of the Shuttle/Centaur G-Prime composite adapters at cryogenic temperatures, and then compare results to data from similar ambient tests and room temperature (RT) tests. A higher failure load value was expected for the cryogenic tests due to the higher Young's modulus and F_{cu} for the laminate at cryogenic temperatures. Table 6-6 gives a summary of the compression test results. The average failure load for the RT damaged specimens (-4, -2) was 3575 lb, while the average failure load for the cryogenic damaged specimens (-3, -1) was 3550 lb (99.3% of the RT failure load). Although, the cryogenic specimens were expected to fail at higher loads, NDI revealed that the cryogenic specimens had been somewhat more damaged than the RT specimens, even though the impact energy was intended to be consistent. The main conclusion drawn from these tests was that no cryogenic correction factor had to be applied to the combined loads RT test panels. However, both the cryogenic and RT damaged panels seemed to have a reduction in strength of approximately 41 to 47% from their respective undamaged panels. A possible explanation for this was the fact that both corrugations of each specimen were damaged, so there was really no alternative load path available.

The test program's other main objective was to determine the effects of defects/damages and repaired areas on the combined load (compression and shear) carrying capability under both static and fatigue test conditions of the G-Prime composite adapters. All of these tests were run at room temperature. Both test specimens were comprised of four corrugations of their respective base layups and two buildup regions, one on either side, for attachment to the shear load reaction fittings. Panel damage types included a resin insert, Teflon insert/patch repair, puncture/repairs, poorly drilled holes, impacts on lower radii regions from the back side, and impacts in the flat region from the front side. Strain gage locations differed between the forward and aft adapter test specimens.

Figure 6-26 shows the static failures for all G-Prime McAir forward adapter test panels (with the 1.25 correction factor applied). All panels, except FA3, were tested to failure by arbitrarily selecting the axial load and then ramping shear to failure. Failure of FA3 was a pure shear load condition. FA3 and FA2 failed at a lesser axial load than desired. FA4 and FA5 did demonstrate that the load-carrying capability of the G-Prime forward adapter was not diminished by the applied fatigue cycling.

Figure 6-27 shows the static failures for all of the G-Prime aft adapter test panels (with the 1.28 correction factor for axial load applied). No damaged G-Prime composite aft adapter panels tested in combined compression and shear at McAir failed outside the design ultimate envelope. Failure to achieve ultimate design load necessitated the comparison of G-Prime composite aft adapter Version 25 design loads to flight verification loads. A comparison of those loads are presented in Figure 6-28. It was determined that that design envelopes used for test purposes proved to be conservative relative to the actual flight loads. The G-Prime composite aft adapter panel demonstrated significant load carrying capability, even when damaged, in relation to flight verification loads. A summary of the combined compression and shear test results is shown in Table 6-7.

Even though graphite/epoxy is a brittle material, it was shown to be resistant to damage growth for use in the adapters. The G-Prime forward adapter proved to be very "damage-tolerant" to nonvisual impact damage and poorly drilled holes. Residual strength static tests of the *damaged* G-Prime forward adapter panels (FA4 and FA5) actually surpassed static tests to failure of previous *undamaged* G-Prime forward adapter panels (FA1 and FA2) and were well beyond the deign ultimate envelope.
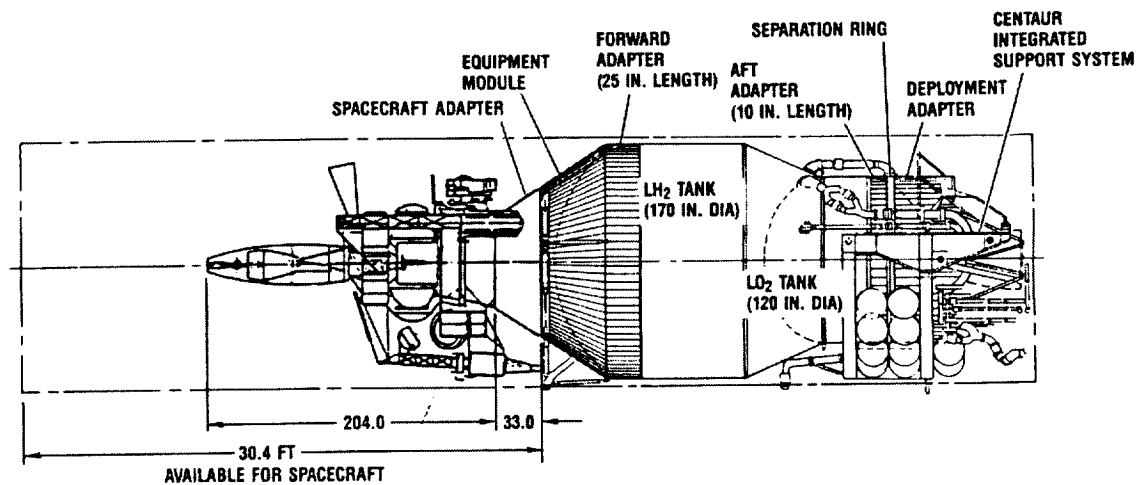
Figure 6-22: Shuttle/Centaur G-Prime configuration.
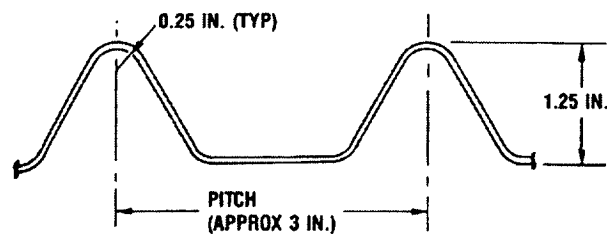
Figure 6-23: The final corrugation cross section was chosen with the approximate geometry above.
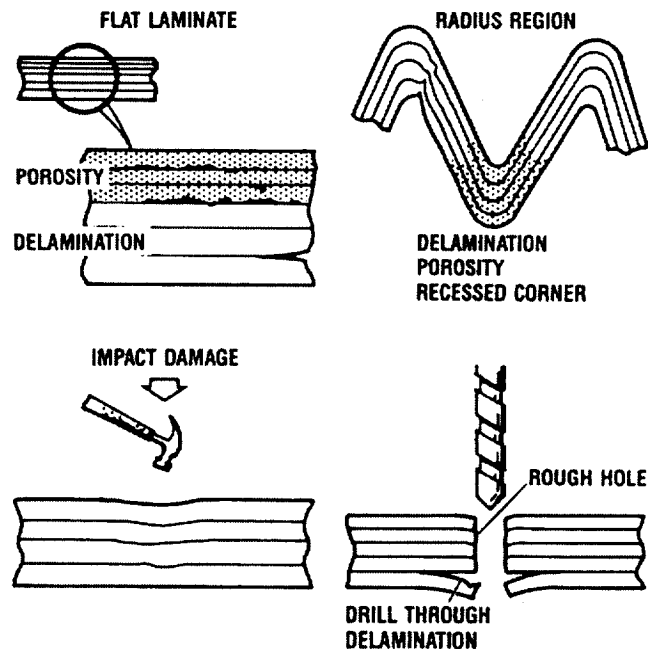
Figure 6-24: Potential threats that exist during fabrication, assembly, and service life.
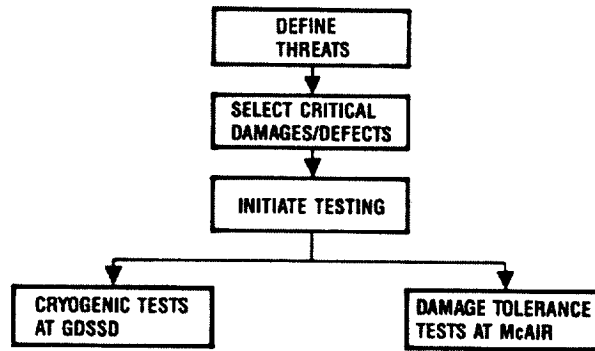
Figure 6-25: Flow diagram for damage tolerance/repair program.

Table 6-6: Test Results for SKCCA-036 Panels ([±55/0/90]$_s$)

Specimen No. SKCCA-036	Damage Type	Test Temperature	Buckling Load (lb)	Failure Load (lb)
-9	No damage	RT	4,700	6,100
-8	No damage	RT	4,600	6,060
-7	No damage	−423F	5,000	6,750
-6	Puncture/repair	RT	4,500	6,700
-5	Puncture/repair	−423F	5,500	7,260
-4	Impact damage	RT	2,900	3,950
-3	Impact damage	−423F	2,500	3,400
-2	Impact damage	RT	2,200	3,200
-1	Impact damage	−423F	2,400	3,700

0175-18

♦ ULTIMATE ENVELOPE   ▲ FA3
◇ LIMIT ENVELOPE   △ FA4
■ FA1   ◉ FA5
□ FA2
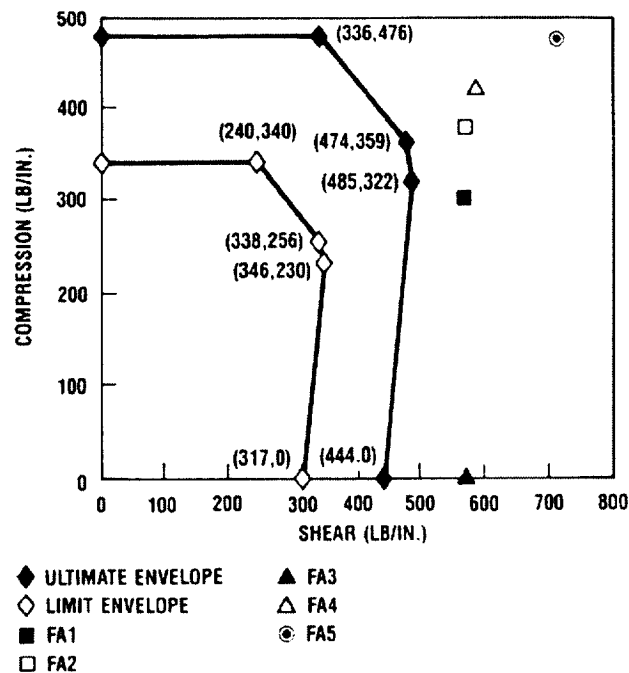
Figure 6-26: Static failure loads for G-Prime McAir forward test panels.

6-30
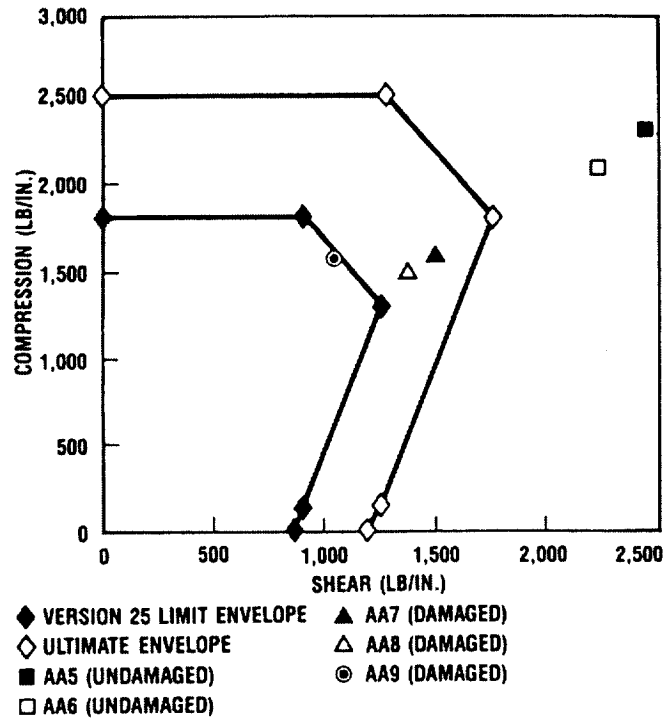
Figure 6-27: Static failure loads for G-Prime McAir aft test panels.
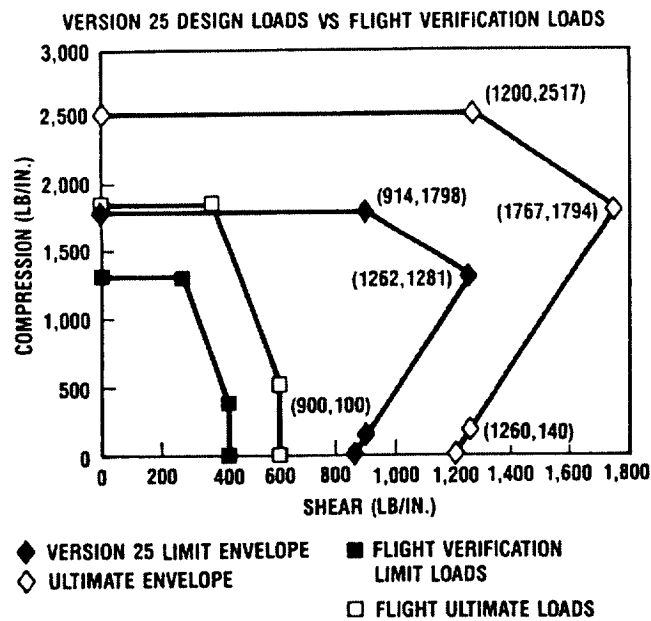
Figure 6-28: G-Prime aft adapter flight verification/design limit loads.

Table 6-7: Results for the McAir G-Prime RT Combined Loads Test Program

Panel no.	Damage configuration (BS = back side FS = front side)	Failure load (lb/in) Axial	Shear
FA3	A poorly drilled 1/4-in. hole, 4.5 ft-lb impact (BS radius), 1.5 ft-lb impact (FS flat), and a resin-rich insert	N/A	571
FA4	A poorly drilled 1/4-in. hole, 4.5 ft-lb impact (BS radius), and 1.5 ft-lb impact (FS flat)	421	583
FA5	A poorly drilled 1/4-in. hole, 4.5 ft-lb impact (BS radius), 1.5 ft-lb impact (FS flat), and a 7-in. teflon insert with repair patch	474	709
AA7	A poorly drilled 1/4-in. hole,5 ft-lb impact (BS radius), puncture with repair patch, and a delamination between tape and cloth at edge*	1,573	1,510
AA8	Two 5 ft-lb impacts (BS radius and FS flat), and a puncture with repair patch	1,475**	1,387 **
AA9	A 5 ft-lb impact (BS radius), 1.875 ft-lb impact (FS flat), and a puncture with repair patch	1,544***	1,044

*Delamination was not intended as part of the original damage configuration but was an accident that occured during panel insertion to the test fixture

**AA8 saw greater compression and shear loads at a previous fatigue cycle (1,573-lb/in. compression and 1,507-lb/in. shear)

***AA9 saw a greater compression load during previus fatigue cycling and static testing (1,798-lb/in. compression with 914-lb/in. shear)

CATEGORY

Composite Damage Tolerance

REFERENCE

Demuts, E., *et al.*, "Assessment of Damage Tolerance in Composites," *Composite Structures*, Vol. 4: 45-58, 1985.

ABSTRACT

Damage tolerance to processing and normal service damage has been assessed for carbon epoxy coupons and built-up panels in uniaxial loading. In coupons, the low velocity impact damage is more severe than damage in holes, delaminations or porosity and it causes compression strength loss from 58% at barely visible threshold to 73% at the easily visible threshold. Damaged coupon fatigue (R=10) S-N curves are relatively flat with 67% strength loss at 10^6 cycles for impact damage. In built-up panels representing multispar (M-S) and multirib (M-R) wing designs, again impact damage is more severe than delaminations and the impacted M-R design is stronger than the impacted M-S design. Damage in two adjacent M-S midbays and at the edge of the M-R stringer flange are the critical locations for impact, but damage area strongly depends on the panel configuration. Impact damage grows under constant amplitude fatigue (R=10) with peak load at 65% of damaged static strength for both M-S and M-R designs. Built-up configuration of the panels provides a significant increase in impact damage tolerance over that of coupons.

SUMMARY

This program is concerned with the resistance of composites to the common types of flaw and damage encountered in the manufacturing, assembly and normal service of an aircraft. Experimental damage tolerance data from conventional carbon epoxy coupons have been collected, assessed and presented. Similar data for specimens of the tougher AS6/2220-3 system at the coupon and three-stringer/stiffener panel level have been presented, where the panel represents a multirib (M-R) wing design. This study makes a comparison of both coupon and panel damage tolerance. The relevant data for the literature review is the results from the coupon data.

The undamaged static compression strength of a composite coupon, as shown in Figure 6-29, is reduced 58% by nonvisible and 73% by visible impact damages. Impact damage is strongly dependent on impactor shape, laminate thickness and its structural support. Cold-dry or hot-wet environments have no significant effect on impact damage static strength. Compression fatigue curves (R=10 and −1) are relatively flat for various impact damages, as shown in Figure 6-30. Data from damaged coupons subjected to aircraft random spectrum rather than constant amplitude fatigue loading produce higher fatigue thresholds than the 60% for R=10. Since composites in fatigue generally display a significant degree of inherent damage tolerance, such damage tolerance may be primarily a static problem.
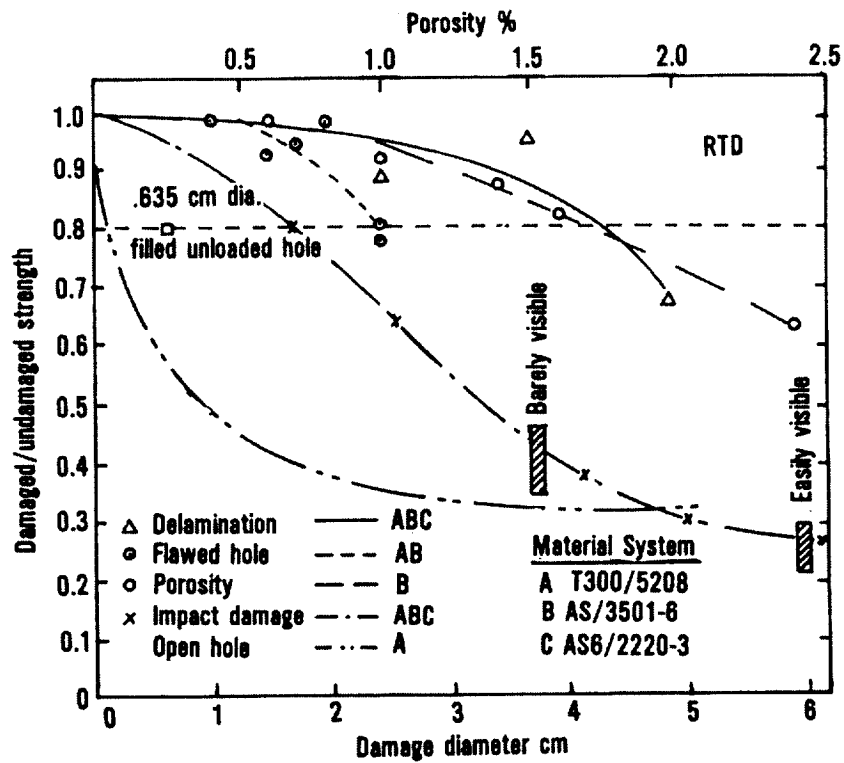
Figure 6-29: Compression static strength comparison – coupons.
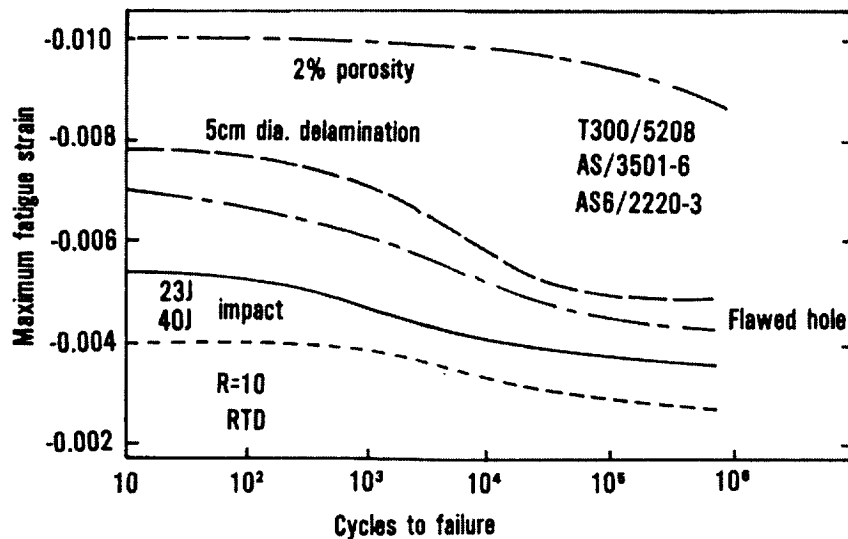
Figure 6-30: Fatigue response comparison – coupons.

7.0 Additional Related Papers

This section contains the review summaries of the following articles.

- Grimes-Ledesma, L. and H. W. Babel, "Comparison of Stress-rupture Life Prediction Techniques for Composite Pressure Vessels," 51st International Astronautical Congress, Rio de Janeiro, Brazil, 2000.
- Hall, C. D., *Integrated Spacecraft Power and Attitude Control Systems Using Flywheels*, AFIT/ENY/TR-000 (DRAFT).
- DeTeresa, S. J., "Materials for Advanced Flywheel Energy-Storage Devices," *MRS Bulletin*, 1999.
- Hinton, M. J. and P. D. Soden, "Predicting Failure in Composite Laminates: The Background to the Exercise," *Composites Science and Technology*, Vol. 58: 1001-1010, 1998.
- Soden, P. D., *et al.*, "A Comparison of the Predictive Capabilities of Current Failure Theories of Composite Laminates," *Composites Science and Technology*, Vol. 58: 1225-1254, 1998.
- Bowler, M. E., "Flywheel Energy Systems: Current Status and Future Prospects," Magnetic Material Producers Association Joint Users Conference, 1997.
- Christopher D. A. and R. F. Beach, "A Flywheel Energy Storage System Test on the International Space Station," *Proceedings of the 32nd Intersociety Energy Conversion Engineering Conference*, Vol. 3:1762-1766, 1997.
- Abacus Technology Corporation, *An Assessment of Flywheel Energy Storage Technology for Hybrid and Electric Vehicles*, 1996.
- Grimsley, F. M., "B-2 Structural Integrity Program," 36th AIAA/ASME/ASCE/AHS/ASC Structures, Structural Dynamics, and Materials Conference, AIAA-95-1466, 1995.
- Faupel, J. H., *Engineering Design – A Synthesis of Stress Analysis and Materials Engineering*, John Wiley & Sons, Inc, New York, 1964.

CATEGORY

Analytical Methods

REFERENCE

Grimes-Ledesma, L. and H. W. Babel, "Comparison of Stress-rupture Life Prediction Techniques for Composite Pressure Vessels," 51st International Astronautical Congress, Rio de Janeiro, Brazil, 2000.

ABSTRACT

There are several analysis methods available that predict the stress-rupture life of composite pressure vessels, but there is no general agreement in the technical community as to the preferred method. Significant differences in life prediction are obtained depending on which model is used. Three analysis methods are described and compared: the regression technique, two-parameter Weibull as described by Thomas, and Robinson's modified Weibull. The regression technique was judged as not being suitable for composite overwrapped pressure vessels (COPVs). The greatest difference in the life prediction between the Thomas and Robinson methods was obtained for glass at long lifetimes, and the least difference for graphite. The available experimental data currently does not permit one method to be selected over another and additional tests are required to make this decision.

SUMMARY

Although COPVs are advantageous in many applications, they are known to be more susceptible to mechanical damage and stress-rupture than metallic pressure vessels. In the 1970s research was begun to study stress-rupture in fiberglass, and researchers have since developed methods of predicting the life of COPVs made with glass, aramid, and graphite fibers.

Three techniques of stress rupture prediction are summarized and compared in this work: ASTM or regression method described in ASTM D2992, the Thomas method, and the Robinson method.

ASTM D2992 Method

This standard was developed to determine the life of fiberglass pipes and fittings. It contains a method for determining both cyclic life and stress-rupture life. Eighteen specimens exposed to differing constant pressures were tested. From the data, a mean lower 95% confidence limit and prediction intervals are calculated for each data point and plotted in Figure 7-1. The figure is based on the typical test data for glass yarn in the appendix of the ASTM standard. Some of the complications associated with the use of this method are:

a) The standard was designed for fiberglass pipe stress-rupture. No standard exists for yarns used as an overwrap.

b) A minimum of 18 specimens must be tested. Specimens are stressed so that there will be failures in 4 time intervals in under 10,000 hours. This requirement, made specifically for glass yarn, is not applicable to aramid or graphite yarn.

Thomas Method

This method uses a standard two-parameter (shape and scale factors) Weibull distribution to describe the distribution of stress-rupture data. Using this method, long-term stress-rupture characteristics can be predicted based on short-term results. After shape and scale parameters are chosen, either the probability of failure (or survival) or the ultimate bottle stress at a particular probability can be calculated. Figure 7-2 shows the plot of three probabilities of survival for glass. The allowable sustained load decreases by about 10% for increases in probability of survival going from 0.995 to 0.99996 and another 10% going to 0.999999.

Two sensitivity studies were conducted: the first to study the effects of varying the shape parameter (alpha), and the second to study the role of sample size in resulting life curves. From the first study, it was found that the life predictions are heavily dependent upon the value of alpha that is chosen for the analysis. As can be seen in Figure 7-3, alpha is nonlinear. This introduces a great amount of sensitivity into the analysis. For the second study, as found in Figure 7-4, there will never be a sample size at which alpha converges to a constant. Although, alpha responds to changes in sample size linearly, alpha and % Ftu are related in a nonlinear way.

Robinson Method

Robinson used the data from strand tests run at Lawrence Livermore to develop design curves, shown in Figure 7-5 for glass. The curves are based on the Weibull distribution, however, Robinson uses a different form of the Weibull equation than is found in most texts. This method is preferred by some COPV manufacturers because it provides less conservative predictions than the Thomas method. One major problem with this method, however, is the inability of many researchers to duplicate design curves for new materials using Robinson's technique.

Comparison of Methods

The Thomas method was first compared with the ASTM D2992 method. As shown in Figure 7-6, the ASTM method is considerably less conservative than the Thomas method for glass fiber. The Thomas method is also found to more accurately fit the observed behavior. Based on this comparison, and the above mentioned complications, it was determined that no further consideration would be given to the ASTM method.

Next the Thomas method was compared to the Robinson method. The main difference between these two methods is in the determination of the parameters. Figure 7-7 shows a graphical comparison of the two methods for glass fiber. The results illustrate that the Robinson method is less conservative than the Thomas method. From the comparisons, the Thomas method was found to be the least complicated and most readily applicable method under all conditions. With appropriate service life, probability of survival, and factor of safety choices, the Thomas method

should supply conservative design life curves for COPVs, based on the COPV test data that exists.

D2992 Example Data Plot
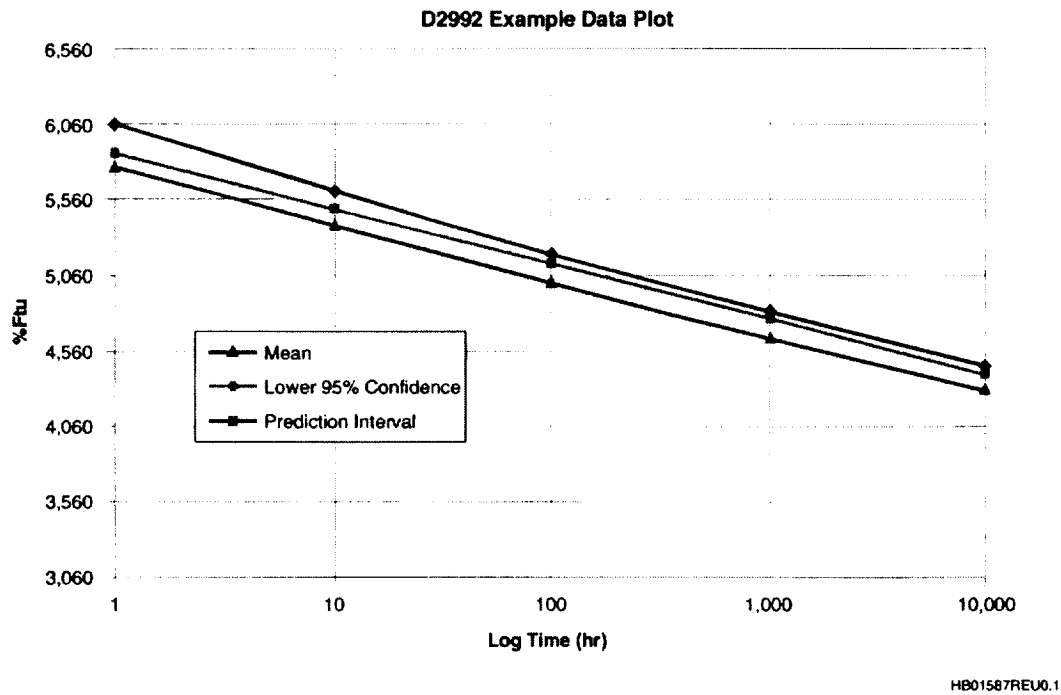
Figure 7-1: The method of ASTM D2992 for glass yarn.

Glass
alpha = 1, beta = 1.4 x 10^{13} $10^{-0.159}$ (%Ftu)
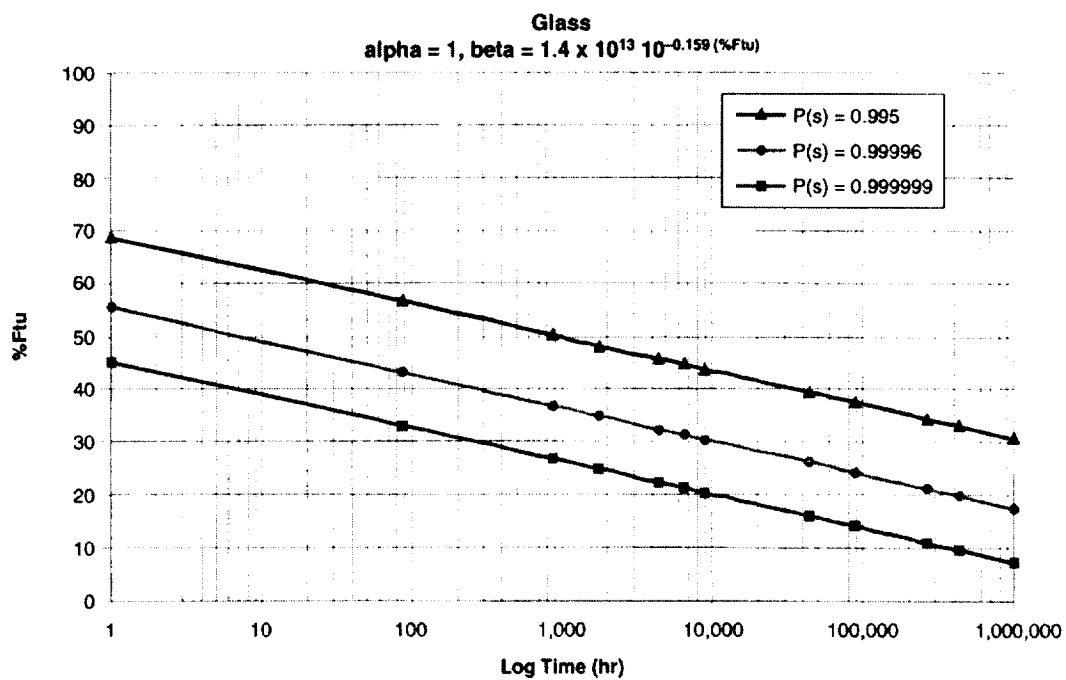
Figure 7-2: Life predictions of COPVs using glass yarn for three probabilities of survival.

7-4
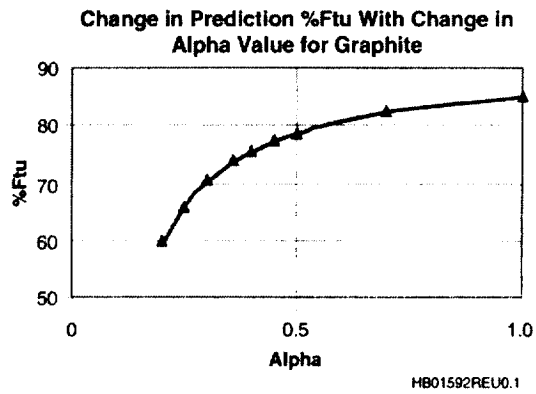
Figure 7-3: Variation in life predication with changes in alpha for graphite.
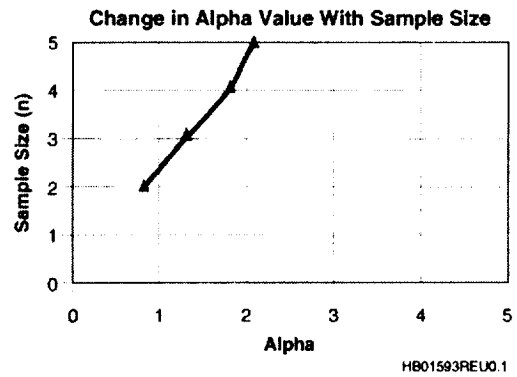
Figure 7-4: Increases in alpha with increased sample size.
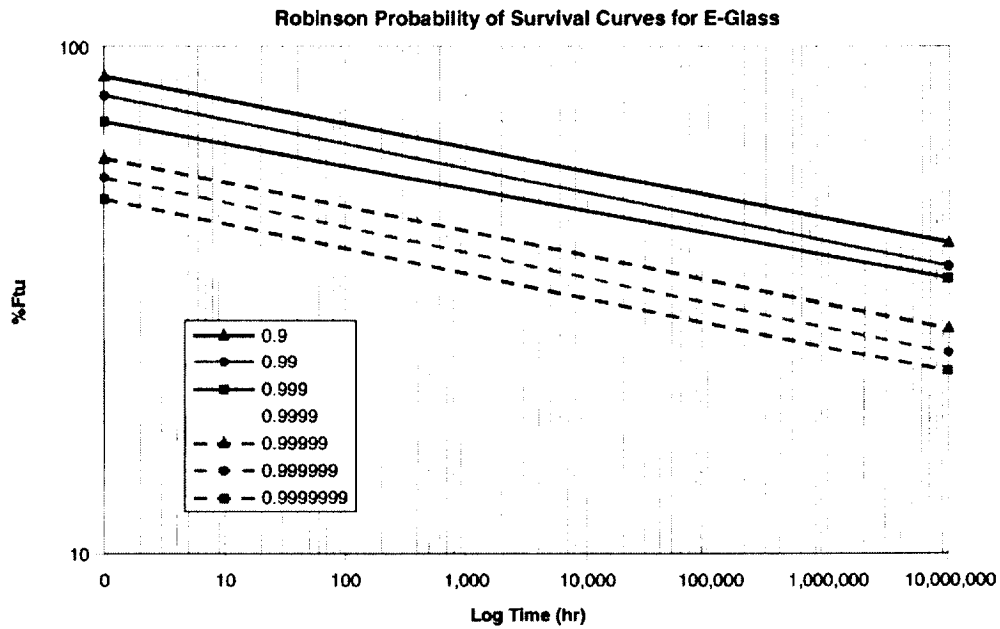
Figure 7-5: Robinson's life predictions for glass.
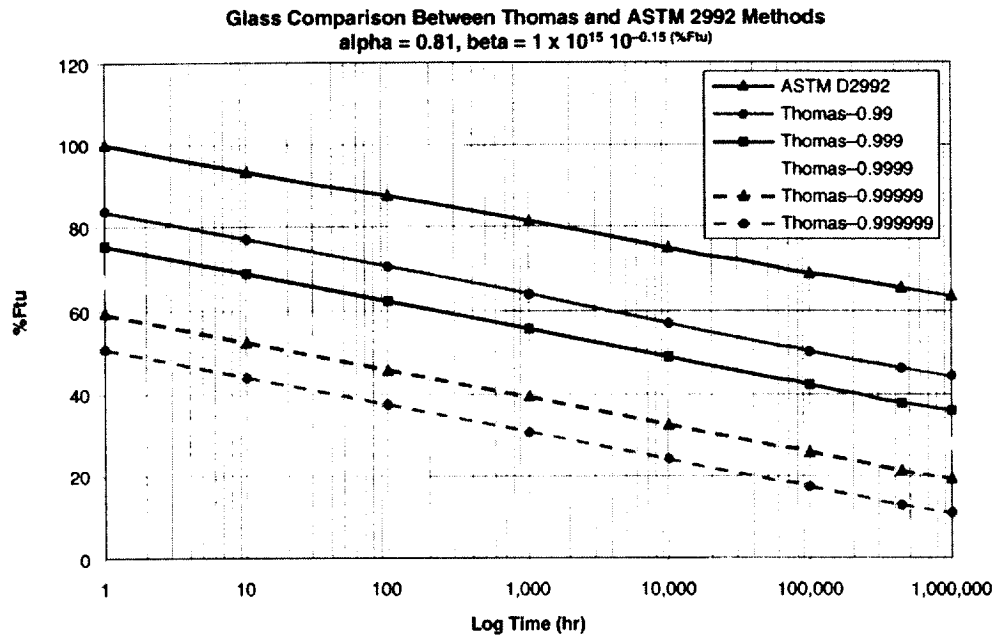
Figure 7-6: Comparison of ASTM D2992 and Thomas method for glass.
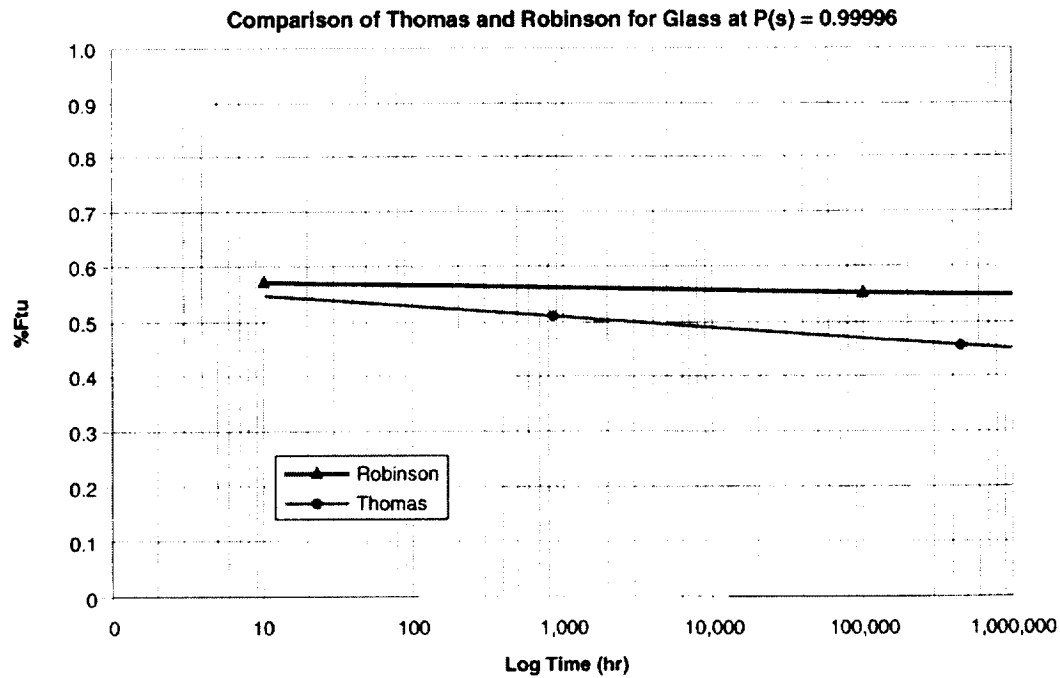
Figure 7-7: Comparison of Robinson and Thomas for glass yarn.

CATEGORY

Technology Overview

REFERENCE

Hall, C. D., *Integrated Spacecraft Power and Attitude Control Systems Using Flywheels*, AFIT/ENY/TR-000 (DRAFT).

INTRODUCTION

The power and energy engineering community has been investigating the use of high performance kinetic energy storage systems since the 1960s, with significant research and development activity throughout the subsequent decades. The list of proposed applications includes primary storage for automobiles, electromechanical actuators for aerospace vehicles, uninterruptible power supplies for critical facilities such as hospitals and computer centers, and secondary battery replacement for satellites. In this last application, the flywheels can perform the additional functions of some of the attitude control sensors and actuators. Both NASA and the USAF are developing programs related to the use of high-speed flywheels in "integrated power and attitude control systems," of IPACS. This multiple-use application is the focus of this report. Specifically, we aim to provide a review of the relevant literature in sufficient detail to allow the reader to understand the basic concepts and to plan for further research leading to the implementation of flywheels in this application.

COMMENTS

This report contains a good examination of the literature on composite flywheel rotors for many applications. It is a good source of references previous to 1998. Many of the references in the paper appear in this literature review.

The paper cites several issues that need to be further investigated before flywheels are used in space applications: the flywheel configuration to be used, attitude determination, containment (a very important issue), magnetic bearings, power buses for higher power systems.

Technology Overview

INTRODUCTION

Flywheels are mechanical devices that store kinetic energy in a rotating mass. A simple example is the potter's wheel. For energy storage and conversion, an efficient method to exchange energy with a flywheel device is by converting the energy between mechanical and electrical forms. Typically a flywheel designed to perform this type of energy exchange is a combination of a motor and a generator. Energy is transferred into the device for storage by using it as a motor to consume electrical energy and spin the mass. This energy can be recovered with an efficiency exceeding 80% by using the flywheel as an electrical generator. Although the concept of storing energy in a rotating mass is an ancient idea, the relatively recent advent of advanced fiber-composite materials offers the potential for improved energy storage and conversion using rotating electromechanical devices.

The achievable energy density (energy/weight) of a simple flywheel design, such as that shown schematically in Figure 7-8, is proportional to the specific strength (strength/density) of the material. The particular type of composite flywheel shown in this figure is composed entirely of circumferentially wrapped fiber. Although other designs have been suggested and constructed, this version is the most common for energy-storage applications. As discussed in the earliest papers on the subject, such as the article by Post and Post,[1] (reference not in summary) the proportionality between energy density and specific strength favors the use of fiber composites. The remarkable combination of mechanical properties and low density achieved with fiber composites has made them attractive and nearly essential for aerospace applications. Unlike these applications, which are driven primarily by a high stiffness-to-weight ratio, flywheels require a combination of high tensile strength and low density. The tradeoff between maximizing the energy-storage capability and establishing safe operating limits is probably the single most critical design problem in commercial flywheel applications. To overcome this problem, a complete understanding of the failure mechanisms and long-term durability of the flywheel materials and structures is needed.

The class of materials known as fiber composites encompasses a wide variety of material types and forms. Their common feature is the combination of high-strength and/or high-modulus fibers bound together by a matrix material. This article discusses the specific case of continuous fibers in a polymeric matrix, which offers the highest specific strengths. The strengths of high-performance fibers are compared. However, differences in the translation of material strength into the flywheel structure, as well as long-term performance, can be overriding concerns, and

both of these are discussed. Additionally, some flywheel design modifications that compensate for weak matrix-dominated failure modes are examined.

SUMMARY

Many new high performance fiber composites have been developed in the last 12 years. Many of these fibers are either already being used or considered for applications such as flywheels and pressure vessels. These types of structures require performance under long-term sustained or cyclic loading. However, long-term lifetime data for many of these materials apparently do not exist or are not readily available in the open literature. The tensile properties of several types of high-performance fibers are listed in Table 7-1 below. The intrinsic specific strength of fibers is only one property that needs to be considered for flywheels.

It is essential to consider the properties of the composite system and not just the fiber and matrix alone. The tensile stress-rupture lifetime behavior of fiber composites was a popular topic of interest in flywheel programs in the 1970s and 1980s. Little data exist for the stress-rupture behavior in the transverse direction; so most flywheel designs seek to minimize radial tensile stresses and avoid premature failure in this weak mode. Figure 7-9 shows an example of the type of data collected by one such program run by the Lawrence Livermore National Laboratory. Some of the following are conclusions that were gleaned from the past research:

a) Both aramid and glass fibers were susceptible to chemical degradation. Stress levels would have to be kept below 40% of the intrinsic strength for a high survival rate after 10 years.

b) Carbon-fiber strands exhibited more statistically variable strengths, but much more resistance to stress rupture.

Using several concentric rings assembled by interference or adhesion is one suggestion to generate a beneficial radial compression stress state. By properly choosing the placement of materials that have modulus and/or density gradients one can create radial compression during spinning. Another configuration is to increase the radial strength by incorporating fiber in this direction. This can be accomplished by the use of polar-weave fabrics and a liquid-resin molding process such as resin transfer molding (RTM). Unfortunately, polar-woven fabrics are very expensive in this application.
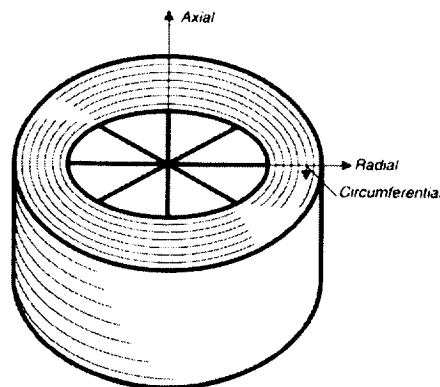
Figure 7-8: Schematic diagram of a rim-type
fiber-composite flywheel.

7-9

Table 7-1: Tensile Properties of High-Performance Fibers

Fiber	Density (g/cm³)	Elastic Modulus (GPa)	Ultimate Tensile Strength (GPa)	Manufacturer
T700 (carbon)	1.80	228	4.83	Toray
T1000G (carbon)	1.80	297	6.38	Toray
E-glass	2.58	72	3.45	OCF
R-glass	2.55	85	4.33	Vetrotex
S2-glass	2.49	87	4.59ª	OCF
Hollex (glass)	1.80	67	3.45ª	OCF
Fused silica	2.20	69	3.45	J.P. Stevens
Kevlar 49 (aramid)	1.45	120	3.62	DuPont
Kevlar 29 (aramid)	1.44	58	3.62	DuPont
Twaron (aramid)	1.44	80	3.15	ENKA
Twaron HM (aramid)	1.45	124	3.15	ENKA
Technora (aramid)	1.39	70	3.04	Teijin
Spectra 900 (PE)	0.97	117	2.68	AlliedSignal
Spectra 1000 (PE)	0.97	173	3.12	AlliedSignal
Dyneema (PE)	0.97	87	2.70	Dyneema VOF
Zylon-HM (PBO)	1.56	269	5.80	Toyobo

ªMeasured using single-filament test; all others measured using impregnated-strand test.
E-glass is electrical glass; S2-glass is a second-generation, high-strength glass; R-glass is a high-strength, high-modulus glass; PBO is polybenzobisoxazole; PE is polyethylene.
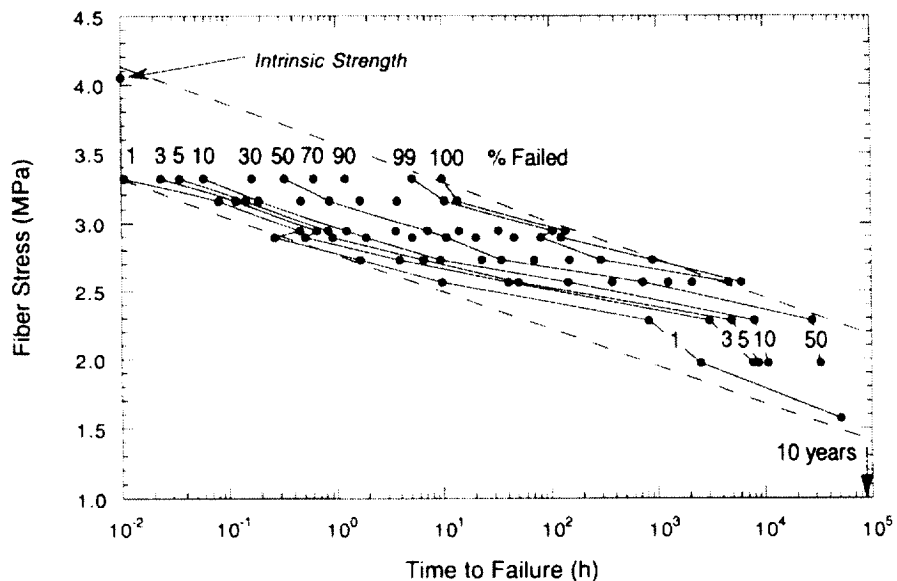
Figure 7-9: Lifetime plot for the stress rupture of S-glass/epoxy strands.

CATEGORY

Failure Theory

REFERENCE

Hinton, M. J. and P. D. Soden, "Predicting Failure in Composite Laminates: The Background to the Exercise," *Composites Science and Technology*, Vol. 58: 1001-1010, 1998.

ABSTRACT

This Special Edition of Composites Science and Technology is dedicated to the subject of failure theories for continuous fibre-reinforced-polymer composite materials (FRPs). The papers were commissioned as a coordinated study (referred to as the 'failure exercise') aimed at providing a comprehensive description of the foremost failure theories available at the present time, a comparison of their predictive capabilities directly with each other, and a comparison of their predictive capabilities against experimental data. This introductory paper sets the scene for the "failure exercise", describing the process by which the participants were selected, the general instructions supplied to each participant and the format for presenting the output of the work.

SUMMARY

Failure theories are mainly used in the initial calculations to establish the approximate dimensions, such as panel thickness, width, etc. Once this has been accomplished, tests are conducted on coupons or structural elements to determine the global design allowables. These allowables are given a wide safety margin to account for the many uncertainties in the manufacturing and handling of composites.

The invitations were sent to proponents of failure theories covering a wide range of approaches: interactive failure theories, physically based failure criteria, damage mechanics, the industrial and standard design code approaches, and commercial software vendors/developers.

Participation in this study was offered to the participants in Table 7-2. Several participants declined the invitation. As can be seen in the summary of the later paper by Soden, *et al.*, 11 groups chose to participate.

Table 7-2: Approaches and Failure Theories Originally Planned in the Exercise

Contributor	Approach represented
Chamis C C (USA)	Micromechanics
Hart-Smith J (USA)	Generalised Tresca and maximum strain theories
Eckold G C (UK)	Design codes
Edge E C (UK)	Industry
Ellis D (UK)	ANSYS
Grayley M E (UK)	ESDU international
Hall R L (USA)	PDA/PATRAN
Hallquist J (USA)	DYNA3D
Johnson A (Germany)	PAMFISS/PAMCRASH
Haug E (France)	PAMSISS/PAMCRASH
Stanton E (UK)	MSA/NASTRAN
Hibbitt D (USA)	ABAQUS
Allen D H, Talreja R, Nairn J, Reifsnider K (USA), McCartney L (UK)	Damage models and cracking of composites
Puck A, Schürmann H, Cuntze R G, Aoki R (Germany)	Puck's theory
Hashin Z and Rotem (Israel)	Rotem and Hashin's theories
Rosen B W (USA)	MIL-HNDBK-17
Zinoviev P (Russia), Skudra A M (Latvia), Chang F-K , Chou T W, Sun C T, Swanson S R (USA), Marom G (Israel), de Wilde P (Belgium), Surrel Y (France), Hansen J S (Canada)	General application and methods
Tsai S W (USA)	Interactive failure theory
Uemura M (Japan)	Statistical prediction of failure
Sandhu R S and Wolfe W E (USA)	Strain energy failure theory

CATEGORY

Miscellaneous

REFERENCE

ABSTRACT

This paper presents a unique and comprehensive comparison between the predictions of internationally recognized failure theories for fibre-reinforced polymer-composite laminates. The theories were applied by their originators (or their colleagues) to carefully selected test cases covering a wide range of lay-ups, materials and in-plane loading conditions. Key features in each theory are identified including: types of failure models employed, whether linear or non-linear analysis was carried out, reliance on software and numerical methods, allowance for thermal stresses and identification of modes of failure.

The results (initial and final failure envelopes and representative stress/strain curves) have been superimposed to show similarities and differences between the predictions of the various theories. In addition, bar charts were constructed to demonstrate the levels of agreement between the predicted initial and final failure stresses and strains. Sources of discrepancies between the predictions of the various failure theories are discussed. The originators have the opportunity to comment on and compare their theoretical predictions with experimental results in the second part of this Exercise which will be published separately.

SUMMARY

The objective was to compare the participants' predictions and identify some of the major differences between them. The exercise makes no attempt to draw conclusions about which theory is the best. The emphasis is on clarifying the differences between them and their predictions. Table 7-3 lists the participants and their respective approaches.

Table 7-4 summarizes the different post-initial-failure models adopted. All these models have the following in common:

- All rely on ply-by-ply analysis.
- All assume that fiber failure, be it in tension or compression, constitutes final failure.
- Almost all models distinguish between failures under transverse tension and that under transverse compression.

The theories also differ in some ways. Two main groups are as follows:

(a) Models employing sudden reduction in the properties of the failed lamina as presented by Tsai, Wolfe, and Sun (linear).

(b) Models employing a gradual drop in the properties of failed lamina as presented by Puck, Edge, Rotem, Zinoviev, Chamis, and Sun (non-linear).

Table 7-5 lists the load cases that the participants were given. The test cases can be grouped into three categories: (a) biaxial failure of unidirectional laminae (Cases 1, 2 and 3), (b) biaxial failure envelopes of multi-directional laminates (Cases 4, 5, 6, 9) and (c) stress/strain curves of laminates under uniaxial and biaxial loading (Cases 7, 8, 10-14).

Table 7-6 shows the test cases attempted by each participant. The method used by McCartney is still new, and he was only able to apply it to two cases. Hart-Smith did not provide solutions for the seven cases involving stress/strain curves. He also failed to predict initial failures in either theory offered.

Tables 7-7 and 7-8 show the areas of largest disagreement in the theories for the unidirectional and multidirectional laminates. Table 7-9 gives the effect of thermal stresses on initial failure predictions for the participants that accounted for thermal effects.

The main finding in the study was that though Cases 1-3 were chosen to compare the theories at the most simplistic level, no two theories gave the same biaxial failure envelopes for all the cases, and the differences were as great as 570% in the strength predictions. Even in the case of the participants that accounted for residual thermal stresses, the ways in which they accounted for them led to large differences in the results for first-ply-failure loads. In many cases, the theories differed in the mode (and occasionally the location) of failure each predicted. In some cases, the mode of failure wasn't clearly identified.

The many differences in the predictions leads one to believe that one theory can under no circumstances account for all the variables correctly to predict failure. Analytical results should never stand alone as definitive results. The use of analytical models to correlate test results should be done in very careful ways.

Table 7-3: Summary of the Participants and Approaches in the Exercise

Contributor(s)	Organisation	Approach represented	Theory designation
Chamis, C. C., Gotsis P. K. and Minnetyan, L.	NASA Lewis, Cleveland, USA	ICAN CODSTRAN (micromechanics analyses)	Chamis(1) Chamis(2)
Hart-Smith, L. J. Hart-Smith, L. J.	Douglas Products Division, Longbeach, USA	Generalised Tresca theory Maximum strain theory	Hart-Smith(1) Hart-Smith(2)
Eckold, G. C.	AEA Technology, Harwell, UK.	British Standard pressure vessel design codes	Eckold
Edge, E. C.	British Aerospace, Military Aircraft Division, Warton, UK	British Aerospace, In-house design method	Edge
McCartney, L. N.	National Physical Laboratory, London, UK	Physically based 'Damage Mechanics'	McCartney
Puck, A. and Schürmann, H.	Technische Hochchule, Darmstadt, Germany	Physically based 3-D phenomenological models	Puck
Wolfe, W. E. and Butalia, T. S.	Department of Civil Engineering, Ohio State University, Ohio, USA	Maximum strain energy method, due to Sandhu	Wolfe
Sun, C. T. and Tao, J. X.	Purdue University School of Aeronautics & Astronautics, West Lafayette, Indiana, USA.	Linear and non-linear analysis (non-linear is FE based)	Sun
Zinoviev, P., Grigoriev, S. V., Labedeva, O. V. and Tairova, L. R.	Institute of Composite Technologies, Orevo, Moskovkaya, Russia.	Development of Maximum stress theory	Zinoviev
Tsai, S. W. and Liu, K.-S.	Aeronautics and Astronautics Department, Stanford University, California, USA.	Interactive progressive quadratic failure criterion	Tsai
Rotem, A.	Faculty of Mechanical Engineering, Technion-Israel Institute of Technology, Haifa, Israel.	Interactive matrix and fibre failure theory	Rotem

7-14

Table 7-4: Summary of the Post-initial Failure Degradation Models Used in the Theories

Name	Failure mode	Properties degraded
Eckold		No post failure
Hart-Smith		No post failure
Rotem	After final matrix failure	$E_2 = 0.0$, $G_{12} = 0.0$, $E_1 = E_1^0 \exp(-k\varepsilon_1)$, k is a large constant
McCartney	Lamina cracking	detailed mathematical analysis for reducing stiffness.
Puck	Cracking under tension Mode (A)	$E_2 = \eta E_2^0$, $G_{12} = \eta G_{12}^0$, $\nu_{12} = \eta \nu_{12}^0$, where η is a parameter which varies with stress
	Cracking under compression Modes (B) and (C)	$G_{12} = \eta_1 G_{12}^0$, $\nu_{12} = \nu_{12}^0$, where η_1 is smaller than η
Chamis	Matrix failure	E_m is replaced by a negligible value and E_2, G_{12}, ν_{12} and E_1 are computed from micromechanics
Edge	Matrix failure	$E_2 = \beta_1 E_2^0$, $G_{12} = \beta_2 G_{12}^0$, $\nu_{12} = \beta_3 \nu_{12}^0$, where β_1, β_2 and β_3 are empirical parameters that decrease with increasing strain
Wolfe	Matrix failure	$E_2 = 0.0$, $G_{12} = 0.0$, $\nu_{12} = 0.0$
Sun (linear)	Shear matrix failure Transverse matrix failure	$E_2 = 0.0$, $G_{12} = 0.0$ $E_2 = 0.0$
Sun (Nonlinear)	Matrix shear failure	$E_2 = E_2^0 \exp(-\alpha_E \lambda)$ and $G_{12} = G_{12}^0 \exp(-\alpha_G \lambda)$, where α_E and α_G are constants, λ is normalised crack density
	Transverse matrix failure	$E_2 = E_2^0 \exp(-\alpha_E \lambda)$
Tsai	Matrix failure $\varepsilon_2 > 0$	$E_m = 0.15 E_m^0$, $\nu_{12} = 0.15 \nu_{12}^0$, where E_2 and G_{12} are computed from micromechanics
	Matrix failure $\varepsilon_2 \leq 0$	$E_2 = 0.01 E_2^0$, $G_{12} = 0.01 G_{12}^0$, $\nu_{12} = 0.01 \nu_{12}^0$, $E_1 = 0.01 E_1^0$
Zinoviev	Open Cracks $\sigma_2 > 0$	For $|\gamma_{12}| < |\gamma_{12}^*|$ (a) when $\varepsilon_2 < \varepsilon_2^*$: $E_2 = \Psi_2 E_2^0$, $G_{12} = \Psi_3 G_{12}^0$ (b) when $\varepsilon_2 = \varepsilon_2^*$: $E_2 = 0.0$, $G_{12} = \Psi_3 G_{12}^0$ For $|\gamma_{12}| = |\gamma_{12}^*|$ (a) when $\varepsilon_2 < \varepsilon_2^*$: $E_2 = \Psi_2 E_2^0$, $G_{12} = 0.0$ (b) when $\Delta\varepsilon_2 > 0$: $E_2 = 0.0$, $G_{12} = 0.0$ (Ψ is a function of strain)
	Closed cracks $\sigma_2 < 0$	For $\Delta\varepsilon_2 < 0$: (a) when $|\gamma_{12}| < |\gamma_{12}^*|$: $G_{12} = \Psi_3 G_{12}^0$ (b) when $\Delta|\gamma_{12}| > 0$: $G_{12} = 0.0$

Table 7-5: Details of the Laminates and Loading Cases

Laminate lay-up	Material	Loading case	Description (a wide range of biaxial stress ratios unless otherwise indicated)
0°	E-glass/LY556/HT907/DY063	1	Biaxial failure stress envelope under transverse and shear loading (σ_y vs τ_{xy})
	T300/BSL914C	2	Biaxial failure stress envelope under longitudinal and shear loading (σ_x vs τ_{xy})
	E-glass/MY750/HY917/DY063	3	Biaxial failure stress envelope under longitudinal and transverse loading (σ_y vs σ_x)
(90°/±30°/90°)	E-glass/LY556/HT907/DY063	4	Biaxial failure stress envelope (σ_y vs σ_x)
		5	Biaxial failure stress envelope (σ_x vs τ_{xy})
(0°/±45°/90°)	AS4/3501-6	6	Biaxial failure stress envelope (σ_y vs σ_x)
		7	Stress-strain curves under uniaxial tensile loading in y direction ($\sigma_y:\sigma_x = 1:0$)
		8	Stress-strain curves for $\sigma_y:\sigma_x = 2:1$
±55°	E-glass/MY750/HY917/DY063	9	Biaxial failure stress envelope (σ_y vs σ_x)
		10	Stress-strain curves under uniaxial tensile loading for $\sigma_y:\sigma_x = 1:0$
		11	Stress-strain curves for $\sigma_y:\sigma_x = 2:1$
(0°/90°)	E-glass/MY750/HY917/DY063	12	Stress-strain curve under uniaxial tensile loading for $\sigma_y:\sigma_x = 0:1$
±45°	E-glass/MY750/HY917/DY063	13	Stress-strain curves for $\sigma_y:\sigma_x = 1:1$
		14	Stress-strain curves for $\sigma_y:\sigma_x = 1:-1$

Table 7-6: Summary of the Loading Cases Analyzed by the Participants

Theory	1	2	3	4	5	6	7	8	9	10	11	12	13	14	Remarks
McCartney	X X	X X	X X	X X	X X	X X	X X	X X	X X	X X	X X	■-	■-	X X	No final failure
Hart-Smith(2)	■■	■■	■■	X■	X■	X■	XX	XX	X■	X X	X X	X X	X X	X X	No stress/strain curves
Hart-Smith(1)	■■	■■	■■	X■	X■	X■	X X	X X	X■	X X	X X	X X	X X	X X	No stress/strain curves
Eckold	■■	X X	■■	■■	X X	X X	X X	X X	■■	■X	■X	■X	■X	■X	No carbon-fibre results
Chamis	■■	■■	■■	■■	■■	■X	■■	■■	■■	■■	■■	■■	■■	■■	
Edge	■■	■■	■■	■■	■■	■■	■■	■■	■■	■■	■■	■■	■■	■■	
Puck	■■	■■	■■	■■	■■	■■	■■	■■	■■	■■	■■	■■	■■	■■	
Rotem	■■	■■	■■	■■	■■	■■	■■	■■	■■	■■	■■	■■	■■	■■	
Sun	■■	■■	■■	■■	■■	■■	■■	■■	■■	■■	■■	■■	■■	■■	
Tsai	■■	■■	■■	■■	■■	■■	■■	■■	■■	■■	■■	■■	■■	■■	
Wolfe	■■	■■	■■	■■	■■	■■	■■	■■	■■	■■	■■	■■	■■	■■	
Zinoviev	■■	■■	■■	■■	■■	■■	■■	■■	■■	■■	■■	■■	■■	■■	

X Case not analysed.
■- Final failure not reached.
■ Initial failure predicted only.
■ Final failure predicted only.

Table 7-7: Ratios of the Highest:Lowest Predicted Unidirectional Lamina Strengths for Selected Stress Ratios

No.	Lamina studied	Stress ratio	Final failure prediction		Highest:lowest ratio of predictions
			Highest	Lowest	
1	E-glass/MY750 (Loading Case 3)	$\sigma_x : \sigma_y = 8 \cdot 83 : -1$	Edge, Zinoviev and Sun	Eckold	3·6
2		$\sigma_x : \sigma_y = -32 : 1$	Eckold	Wolfe	4·77
3		$\sigma_x : \sigma_y = 7 \cdot 8 : 1$	Hart-Smith(2)	Rotem	4·4
4		$\sigma_x : \sigma_y = -3 \cdot 75 : 1$	Hart-Smith(2)	Eckold	5·7
5		$\sigma_x : \sigma_y = -14 : -1$	Tsai	Eckold	2·72
6	E-glass/LY556 (Loading Case 1)	$\sigma_y : \tau_{xy} = -1 \cdot 58 : 1$	Edge, Hart-Smith(2), Zinoviev	Eckold	3·22
7		$\sigma_y : \tau_{xy} = 1 : 2 \cdot 06$	Hart-Smith(2), Zinoviev, Eckold	Tsai	1·54
8	T300/914C (Loading Case 2)	$\sigma_x : \tau_{xy} = -12 \cdot 5 : 1$	Zinoviev, Sun, Hart-Smith(1), Hart-Smith(2)	Edge	1·64
9		$\sigma_x : \tau_{xy} = 18 \cdot 75 : 1$	Edge, Zinoviev, Hart-Smith(1), Hart-Smith(2), Sun	Chamis	1·414

7-17

Table 7-8: Summary of Theoretical Results Showing the Range of Initial and Final Failure Predictions for Multidirectional Laminates

No.	Laminate studied	Stress ratio	Final failure prediction			Initial failure prediction			Largest final/initial prediction	
			Highest	Lowest	Ratio	Highest	Lowest	Ratio	Name	Ratio
1	(±30°/90°) GRP (loading Case 5)	$\sigma_x : \tau_{xy} = -2.35 : 1$	Puck	Chamis(2)	3.8	Sun	Chamis(2)	4.16	Puck	1.99
2		$\sigma_x : \tau_{xy} = 1 : 1$	Hart-Smith(1)	Wolfe	5.21	Tsai	Chamis(2)	5.74	Edge	12.8
3		$\sigma_x : \tau_{xy} = 0 : 1$	Puck	Chamis(2)	4.71	Zinoviev	Chamis(2)	2.91	Puck	6
4		$\sigma_x : \tau_{xy} = -1 : 0$	Eckold	Tsai	3.58	Sun	Eckold	4.61	Eckold	12
5		$\sigma_x : \tau_{xy} = 1 : 0$	Eckold	Chamis(2)	3.13	Tsai	Chamis(2)	6.5	Eckold	24
6	(±30°/90°) GRP (Loading Case 4)	$\sigma_y : \sigma_x = 1 : 3$	Hart-Smith(1)	Rotem	6.2	Eckold	Chamis(2)	12.8	Edge	34
7		$\sigma_y : \sigma_x = 1 : -1$	Hart-Smith(1)	Chamis(2)	8.42	Zinoviev	Chamis(2)	2.83	Eckold	5.7
8		$\sigma_y : \sigma_x = -1 : -3$	Eckold	Zinoviev	3.1	Sun	Eckold	1.47	Eckold	3.74
9		$\sigma_y : \sigma_x = 1 : 1$	Hart-Smith(2)	Wolfe	7	Tsai	Chamis(2)	5.03	Chamis(2)	19
10		$\sigma_y : \sigma_x = -1 : -1$	Edge	Tsai	1.66	Chamis(1)	Eckold	4	Eckold	3.66
11		$\sigma_y : \sigma_x = 1 : 0$	Hart-Smith(1)	Wolfe	2.42	Tsai	Chamis(2)	2.94	Edge	7.5
12		$\sigma_y : \sigma_x = -4.26 : 1$	Zinoviev	Chamis(2)	2.11	Zinoviev	Chamis(2)	7.46	Eckold	5
13	(0°/±45°/90°) CFRP (Loading Case 6)	$\sigma_y : \sigma_x = 0 : -1$	Rotem	Wolfe	1.33	Sun	Chamis(2)	9.23	Zinoviev	1.24
14		$\sigma_y : \sigma_x = 1.5 : -1$	Zinoviev	Wolfe	2.71	Zinoviev	Chamis(2)	19.6	Edge	15.7
15		$\sigma_y : \sigma_x = -1 : -1$	Tsai	Wolfe	1.72	Tsai	Wolfe	1.72	All	1
16		$\sigma_y : \sigma_x = 2 : 1$	Sun	Rotem	2.63	Chamis(1)	Chamis(2)	18	Chamis(2)	51
17		$\sigma_y : \sigma_x = 1 : 0$	Zinoviev	Chamis(2)	2	Zinoviev	Chamis(2)	16	Chamis(2)	24
18		$\sigma_y : \sigma_x = 1 : 1$	Zinoviev	Rotem	3.28	Chamis(1)	Chamis(2)	17	Edge	28
19	(±55°) GRP (Loading Case 9)	$\sigma_y : \sigma_x = 0 : -1$	Zinoviev	Eckold	2.53	Edge	Eckold	3.64	Eckold	1.47
20		$\sigma_y : \sigma_x = -1 : 0$	Eckold	Chamis(2)	3.61	Sun	Eckold	4.95	Eckold	9.6
21		$\sigma_y : \sigma_x = -2 : -1$	Eckold	Chamis(2)	4.13	Wolfe	Eckold	2.82	Eckold	5
22		$\sigma_y : \sigma_x = 2 : 1$	Hart-Smith(1)	Wolfe	8.7	Eckold	Chamis(2)	3.66	Chamis(2)	19
23		$\sigma_y : \sigma_x = 1 : 0$	Eckold	Chamis(2)	4.47	Puck	Eckold	4.88	Eckold	9.55
24	(±45°) GRP (Loading Cases 13 and 14)	$\sigma_y : \sigma_x = 1 : 1$	Chamis 2	Wolfe	9.7	Eckold	Puck	3.71	Puck	13
25		$\sigma_y : \sigma_x = 1 : -1$	Edge	Chamis(2)	5.8	Edge	Chamis(2)	1.48	Edge	4
26	(0°/90°) GRP Loading Case 12	$\sigma_y : \sigma_x = 0 : 1$	Puck	Wolfe	2.28	Eckold	Edge	2.83	Puck	12

Table 7-9: Examples of the Effect of Thermal Stresses on Initial Failure Prediction

Laminate	SR	Mode of failure	Initial failure stresses (MPa)	
			Without thermal stresses	With thermal stresses
0°/90° GRP	1:0	Transverse tension	78[a]	55.4[b]
±55° GRP	2:1	Transverse tension	112[a]	68.6[b]
0°/±45°/90° CFRP	1:1	Transverse tension	241[a]	35[b]
0°/±45°/90° CFRP	1.5:−1	Transverse tension[*]	241[a]	12.24[c]

[a]Zinoviev.
[b]Edge.
[c]Chamis (2).
[*]Mode of failure valid for Zinoviev's results only.

CATEGORY

Technology Overview

REFERENCE

Bowler, M. E., "Flywheel Energy Systems: Current Status and Future Prospects," Magnetic Material Producers Association Joint Users Conference, September 22-23, 1997.

SUMMARY

Archeologists describe the flywheel as an early example of industrial automation; it was used in the potter's wheel to enable the production of pottery at a rate faster than hand molding. Later, several forms of engine technology required flywheels for damping the effects of shaft speed fluctuations. More recently, machines such as automobiles and presses have rendered the flywheel ubiquitous. Fundamentally, flywheels are enabling devices, embodying the essence of mechanics. They are universally appreciated as a kinetic store of energy.

Flywheel energy storage grows in proportion to flywheel mass and the square of its rotational velocity. Selection of rotating speed and mass is limited by stress. For a thin rotating ring, the relationship between stress and kinetic energy is

$$2KE = mr^2\omega^2 = m\sigma_h/\rho$$

where m is the mass; r is the mean radius; ω is the rim angular velocity in radians per second; σ_h is the allowable hoop stress; ρ is the density of the selected material; and KE is kinetic energy. This relation suggests that maximum energy storage is achieved by use of materials with very high specific strength, σ_h/ρ. Useful flywheels evolve from thin rings to carefully engineered sections that make effective use of the swept volume, yielding the result

$$2KE = mk^2\omega^2$$

where k is the radius of gyration and mk^2 is therefore I, the polar moment of inertia. This deceptively simple measure requires the flywheel system designer to distribute rotating elements efficiently, considering the ensemble of stresses, final system mass as a measure of storage efficacy, means for rotor suspension, and means for energy extraction and input.

The present resurgence of interest in flywheels centers on complete systems incorporating not only the flywheel energy store, but also a motor-generator, and power conditioning electronics, together with an interface to an application, which may vary from motor vehicle, to super UPS, to a power source for pulse-forming networks. In each of these and other applications, the realization of a practical system requires effective use of several disparate technologies:

- high strength composites;
- high remanence permanent magnets;

- power electronics for VVVF machines;
- high speed bearings.

These technologies are melded together by use of effective system engineering techniques, including systems architecture simulation and analysis. When combined with integrated product development CAD/CAM methods, a useful new product emerges.

COMMENTS

The article concentrates on flywheel use for terrestrial applications. In these uses, the flywheel need only operate for limited amounts of time. Although flywheels have their place in energy storage for long term applications, the article focuses on flywheels for short-term energy sources. Figure 7-10 is a Ragone Diagram that shows the location of different energy storage technologies relative to each other in the context of peak power vs. specific energy.

The composite rotor is a key component in the flywheel assembly. The maximum radial, axial, and hoop stresses must all be taken into account with appropriate knockdown factors to ensure safe operation of the rotor. Radial tensile stress can be reduced by either mass loading the rotor, creating offsetting radial compression, or by assembling the rotor from multiple thin cross-section interference-fit rings. The Trinity mass loaded single thick ring (STR) rotor is shown in Figure 7-11. The rotor is "mass loaded" with Halbach array magnet segments. The mass loading drives the composite into radial compression, resulting in very low levels of radial tensile stress at the design maximum operating speed.

The failure of a flywheel results in the ejection of mass loads and the separation of band segments of the composite rotor. This combination of dense objects moving relatively slowly and large, less dense faster moving objects is such that perforation of the containment mechanism should be prevented by a relatively thin, high tensile strength metal liner. A fully elastic containment device has been developed by reliance on a mixed structure combining a high strength metallic liner with a high strength composite overwrap as shown in Figure 7-12.
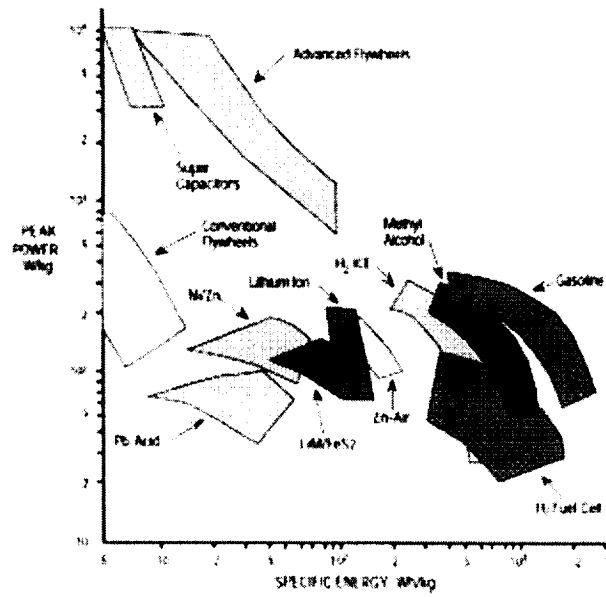
7-21

Figure 7-10: Energy density vs. power density.
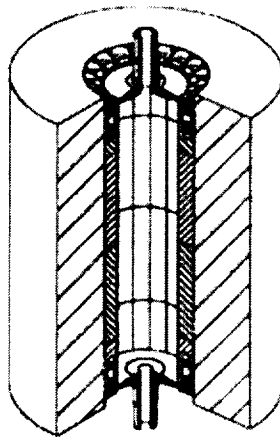
Figure 7-11: Trinity STR rotor.

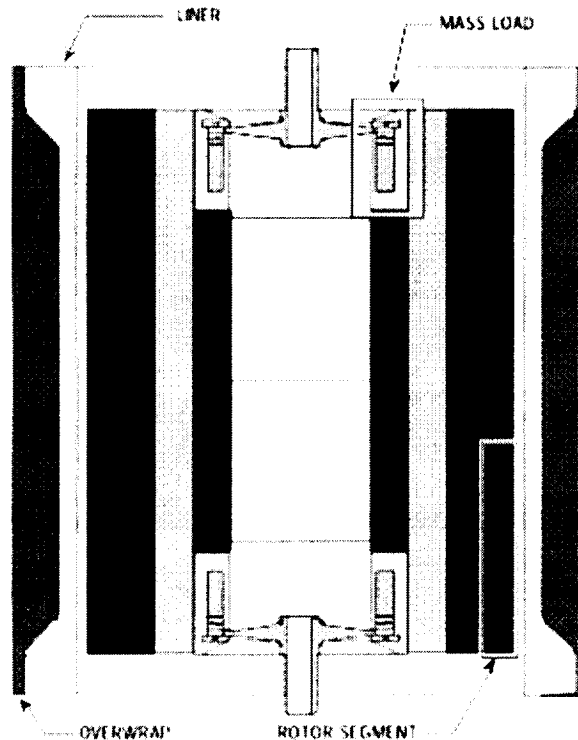**Figure 7-12: Flywheel system rotors will have one or more failure modes, which in turn create one or more forms of containment structural loading. Commercial systems must be capable of 100% containment irrespective of failure mode. This test/prototype containment illustrates an alloy steel liner with a carbon fiber overwrap. End plates, incorporating proprietary elements and therefore not shown, are steel and aluminum.**

Testing

INTRODUCTION

Purpose/Goal
Batteries wear out due to the normal charge/discharge cycling within 3-5 years of operation. Flywheels are expected to have a life expectancy of at least 10 years. Ultimate lifetimes of 20 years are anticipated. The purpose of this program is to develop and demonstrate a flywheel energy storage device on the International Space Station as a flight experiment. The long term goal of this activity is to upgrade the energy storage capability of ISS by replacing degraded batteries with flywheel energy storage units.

Basic Configuration
The basic flywheel demonstration until will consist of two counter-rotating units in a single package to cancel angular momentum affects. Each flywheel will have redundant electro-magnetic bearings. Energy will be passed into and out of the flywheel through a motor/generator that serves as a motor to spin up the flywheel during charge and as a generator to take energy out of the flywheel during discharge. A bi-directional, 3-phase inverter interfaces the motor/generator to the local energy storage bus. All control electronics will be redundant. The development unit is referred to as the Flywheel Energy Storage Demonstrate Unit (FESDU).

Safety
The Development Plan places early emphasis on safety to minimize program risk and cost. Safe operation will be achieved by derating the flywheel. The derating process includes testing to establish the rotation speed where failure occurs; calculating a safety derating factor based on stress-failure analyses; and deriving a maximum safe operating speed.

SUMMARY

The paper's main focus is a comparison of the energy storage capabilities of flywheels versus batteries. Table 7-10 shows a summary of performance factors for chemical batteries currently used on the International Space Station (ISS) and the potential performance of a replacement flywheel string.

The composite rotor is just one component in such a system. In the basic configuration the flywheel rotor will be made of composite materials. It will either be filament-wound or a resin-impregnated woven fabric design. The design is for a maximum operating speed of 60,000 rpm. The initial unit (one to be tested on the ISS before a full scale replacement of the chemical

batteries) will have a fatigue life of two years in LEO. The full scale production models will have a fatigue life of at least ten years.

Safety is an issue, however, and the composite rotor is a very important issue in studies of safety. Health monitoring sensors will also be provided to evaluate the performance of all parameters of the flywheel system, including structure, electromagnetic bearings, the motor/generator, and electronics. Since a massive containment structure is not feasible for most space applications, the basic means of achieving safe operation is to derate the flywheel's maximum speed to well below that which would cause a catastrophic failure. The operating range will probably be approximately 20,000 to 60,000 rpm. A flywheel system will need a lightweight containment structure to protect the flywheel from micrometeorites and other space debris. Such containment will include:

- A vacuum enclosure for the basic rotating device,
- The Battery Charge Discharge Unit (BCDU) enclosure, and
- The Interface Enclosure Unit (enclosed on 5 of 6 sides)

Table 7-10: Key Performance Parameters

	BATTERY STRING	FLYWHEEL STRING
Charge Efficiency	80.0%	98.5%
Discharge Efficiency	100.0%	98.5%
BCDU	91.0%	N/A
Inverter	N/A	96.5%

Note: The round-trip efficiency of the battery is approximately 80%. For convenience we have assumed that all loses are in the charge mode.

7-25

CATEGORY

Technology Overview

REFERENCE

Abacus Technology Corporation, *An Assessment of Flywheel Energy Storage Technology for Hybrid and Electric Vehicles*, 1996.

ABSTRACT

Hybrid and electric vehicles have the potential to provide significant improvements in automotive fuel economy and air pollution emission levels relative to conventional light duty vehicles. These vehicle types will require a safe, low cost, high-performance energy storage system. High-performance flywheels can potentially fill these requirements, and may provide an enabling technology for hybrid and electric vehicles. This report provides an assessment of advance flywheel energy storage technology.

SUMMARY

This report was prepared by Abacus Technology Corporation for the United States Department of Energy, Office of Transportation Technologies, Electric and Hybrid Propulsion Division. Major findings documented in this report that are related to rotors are as follows:

a) **Flywheel safety technology needs to be improved.**

Design approaches for preventing and/or containing flywheel failures need to be improved. An improved understanding of the potential failure modes of high performance flywheels is needed because the design of the containment vessel is strongly dependent on the failure mode and energy of the flywheel. Improved containment vessel design is of significant importance because the weight of the containment vessel can significantly reduce a flywheel system's overall specific power and specific energy performance.

b) **Flywheel cost needs to be reduced.**

Flywheels are expensive primarily due to the cost of high performance fibers used to make fiber composite rotors and the cost of high-power switches used in power electronics. Cost reductions in these areas are essential. Reductions in containment vessel and bearing cost are also important.

c) **Significant advances in flywheel technology are being realized by teams developing flywheels for non-automotive applications.**

Several teams are developing flywheel technology for electric utility and other stationary applications. Significant technological advances are being realized by these groups, and many of these technologies could be readily adapted to flywheels for vehicles.

d) With regard to the Partnership for the New Generation of Vehicles (PNGV) Program Plan, advanced technology flywheel development may be falling behind schedule.

Demonstrating a fully-integrated prototype flywheel by 1998 that meets PNGV program goals will require an aggressive development effort.

e) Low technology flywheel systems may provide the greatest near-term potential, at least in larger vehicles.

Magnet Motor's low-technology hybrid transit bus flywheel system has demonstrated high levels of safety and reliability, and performance approaching the minimum goals of the U.S. hybrid vehicle programs. The Rocketdyne Division of Rockwell International developed a flywheel system using a titanium rotor to meet the modest performance requirements of a hybrid transit bus application. For systems using metal rotors, Rocketdyne has demonstrated reliable containment structures that weigh approximately ¼ of the total system weight.

f) Flywheel development teams are generally working independently, but several very challenging tasks are faced by all and could be appropriate areas for cooperative efforts.

Coordination of "pre-competitive" development efforts and/or increased availability of non-confidential engineering information could potentially accelerate the development pace of advanced flywheels. Technical areas for possible cooperative development are suggested.

Table 7-11 compares the strength, density, theoretical maximum specific energy, and relative maximum specific energy of several flywheel rotor materials. Most advanced rotor designs (Figure 7-13) are made up of several individual rings with different composite materials that are "thermally assembled". The resulting rotor has residual compressive "prestresses" when at rest. These prestresses partially cancel the tensile stresses created when the rotor is spinning at operating speed, allowing the rotor to spin faster, and store more energy than it could without the prestresses. Manufacturing processes for composite rotors are heavily researched and discussed in the report. The forming of the rotor rings by winding epoxy-coated filaments of the fiber material around a mandrel, which is later removed, is currently the process of choice. The number of rings used and the method of assembly are also discussed. This appears to be an ever-evolving technology, however.

Containment of a failed flywheel rotor is also an important issue. The requirement of a robust yet small and lightweight system that completely contains all the debris is an issue in the automotive world also. Some issues that need to be considered when designing a containment system are: rotor burst vs. rotor unraveling, thermal rise, overpressure, chemical explosion, momentum exchange, and external failure initiators.

Rocketdyne has designed a successful containment device for metal rotors. The rotor is designed to fail by yielding, which causes it to expand radially. The rotor would then come in contact with the inner surface of the containment vessel. The friction from this contact would dissipate enough energy to avoid a catastrophic failure. This technology can be applied to lightweight composite rotors as well.

**Table 7-11: Comparison of Candidate Flywheel Rotor Material Properties**

Material	Composite Strength (GPA)*	Composite Density (kg/m^3)	Theoretical Maximum Specific Energy (Wh/kg)	Relative Maximum Specific Energy (Steel = 1.0)
Graphite (fiber) 1995[†]	4.8	1609	414	11.2
Graphite (fiber) 1989[†]	3.4	1609	293	7.9
Spectra® (fiber)	1.4	1039	187	5.1
Kevlar®	1.8	1375	182	4.9
S-glass (fiber)[†]	2.1	2190	133	3.6
E-glass (fiber)[†]	1.8	2205	113	3.1
Silicon-nitride ceramic	0.92	3250	39	1.1
Maraging steel[†]	2.1	7860	37	1.0
Titanium alloy	1.2	4500	37	1.0
7075-T6 aluminum	0.57	2780	28	0.76
Magnesium alloy	0.28	1790	22	0.59

* Ultimate strength for fibers, yield strength for metals, modulus of rupture for ceramic (Kyocera SN252).
[†] Materials commonly used in flywheel rotors to date (circa 1996).
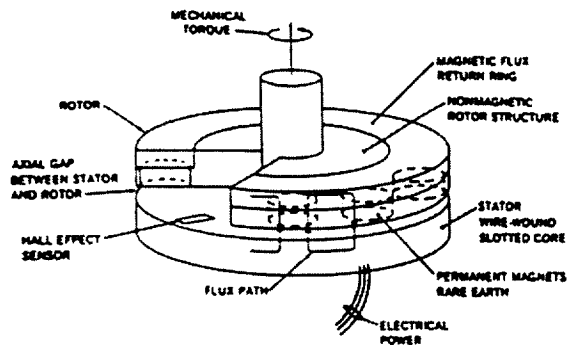
Axial Gap
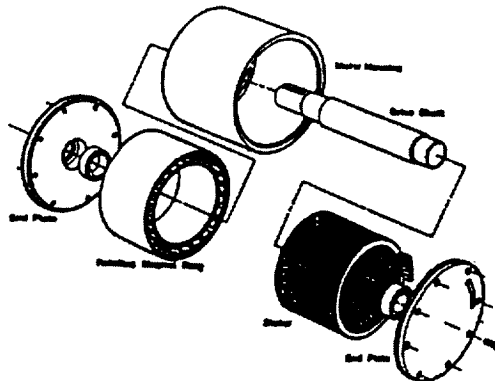
Radial Gap

Sources: Oak Ridge National Laboratory; Unique Mobility

Figure 7-13: Typical motor/generator geometries.

CATEGORY

Structural Integrity

REFERENCE

Grimsley, F. M., "B-2 Structural Integrity Program," 36th AIAA/ASME/ASCE/AHS/ASC Structures, Structural Dynamics, and Materials Conference, AIAA-95-1466, 1995.

ABSTRACT

The B-2 "Stealth" Bomber represents a revolutionary step in the history of aircraft design. Its design combines traditional design drivers blended with stealth technology. The basic mission of the B-2 is to undetected penetration of enemy airspace to hold high value military targets at risk. This mission required a tailored structure that combined non-traditional "flying wing" design with large scale usage of structural composite materials including primary load paths.

The B-2's unique flying wing configuration was built in sections by various subcontractors. A three view drawing of the B-2 is shown in Figure 7-14. The actual size of the B-2 is deceptive, the B-2 is approximately as wide as a B-52 and as long as a F-15. This unique configuration also resulted in a dual structural load path as shown in Figure 7-15. The load distribution from the front and rear load path is approximately 50-50.

The purpose of this paper is to highlight the structural development of the B-2 using the United States Air Force Structural Integrity Program (ASIP) as a guide. The purpose of ASIP is to integrate the design, materials and aircraft expected usage to meet all operational design goals and at the same time create an airframe that is safe and durable for its entire design life. In addition, ASIP provides a force management tool that allows for efficient force management as the fleet ages.

SUMMARY

Laminate Design Allowables

- Ultimate allowable strain not exceeded at Design Ultimate Load
- Maximum Strain Theory

Constant Section Fuel Box Tests

The constant section fuel box tests consisted of an outer portion of the wing. Five were simulated flight loading that exercised the ultimate strength capability of the box with respect to bending, torsion and fuel pressure.

One was tested for durability and damage tolerance. The testing consisted of two lifetimes of fatigue testing followed by one lifetime of damage tolerance testing. The damage tolerance

testing consisted of cycling the box with multiple impacts, saw cuts and other typical types of damage. Insignificant damage growth was observed during testing. Finally, the box was tested to failure with the box failing as predicted.

Outer Wing Test

The outer wing component test consisted of a thirty foot fuel box. At the time of testing (August, 1986), it was the largest all composite structure ever tested. It was a thirty foot section of the outboard wing section and was built to production specifications. The testing consisted of statically testing the wing to fifteen conditions that included both flight and fuel pressure loads. In addition, a residual strength test was conducted after subjecting the wing to impact damage at five critical locations. The wing failed at 122% of design ultimate load which was 10% higher than predicted and impact damage sites were not a factor.

Intermediate Wing Test

The final major component test was the C401 test article, shown in Figure 7-17. The box consisted of a twenty foot sect in of the forward load path located in the intermediate section. It was production representative, contained fuel stimulant and was used to qualify the fuel tank sealing concept. The box was tested for two lifetimes of simulated flight loading with no leaks and no major structural deficiencies. Finally, the box was residually tested after impact damage to 114% of design ultimate load. Impact damage was not a factor in failure, however a test fixture may have contributed.
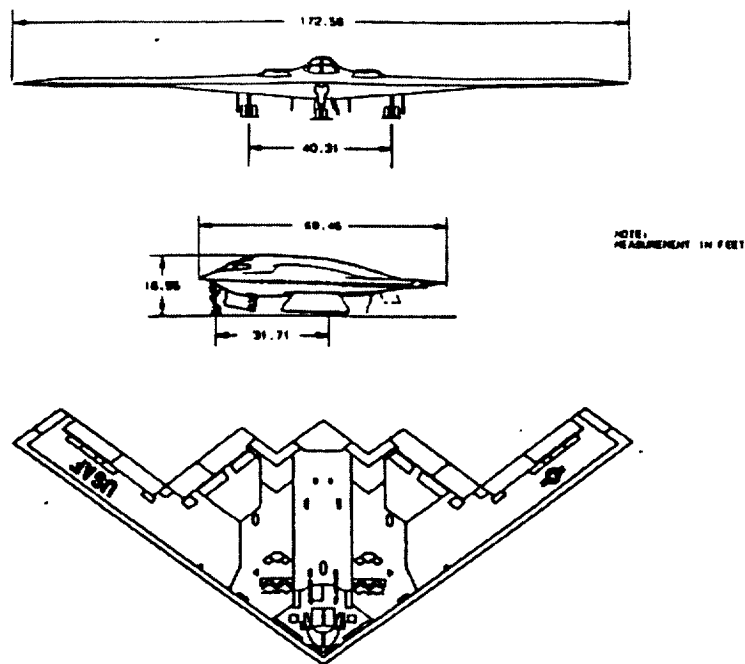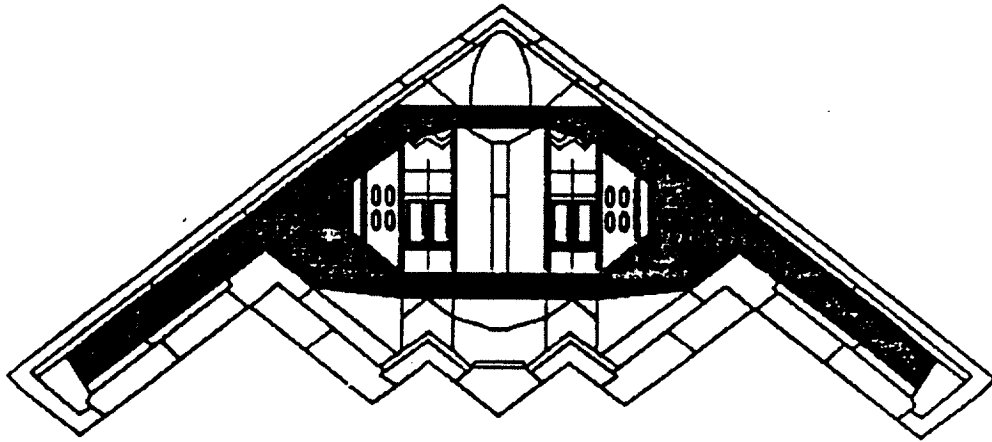

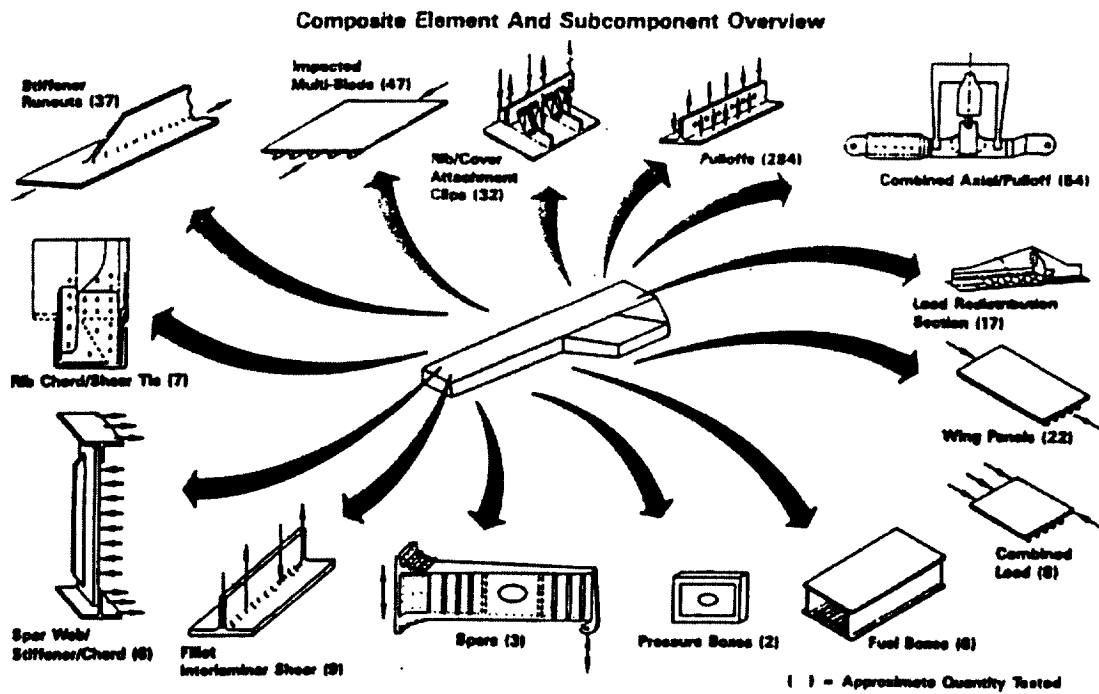**Figure 7-14: Three view of B-2.**

Figure 7-15: B-2 structural load path.

Figure 7-16: Composite element and subcomponent tests.

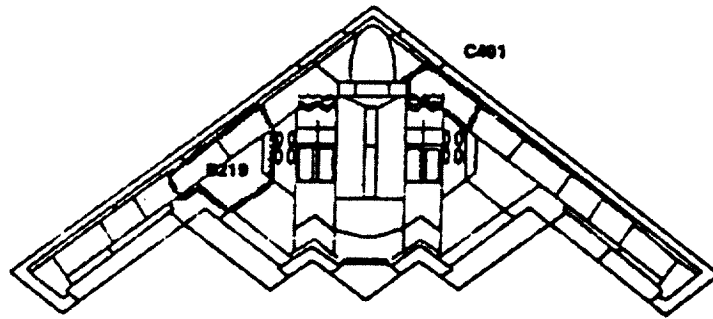**Figure 7-17: Major component tests.**

Analytical Methods

Faupel, J. H., *Engineering Design – A Synthesis of Stress Analysis and Materials Engineering*, John Wiley & Sons, Inc, New York, 1964.

SUMMARY

This text was referenced to find the hoop (σ_h) and radial (σ_r) stress on different types of rotating cylinders.

For a circular disk of uniform thickness rotating about its polar axis of symmetry as shown in Figure 7-18, the stresses are

$$\sigma_h = \frac{3+v}{8(1-v^2)} EN \left(r_i^2 + r_o^2 - \frac{1+3v}{3+v} r^2 + \frac{r_o^2 r_i^2}{r^2} \right)$$

,

$$\sigma_r = \frac{3+v}{8(1-v^2)} EN \left(r_i^2 + r_o^2 - r^2 - \frac{r_o^2 r_i^2}{r^2} \right)$$

where $N = (1 - v^2)(\gamma \omega^2 / gE)$.

The maximum values are

$$(\sigma_h)_{max} = \frac{\gamma \omega^2 r_o^2}{g} \left(\frac{3+v}{4} \right) \left(1 + \frac{1-v}{3+v} \frac{r_i^2}{r_o^2} \right)$$

.

$$(\sigma_r)_{max} = \frac{\gamma \omega^2 r_o^2}{g} \left(\frac{3+v}{8} \right) \left(1 - \frac{r_i}{r_o} \right)^2$$

For a rotating solid disk,

$$\sigma_h = \frac{\gamma \omega^2 r_o^2}{g} \left(\frac{3+v}{8} \right) \left(1 - \frac{1+3v}{3+v} \frac{r^2}{r_o^2} \right)$$

,

$$\sigma_r = \frac{\gamma \omega^2 r_o^2}{g} \left(\frac{3+v}{8} \right) \left(1 - \frac{r^2}{r_o^2} \right)$$

from which

$$(\sigma_h)_{\max} = (\sigma_r)_{\max} = \frac{\gamma \omega^2 r_o^2}{g} \left(\frac{3+v}{8} \right) \ .$$

Likewise, the corresponding equations for rotating cylinders are as follows:

Solid Cylinder:

$$\sigma_r = \frac{3-2v}{8(1-v)} \left(\frac{\gamma \omega^2}{g} \right) (r_o^2 - r^2)$$

$$\sigma_h = \frac{\gamma \omega^2}{8g(1-v)} \left[r_o^2 (3-2v) - r^2 (1-2v) \right]$$

Hollow Cylinder:

$$\sigma_r = \frac{3-2v}{8(1-v)} \left(\frac{\gamma \omega^2}{g} \right) \left[r_o^2 - r_i^2 - r^2 - \left(\frac{r_o r_i}{r} \right)^2 \right]$$

$$\sigma_h = \frac{3-2v}{8(1-v)} \left(\frac{\gamma \omega^2}{g} \right) \left[r_o^2 + r_i^2 + \left(\frac{r_o r_i}{r} \right)^2 - r^2 \left(\frac{1-2v}{3-2v} \right) \right]$$

Flywheels must be properly designed so that when they are active, they rotate within an allowable range. For a solid disk, the allowable speed is

$$\omega_{solid} = \frac{1}{r_o} \sqrt{\frac{8g\sigma_w}{(3+v)\gamma}} \ ,$$

where σ_w is the working stress (a fraction of σ_y, the material yield strength). This function is plotted in Figure 7-19 below.

For a hollow disk the critical location is at the bore, and the allowable speed is

7-34

$$\omega_{hollow} = \left[\frac{8g\sigma_w}{(3+v)\gamma r_o} \left(\frac{1}{2+(r_i/r_o)^2(1-(1+3v)/(3+v))} \right) \right]^{\frac{1}{2}}$$

which is plotted in Figure 7-20. There is also interest in disk rotation beyond the elastic limit in order to obtain a favorable residual stress distribution and so obtain added elastic strength for the same material weight.

The burst speed is another important design consideration and is required in order to assign a realistic factor of safety to the overall structure. Consider a solid cylinder. The rotational speed required to cause the entire thickness to become plastic is

$$\omega_y = (2/r_o)\sqrt{\sigma_y g/\gamma} \quad ,$$

which represents the lower limit of bursting speed. The upper limit is obtained by substituting the material ultimate strength, σ_u, for the yield strength, σ_y, in the above equation, giving

$$\omega_u = (2/r_o)\sqrt{\sigma_u g/\gamma} \quad .$$

Then, by limit analysis

$$\omega_{burst} = \frac{\omega_y + \omega_u}{2} = \frac{\sqrt{g/\gamma}(\sqrt{\sigma_y} + \sqrt{\sigma_u})}{r_o} \quad .$$

Similarly, for a solid disk

$$\omega_y = (\sqrt{3}/r_o)\sqrt{\sigma_y g/\gamma}$$

$$\omega_u = (\sqrt{3}/r_o)\sqrt{\sigma_u g/\gamma}$$

$$\omega_{burst} = \frac{\sqrt{3g/\gamma}}{2r_o}(\sqrt{\sigma_y} + \sqrt{\sigma_u})$$

In the previous equation development, the effect of a boundary force was neglected. An example of a boundary force is the press-fit pressure of a cylinder on a shaft. When boundary forces are present, the resultant stresses are obtained by superposition of the applied boundary stresses and the inertia stresses. In a hollow disk shrunk on a shaft, the radial stress at $r = a$ gives,

$$(\sigma_r)_{max} = \frac{\beta_1 \omega^2 (b^4 - a^4) + a^2 p}{b^2 - a^2} + b^2 \left(\frac{p}{a^2 - b^2} - \beta_1 \omega^2 \right) - \beta_1 \omega^2 a^2$$

,

$$(\sigma_h)_{max} = \frac{\beta_1 \omega^2 (b^4 - a^4) + a^2 p}{b^2 - a^2} - b^2 \left(\frac{p}{a^2 - b^2} - \beta_1 \omega^2 \right) - \beta_1 \omega^2 a^2$$

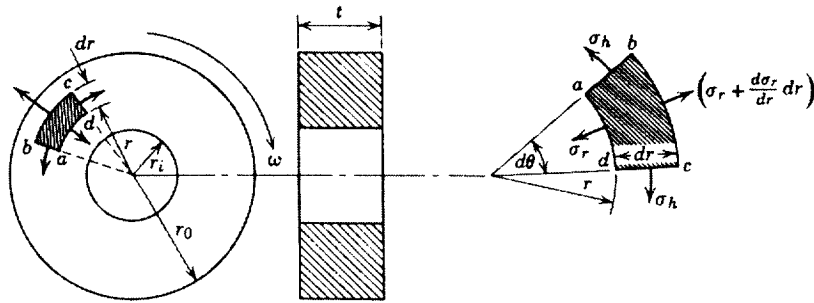where $r = b$ the outer edge, and

$$\beta_1 = \frac{(3 + \nu)\gamma}{8g} \quad .$$

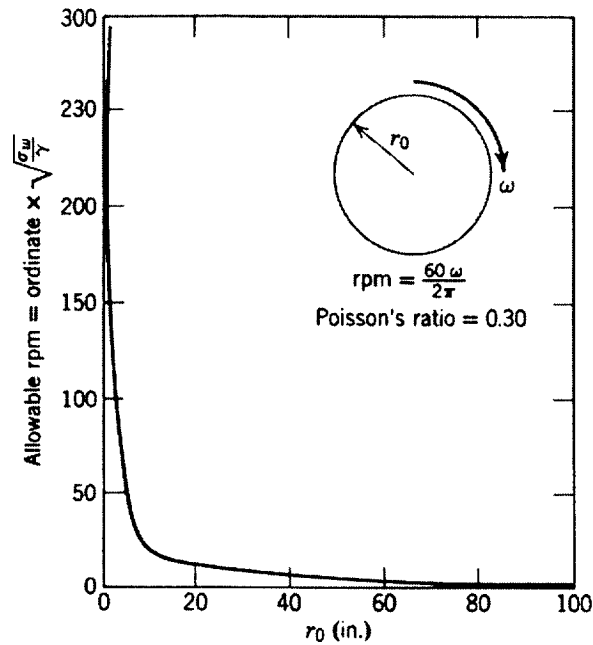Figure 7-18: Geometry and equilibrium of rotating disk.

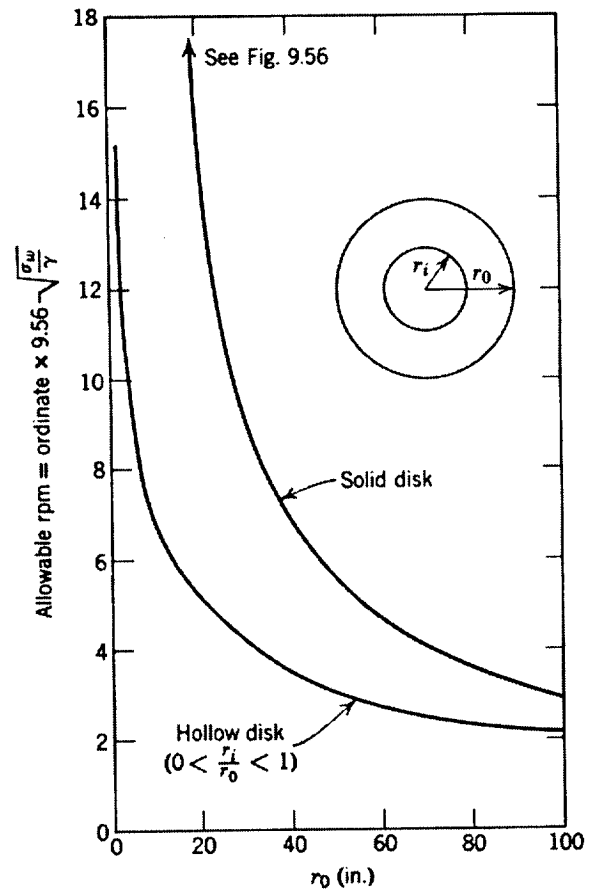Figure 7-19: Design curve for rotating solid disk.

7-36

Figure 7-20: Design curves for rotating disks.

REPORT TITLE

Flywheel Rotor Safe-Life Technology Literature Search Summary

REPORT NO. TOR-2002(2140)-1	PUBLICATION DATE 28 March 2002	SECURITY CLASSIFICATION Unclassified

1. FOR OFF-SITE PERSONNEL, SHOW LOCATION SYMBOL, e.g., JOHN Q. PUBLIC/VAFB

2. IF LIST IS ALTERED, INITIAL CHANGE(S) AND SHOW AFFILIATION *FOR SECRET REPORTS, SHOW BLDG AND ROOM, NOT MAIL STATION

NAME (Include Initials)		MAIL CODE*	NAME (Include Initials)	MAIL CODE*
A. L.	Amram	M4/954		
J. B.	Chang	M4/921		
S. T.	Chiu	M4/912		
D. A.	Christopher	M4/940		
E. K.	Hall	M4/921		
A. R.	Hopkins	M2/242		
H. A.	Katzman	M2/248		
A. C.	Liang	M4/945		
S. R.	Lin	M4/912		
R. A.	Lipeles	M2/242		
N. E.	Martino	M4/912		
D. C.	Marvin	ACP/507		
I. A.	Min	M4/940		
T. J.	Mosher	M4/940		
P. B.	Pollock	M4/912		
J.K.H.	Ratner	M4/921		
E. R.	Scheyhing	M4/899		
G. N.	Smit	M4/954		
R. J.	Zaldivar	M2/242		
	AOLIB (4, 5522, 231, SG)	M1/199		

FINAL APPROVER DRAW LINE(S) ACROSS UNFILLED SPACE AND INITIAL TO PRECLUDE ADDITIONS

APPROVED _____ DATE _5/27/02_

IF LIST COMPRISES TWO OR MORE SHEETS, COMPLETE ABOVE BLOCK ON LAST SHEET ONLY

REPORT TITLE
FLYWHEEL ROTOR SAFE-LIFE TECHNOLOGY LITERATURE SEARCH SUMMARY

REPORT NO. TOR-2002(2140)-1	PUBLICATION DATE April 2002	SECURITY CLASSIFICATION Unclassified

MILITARY AND GOVERNMENT OFFICES	ASSOCIATE CONTRACTORS AND OTHERS

1. SHOW FULL MAILING ADDRESS: INCLUDE ZIP CODE, MILITARY OFFICE SYMBOL, AND "ATTENTION" LINE.
2. IF LIST IS ALTERED, INITIAL CHANGE(S) AND SHOW AFFILIATION.

Air Force Research Lab.
Kirtland Air Force Base
3550 Aberdeen Ave.
Albuquerque, NM 87117
Attn: Jerry Fausz
    2nd Lt. Kathryn Parker,
    Space Vehicle   Directorate

NASA Center for Aerospace Information
    Acquisitions (13)
7121 Standard Drive
Hanover, MD 21076-1320

NASA Glenn Research Center
2100 Brookpark Road
Cleveland, OH 44135-3127
Attn: George Baaklini, MS 6-1
    Kevin Konno, MC 86-15

NASA Glenn Research Center
2100 Brookpark Road
Cleveland, OH 44135-3191
Attn: Indyne Publ Coord Office, MS 21-8
    Library Acquisitions, MS 60-3 (2)

NASA/GRC at Lewis
Power Systems Project Office
21000 Brookpark Rd, 500-203
Cleveland, OH 44135-3127
Attn: Kerry McLallian

U. S. Army Research Lab
Aberdeen Proving Ground, MD 21005-5066
Attn: Jerome Tzeng

Barbour Stockwell, Inc.
55 Sixth Road
Woburn, MA 01801
Attn: Kenneth Mailler

Beacon Power
234 Ballardvale Street
Wilmington, MA 01887
Attn: Michael Favaloro

Boeing Corporation
P. O. Box 3999
Seattle, WA 98124
Attn: Arthur Day, MS 73-09
    Jim Schindler, MS 73-09

Center for Electromechanics
University of Texas at Austin
Austin, TX 78712
Attn: Richard Thompson, PRC Mail Code R7000

Flywheel Energy Systems, Inc.
25C Northside Road
Nepean, ON
Canada, K2H 8S1
Attn: Dean Flanagan

Honeywell Engine and Systems
1300 W. Warner Road
Tempe, AZ 85284
Attn: Joseph Klupar

FINAL APPROVER DRAW LINE(S) ACROSS UNFILLED SPACE AND INITIAL TO PRECLUDE ADDITIONS

DISTRIBUTION LIMITATIONS MARKED ON THE COVER/TITLE PAGE ARE AUTHORIZED BY SIGNATURE BELOW

APPROVED _____ DATE _____
(AEROSPACE)

APPROVED BY _____ DATE _____
(AF OFFICE)   (NOT REQUIRED FOR ATR CATEGORY)

IF LIST COMPRISES TWO OR MORE SHEETS, COMPLETE ABOVE BLOCK ON LAST SHEET ONLY

AEROSPACE FORM 2380 REV 11-85

REPORT TITLE

FLYWHEEL ROTOR SAFE-LIFE TECHNOLOGY LITERATURE SEARCH SUMMARY

REPORT NO. TOR-2002(2140)-1	PUBLICATION DATE April 2002	SECURITY CLASSIFICATION Unclassified

MILITARY AND GOVERNMENT OFFICES	ASSOCIATE CONTRACTORS AND OTHERS

1. SHOW FULL MAILING ADDRESS: INCLUDE ZIP CODE, MILITARY OFFICE SYMBOL, AND "ATTENTION" LINE.
2. IF LIST IS ALTERED, INITIAL CHANGE(S) AND SHOW AFFILIATION.

John Coyner
10061 S. Deer Creek Road
Littleton, CO 80127

Lincoln Composites
4300 Industrial Avenue
Lincoln, NE 68504
Attn: Alvin Cederberg

Lockheed Martin
Commercial Space Systems
100 Campus Drive
Newtown, PA 18940
Attn: Robert Bauer, MS 250-A

National Research Council
Montreal Road
Ottowa, ON
Canada K1A OR6
Attn: David Zimcik

Oak Ridge National Lab
P. O. Box 2009
Oak Ridge, TN 37831-8051
Attn: Jim Hansen

Pennsylvania State University
212 Earth-Energy Science Building
University Park, PA 16802
Attn: Charles Bakis

Test Devices, Inc.
6 Loring Street
Hudson, MA 01749
Attn: Eric Sonnichsen

Toray Composites America Inc.
19002 50th Ave. East
Tacoma, WA 98446
Attn: Dave Cohen

FINAL APPROVER DRAW LINE(S) ACROSS UNFILLED SPACE AND INITIAL TO PRECLUDE ADDITIONS

DISTRIBUTION LIMITATIONS MARKED ON THE COVER/TITLE PAGE ARE AUTHORIZED BY SIGNATURE BELOW

APPROVED _____ DATE 5/31/02
(AEROSPACE)

APPROVED BY _____ DATE 6/13/02
(AF OFFICE)   (NOT REQUIRED FOR ATR CATEGORY)

IF LIST COMPRISES TWO OR MORE SHEETS, COMPLETE ABOVE BLOCK ON LAST SHEET ONLY

REPORT DOCUMENTATION PAGE

Public reporting burden for this collection of information is estimated to average 1 hour per response, including the time for reviewing instructions, searching existing data sources, gathering and maintaining the data needed, and completing and reviewing the collection of information. Send comments regarding this burden estimate or any other aspect of this collection of information, including suggestions for reducing this burden, to Washington Headquarters Services, Directorate for Information Operations and Reports, 1215 Jefferson Davis Highway, Suite 1204, Arlington, VA 22202-4302, and to the Office of Management and Budget, Paperwork Reduction Project (0704-0188), Washington, DC 20503.

1. AGENCY USE ONLY (Leave blank)	2. REPORT DATE	3. REPORT TYPE AND DATES COVERED
	July 2002	Final Contractor Report

4. TITLE AND SUBTITLE

Flywheel Rotor Safe-Life Technology
Literature Search Summary

5. FUNDING NUMBERS

WU–755–1A–09–00
F04701–00–C–0009

6. AUTHOR(S)

J.K.H. Ratner, J.B. Chang, and D.A. Christopher

7. PERFORMING ORGANIZATION NAME(S) AND ADDRESS(ES)

Aerospace Corporation
Engineering and Technology Group
El Segundo, California

8. PERFORMING ORGANIZATION REPORT NUMBER

E–13506

9. SPONSORING/MONITORING AGENCY NAME(S) AND ADDRESS(ES)

National Aeronautics and Space Administration
Washington, DC 20546–0001

10. SPONSORING/MONITORING AGENCY REPORT NUMBER

NASA CR—2002-211810
TOR–2002(2140)–1

11. SUPPLEMENTARY NOTES

Project Manager, Kerry L. McLallin, Power and Propulsion Office, NASA Glenn Research Center, organization code 6910, 216–433–5389.

12a. DISTRIBUTION/AVAILABILITY STATEMENT

Unclassified - Unlimited
Subject Category: 24   Distribution: Nonstandard

Available electronically at http://gltrs.grc.nasa.gov

This publication is available from the NASA Center for AeroSpace Information, 301–621–0390.

12b. DISTRIBUTION CODE

13. ABSTRACT (Maximum 200 words)

Since the 1960s, research has been conducted into the use of flywheels as energy storage systems. The proposed applications include energy storage for hybrid and electric automobiles, attitude control and energy storage for satellites, and uninterruptible power supplies for hospitals and computer centers. For many years, however, the use of flywheels for space applications was restricted by the total weight of a system employing a metal rotor. With recent technological advances in the manufacturing of composite materials, however, lightweight composite rotors have begun to be proposed for such applications. Flywheels with composite rotors provide much higher power and energy storage capabilities than conventional chemical batteries. However, the failure of a high speed flywheel rotor could be a catastrophic event. For this reason, flywheel rotors are classified by the NASA Fracture Control Requirements Standard as fracture critical parts. Currently, there is no industry standard to certify a composite rotor for safe and reliable operation for the required lifetime of the flywheel. Technical problems hindering the development of this standard include composite manufacturing inconsistencies, insufficient nondestructive evaluation (NDE) techniques for detecting defects and/or impact damage, lack of standard material test methods for characterizing composite rotor design allowables, and no unified proof (over-spin) test for flight rotors. As part of a flywheel rotor safe-life certification program funded by the government, a review of the state of the art in composite rotors is in progress. The goal of the review is to provide a clear picture of composite flywheel rotor technologies. The literature review has concentrated on the following topics concerning composites and composite rotors: durability (fatigue) and damage tolerance (safe-life) analysis/test methods, in-service NDE and health monitoring techniques, spin test methods/procedures, and containment options. This report presents the papers selected for their relevance to this topic and summarizes them.

14. SUBJECT TERMS

Flywheels; Rotors; Composite materials; Carbon fibers; Material tests; Fatigue tests; Nondestructive tests

15. NUMBER OF PAGES

266

16. PRICE CODE

17. SECURITY CLASSIFICATION OF REPORT	18. SECURITY CLASSIFICATION OF THIS PAGE	19. SECURITY CLASSIFICATION OF ABSTRACT	20. LIMITATION OF ABSTRACT
Unclassified	Unclassified	Unclassified	